MECHANICAL PROPERTIES AND PERFORMANCE OF A NOVEL NANO-ENGINEERED UNITIZED COMPOSITE FOR AEROSPACE SYSTEMS

THESIS

Benjamin C. Lam, Second Lieutenant, USAF

AFIT-ENY-MS-21-M-306

DEPARTMENT OF THE AIR FORCE
AIR UNIVERSITY

AIR FORCE INSTITUTE OF TECHNOLOGY

Wright-Patterson Air Force Base, Ohio

AFIT-ENY-MS-21-M-306

MECHANICAL PROPERTIES AND PERFORMANCE OF A NOVEL NANO-ENGINEERED UNITIZED COMPOSITE FOR AEROSPACE SYSTEMS

THESIS

Presented to the Faculty

Department of Aeronautics and Astronautics

Graduate School of Engineering and Management

Air Force Institute of Technology

Air University

Air Education and Training Command

In Partial Fulfillment of the Requirements for the

Degree of Master of Science in Material Science

Benjamin C. Lam, BS

Second Lieutenant, USAF

March 2021

AFIT-ENY-MS-21-M-306

MECHANICAL PROPERTIES AND PERFORMANCE OF A NOVEL NANO-ENGINEERED UNITIZED COMPOSITE FOR AEROSPACE SYSTEMS

Benjamin C. Lam, BS

Second Lieutenant, USAF

Committee Membership:

Dr. Marina Ruggles-Wrenn
Chair

Major John Brewer
Member

Dr. Eric Jones
Member

Abstract

Carbon nanotubes (CNTs) exhibit outstanding mechanical properties, such as exceptionally high tensile stiffness and strength, combined with excellent electrical and thermal characteristics. The challenge is to implement the carbon nanotubes and their exceptional characteristics into macroscopic composites for aerospace applications. This research investigates the mechanical properties and performance of a newly developed hybrid nano-engineered composite. The carbon fiber/polymer matrix composite studied in this effort incorporates a forest of vertically aligned CNTs called NanoStitch. The NanoStitch reinforcement is inserted between plies of the carbon fiber/epoxy prepreg with CNTs oriented normal to the fiber direction. A control polymer matrix composite (PMC) without NanoStitch reinforcement was also studied in order to assess the effects of the NanoStitch layers on the composite's mechanical properties and performance. Basic tensile properties of both material systems were investigated for both on-axis [0/90] and off-axis [±45] fiber orientations at room temperature. Tension-tension fatigue tests were performed with a frequency of 1.0 Hz and a ratio of minimum stress to maximum stress of R= 0.05. Fatigue run-out was set to $2x10^5$ cycles. In addition to constructing fundamental fatigue S-N diagrams, strain accumulation and modulus change with cycles in each fatigue test were examined. The presence of the NanoStitch reinforcement did not result in a decrease in tensile properties compared to the control PMC. For both 0/90 and ±45 fiber orientations the two material systems produced similar values of the tensile modulus and ultimate tensile strength. Likewise, the two material systems exhibit similar

fatigue resistance. The presence of the NanoStitch reinforcement did not decrease the fatigue limit nor degraded cyclic life of the composite. Additionally, creep and recovery tests were performed to study the time-dependent deformation behavior of the nano-engineered composite with ±45 fiber orientation. The test results were analyzed in context of Schapery's nonlinear viscoelastic model. The model was successfully characterized and validated using experimental data. Thus it was determined that Schapery's viscoelastic deformation theory can be used to predict the off-axis deformation behavior of the hybrid nano-engineered composite.

Acknowledgments

I would like to express my sincere appreciation to my faculty advisor, Dr. Marina Ruggles-Wrenn, for her guidance and support throughout the course of this thesis effort. The insight and experience was certainly appreciated.

2d Lt Benjamin C. Lam

Table of Contents

Page

ABSTRACT ..... **IV**

TABLE OF CONTENTS ..... **VII**

LIST OF FIGURES ..... **X**

LIST OF TABLES ..... **XXVIII**

I. INTRODUCTION **1**

1.1 MOTIVATION 1

1.2 PROBLEM STATEMENT 2

1.3 RESEARCH OBJECTIVES/QUESTIONS/HYPOTHESES 3

1.4 METHODOLOGY 4

II. BACKGROUND **6**

2.1 COMPOSITES OVERVIEW 6

2.2 FIBER REINFORCED POLYMER COMPOSITES/POLYMER MATRIX COMPOSITES 7

2.2.1 Common Commercial Carbon Fibers *8*

2.3 COMPOSITE TENSILE AND FATIGUE RESPONSE 8

2.4 COMPOSITE LAYUP 10

2.5 3D REINFORCEMENT 11

2.6 HYBRID COMPOSITE WITH NANOSTITCH REINFORCEMENT - PREVIOUS RESEARCH 12

2.6.1 Tension Bearing Strength Research *13*

2.6.2 Failure Mechanics Research. 14

III. MATERIAL AND TEST SPECIMEN 16

3.1 FIBER REINFORCED POLYMER COMPOSITE 16

3.2 CARBON NANOTUBE FOREST 17

3.3 TEST SPECIMEN DIMENSIONS 18

3.4 TEST SPECIMEN PREPARATION 18

IV. EXPERIMENTAL SETUP AND TESTING PROCEDURES 21

4.1 TESTING EQUIPMENT 21

4.2 MECHANICAL TEST PROCEDURES 23

4.2.1 Uniaxial Tension to Failure Tests. 23

4.2.2 Tension-Tension Cyclic Fatigue Tests. 23

4.3 CHARACTERIZATION OF SCHAPERY'S NONLINEAR VISCOELASTIC MODEL 25

4.4 OPTICAL MICROSCOPY 27

V. EXPERIMENTAL RESULTS AND DISCUSSION 29

5.1 ASSESSMENT OF SPECIMEN-TO-SPECIMEN VARIABILITY 29

5.2 UNIAXIAL TENSION TO FAILURE TESTS 30

5.2.1 Tension to Failure Testing of 0/90 Composites. 30

5.2.2 Tension to Failure Tests of ±45 Composites. 35

5.3 TENSION-TENSION FATIGUE TESTS 38

5.3.1 Tension-Tension Fatigue Testing of 0/90 Composites. 38

5.3.2 0/90 Retained Properties. 45

5.3.3 Tension-Tension Fatigue Testing of ±45 Composites. 46

5.3.4 ±45 Retained Properties. *56*

5.4 SCHAPERY'S NONLINEAR VISCOELASTIC MODEL – FORMULATION AND CHARACTERIZATION 59

5.5 OPTICAL MICROSCOPY ANALYSIS 70

VI. CONCLUSIONS AND RECOMMENDATIONS 76

6.1 CONCLUSIONS OF RESEARCH 76

6.3 RECOMMENDATIONS FOR FUTURE RESEARCH 77

APPENDIX: ADDITIONAL OPTICAL MICROGRAPHS 79

BIBLIOGRAPHY 139

List of Figures

Figure Page

Figure 1: Stress-strain curve from specimen NS-02-06 showing that the modulus is found from the slope of the curve in the linear region and the UTS is found from the maximum stress experienced by the specimen, represented by the dashed line..... 9

Figure 2: Stress (S) vs. logarithm of cycles (N). (a) S-N Curve of a material with a fatigue limit. (b) S-N Curve of a material without a fatigue limit [6] Reproduced from Material Science and Engineering: An Introduction, Figure 8.19, Copyright©, with permission from Wiley..... 10

Figure 3: (Left) Schematic of single sheet layup. (Right) Schematic of four sheet quasi-isotropic layup [6]. Reproduced from Material Science and Engineering: An Introduction, Figure 16.16, Copyright©, with permission from Wiley. 11

Figure 4: (left) Schematic of vertically aligned carbon nanotube reinforcements. (right) Schematic of nanotube reinforcements grown directly on the fibers. Reproduced from [1]. 12

Figure 5: Bearing stress-strain curves for tension-bearing tests. For comparative purposes, the curves of the different specimens are offset on the x axis [11]. Reproduced from In-Plane Strength Enhancement of Laminated Composites via Aligned Carbon Nanotube Interlaminar Reinforcement, Figure 4, Copyright©, with permission from Elsevier..... 13

Figure 6: Post-failure SEM image of cracked baseline (left) and NanoStitched (right) material. The red line is the crack path [10]. Reproduced from Interlaminar to Intralaminar Mode I and II Crack Bifurcation Due to Aligned Carbon Nanotube

Reinforcement of Aerospace-Grade Advanced Composites, Figure 4, Copyright©, with permission from Elsevier. 15
Figure 7: Dogbone-shaped test specimen. All dimensions in inches..... 18
Figure 8: (a) Top and (b) side view of specimen with fiberglass tabs applied 20
Figure 9: Picture of the: (a) MTS testing unit used to test samples, (b) load cell with sample, (c) 10-mm gauge Extensometer, (d) 8-mm gauge Extensometer. 22
Figure 10: Schematic of a creep and recovery test. (a) stress input and (b) strain response 26
Figure 11: Zeiss SteREO optical microscope and associated equipment 28
Figure 12: Tensile stress-strain curves obtained for 0/90 baseline composite at room temperature in laboratory air 31
Figure 13: Tensile stress-strain curves obtained for 0/90 NanoStitch composite at room temperature in laboratory air 32
Figure 14: A comparison of the tensile stress-strain curves obtained for 0/90 baseline composite and 0/90 NanoStitch composite. 33
Figure 15: Linear region of the tensile stress-strain curves obtained for three 0/90 baseline composite specimens and three 0/90 NanoStitch composite specimens. The linear regions of the tensile stress-strain curves were used to determine the elastic modulus values for each test specimen. 34
Figure 16: Typical tensile stress-strain curve obtained for ±45 baseline composite at room temperature in laboratory air. 36
Figure 17: Typical tensile stress-strain curve obtained for ±45 NanoStitch composite at room temperature in laboratory air. 37

Figure 18: Fatigue S-N curves for baseline and NanoStitch specimens with 0/90 fiber orientation 39

Figure 19: Typical hysteresis stress-strain response of the NanoStitch specimens with 0/90 fiber orientation that achieved runout of 200,000 cycles. Hysteresis stress-stain loops for cycles 100 to 200,000 are shifted by 0.001 m/m for presentation purposes. 40

Figure 20: Hysteresis stress-strain response of the NanoStitch specimen with 0/90 fiber orientation tested in fatigue with the maximum stress of 997 MPa (90% UTS), N_f = 158,023 cycles. Hysteresis stress-strain loops for cycles 1000 to 150,000 are each shifted by 0.001 m/m along the strain axis for presentation purposes. 42

Figure 21: Normalized modulus vs. fatigue cycles for the baseline composite specimens and the NanoStitch composite specimens with 0/90 fiber orientation 43

Figure 22: Strain accumulation with fatigue cycles for the baseline composite specimens and the NanoStitch composite specimens with 0/90 fiber orientation 44

Figure 23: Effects of prior fatigue on tensile stress-strain behavior of the baseline composite and the NanoStitch composite with 0/90 fiber orientation 46

Figure 24: Fatigue S-N curves for baseline and NanoStitch specimens with ±45 fiber orientation. Arrow indicates that failure of specimen did not occur when the test was terminated. 49

Figure 25: Fatigue S-N curves for baseline and NanoStitch specimens with 0/90 and ±45 fiber orientation. Arrow indicates that failure of specimen did not occur when the test was terminated. Maximum stress is shown as %UTS 50

Figure 26: Hysteresis stress-strain response of the baseline specimen with ±45 fiber orientation (σ_{max} = 159 MPa, N_f = 18,384). Hysteresis stress-strain loops for cycles 100 to 10,000 are each shifted by 0.001 m/m along the strain axis for presentation purposes. 51

Figure 27: Normalized modulus vs. fatigue cycles for the baseline composite specimens with ±45 fiber orientation. Specimens B-05-24 and B-05-05 achieved fatigue runout of 200,000 cycles without failure. 52

Figure 28: Normalized modulus vs. fatigue cycles for the NanoStitch composite specimens with ±45 fiber orientation. Specimens NS-02-03 and NS-02-06 achieved runout of 200,00 cycles without failure. 53

Figure 29: Strain accumulation with fatigue cycles for the baseline composite specimens with ±45 fiber orientation. Specimens B-05-24 and B-05-05 achieved fatigue runout of 200,000 cycles without failure. 55

Figure 30: Strain accumulation with fatigue cycles for the NanoStitch composite specimens with ±45 fiber orientation. Specimens NS-02-03 and NS-02-06 achieved fatigue runout of 200,000 cycles without failure. 56

Figure 31: Effects of prior fatigue on tensile stress-strain behavior of (a) the baseline composite and (b) the NanoStitch composite with ±45 fiber orientation 58

Figure 32: Strain vs. time curves obtained for the NanoStitch composite specimens with ±45 fiber orientation during the creep portion of the creep and recovery tests performed with creep stress of 37 MPa (15% UTS), 49 MPa (20% UTS), 74 MPa (30% UTS), 98 MPa (40% UTS), 123 MPa (50% UTS), and 147 MPa (60% UTS). 63

Figure 33: Isochronous stress-strain curves based on the strain vs. time data obtained for the NanoStitch composite specimen with ±45 fiber orientation during the creep portion of the creep and recovery tests performed with creep stresses of 37 MPa (15% UTS), 49 MPa (20% UTS), 74 MPa (30% UTS), 98 MPa (40% UTS), 123 MPa (50% UTS), and 147 MPa (60% UTS). 64

Figure 34: Creep at 147 MPa (60% UTS). A comparison between experimental data (solid black line) and predicted strain response (solid red line)..... 68

Figure 35: A comparison between experimental and predicted creep curves obtained for the NanoStitch composite with ±45 fiber orientation at 74 MPa (30% UTS), 98 MPa (40% UTS), and 147 MPa (60% UTS). 69

Figure 36: Stitched images of the 0/90 baseline composite specimen B-02-15 tested in tension to failure. (a-b) face view and (c-d) side view. 70

Figure 37: Stitched images of the 0/90 NanoStitch composite specimen NS-07-26 tested in tension to failure. (a-b) face view and (c-d) side view. 71

Figure 38: Stitched images of the 0/90 baseline composite specimen B-02-16 tested in tension-tension fatigue (σ_{max} = 827 MPa, N_f > 200,000 – fatigue runout), then failed in a tension test. (a) face view and (b) side view. 72

Figure 39: Stitched images of the 0/90 NanoStitch composite specimen NS-07-08 tested in tension-tension fatigue (σ_{max} = 887 MPa, N_f > 200,000 – fatigue runout), then failed in a tension test. (a) face view and (b) side view. 72

Figure 40: Stitched images of the ±45 baseline composite specimen B-05-10 tested in tension-tension fatigue (σ_{max} = 194 MPa, N_f = 10). (a) face view and (b) side view. 73

Figure 41: Stitched images of the ±45 NanoStitch composite specimen NS-02-25 tested in tension-tension fatigue (σ_{max} = 151 MPa, N_f = 20,831). (a) face view and (b) side view. 74
Figure 42: Stitched images of the ±45 baseline composite specimen B-05-05 tested in tension-tension fatigue (σ_{max} = 131 MPa, N_f > 200,000 – fatigue runout), then failed in a tension test. (a) face view and (b) side view. 74
Figure 43: Stitched images of the ±45 NanoStitch composite specimen NS-02-11 tested in tension-tension fatigue (σ_{max} = 163 MPa, N_f = 7,433). (a) face view and (b) side view. 75
Figure 44: Images of the 0/90 baseline composite specimen B-02-22 tested in tension to failure. (a-e) face view. 79
Figure 45: Images of the 0/90 baseline composite specimen B-02-22 tested in tension to failure. (a-d) face view. 79
Figure 46: Images of the 0/90 baseline composite specimen B-02-22 tested in tension to failure. (a-d) side view. 80
Figure 47: Images of the 0/90 baseline composite specimen B-02-22 tested in tension to failure. (a-d) side view. 80
Figure 48: Images of the 0/90 baseline composite specimen B-02-12 tested in tension to failure. (a-e) face view. 81
Figure 49: Images of the 0/90 baseline composite specimen B-02-12 tested in tension to failure. (a-d) face view. 81
Figure 50: Images of the 0/90 baseline composite specimen B-02-12 tested in tension to failure. (a-e) side view..... 82

Figure 51: Images of the 0/90 baseline composite specimen B-02-12 tested in tension to failure. (a-d) side view. 82
Figure 52: Images of the ±45 baseline composite specimen B-05-06 tested in tension to failure. (a-c) face view. 83
Figure 53: Images of the ±45 baseline composite specimen B-05-06 tested in tension to failure. (a-c) face view. 83
Figure 54: Images of the ±45 baseline composite specimen B-05-06 tested in tension to failure. (a-c) side view..... 83
Figure 55: Images of the ±45 baseline composite specimen B-05-06 tested in tension to failure. (a-c) side view..... 84
Figure 56: Images of the ±45 baseline composite specimen B-05-15 tested in tension to failure. (a-c) face view. 84
Figure 57: Images of the ±45 baseline composite specimen B-05-15 tested in tension to failure. (a-c) face view. 84
Figure 58: Images of the ±45 baseline composite specimen B-05-15 tested in tension to failure. (a-c) side view..... 85
Figure 59: Images of the ±45 baseline composite specimen B-05-15 tested in tension to failure. (a-c) side view..... 85
Figure 60: Images of the ±45 baseline composite specimen B-05-19 tested in tension to failure. (a-c) face view. 85
Figure 61: Images of the ±45 baseline composite specimen B-05-19 tested in tension to failure. (a-c) face view. 86

Figure 62: Images of the ±45 baseline composite specimen B-05-19 tested in tension to failure. (a-c) side view. 86
Figure 63: Images of the ±45 baseline composite specimen B-05-19 tested in tension to failure. (a-c) side view. 86
Figure 64: Images of the 0/90 NanoStitch composite specimen NS-07-07 tested in tension to failure. (a-e) face view. 87
Figure 65: Images of the 0/90 NanoStitch composite specimen NS-07-07 tested in tension to failure. (a-d) face view. 87
Figure 66: Images of the 0/90 NanoStitch composite specimen NS-07-07 tested in tension to failure. (a-d) side view. 88
Figure 67: Images of the 0/90 NanoStitch composite specimen NS-07-07 tested in tension to failure. (a-d) side view. 88
Figure 68: Images of the 0/90 NanoStitch composite specimen NS-07-17 tested in tension to failure. (a-e) face view. 89
Figure 69: Images of the 0/90 NanoStitch composite specimen NS-07-17 tested in tension to failure. (a-e) face view. 89
Figure 70: Images of the 0/90 NanoStitch composite specimen NS-07-17 tested in tension to failure. (a-d) side view. 90
Figure 71: Images of the 0/90 NanoStitch composite specimen NS-07-17 tested in tension to failure. (a-e) side view. 90
Figure 72: Images of the ±45 NanoStitch composite specimen NS-02-02 tested in tension to failure. (a-c) face view. 91

Figure 73: Images of the ±45 NanoStitch composite specimen NS-02-02 tested in tension to failure. (a-c) face view. 91
Figure 74: Images of the ±45 NanoStitch composite specimen NS-02-02 tested in tension to failure. (a-b) side view. 91
Figure 75: Images of the ±45 NanoStitch composite specimen NS-02-02 tested in tension to failure. (a-b) side view. 92
Figure 76: Images of the ±45 NanoStitch composite specimen NS-02-12 tested in tension to failure. (a-d) face view. 92
Figure 77: Images of the ±45 NanoStitch composite specimen NS-02-12 tested in tension to failure. (a-c) face view. 93
Figure 78: Images of the ±45 NanoStitch composite specimen NS-02-12 tested in tension to failure. (a-e) face view. 93
Figure 79: Images of the ±45 NanoStitch composite specimen NS-02-12 tested in tension to failure. (a-d) face view. 94
Figure 80: Images of the ±45 NanoStitch composite specimen NS-02-12 tested in tension to failure. (a-c) side view. 94
Figure 81: Images of the ±45 NanoStitch composite specimen NS-02-12 tested in tension to failure. (a-f) side view. 95
Figure 82: Images of the ±45 NanoStitch composite specimen NS-02-20 tested in tension to failure. (a-c) face view. 95
Figure 83: Images of the ±45 NanoStitch composite specimen NS-02-20 tested in tension to failure. (a-c) face view. 96

Figure 84: Images of the ±45 NanoStitch composite specimen NS-02-20 tested in tension to failure. (a-b) side view. 96
Figure 85: Images of the ±45 NanoStitch composite specimen NS-02-20 tested in tension to failure. (a-b) side view. 96
Figure 86: Images of the ±45 NanoStitch composite specimen NS-02-07 tested in tension to failure. (a-c) face view. 97
Figure 87: Images of the ±45 NanoStitch composite specimen NS-02-07 tested in tension to failure. (a-c) face view. 97
Figure 88: Images of the ±45 NanoStitch composite specimen NS-02-07 tested in tension to failure. (a-b) side view. 97
Figure 89: Images of the ±45 NanoStitch composite specimen NS-02-07 tested in tension to failure. (a-b) side view. 98
Figure 90: Images of the 0/90 baseline composite specimen B-02-19 tested in tension-tension fatigue (σ_{max} = 932 MPa, N_f > 200,000 – fatigue runout), then failed in a tension test. (a-e) face view. 98
Figure 91: Images of the 0/90 baseline composite specimen B-02-19 tested in tension-tension fatigue (σ_{max} = 932 MPa, N_f > 200,000 – fatigue runout), then failed in a tension test. (a-f) face view. 99
Figure 92: Images of the 0/90 baseline composite specimen B-02-19 tested in tension-tension fatigue (σ_{max} = 932 MPa, N_f > 200,000 – fatigue runout), then failed in a tension test. (a-e) side view. 99

Figure 93: Images of the 0/90 baseline composite specimen B-02-19 tested in tension-tension fatigue (σ_{max} = 932 MPa, N_f > 200,000 – fatigue runout), then failed in a tension test. (a-d) side view. 100
Figure 94: Images of the 0/90 NanoStitch composite specimen NS-07-16 tested in tension-tension fatigue (σ_{max} = 997 MPa, N_f = 158,023). (a-d) face view. 100
Figure 95: Images of the 0/90 NanoStitch composite specimen NS-07-16 tested in tension-tension fatigue (σ_{max} = 997 MPa, N_f = 158,023). (a-e) face view. 101
Figure 96: Images of the 0/90 NanoStitch composite specimen NS-07-16 tested in tension-tension fatigue (σ_{max} = 997 MPa, N_f = 158,023). (a-d) face view. 101
Figure 97: Images of the 0/90 NanoStitch composite specimen NS-07-16 tested in tension-tension fatigue (σ_{max} = 997 MPa, N_f = 158,023). (a-e) face view. 102
Figure 98: Images of the 0/90 NanoStitch composite specimen NS-07-16 tested in tension-tension fatigue (σ_{max} = 997 MPa, N_f = 158,023). (a-d) side view. 102
Figure 99: Images of the 0/90 NanoStitch composite specimen NS-07-16 tested in tension-tension fatigue (σ_{max} = 997 MPa, N_f = 158,023). (a-e) side view. 103
Figure 100: Images of the 0/90 NanoStitch composite specimen NS-07-16 tested in tension-tension fatigue (σ_{max} = 997 MPa, N_f = 158,023). (a-d) side view. 103
Figure 101: Images of the 0/90 NanoStitch composite specimen NS-07-16 tested in tension-tension fatigue (σ_{max} = 997 MPa, N_f = 158,023). (a-e) side view. 104
Figure 102: Images of the ±45 baseline composite specimen B-05-08 tested in tension-tension fatigue (σ_{max} = 159 MPa, N_f = 18,384). (a-d) face view. 104

Figure 103: Images of the ±45 baseline composite specimen B-05-08 tested in tension-tension fatigue (σ_{max} = 159 MPa, N_f = 18,384). (a-c) face view. 105
Figure 104: Images of the ±45 baseline composite specimen B-05-08 tested in tension-tension fatigue (σ_{max} = 159 MPa, N_f = 18,384). (a-d) side view. 105
Figure 105: Images of the ±45 baseline composite specimen B-05-24 tested in tension-tension fatigue (σ_{max} = 105 MPa, N_f > 200,000 – fatigue runout), then failed in a tension test. (a-c) face view. 106
Figure 106: Images of the ±45 baseline composite specimen B-05-24 tested in tension-tension fatigue (σ_{max} = 105 MPa, N_f > 200,000 – fatigue runout), then failed in a tension test. (a-d) face view. 106
Figure 107: Images of the ±45 baseline composite specimen B-05-24 tested in tension-tension fatigue (σ_{max} = 105 MPa, N_f > 200,000 – fatigue runout), then failed in a tension test. (a-f) side view. 107
Figure 108: Images of the ±45 baseline composite specimen B-05-14 tested in tension-tension fatigue (σ_{max} = 181 MPa, N_f = 3,918). (a-d) face view. 107
Figure 109: Images of the ±45 baseline composite specimen B-05-14 tested in tension-tension fatigue (σ_{max} = 181 MPa, N_f = 3,918). (a-d) face view. 108
Figure 110: Images of the ±45 baseline composite specimen B-05-14 tested in tension-tension fatigue (σ_{max} = 181 MPa, N_f = 3,918). (a-d) side view. 108
Figure 111: Images of the ±45 baseline composite specimen B-05-23 tested in tension-tension fatigue (σ_{max} = 206 MPa, N_f = 2,070). (a-e) face view. 109

Figure 112: Images of the ±45 baseline composite specimen B-05-23 tested in tension-tension fatigue (σ_{max} = 206 MPa, N_f = 2,070). (a-d) face view. 109
Figure 113: Images of the ±45 baseline composite specimen B-05-23 tested in tension-tension fatigue (σ_{max} = 206 MPa, N_f = 2,070). (a-f) side view. 110
Figure 114: Images of the ±45 NanoStitch composite specimen NS-02-06 tested in tension-tension fatigue (σ_{max} = 137 MPa, N_f > 200,000 – fatigue runout), then failed in a tension test. (a-d) face view. 110
Figure 115: Images of the ±45 NanoStitch composite specimen NS-02-06 tested in tension-tension fatigue (σ_{max} = 137 MPa, N_f > 200,000 – fatigue runout), then failed in a tension test. (a-d) face view. 111
Figure 116: Images of the ±45 NanoStitch composite specimen NS-02-06 tested in tension-tension fatigue (σ_{max} = 137 MPa, N_f > 200,000 – fatigue runout), then failed in a tension test. (a-f) side view. 111
Figure 117: Images of the ±45 NanoStitch composite specimen NS-02-24 tested in tension-tension fatigue (σ_{max} = 187 MPa, N_f = 6,603). (a-e) face view. 112
Figure 118: Images of the ±45 NanoStitch composite specimen NS-02-24 tested in tension-tension fatigue (σ_{max} = 187 MPa, N_f = 6,603). (a-e) face view. 112
Figure 119: Images of the ±45 NanoStitch composite specimen NS-02-24 tested in tension-tension fatigue (σ_{max} = 187 MPa, N_f = 6,603). (a-d) side view. 113
Figure 120: Images of the ±45 NanoStitch composite specimen NS-02-24 tested in tension-tension fatigue (σ_{max} = 187 MPa, N_f = 6,603). (a-d) side view. 113

Figure 121: Images of the ±45 NanoStitch composite specimen NS-02-03 tested in tension-tension fatigue (σ_{max} = 137 MPa, N_f > 200,000 – fatigue runout), then failed in a tension test. (a-d) face view. 114
Figure 122: Images of the ±45 NanoStitch composite specimen NS-02-03 tested in tension-tension fatigue (σ_{max} = 137 MPa, N_f > 200,000 – fatigue runout), then failed in a tension test. (a-d) face view. 114
Figure 123: Images of the ±45 NanoStitch composite specimen NS-02-03 tested in tension-tension fatigue (σ_{max} = 137 MPa, N_f > 200,000 – fatigue runout), then failed in a tension test. (a-f) side view. 115
Figure 124: Images of the ±45 NanoStitch composite specimen NS-02-15 tested in tension-tension fatigue (σ_{max} = 207 MPa, N_f = 3,883). (a-f) face view. 115
Figure 125: Images of the ±45 NanoStitch composite specimen NS-02-15 tested in tension-tension fatigue (σ_{max} = 207 MPa, N_f = 3,883). (a-f) face view. 116
Figure 126: Images of the ±45 NanoStitch composite specimen NS-02-15 tested in tension-tension fatigue (σ_{max} = 207 MPa, N_f = 3,883). (a-f) side view. 116
Figure 127: Images of the ±45 NanoStitch composite specimen NS-02-15 tested in tension-tension fatigue (σ_{max} = 207 MPa, N_f = 3,883). (a-f) side view. 117
Figure 128: Images of the ±45 NanoStitch composite specimen NS-02-21 tested in tension-tension fatigue (σ_{max} = 164 MPa, N_f = 9,859). (a-d) face view. 117
Figure 129: Images of the ±45 NanoStitch composite specimen NS-02-21 tested in tension-tension fatigue (σ_{max} = 164 MPa, N_f = 9,859). (a-d) face view. 118

Figure 130: Images of the ±45 NanoStitch composite specimen NS-02-21 tested in tension-tension fatigue (σ_{max} = 164 MPa, N_f = 9,859). (a-d) side view. 118
Figure 131: Images of the ±45 NanoStitch composite specimen NS-02-22 tested in tension-tension fatigue (σ_{max} = 151 MPa, N_f = 57,033). (a-c) face view. 119
Figure 132: Images of the ±45 NanoStitch composite specimen NS-02-22 tested in tension-tension fatigue (σ_{max} = 151 MPa, N_f = 57,033). (a-d) face view. 119
Figure 133: Images of the ±45 NanoStitch composite specimen NS-02-22 tested in tension-tension fatigue (σ_{max} = 151 MPa, N_f = 57,033). (a-d) side view. 120
Figure 134: Images of the ±45 NanoStitch composite specimen NS-02-05 tested in tension-tension fatigue (σ_{max} = 213 MPa, N_f = 1,465). (a-e) face view. 120
Figure 135: Images of the ±45 NanoStitch composite specimen NS-02-05 tested in tension-tension fatigue (σ_{max} = 213 MPa, N_f = 1,465). (a-e) face view. 121
Figure 136: Images of the ±45 NanoStitch composite specimen NS-02-05 tested in tension-tension fatigue (σ_{max} = 213 MPa, N_f = 1,465). (a-e) side view. 121
Figure 137: Images of the ±45 NanoStitch composite specimen NS-02-05 tested in tension-tension fatigue (σ_{max} = 213 MPa, N_f = 1,465). (a-d) side view. 122
Figure 138: Images of the ±45 NanoStitch composite specimen NS-02-16 tested in tension-tension fatigue (σ_{max} = 189 MPa, N_f = 6,417). (a-e) face view. 122
Figure 139: Images of the ±45 NanoStitch composite specimen NS-02-16 tested in tension-tension fatigue (σ_{max} = 189 MPa, N_f = 6,417). (a-e) face view. 123
Figure 140: Images of the ±45 NanoStitch composite specimen NS-02-16 tested in tension-tension fatigue (σ_{max} = 189 MPa, N_f = 6,417). (a-d) side view. 123

Figure 141: Images of the ±45 NanoStitch composite specimen NS-02-16 tested in tension-tension fatigue (σ_{max} = 189 MPa, N_f = 6,417). (a-b) side view. 124
Figure 142: Images of the ±45 baseline composite specimen B-05-07 tested in tension-tension fatigue (σ_{max} = 164 MPa, N_f = 1). (a-c) face view. 124
Figure 143: Images of the ±45 baseline composite specimen B-05-07 tested in tension-tension fatigue (σ_{max} = 164 MPa, N_f = 1). (a-b) face view. 125
Figure 144: Images of the ±45 baseline composite specimen B-05-07 tested in tension-tension fatigue (σ_{max} = 164 MPa, N_f = 1). (a-d) side view. 125
Figure 145: Images of the ±45 baseline composite specimen B-05-12 tested in tension-tension fatigue (σ_{max} = 180 MPa, N_f = 138). (a-d) face view. 126
Figure 146: Images of the ±45 baseline composite specimen B-05-12 tested in tension-tension fatigue (σ_{max} = 180 MPa, N_f = 138). (a-d) face view. 126
Figure 147: Images of the ±45 baseline composite specimen B-05-12 tested in tension-tension fatigue (σ_{max} = 180 MPa, N_f = 138). (a-b) side view. 127
Figure 148: Images of the ±45 baseline composite specimen B-05-12 tested in tension-tension fatigue (σ_{max} = 180 MPa, N_f = 138). (a-d) side view. 127
Figure 149: Images of the ±45 baseline composite specimen B-05-17 tested in tension-tension fatigue (σ_{max} = 155 MPa, N_f = 11,354). (a-e) face view. 128
Figure 150: Images of the ±45 baseline composite specimen B-05-17 tested in tension-tension fatigue (σ_{max} = 155 MPa, N_f = 11,354). (a-e) face view. 128
Figure 151: Images of the ±45 baseline composite specimen B-05-17 tested in tension-tension fatigue (σ_{max} = 155 MPa, N_f = 11,354). (a-d) side view. 129

Figure 152: Images of the ±45 baseline composite specimen B-05-17 tested in tension-tension fatigue (σ_{max} = 155 MPa, N_f = 11,354). (a-c) side view. 129
Figure 153: Images of the ±45 baseline composite specimen B-05-11 tested in tension-tension fatigue (σ_{max} = 177 MPa, N_f = 311). (a-d) face view. 130
Figure 154: Images of the ±45 baseline composite specimen B-05-11 tested in tension-tension fatigue (σ_{max} = 177 MPa, N_f = 311). (a-d) face view. 130
Figure 155: Images of the ±45 baseline composite specimen B-05-11 tested in tension-tension fatigue (σ_{max} = 177 MPa, N_f = 311). (a-d) side view. 131
Figure 156: Images of the ±45 baseline composite specimen B-05-25 tested in tension-tension fatigue (σ_{max} = 144 MPa, N_f = 1,237). (a-d) face view. 131
Figure 157: Images of the ±45 baseline composite specimen B-05-25 tested in tension-tension fatigue (σ_{max} = 144 MPa, N_f = 1,237). (a-d) face view. 132
Figure 158: Images of the ±45 baseline composite specimen B-05-25 tested in tension-tension fatigue (σ_{max} = 144 MPa, N_f = 1,237). (a-d) side view. 132
Figure 159: Images of the ±45 NanoStitch composite specimen NS-02-01 tested in tension-tension fatigue (σ_{max} = 212 MPa, N_f = 5). (a-d) face view. 133
Figure 160: Images of the ±45 NanoStitch composite specimen NS-02-01 tested in tension-tension fatigue (σ_{max} = 212 MPa, N_f = 5). (a-d) face view. 133
Figure 161: Images of the ±45 NanoStitch composite specimen NS-02-01 tested in tension-tension fatigue (σ_{max} = 212 MPa, N_f = 5). (a-c) side view. 134
Figure 162: Images of the ±45 NanoStitch composite specimen NS-02-01 tested in tension-tension fatigue (σ_{max} = 212 MPa, N_f = 5). (a-b) side view. 134

Figure 163: Images of the ±45 NanoStitch composite specimen NS-02-26 tested in tension-tension fatigue (σ_{max} = 209 MPa, N_f = 7). (a-d) face view. 135
Figure 164: Images of the ±45 NanoStitch composite specimen NS-02-26 tested in tension-tension fatigue (σ_{max} = 209 MPa, N_f = 7). (a-d) face view. 135
Figure 165: Images of the ±45 NanoStitch composite specimen NS-02-26 tested in tension-tension fatigue (σ_{max} = 209 MPa, N_f = 7). (a-e) side view. 136
Figure 166: Images of the ±45 NanoStitch composite specimen NS-02-14 tested in tension-tension fatigue (σ_{max} = 214 MPa, N_f = 14). (a-d) face view. 136
Figure 167: Images of the ±45 NanoStitch composite specimen NS-02-14 tested in tension-tension fatigue (σ_{max} = 214 MPa, N_f = 14). (a-d) face view. 137
Figure 168: Images of the ±45 NanoStitch composite specimen NS-02-14 tested in tension-tension fatigue (σ_{max} = 214 MPa, N_f = 14). (a-d) side view. 137
Figure 169: Images of the ±45 NanoStitch composite specimen NS-02-14 tested in tension-tension fatigue (σ_{max} = 214 MPa, N_f = 14). (a-d) side view. 138

List of Tables

Table Page

Table 1: Properties of Toray T300 carbon fiber at room temperature [8] 8

Table 2: Properties of Hexcel HexTow AS4 carbon fibers at room temperature[9] 8

Table 3: Properties of CYCOM IM7/977-3 tape at room temperature [13] 16

Table 4: Properties of Hexcel IM7 carbon fibers at room temperature [14] 17

Table 5: Properties of CYCOM 977-3 epoxy at room temperature [13] 17

Table 6: Panel specifics and labeling example 19

Table 7: Average panel thickness with standard deviation and covariance..... 19

Table 8: Specimen gauge section dimensions 19

Table 9: Test stress levels and respective load and unload rate..... 27

Table 10: Average elastic modulus results for each composite panel 29

Table 11: Average UTS results for each Composite panel..... 29

Table 12: Summary of tensile properties of the 0/90 composite panels 30

Table 13: Summary of tensile properties of the ±45 composite panels 35

Table 14: A summary of tension-tension fatigue results for the 0/90 specimens of baseline and NanoStitch composites 38

Table 15: Retained tensile properties of the 0/90 composite specimens subjected to 200,000 cycles of prior tension-tension fatigue. 45

Table 16: A summary of tension-tension fatigue results for the ±45 specimens of baseline and NanoStitch composites 47

Table 17: Retained tensile properties of the ±45 composite specimens subjected to 200,000 cycles of prior tension-tension fatigue. 57

Table 18: Stress-dependent material functions $g0$, $g1$, $g2$, and $a\sigma$. 67

MECHANICAL PROPERTIES AND PERFORMANCE OF A NOVEL NANO-ENGINEERED UNITIZED COMPOSITE FOR AEROSPACE SYSTEMS

I. Introduction

1.1 Motivation

Composites have been around for a long time, some of the earliest accounts of which date back to ancient Egyptian times when they used straw as reinforcement in bricks, and are used in almost every industry today, from transportation to sports to textiles. They are defined as the combination of two or more materials of the same or different class. The ultimate desire of which is combining their good properties to improve the composite's overall properties to perform better than each material alone for a desired characteristic. The possibilities are endless and there is always more and more research being done on composites, as science continues to push the limit of current materials. One such class of composites that is being given a lot of attention is fiber reinforced polymer composites (FRPC), which are generally made up of carbon fiber sheets that are glued together with an epoxy, referred to as the matrix. These FRPCs take advantage of the reduction in weight of polymers, while trying to retain the strength of metals and the stiffness of ceramics through fiber reinforcements. In the Air Force, FRPCs are being looked at to replace parts in aircrafts, amongst other things, in order to reduce their weight, therefore increasing their performance and decreasing their susceptibility and vulnerability. A prime example of this is the latest generation of fighter

aircraft, such as the F-35. Composites offer many advantages over conventional aircraft materials, such as steel and aluminum, such as weight reduction and resistance to corrosion. This is critical in the Air Force, not only because lives are priceless, but aircraft are extremely expensive and are constantly increasing in cost as more technology and improvements are added to aircraft in order to gain that performance advantage over our adversaries. As such, it is in the Air Force's best interest to decrease the amount of repairs and replacement aircraft that are necessary.

1.2 Problem Statement

Fiber reinforced polymer composites have many applications in the Air Force. High-performance FRPCs used in aerospace structures typically are engineered to exhibit excellent in-plane mechanical properties. Composites offer the best mechanical performance when the in-plane load is applied along the direction of the fibers. However, poor through-thickness and interlaminar properties often limit performance and durability of the FRP material systems. Hence, one of the challenges with FRPCs is delamination of the carbon fiber-reinforced plies. Even though the fibers carry the majority of the load, the matrix still absorbs some of the load and holds the fibrous plies together. Thus ply delamination is a damage mode that contributes to the reduction in mechanical performance and durability of the composite. Because there is typically no through-thickness reinforcement in 2D FRPCs, much research has been devoted to improving the interlaminar properties of the FRP laminates.

Recent studies [1]–[5] explored novel approaches to improve interlaminar properties of the FRP laminates by incorporating aligned carbon nanotubes (CNTs) into

macroscopic unitized aerospace composites. Since there is no reinforcement in the ply interface, the resin-dominated interlaminar region provides a preferred path for crack propagation. One promising approach to improve interlaminar properties of the FRPCs laminates incorporates a “forest” of vertically aligned CNTs, called NanoStitch, between the plies of the carbon/epoxy prepreg with CNTs oriented normal to the fiber direction. The CNTs in the NanoStitch reinforce the resin-rich region between the composite plies and facilitate the ply-to-ply load transfer. The resulting NanoStitch-FRP system exhibits improved interlaminar properties [4], [5] as well as more favorable damage modes and higher failure loads.

The novel hybrid carbon fiber/NanoStitch polymer composite shows significant promise for aerospace systems. However, before this material system can be used in structural applications, its structural integrity and environmental durability must be assured. An in-depth study of its deformation behavior, damage, and failure mechanisms under various loading histories is needed.

1.3 Research Objectives/Questions/Hypotheses

The proposed effort seeks to investigate the mechanical behavior and to evaluate the mechanical properties of the novel hybrid carbon fiber/NanoStitch polymer composite material. Specific objectives of this research are threefold. First, basic mechanical properties, such as in-plane tensile stiffness and strength, are evaluated in basic mechanical tests at room-temperature. Properties of the hybrid carbon fiber/NanoStitch polymer matrix composite (PMC) with 0/90 and ±45 fiber orientations must be assessed. Second, the in-plane performance of this material under tension-tension cyclic fatigue is

assessed. A control PMC without NanoStitch reinforcement is also studied in order to assess the effects of the NanoStitch layers on the composite's mechanical properties and fatigue performance. Third, the time-dependent deformation behavior of the hybrid composite is evaluated in creep/recovery tests. The objective is to analyze the test results in context of Schapery's nonlinear viscoelastic model and, if possible, to characterize model parameters.

1.4 Methodology

The following steps were employed to achieve the objective outlined above:

1. Perform monotonic tension to failure tests at room temperature to determine elastic modulus and ultimate tensile strength of both the hybrid composite and the control composite. Specimens with both 0/90 and ±45 fiber orientations are tested to evaluate both on-axis and off-axis properties and performance. Multiple tests per condition are conducted to assess specimen-to-specimen variability.
2. Compare experimental results obtained for the hybrid composite to those obtained for the control composite to determine any significant effects of the NanoStitch reinforcement on the tensile properties and performance.
3. Perform tension-tension fatigue tests at room temperature to determine both on-axis (0/90) and off axis (± 45) fatigue behavior. Construct S-N curves. Determine fatigue limit for the run-out condition of $2x10^5$ cycles.
4. Compare fatigue performance of the hybrid composite to that of the control composite for both 0/90 and ±45 fiber orientations to evaluate the effects of the NanoStitch reinforcement fatigue performance.

5. Examine specimens under an optical microscope to assess damage and failure mechanisms operating in tension-tension cyclic fatigue.
6. Perform creep/recovery tests to investigate the time-dependent deformation behavior of the hybrid composite with ±45 fiber orientation. Analyze the test results in the context of Schapery's nonlinear viscoelastic model. Determine whether this continuum-based viscoelastic deformation theory can be used to represent the time-dependent deformation behavior of the hybrid material.

II. Background

2.1 Composites Overview

As mentioned in the previous chapter, composites are a class of materials that combines two or more materials in different phases, generally known as the matrix and reinforcement phases. The matrix phase is what "holds" everything together, transfers the load to the reinforcement phase, and carries a majority of the load in the out-of-plane direction. It's typically made of some sort of epoxy or resin. The reinforcement phase is what mainly gives the material its strength and stiffness, and carries the majority of the load in the direction of the reinforcements, usually in the form of fibers or particles. In terms of distribution, particle reinforcements are randomly distributed throughout the matrix, while fiber reinforcement can either be short and randomly distributed or aligned long or short fibers[6]. Aligned fibers are generally organized in sheets, whether unidirectional or woven, and each sheet is either called a ply or lamina. Multiple sheets can be combined in different orientations with resin (matrix) to form a laminate. Since these laminates are composed of sheets and the matrix tends to be the weakest part of composite, often times, the sheets can separate when the material fails, causing what is called delamination.

The aim of composites is to improve overall desirable properties that exceed the desired properties of each, individual material involved. The properties of the composite are dependent on the properties of the constituent phases, their relative amounts, and the geometry/dimensions of the reinforcement phase[6]. In the aerospace industry, the desire is to reduce weight by replacing traditionally metal parts with composite parts. However,

there are some drawbacks to composite materials, such as increased initial cost and lower damage tolerance, which increases the cost and time of repairs. Because of this, there is an extra consideration in terms of military application, due to the increased risk of damage, compared to civilian applications.

2.2 Fiber Reinforced Polymer Composites/Polymer Matrix Composites

Fiber Reinforced Polymer Composites (FRPCs), also known as, Polymer Matrix Composites (PMCs), generally consists of two phases a resin matrix phase and a fiber reinforcement phase. FRPCs is one of the most diversely used composites, due to its superior room temperature performance, ease of fabrication, and lower cost[6]. In terms of matrix material, epoxy resin is the most commonly used, but polyimides, polyphenylene sulfides, or polysulfones are used as well[7]. As for the reinforcement phase, the most common fibers used are: glass, carbon, and aramid. Carbon fibers will be examined in this research and are often used because[6]:

1. Carbon fibers tend to have higher specific modulus and specific strength in comparison to other fiber materials
2. They retain their modulus and strength at elevated temperatures, however, may oxidize at high temperatures
3. At room temperature, they usually aren't affected by moisture or solvents, acids, and bases
4. They exhibit wide range of physical and mechanical properties, so can be tailored to meet specific engineering needs
5. Their manufacturing process tends to be cheaper than other fiber composites

2.2.1 Common Commercial Carbon Fibers.

There are many types and manufacturers of carbon fibers in the commercial aerospace industry, but two common ones are the T300 carbon fiber made by Toray Composite Materials and HexTow AS4 carbon fiber made by Hexcel. Properties for both of these fibers are tabulated in Table 1 and 2.

Table 1: Properties of Toray T300 carbon fiber at room temperature [8]

Property	Value
Filament Count	3,000
Tensile Strength	3530 MPa
Tensile Modulus	230 GPa
Failure Strain	1.5%

Table 2: Properties of Hexcel HexTow AS4 carbon fibers at room temperature [9]

Property	Value
Filament Count	3,000
Tensile Strength	4723 MPa
Tensile Modulus	231 GPa
Failure Strain	1.8%

2.3 Composite Tensile and Fatigue Response

In this research, tensile properties will be analyzed, such as Young's Modulus, E, Ultimate Tensile Strength (UTS), and fatigue life. An example of a stress-strain curve for a FRPC can be seen in Figure 1, where the Young's Modulus is determined from the slope of the linear region of the stress-strain curve and the UTS is the highest stress the material experiences before failure, which doesn't necessarily coincide with the failure point.

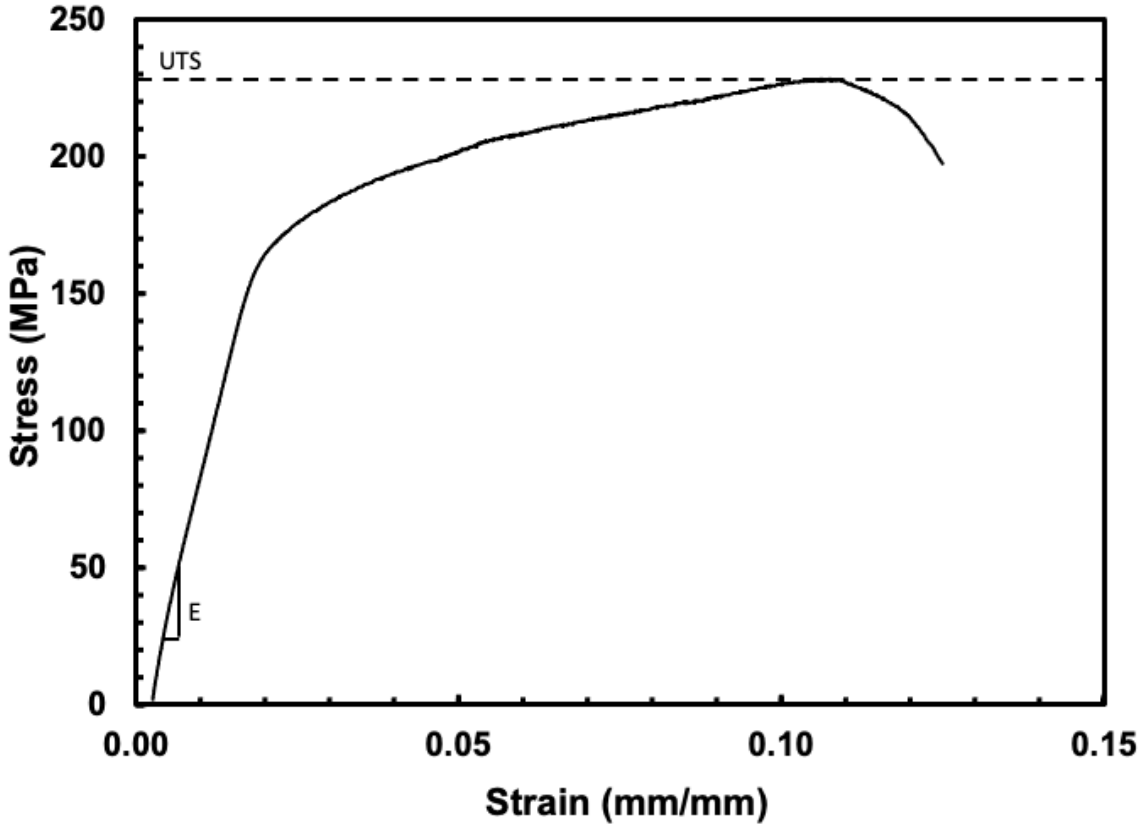

Figure 1: Stress-strain curve from specimen NS-02-06 showing that the modulus is found from the slope of the curve in the linear region and the UTS is found from the maximum stress experienced by the specimen, represented by the dashed line

The purpose of fatigue tests is to examine the effect of stress being cyclically applied to a material. The fatigue life of a material is another important property that is determined by cycling through a pre-determined peak and valley stress value. The resulting lifetime can be represented on a stress vs. cycles curve (S-N curve), as seen in Figure 2. The fatigue limit seen in Figure 2 represents the stress limit, below which the material can be theoretically cycled infinitely without experiencing failure.

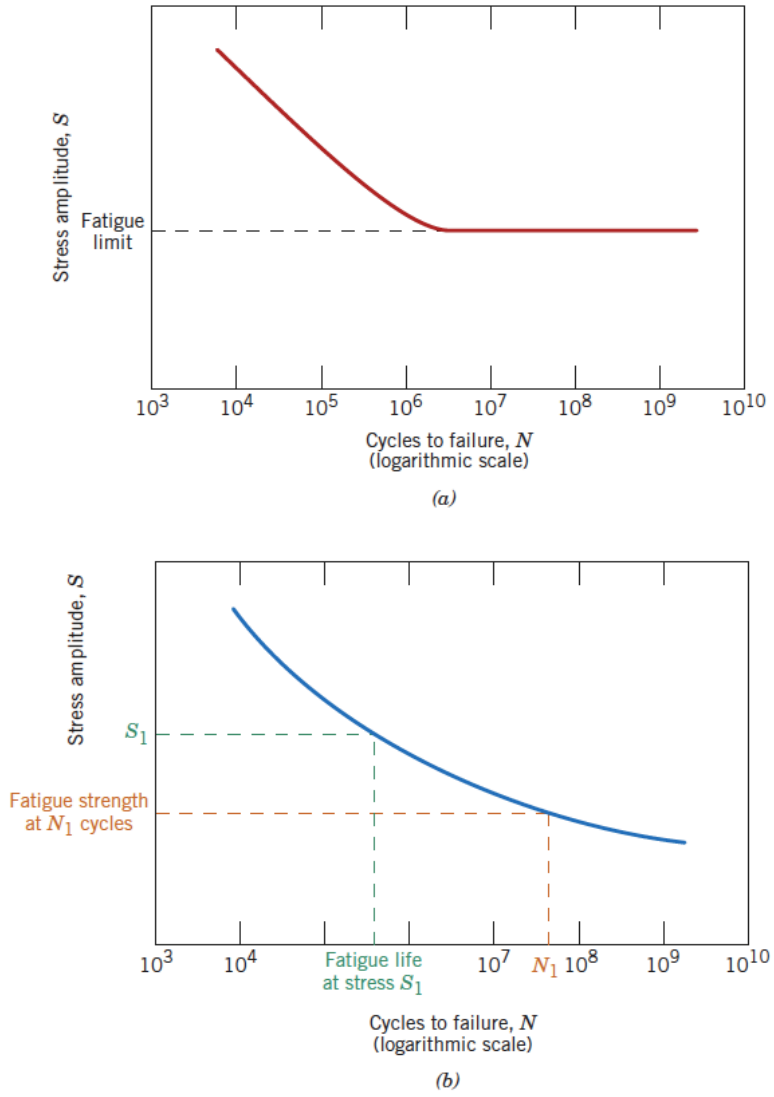

Figure 2: Stress (S) vs. logarithm of cycles (N). (a) S-N Curve of a material with a fatigue limit. (b) S-N Curve of a material without a fatigue limit [6] Reproduced from Material Science and Engineering: An Introduction, Figure 8.19, Copyright©, with permission from Wiley.

2.4 Composite Layup

There are many ways to orient unidirectional fiber sheets in respect to each other and applied loads. They can be as simple as a single sheet layup to more complex quasi-isotropic four sheet layups and beyond. Figure 3 shows an example of a laminar

composite layup. Two sheet layups can also be used, such as 0/90 and -45/+45. The other design factor to consider when laying up fiber sheets is symmetrical versus asymmetrical. Symmetrical layup means that the sheets are symmetrical about the centerline, such as 0/90/+45/-45/-45/+45/90/0. Asymmetrical layup means that the sheets are not symmetrical about the centerline, such as 0/90/+45/-45/0/90/+45/-45.

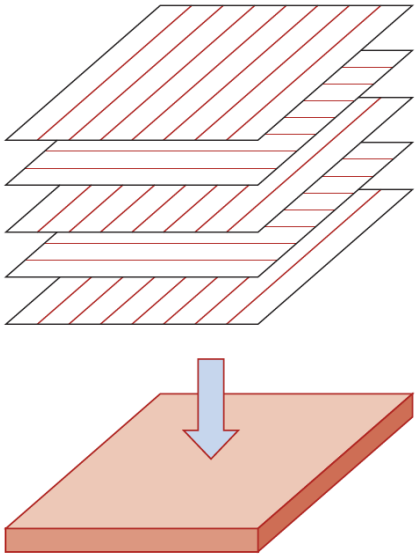

Figure 3: (Left) Schematic of single sheet layup. (Right) Schematic of four sheet quasi-isotropic layup [6]. Reproduced from Material Science and Engineering: An Introduction, Figure 16.16, Copyright©, with permission from Wiley.

2.5 3D Reinforcement

When it comes to FRPCs, their fracture mechanics are complex and can vary from material to material. Some of the common mechanisms include matrix cracking, fiber pullout/breakage, and delamination. Often, these all contribute to the failure of the material, however, unlike other materials, it is often non-homogenous and can occur simultaneously in several different parts of the material. This non-homogenous damage

will also result in non-homogenous deformation under cyclic loading. Generally, in FRPCs the matrix is weaker than the fibers, therefore, tends to fail earlier than the fibers, which leads to matrix cracking and delamination. One way that has been proposed to strengthen FRPCs is 3D reinforcements through reinforcing the matrix region and increasing the load necessary to cause delamination. Within that proposal, there have been multiple methods explored, such as 3D weave patterns of the fibers, adding chopped fibers to the matrix layer, and Carbon Nanotubes (CNTs) either grown directly onto the fibers or vertically aligned to form a forest of Vertically Aligned Carbon Nanotubes (VACNT), known as Nanostitch [1]. A schematic of both of these methods can be seen in Figure 4.

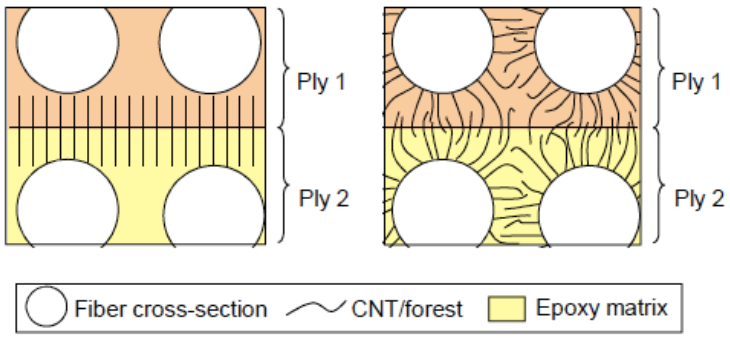

Figure 4: (left) Schematic of vertically aligned carbon nanotube reinforcements. (right) Schematic of nanotube reinforcements grown directly on the fibers. Reproduced from [1].

These CNTs are proposed to reduce delamination and even in some cases, change the fracture mechanics behavior of the material[3], [4], [10].

2.6 Hybrid Composite with NanoStitch Reinforcement - Previous Research

There has been some research done on the new NanoStitch material, but the majority of it is focused on its shear properties. There has not been any research done on

the cyclic fatigue behavior of the material under uniaxial tension-tension loading. MIT and N12 Technologies, the synthesizers of the NanoStitch material, have conducted research on the material to determine basic mechanical properties. Some of this related research and their results will be discussed in support of this study.

2.6.1 Tension Bearing Strength Research.

A study conducted by a group out of Sweden and MIT [11], involved a bearing tension test on the NanoStitch material. It is not the same type of tension testing that will be performed in this study, but still yielded relevant tension testing results. They observed that the ultimate bearing strength was not significantly enhanced by the VACNTs, however, delamination was observed to be reduced. In the baseline material, a load drop is observed around 550 MPa, which is a result of the outer plies delaminating, but in the VACNT reinforced material, there is no load drop, which indicates that delamination did not occur in the middle of the load up process[11]. This can be seen in Figure 5.

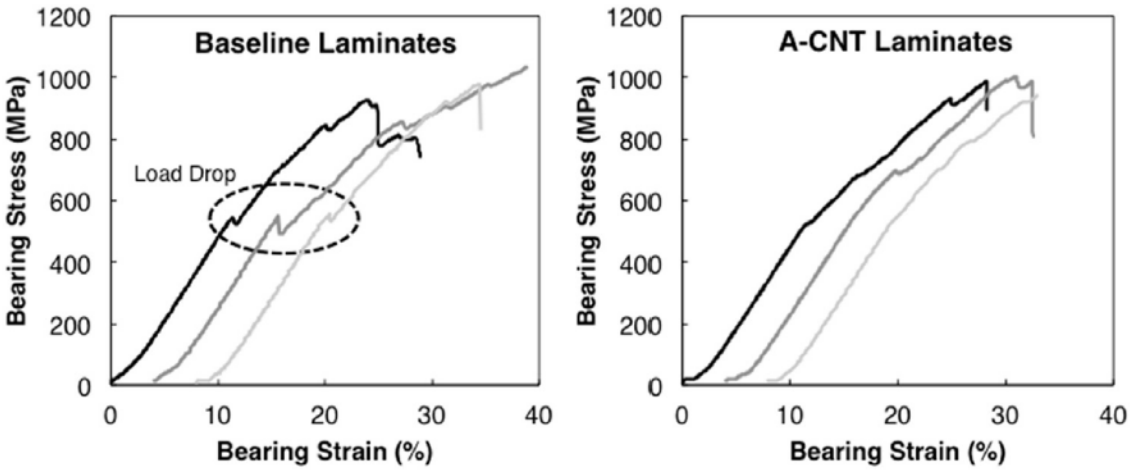

Figure 5: Bearing stress-strain curves for tension-bearing tests. For comparative purposes, the curves of the different specimens are offset on the x axis [11]. Reproduced from In-Plane Strength Enhancement of Laminated Composites via Aligned Carbon Nanotube Interlaminar Reinforcement, Figure 4, Copyright©, with permission from Elsevier.

2.6.2 Failure Mechanics Research.

Generally, FRPCs tend to fail along the fiber plies, in the interlaminar region. This is what results in delamination. With VACNT reinforcement, it has been shown that that failure mode can drastically change from failing in the interlaminar region through delamination to failing intralaminarly through fiber breakage[5]. In a Mode I fracture test, the NanoStitch added interlaminar toughness to the material and forced the crack away from the toughened interlaminar region to the weaker intralaminar region of the plies themselves[10]. Cracks follow the path of least resistance and with the VACNT forest reinforcement, that path became the intralaminar region. An SEM image of the samples from the authors of the study are shown in Figure 6. In Figure 6, it can be clearly seen that the crack path of the baseline material is parallel to the fiber plies and in the interlaminar (matrix) region, whereas, in the NanoStitched material, the crack path appears within the fiber plies. They also performed computer modeling, which shows that the reinforced matrix is at least 10% tougher than the unreinforced matrix[10].

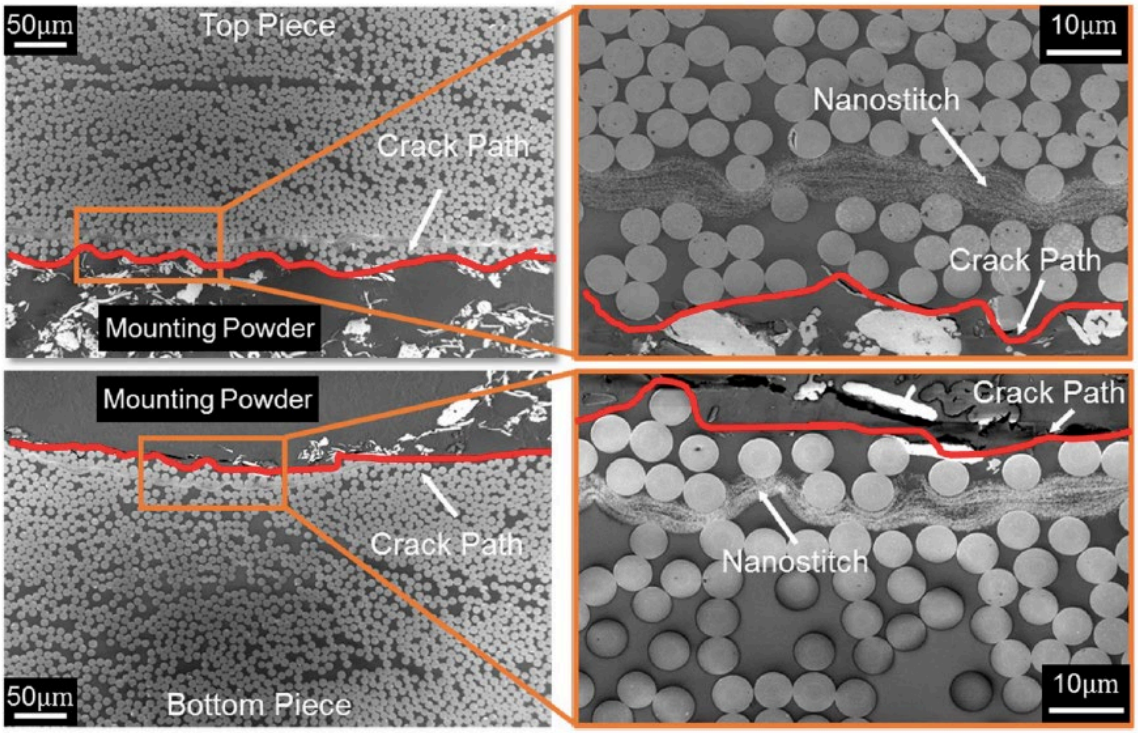

Figure 6: Post-failure SEM image of cracked baseline (left) and NanoStitched (right) material. The red line is the crack path [10]. Reproduced from Interlaminar to Intralaminar Mode I and II Crack Bifurcation Due to Aligned Carbon Nanotube Reinforcement of Aerospace-Grade Advanced Composites, Figure 4, Copyright©, with permission from Elsevier.

III. Material and Test Specimen

This section gives an overview of the material being studied and how the specimen were prepared for testing. One panel of each 0/90 and ±45 fiber orientation of baseline and NanoStitched material, four in total, manufactured by University of Dayton Research Institute, were used for this study.

3.1 Fiber Reinforced Polymer Composite

IM7/977-3 prepreg, which is commonly used in the aerospace industry[12] was used to manufacture the panels. Basic properties of the IM7/977-3 tape are tabulated in Table 3. The reinforcement was provided by unidirectional IM7 carbon fibers manufactured by Hexcel (Table 4), while the epoxy resin used was Solvay CYCOM 977-3 (Table 5). The panels measuring 13'' x 14'' consisted of 20 plies in the following layups: $[0/90]_{5s}$ for the 0/90 panels and $[+45/-45]_{5s}$ for the ±45 panels. The panels were cured in vacuum, under 85 psig of pressure and 350ºF (450K) for six hours in an autoclave.

Table 3: Properties of CYCOM IM7/977-3 tape at room temperature [13]

Property	Value
Tensile Strength	2510 MPa
Tensile Modulus	162 GPa
Failure Strain	1.46%
FAW [12]	145 gsm

Table 4: Properties of Hexcel IM7 carbon fibers at room temperature [14]

Property	Value
Filament Count	12,000
Tensile Strength	5688 MPa
Tensile Modulus	276 GPa
Ultimate Elongation at Failure	1.8%
Density	1.78 g/cm^3
Weight/Length	0.446 g/m
Filament Diameter	5.2 microns
Carbon Content	95%

Table 5: Properties of CYCOM 977-3 epoxy at room temperature [13]

Property	Value
Flexural Strength	144 MPa
Flexural Modulus	3.8 GPa
K_{1C}	0.9 MPa*m$^{1/2}$
G_{1C}	217 J/m^2

3.2 Carbon Nanotube Forest

The vertically aligned carbon nanotubes are grown on a flat substrate using chemical vapor deposition to create the "NanoStitch"[1] and inserted between the prepreg plies. In order to begin growing the fibers, the silicon substrate is first prepared by e-beam depositing Al_2O_3, then coated with a Fe catalyst precursor, before being treated with heat and a reduction gas (H_2)[1]. The catalyst at this point are nano-sized, which allows the CNTs to nucleate when the gaseous carbon source (C_2H_4) is introduced.

In order to apply the VACNTs, the IM7/977-3 prepeg is rolled onto a metal cylinder, with the sticky, prepeg side exposed. Then the cylinder is rolled over the silicon substrate with the grown CNTs, therefore, successfully depositing the CNTs onto the prepeg ply and removing it from the silicon substrate[1]. From there, the method described in section 3.1 is followed to layup the panels.

3.3 Test Specimen Dimensions

For both the uniaxial tension tests and the tension-tension fatigue tests a standard dogbone-shaped specimen geometry was used. This specimen geometry ensured that failure would occur within the gauge section of the specimen. Figure 7 depicts the dimensions of the test specimens.

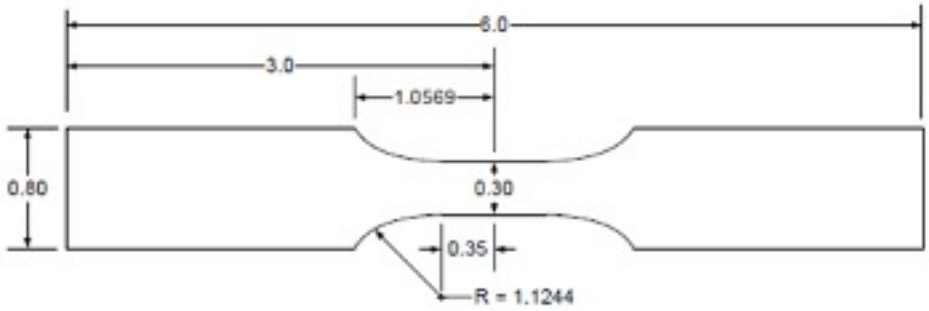

Figure 7: Dogbone-shaped test specimen. All dimensions in inches.

3.4 Test Specimen Preparation

The AFIT Model and Fabrication Shop machined the test specimens from the baseline and NanoStitch panels using diamond-grinding. The specimens were cut in a way that would maintain the 0/90 and ±45 fiber orientation of the panels with respect to the direction that uniaxial loading will be applied. Once the specimens were returned from the machine shop, each specimen's gauge section was measured, using a Mitutoyo Absolute Solar Digimatic Caliper, Model N0. CD-S6"CT, and labeled according to material system and fiber orientation. For example, B-05-14, where the "B" indicates that it is a baseline material, the first number, "05", indicates the fiber orientation, and the second number, "14", indicates the specimen number from the B-05 panel. The specifics of each panel and example label can be seen in Table 6.

Table 6: Panel specifics and labeling example

Material System	Fiber Orientation	Panel Label	Example Specimen Label	Total # of Specimens
Baseline	0/90	B-02	B-02-07	26
NanoStitch	0/90	NS-07	NS-07-12	28
Baseline	±45	B-05	B-05-03	26
NanoStitch	±45	NS-02	NS-02-21	26
NanoStitch	±45	NS-04	NS-04-16	28

The thickness of each specimen did not vary significantly between each other or between panels. They all had low standard deviations and covariance. The average thicknesses along with their associated standard deviations and covariance are listed in Table 7. Other specimen gauge section dimensions are given in Table 8.

Table 7: Average panel thickness with standard deviation and covariance

Material System	Fiber Orientation	Panel Label	Avg Thickness (mm)	Std Deviation	Covariance (%)
Baseline	0/90	B-02	2.70	0.06	2.16
NanoStitch	0/90	NS-07	2.71	0.04	1.31
Baseline	±45	B-05	2.69	0.10	3.90
NanoStitch	±45	NS-02	2.72	0.08	2.90
NanoStitch	±45	NS-04	2.72	0.05	1.72

Table 8: Specimen gauge section dimensions

Material System	Fiber Orientation	Panel Label	Avg Thickness (mm)	Avg Width (mm)	Avg X-Sect Area (mm^2)
Baseline	0/90	B-02	2.70	7.71	20.83
NanoStitch	0/90	NS-07	2.71	7.69	20.80
Baseline	±45	B-05	2.69	7.71	20.73
NanoStitch	±45	NS-02	2.72	7.69	20.92
NanoStitch	±45	NS-04	2.72	7.73	21.01

The gauge section widths also did not vary much between specimens, which, in turn, means that the average cross sectional areas also did not vary much. Regardless, each individual specimen's gauge section's dimensions were used for any kind of data analysis and calculations for tests performed on the specimen, rather than the averages for each panel.

Fiberglass tabs were affixed to the ends of each specimen in order prevent damage to the specimen from the rough surface of the wedge grips, which could become crack initiators. Each sample was wiped down with Kimtech Science Kimwipes to remove surface particulates from machining, before attaching fiberglass tabs. The tabs were cut down to 4x2cm rectangles, which provides adequate surface area for the grips. They were then affixed using VPG Micro Measurements M-Bond 200 adhesive. A picture of the applied tabs can be seen in Figure 8.

Figure 8: (a) Top and (b) side view of specimen with fiberglass tabs applied

IV. Experimental Setup and Testing Procedures

This section outlines the testing procedures and equipment used in this study, along with the optical microscopy equipment employed to take images.

4.1 Testing Equipment

All mechanical tests were performed with a vertically configured model 810 MTS servo-hydraulic testing machine with a 100 kN (22 kip) model 647.10A load cell, an MTS model 661.20E-03 force transducer, and a 100 kN (22kip) MTS model 609.10A-01 alignment fixture. MTS model 647.10 wedge grips with a grip pressure of 15 MPa were used to grip the specimen. An MTS model 632.13F-20 10-mm gauge extensometer with knife edges was used to measure the strain. However, part way through the study, the extensometer was damaged and was replaced with an MTS model 632.26F-20 8-mm gauge extensometer.

A FlexTest 40 digital controller was used for controlling input signals and acquiring data. Operations were performed using the MTS station manager, which utilized a configuration file that was created using the MTS station building release 5.2B. Procedures were developed using the station manager to automate both the tension to failure test and the tension-tension fatigue tests. Figure 9 shows the MTS equipment used to test the samples.

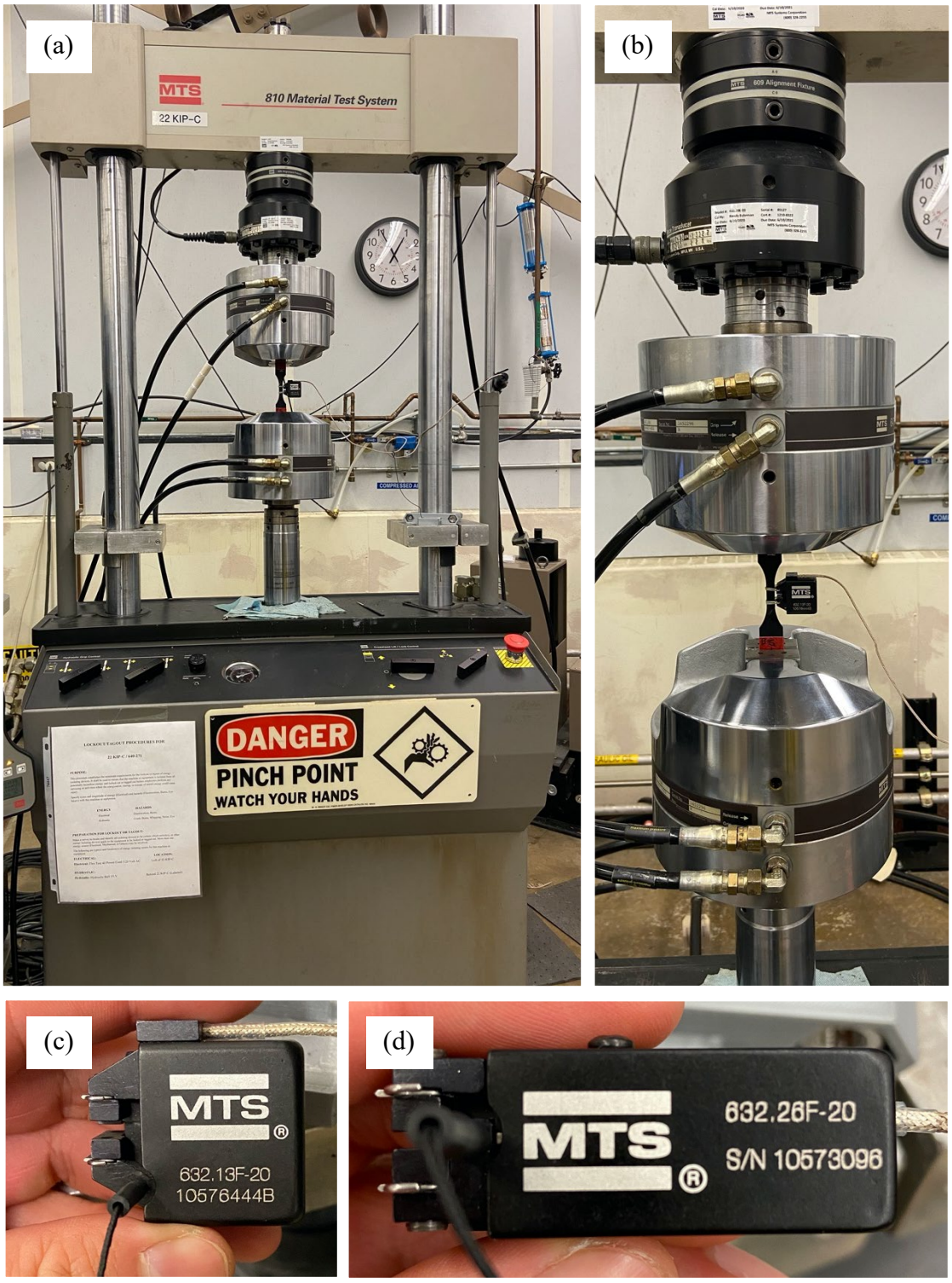

Figure 9: Picture of the: (a) MTS testing unit used to test samples, (b) load cell with sample, (c) 10-mm gauge Extensometer, (d) 8-mm gauge Extensometer.

4.2 Mechanical Test Procedures

4.2.1 Uniaxial Tension to Failure Tests.

The purpose of the uniaxial tension to failure test was to produce a stress strain curve in order to determine the modulus of elasticity and Ultimate Tensile Strength (UTS), which were used to determine parameters for the fatigue tests. The tests were performed at room temperature. Three specimen from each of the four composite panels (0/90 control composite, ±45 control composite, 0/90 hybrid composite, ±45 hybrid composite) were tested to find the average property values for each composite and each fiber orientation.

Tension to failure tests were conducted in displacement control at a constant rate of 0.025 mm/s. The following data were recorded during the test: time, displacement command, displacement, force command, force, and strain. Failure was accompanied by a dramatic drop in the load being carried by the specimen. The test was terminated manually once failure had occurred.

4.2.2 Tension-Tension Cyclic Fatigue Tests.

The purpose of the tension-tension cyclic fatigue tests is to determine the fatigue life of the material and create stress-cycle curves (S-N curves), as well as to determine other characteristics of the fatigue response, such as strain accumulation and change in elastic modulus with cycles. All fatigue tests were performed with a minimum to maximum stress ratio of 0.1 (R = 0.1) at a frequency of 1 Hz. Fatigue run-out condition was defined as survival of $2x10^5$ cycles without failure. Different maximum stress levels were used for the baseline composite and the hybrid composite as well as for specimens with 0/90 and ±45 fiber orientations. Maximum stress ranged from 80% to 90% UTS for

the 0/90 specimens and from 40% to 80% UTS for the ±45 specimens. The average UTS values obtained from the tension-to-failure tests were used to determine the stress levels used for the fatigue testing. Duplicate tests were performed to gain statistical confidence.

The procedure for the cyclic fatigue test was created using the MTS software. This procedure consisted of four segments: load-up, cyclic loading, unload to zero load, and tension to failure. The first three segments were carried out in load control. The fourth segment (performed only if a test specimen achieved fatigue runout) was performed in displacement control. In the load-up segment, the specimen is loaded up to the minimum fatigue stress, as determined by the maximum fatigue stress and the R-ratio, in 30 seconds. During this segment, the following data were taken every 0.01 s: time, force command, force, displacement command, displacement, and strain.

Once the minimum stress was reached, the next segment of tension-tension fatigue test, namely cyclic loading, would commence. During this segment two types of data were collected: full cycle data and peak valley data. The full cycle data was collected every 0.02s and included: time, force command, force, displacement command, displacement, strain, and cycle count. Full cycle data were collected for selected cycles in the following manner:

- Every cycle between cycle 1 and 25
- Every 10^{th} cycle between cycle 30 and 100
- Every 100^{th} cycle between cycle 100 and 1,000
- Every $1{,}000^{th}$ cycle between cycle 1,000 and 10,000
- Every $10{,}000^{th}$ cycle between cycle 10,000 and 200,000

The peak valley data, collected at the maximum and minimum load of every cycle, consisted of: time, force command, force, displacement command, displacement, strain, and segment (or half cycle) count.

If the specimen achieved run-out of 200,000 cycles, it would be unloaded to zero load in 10 seconds. The same data were collected during the unloading segment as the full cycle load-up segment except every 0.1 s. Once zero load was reached, control would switch from load to displacement and a tension to failure test would be conducted to characterize the retained tensile properties of the post-fatigued specimen. During this segment, the specimen was tested at a rate of 0.025 mm/s, as in the tension to failure tests of virgin specimens. Data were collected every 0.01 seconds and included: time, force command, force, displacement command, displacement, and strain.

4.3 Characterization of Schapery's Nonlinear Viscoelastic Model

It is often times desirable to have a mathematical model to predict material behavior without having to perform experiments. One such model is the Schapery nonlinear viscoelastic model. This particular model can be characterized through a series of creep and recovery tests, where the specimen is quickly loaded up to a set stress level, held at constant stress and allowed to creep, quickly unloaded to zero stress, and then allowed to recover at zero stress. A schematic of the creep and recovery test is shown in Figure 10. Table 9 summarizes the different creep and recovery tests that were performed and provides the loading/unloading rate and the recovery time used in each test.

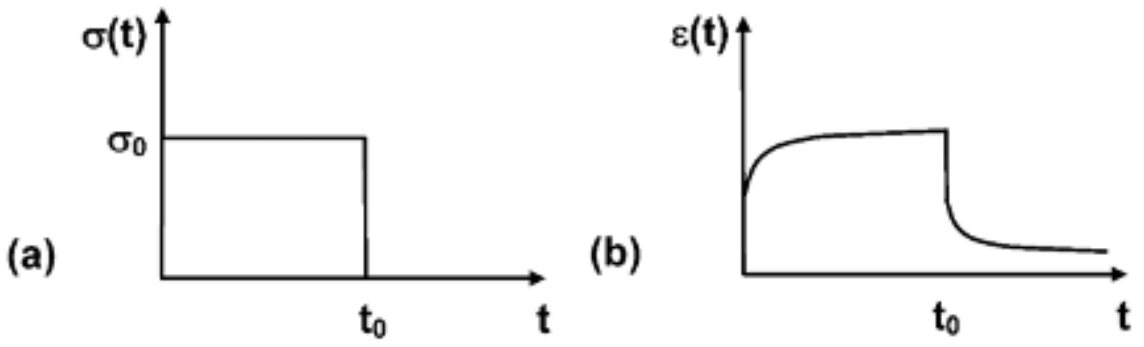

Figure 10: Schematic of a creep and recovery test. (a) stress input and (b) strain response

The creep and recovery test is performed in force command. First the specimen is loaded up to the desired stress level. Ideally, as seen in Figure 10, the loading would happen instantaneously, in a stepwise fashion. However, in order to avoid undesirable dynamic effects in the servo-controlled testing system, the specimen is loaded up with a fast, but finite stress rate (see Table 9 for loading/unloading rates used in each test). Next, the specimen is held at a constant stress level for one hour, in order to allow the specimen to creep. Immediately after the creep period, the specimen is unloaded to zero stress. Then the specimen is held at zero stress for the duration specified in Table 9, to allow the specimen to recover strain at zero stress. During the recovery period, the lower grip is released to ensure true zero stress is being applied to the test specimen. To prevent the drifting of the actuator likely to occur at zero force command, control is shifted from force to displacement for the rest of the recovery period. While in displacement control, the position of the actuator is frozen, preventing any type of drifting and potential destruction of equipment or specimen.

During the loading and unloading to zero stress portions of the test, the following data were collected every 0.1 s: time, displacement, force command, force, and strain. During the creep and recovery periods, the same data were collected at one second intervals. The data for each of the four portions of the test (loading, creep, unloading to zero stress, and recovery) were stored in individual files, resulting in four data files.

Table 9: Test stress levels and respective load and unload rate

Creep Stress (% UTS)	Creep Stress (MPa)	Loading/Unloading Rate (MPa/s)	Recovery Duration (s)
15%	36.8	3	7,200
20%	49.0	3	7,200
30%	73.5	5	7,200
40%	98.0	5	7,200
50%	122.5	5	10,800
60%	147.0	5	10,800

4.4 Optical Microscopy

Each specimen was examined under an optical microscope after it was tested either in tension to failure or under tension-tension fatigue. Examination was performed with a Zeiss SteREO Discovery.V12 stereoscopic optical microscope, controlled by a Zeiss SYCOP 3 control panel and a Zeiss EMS 3 controller. Optical micrographs were taken with a Zeiss AxioCam 305 color digital camera. Illumination was provided by a Zeiss KL 2500 LCD cold light source. The microscope interfaced with the computer through the Zeiss ZEN Core V2.7 software, which controlled digital parameters for the image taking and took the images. All images in this study were taken at 8X magnification. Figure 11 shows the optical microscope and its associated equipment.

Figure 11: Zeiss SteREO optical microscope and associated equipment

V. Experimental Results and Discussion

5.1 Assessment of Specimen-to-Specimen Variability

Specimens from the same panel may vary slightly in dimensions, as well as, in mechanical properties, due to minor differences/imperfections in the manufacturing and machining process. In this study, four different panels were used: baseline composite 0/90 panel B-02, baseline composite ±45 panel B-05, NanoStitch composite 0/90 panel NS-07, and NanoStitch composite ±45 panel NS-02. Three specimens from each panel were tested in tension to failure to measure the elastic modulus and the UTS. Panel and specimen dimensions were summarized earlier in Tables 7 and 8. The average values of the elastic modulus and UTS for each panel are presented in Tables 10 and 11, respectively. The modulus was determined through tension to failure tests as outlined in Section 4.2.1, by finding the slope of the linear portion of stress-strain curve.

Table 10: Average elastic modulus results for each composite panel

Panel	Type	Avg Modulus (GPa)	Std Deviation (GPa)	Coeff. Of Variation (%)
B-02	Baseline 0/90	79.63	1.26	1.58
NS-07	NanoStitch 0/90	82.13	0.74	0.90
B-05	Baseline ±45	17.17	0.57	3.31
NS-02	NanoStitch ±45	19.40	1.35	6.97

Table 11: Average UTS results for each Composite panel

Panel	Type	Average UTS (MPa)	Std Deviation (MPa)	Coeff. Of Variation (%)
B-02	Baseline 0/90	1041	3.21	0.31
NS-07	NanoStitch 0/90	1116	34.39	3.08
B-05	Baseline ±45	276	3.79	1.37
NS-02	NanoStitch ±45	285	2.08	0.73

As can be seen in Tables 10 and 11, the largest variations in modulus and UTS are seen for the NanoStitch panels and the baseline composite ±45 panel. Nevertheless, all coefficients of variation presented in Tables D and E are small (below 10%). Hence the specimen-to-specimen variability can be considered negligible.

5.2 Uniaxial Tension to Failure Tests

5.2.1 Tension to Failure Testing of 0/90 Composites.

Each average elastic modulus and UTS value seen in Tables 10 and 11 was calculated based on the experimental results obtained in three tests. Tensile properties obtained in all tension to failure tests of 0/90 specimens performed in this work are summarized in Table 12.

Table 12: Summary of tensile properties of the 0/90 composite panels

Type	Specimen	Modulus (GPa)	UTS (MPa)
Baseline	B-02-12	79.8	1037
	B-02-15	78.3	1042
	B-02-22	80.8	1043
NanoStitch	NS-07-07	82.7	1145
	NS-07-17	81.3	1078
	NS-07-26	82.4	1125

As seen in Table 10, the average values of the elastic modulis were 79.63 GPa for the 0/90 baseline composite and 82.13 GPa for the 0/90 NanoStitch composite. Furthermore, results in Table 12 show little specimen-to-specimen variability in the modulus values produced for 0/90 specimens of either composite system, which is corroborated by a 1.58% covariance for the 0/90 baseline material and 0.90% for the NanoStitch material. Tensile stress-strain curves produced in tension tests of 0/90

baseline composite specimens and 0/90 NanoStitch composite specimens are shown in Figures 12 and 13, respectively. Several stress-strain curves in Figures 12 and 13 exhibit slight stiffening as the loading progresses. This phenomenon is likely due to straightening of carbon fibers during the tension test or minor fiber/matrix damage occurring.

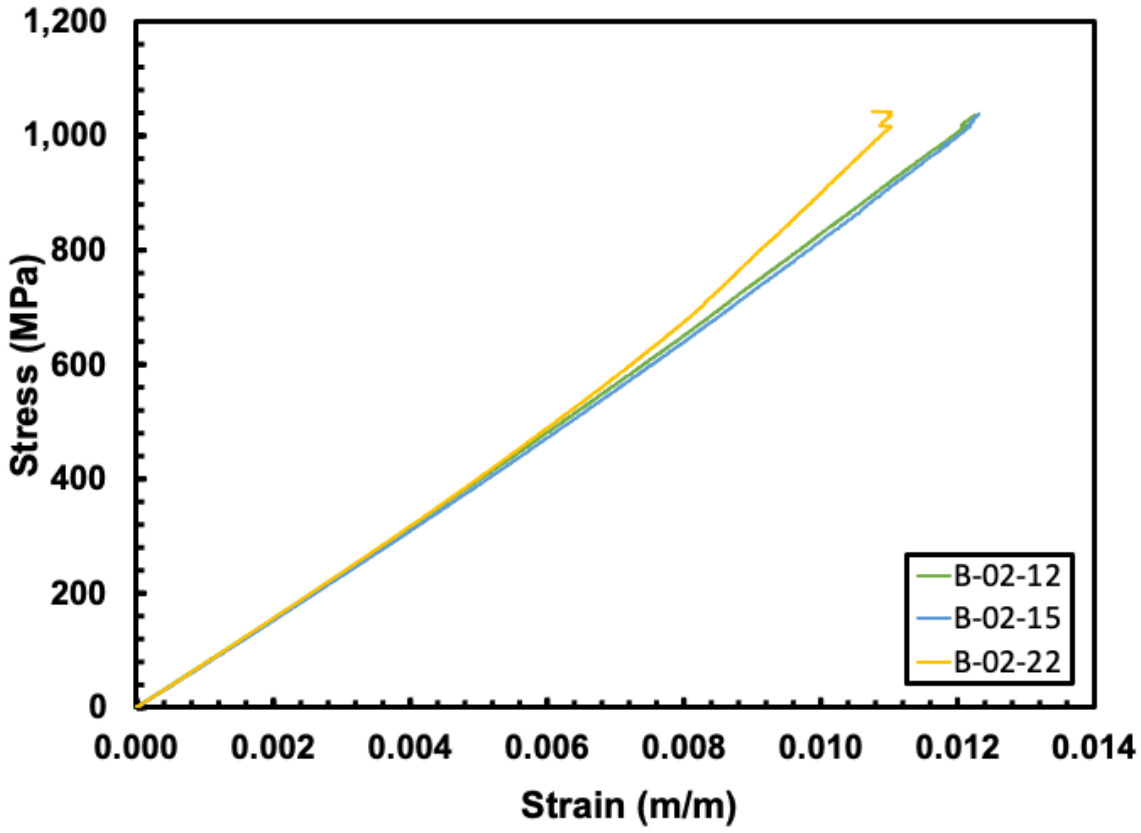

Figure 12: Tensile stress-strain curves obtained for 0/90 baseline composite at room temperature in laboratory air

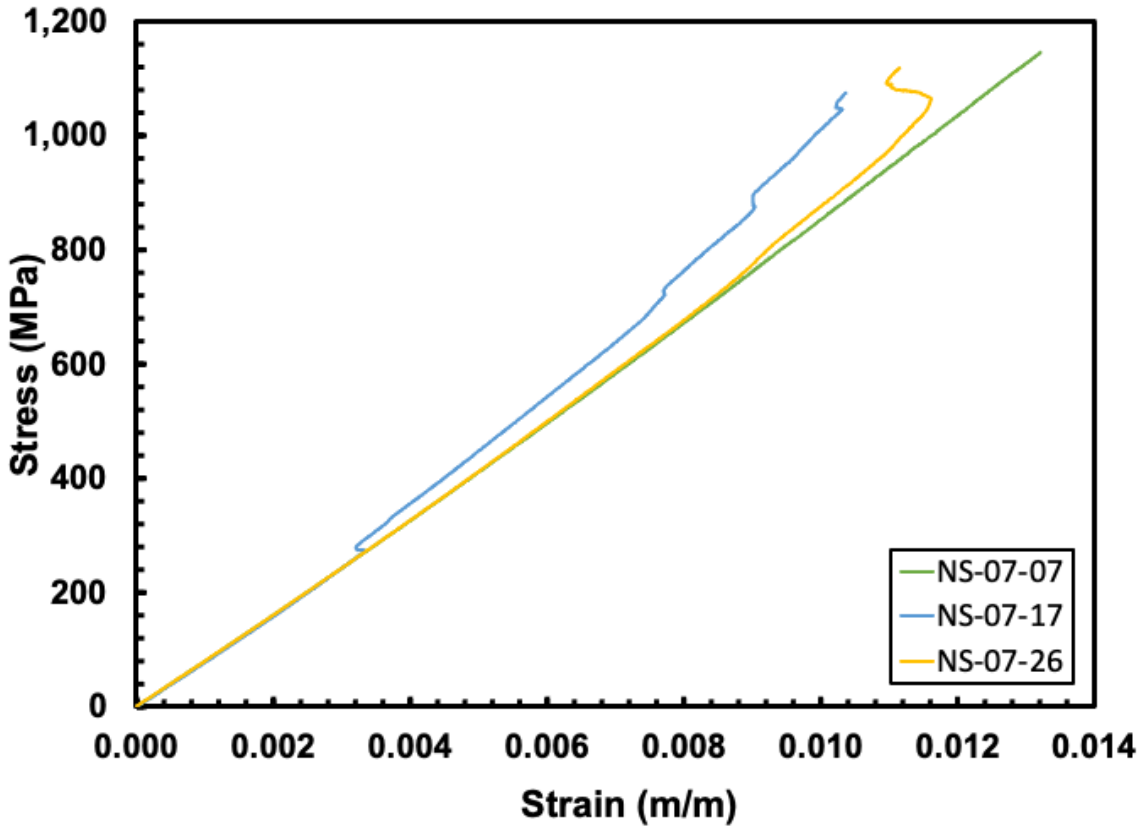

Figure 13: Tensile stress-strain curves obtained for 0/90 NanoStitch composite at room temperature in laboratory air

Figure 14 combines the stress-strain curves produced in six tension-to-failure tests of 0/90 specimens and indicates the average UTS of each composite material. Note that the UTS is 1041 MPa for the 0/90 baseline composite and 1116 MPa for the 0/90 NanoStitch composite. Stress-strain curves in Figure 14 reveal some specimen-to-specimen variability in tensile stress-strain behavior and tensile properties for the 0/90 specimens of both baseline and NanoStitch composites. However, the variability is small enough to be neglected.

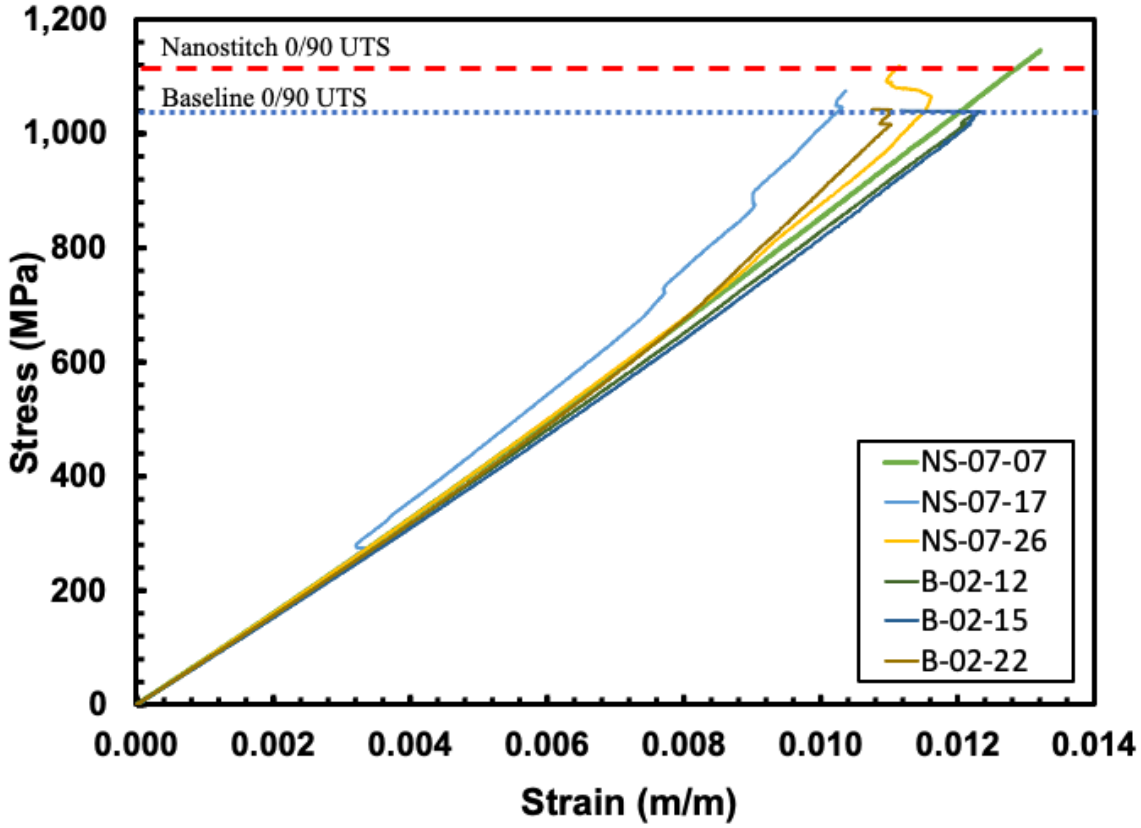

Figure 14: A comparison of the tensile stress-strain curves obtained for 0/90 baseline composite and 0/90 NanoStitch composite.

As mentioned above, the elastic modulus values were determined by examining the linear regions of the tensile stress-strain curves produced in tension tests. The linear region of the tensile stress-strain curves obtained for three 0/90 baseline composite specimens and three 0/90 NanoStitch composite specimens are shown in Figure 15.

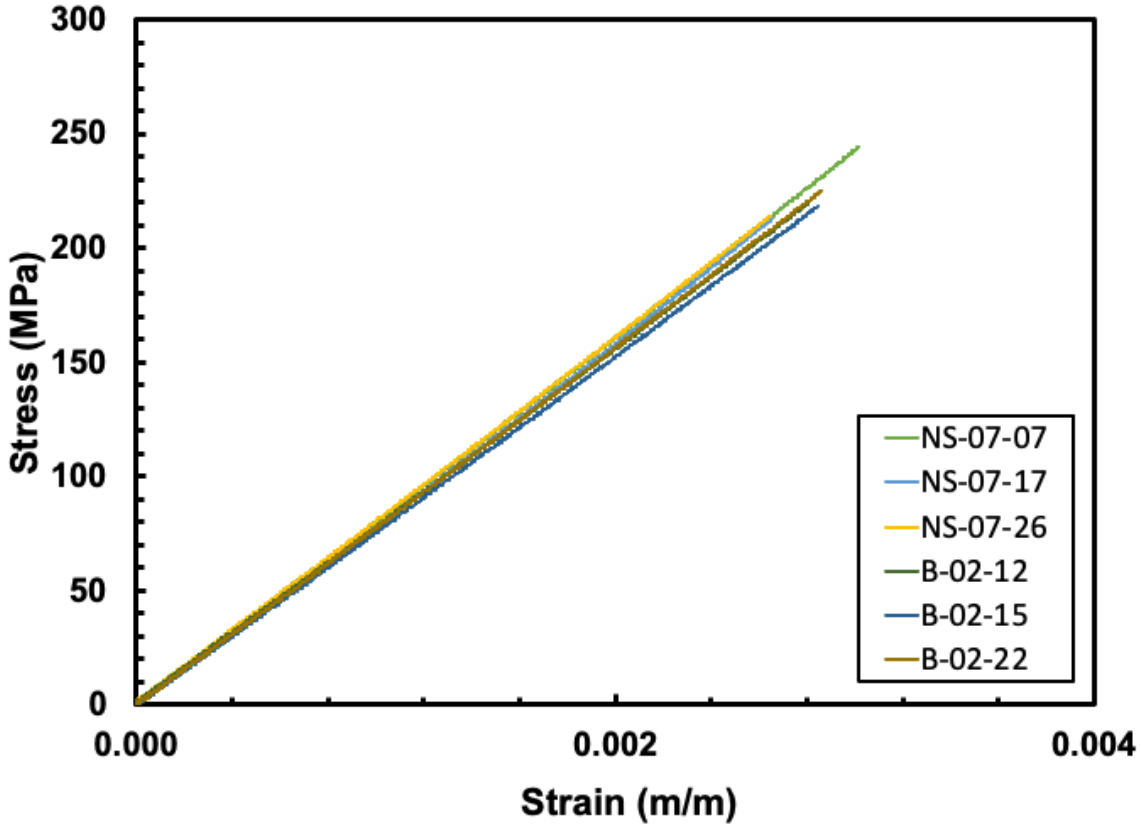

Figure 15: Linear region of the tensile stress-strain curves obtained for three 0/90 baseline composite specimens and three 0/90 NanoStitch composite specimens. The linear regions of the tensile stress-strain curves were used to determine the elastic modulus values for each test specimen.

The developers of the NanoStitch composite, N12 Technologies, focused on improving the interlaminar properties. As reported in references [1], [5], [11] the interlaminar shear properties of the composite were indeed improved by adding NanoStitch layers. However, it is recognized that an improvement in some mechanical properties is frequently obtained at the cost of degrading other properties. Hence, it is important to assess the effects of adding the NanoStitch layers on the in-plane properties of the composite. Results presented above demonstrate that the addition of the CNT reinforcement between the plies of the composite does not degrade tensile modulus or

UTS of the composite material with 0/90 fiber orientation. In fact, the average modulus of the 0/90 NanoStitch composite is some 3% higher than that of the 0/90 baseline composite, while the average UTS of the 0/90 NanoStitch composite is a little over 7% higher than the UTS of the 0/90 baseline composite.

5.2.2 Tension to Failure Tests of ±45 Composites.

Each average elastic modulus and UTS values seen in Table 10 and11 were calculated based on the experimental results obtained in sets of three tests for each fiber orientation and composite type. Tensile properties obtained in all tension to failure tests of ±45 specimens performed in this work are summarized in Table 13.

Table 13: Summary of tensile properties of the ±45 composite panels

Type	Specimen	Modulus (GPa)	UTS (MPa)
Baseline	B-05-06	16.7	279
	B-05-15	17.8	278
	B-05-19	17.0	272
NanoStitch	NS-02-02	20.8	287
	NS-02-07	18.1	283
	NS-02-20	19.3	286

As can be seen in Table 10, the average values of the elastic modulus were 17.17 GPa for the ±45 baseline composite and 19.40 GPa for the ±45 NanoStitch composite. Furthermore, results in Table 13 show little specimen-to-specimen variability in the modulus and UTS values produced for ±45 specimens of either composite system. Tensile stress-strain behavior of the ±45 baseline composite and ±45 NanoStitch composite are typified in Figures 16 and 17, respectively.

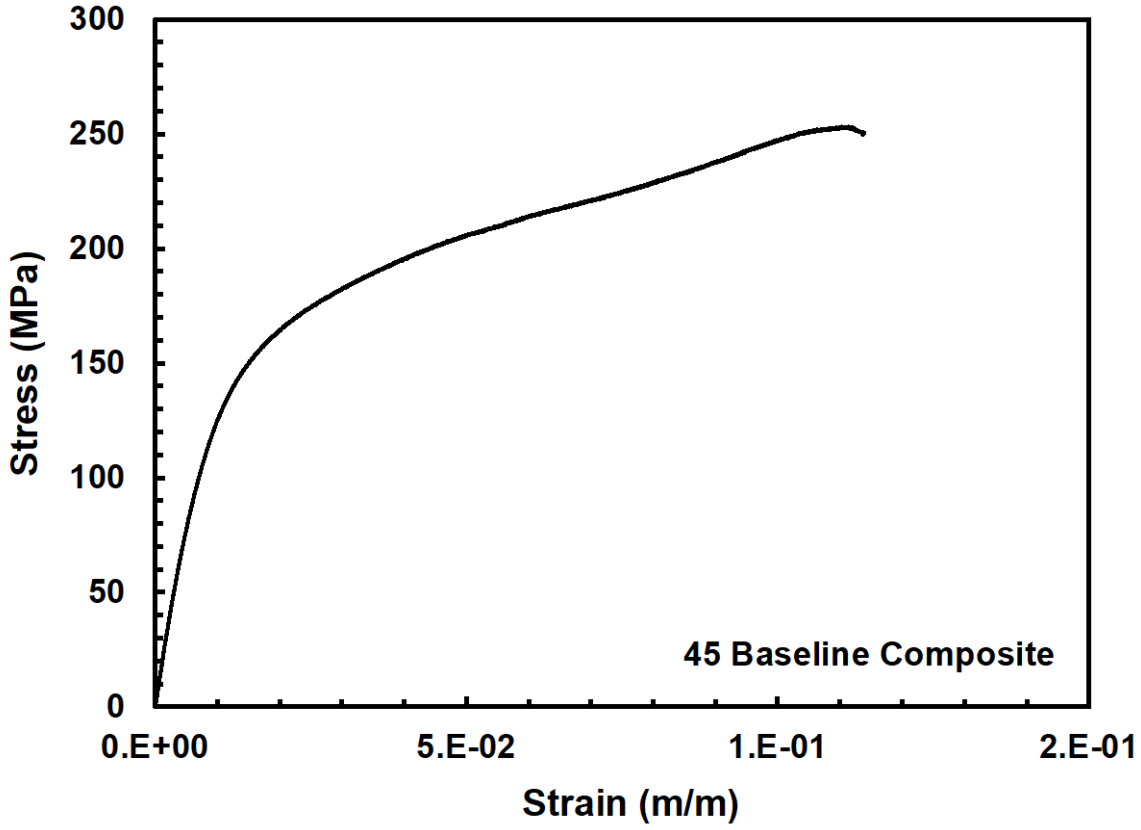

Figure 16: Typical tensile stress-strain curve obtained for ±45 baseline composite at room temperature in laboratory air.

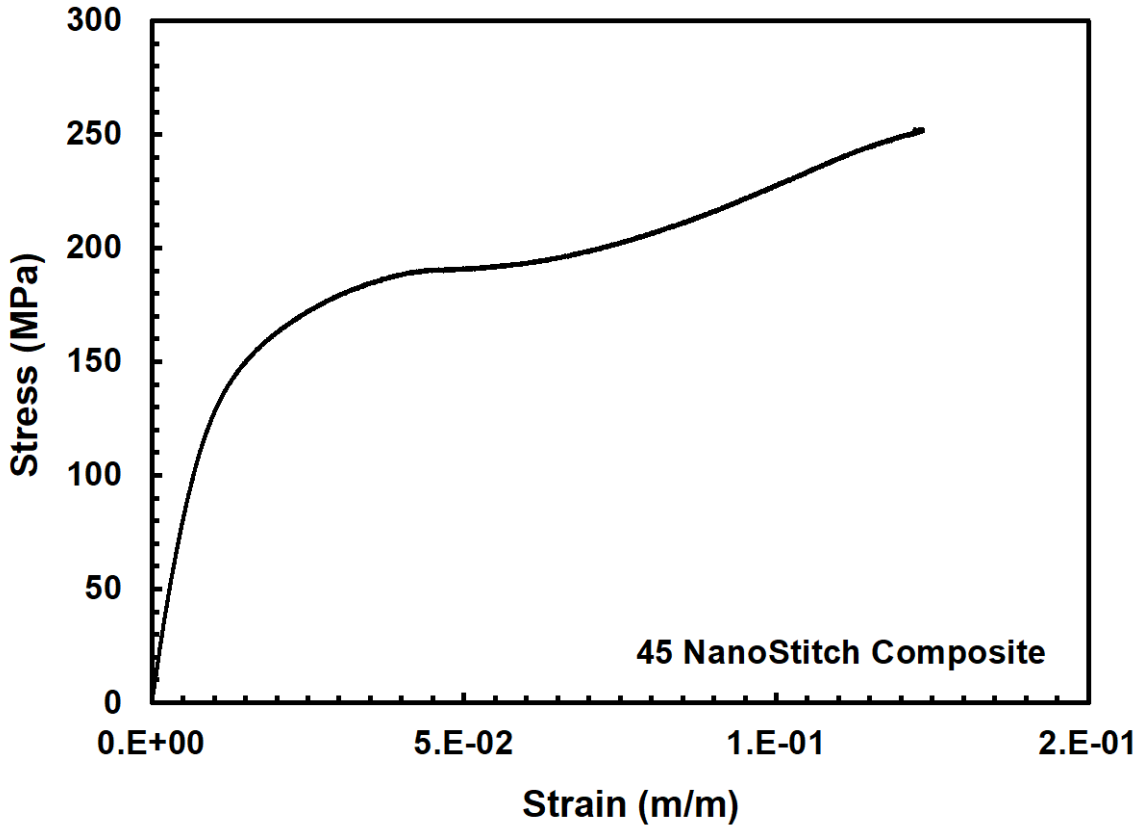

Figure 17: Typical tensile stress-strain curve obtained for ±45 NanoStitch composite at room temperature in laboratory air.

Comparing the baseline material to the NanoStitch material, there is a 12.99% increase in the elastic modulus and a 3.26% increase in the UTS. The CNT reinforcement seems to stiffen the material, but does not increase its overall strength by much. This is more apparent in the ±45° specimens than in the 0/90° specimens, because the matrix carries more of the load in this orientation and the CNTs reinforce the interlaminar matrix, rather than the fibers.

5.3 Tension-Tension Fatigue Tests

All tension-tension fatigue tests were conducted at room temperature in laboratory air with a maximum to minimum stress ratio of 0.1 (R = 0.1) at a frequency of 1 Hz. Fatigue run out was set to $2x10^5$ cycles. The maximum stress was determined by averaging the first ten peak stress values of the fatigue cycling.

5.3.1 Tension-Tension Fatigue Testing of 0/90 Composites.

A summary of the tension-tension fatigue tests performed on the 0/90 specimens is presented in Table 14.

Table 14: A summary of tension-tension fatigue results for the 0/90 specimens of baseline and NanoStitch composites

Type	Specimen	Max Stress (MPa)	Max Stress (% UTS)	Target Max Stress (% UTS)	Cycles to Failure (N)
Baseline	B-02-16	827	79.56	80	Run Out
	B-02-19	932	89.56	90	Run Out
NanoStitch	NS-07-08	887	79.48	80	Run Out
	NS-07-16	997	89.34	90	158,023

The results of the tension-tension fatigue tests for the 0/90 specimens of both baseline and NanoStitch composites are also presented in Figure 18 as stress vs. cycles to failure (S-N) curves. The baseline composite achieved runout of $2x10^5$ cycles in test performed with the maximum stress of 932 MPa (90% UTS). The NanoStitch composite achieved fatigue runout at the maximum stress of 887 MPa (80% UTS). However, the NanoStitch composite survived 158,023 cycles at the maximum fatigue stress of 997 MPa (90% UTS). Excellent tension-tension fatigue performance of both composite with 0/90 fiber orientation is not surprising.

Figure 19 shows typical evolution of the stress-strain hysteresis response for 0/90 NanoStitch specimens that achieved fatigue runout of 200,000 cycles. Because the composite accumulates little strain with fatigue cycles, the hysteresis stress-strain loops in Figure 19 were each shifted by 0.001 m/m along the strain axis for the sake of presentation. As seen in Figure 19, the slope of the hysteresis stress-strain loops remains virtually unchanged from cycle one to cycle 200,000, indicating that little to no damage occurred to the load-bearing fibers during fatigue cycling.

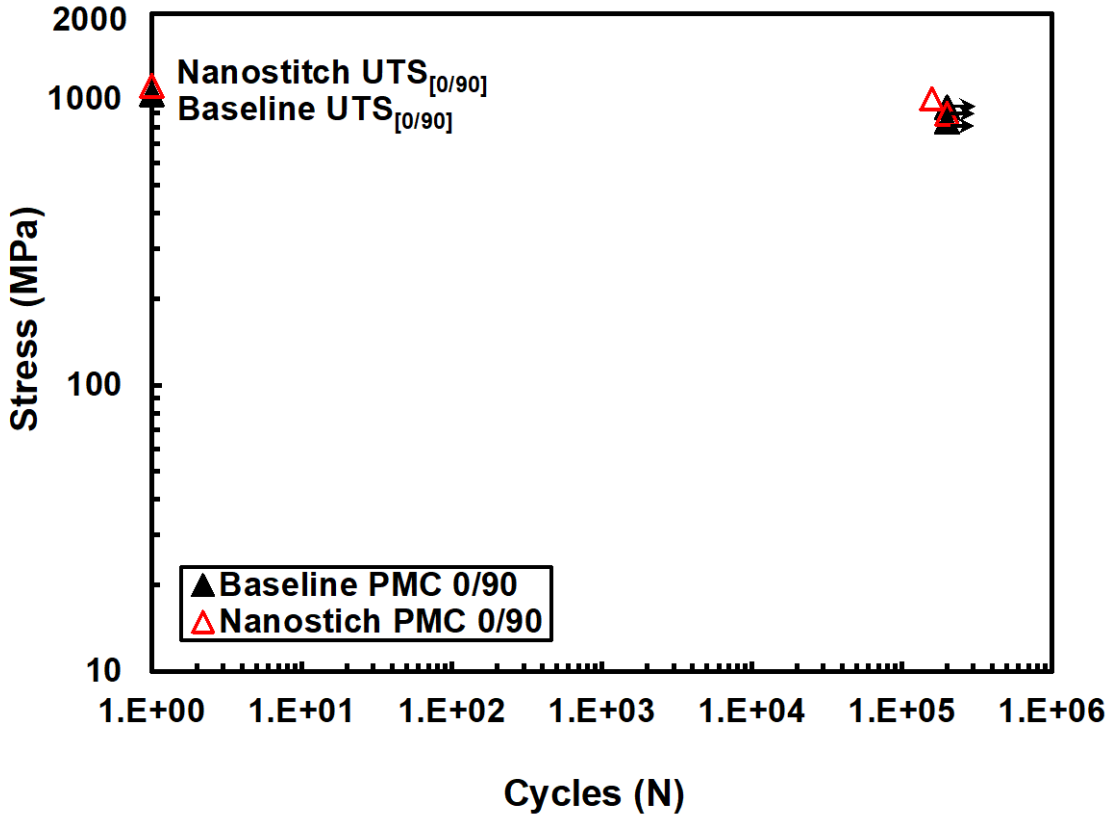

Figure 18: Fatigue S-N curves for baseline and NanoStitch specimens with 0/90 fiber orientation

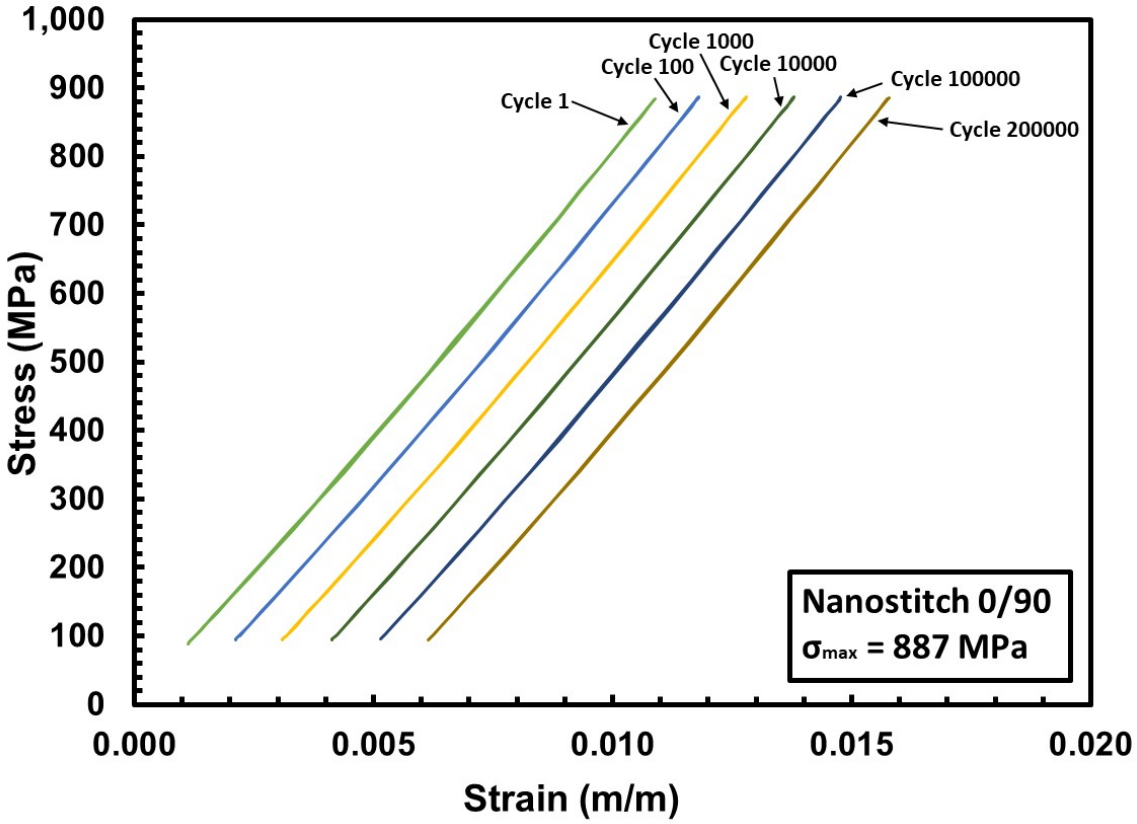

Figure 19: Typical hysteresis stress-strain response of the NanoStitch specimens with 0/90 fiber orientation that achieved runout of 200,000 cycles. Hysteresis stress-stain loops for cycles 100 to 200,000 are shifted by 0.001 m/m for presentation purposes.

Changes in shape and area of the hysteresis stress-strain loops with fatigue cycles generally reflect changes in mechanical properties of the composite. The area of the hysteresis loop indicates the energy dissipated in each cycle and is associated with the linear and non-linear deformation. As seen in Figure 19, the hysteresis area remains virtually unchanged (the stress-strain loops remain very narrow), therefore the response of the 0/90 composite remains nearly linear elastic.

A different trend in the evolution of the hysteresis stress-strain response is seen in Figure 20, showing results obtained for the 0/90 NanoStitch specimen tested in fatigue with the maximum stress of 997 MPa (90% UTS). Recall that this specimen did not

achieve fatigue runout, but failed after 158,023 cycles. The area of the hysteresis loop increases with fatigue cycles pointing to growing damage within the composite. The increase in hysteresis area also indicates non-linear deformation. The shape of the stress-strain hysteresis loops also changes during the test. Hysteresis loops produced during cycles 1-1000 are narrow, the loading paths are nearly the same as the unloading paths, indicating early linear stress-strain behavior. As the cycling progresses, the loading and the unloading paths of the hysteresis loops become non-linear, the stress-strain hysteresis loops also acquire an "S" shape. These trends are indicative of growing damage in the composite, which culminates in the ultimate composite failure [15].

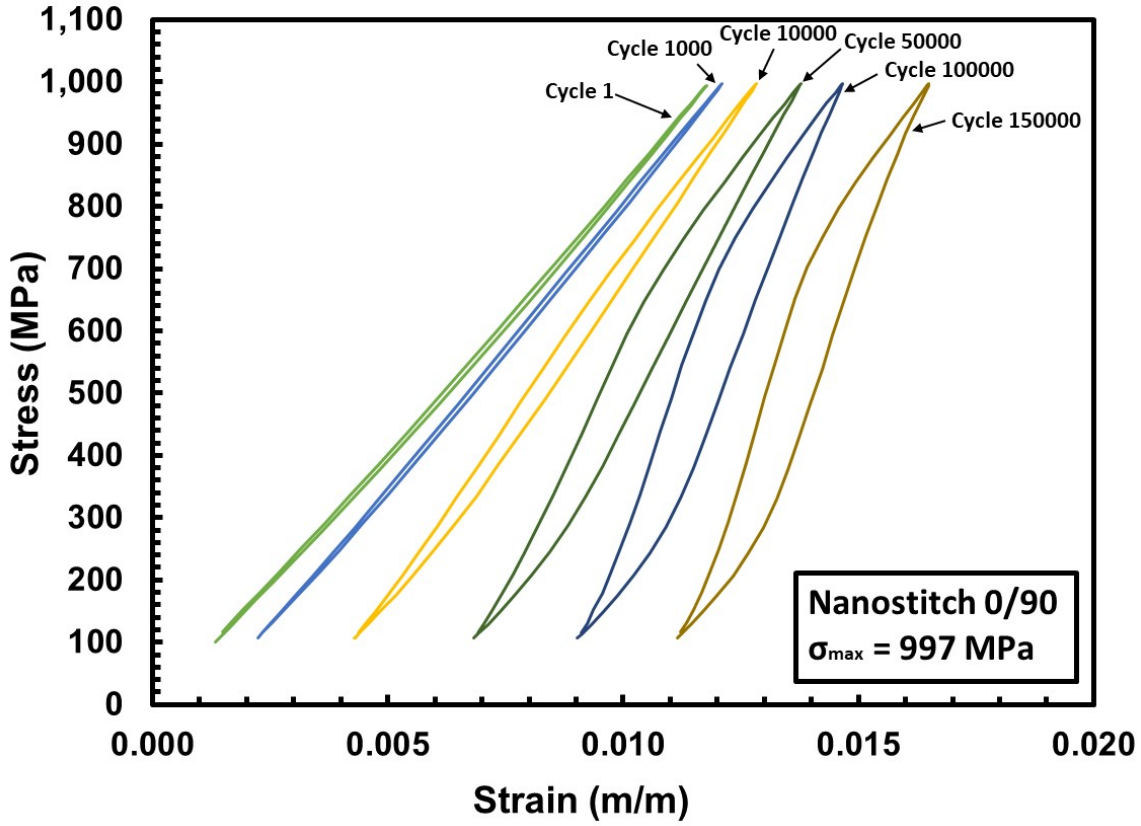

Figure 20: Hysteresis stress-strain response of the NanoStitch specimen with 0/90 fiber orientation tested in fatigue with the maximum stress of 997 MPa (90% UTS), N_f = 158,023 cycles. Hysteresis stress-strain loops for cycles 1000 to 150,000 are each shifted by 0.001 m/m along the strain axis for presentation purposes.

Change in hysteresis modulus (determined from the maximum and minimum stress-strain data points during a load cycle) with fatigue cycles reflect damage growth in the composite during fatigue test. Figure 21 presents the change in normalized modulus (i.e. modulus normalized by the modulus produced in the first cycle) with fatigue cycles for the 0/90 specimens of the baseline composite and the NanoStitch composite. Little, if any change in modulus is seen for the composite specimens that achieved fatigue runout and produced narrow and nearly linear stress-strain hysteresis loops. In these tests, damage development is minimal. Conversely, there is a considerable rise in the

normalized hysteresis modulus for the NanoStitch specimen tested with the maximum stress of 997 MPa (90% UTS). Again, we note that this specimen did not achieve fatigue runout, but failed after 158,023 cycles. Typically, the normalized modulus decreases as damage develops and test specimen approaches failure. The atypical behavior of the normalized hysteresis modulus seen for this specimen is attributed to the irregular "S"-shaped hysteresis stress-strain loops produced during the test. The hysteresis modulus is not a reliable measure of damage development in cycles with the irregular "S"-shaped hysteresis stress-strain behavior. Hence the increase in normalized modulus observed for this particular specimen should be disregarded.

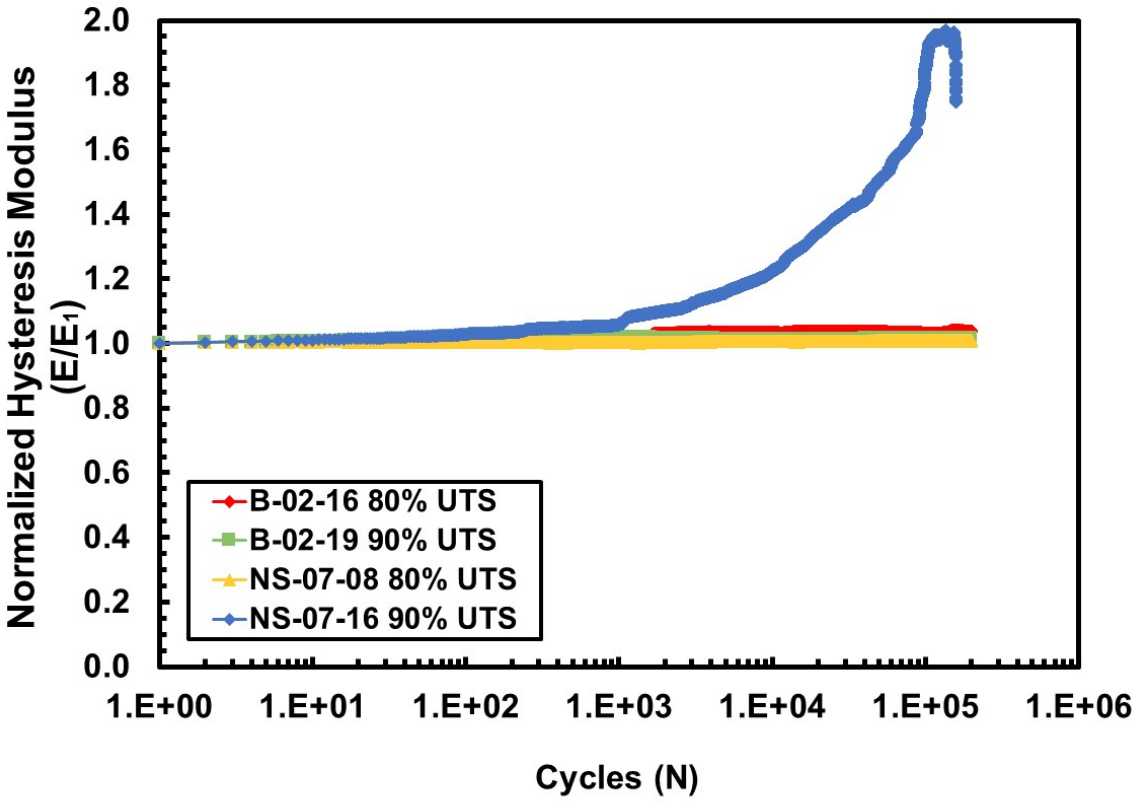

Figure 21: Normalized modulus vs. fatigue cycles for the baseline composite specimens and the NanoStitch composite specimens with 0/90 fiber orientation

Strain accumulation with fatigue cycles for the 0/90 specimens of both the baseline and the NanoStitch composites that achieved fatigue runout of 200,000 cycles is presented in Figure 22. It can be noted that there is virtually no strain ratchetting (defined as strain accumulation with cycles). The results in Figure 22 support an earlier observation that these specimens exhibit little, if any, loss of stiffness during cycling. Furthermore, these specimens exhibit very narrow and nearly linear hysteresis stress-strain behavior. These combined observations indicate that little damage developed in the composites during fatigue test.

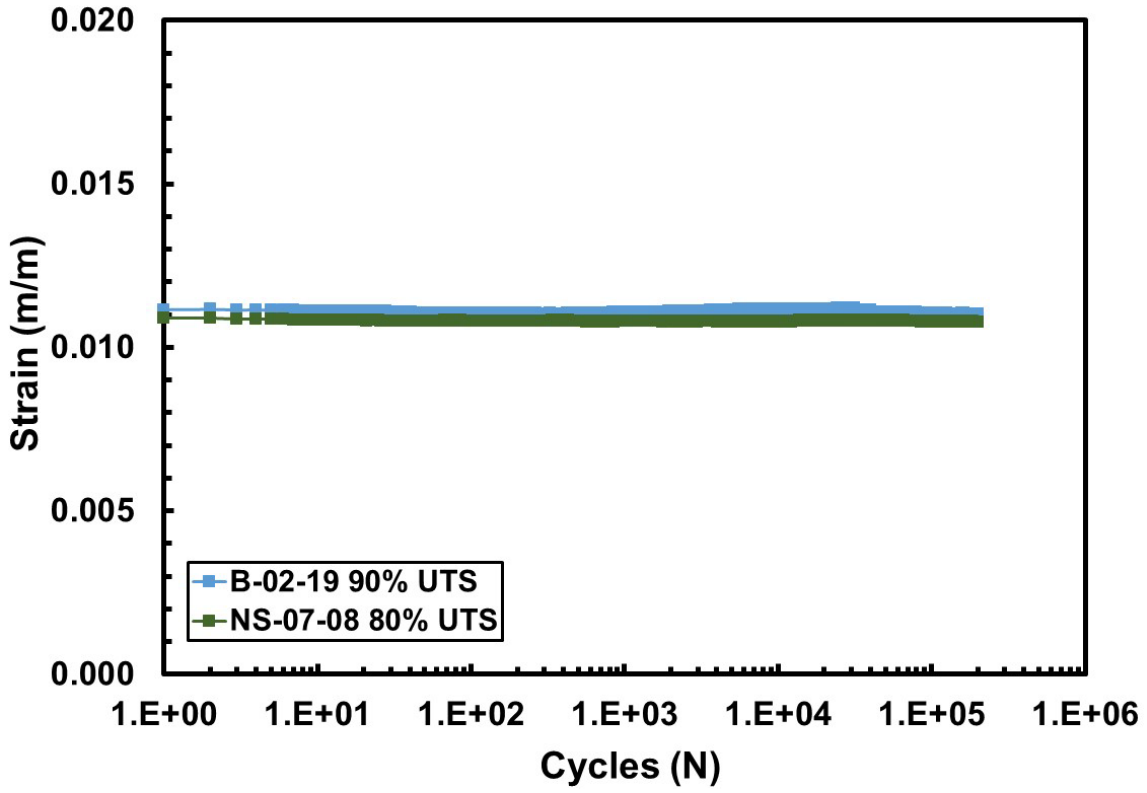

Figure 22: Strain accumulation with fatigue cycles for the baseline composite specimens and the NanoStitch composite specimens with 0/90 fiber orientation

5.3.2 0/90 Retained Properties.

All specimens that achieved fatigue runout were tested in tension to failure tests to measure the retained properties. The tensile test was performed according to the procedure described in Section 5.2. The retained tensile properties are presented in Table 15, along with the initial modulus measurements.

Table 15: Retained tensile properties of the 0/90 composite specimens subjected to 200,000 cycles of prior tension-tension fatigue.

Type	Specimen	Initial Modulus (GPa)	Retained Modulus (GPa)	Retained UTS (MPa)
Baseline	B-02-16	82.2	80.0	1148
	B-02-19	82.6	76.2	1161
NanoStitch	NS-07-08	81.2	75.3	1135

The baseline composite specimen tested with the maximum stress of 80% UTS retained 97.32% of its elastic modulus, while the NanoStitch specimen tested with the maximum stress of 80% UTS retained 92.73% of its modulus. A somewhat lower modulus retention noted for the NanoStitch composite may be attributed to additional crack initiation points and matrix defects introduced during fabrication with the added CNTs. Not surprisingly the baseline composite specimen tested with the higher maximum stress of 90% UTS retained a lower percentage (92.25%) of its modulus. We also note that both the 0/90 baseline composite and the 0/90 NanoStitch composite retain 100% of their tensile strength.

Figure 23 shows the effects of prior fatigue on tensile stress-strain behavior of the baseline composite and the NanoStitch composite with 0/90 fiber orientation. The stress-strain behavior of all pre-fatigued specimens remains nearly linear to failure. Evidently

prior fatigue has little influence on the post-fatigue stress-strain response of the baseline composite and the NanoStitch composite with 0/90 fiber orientation.

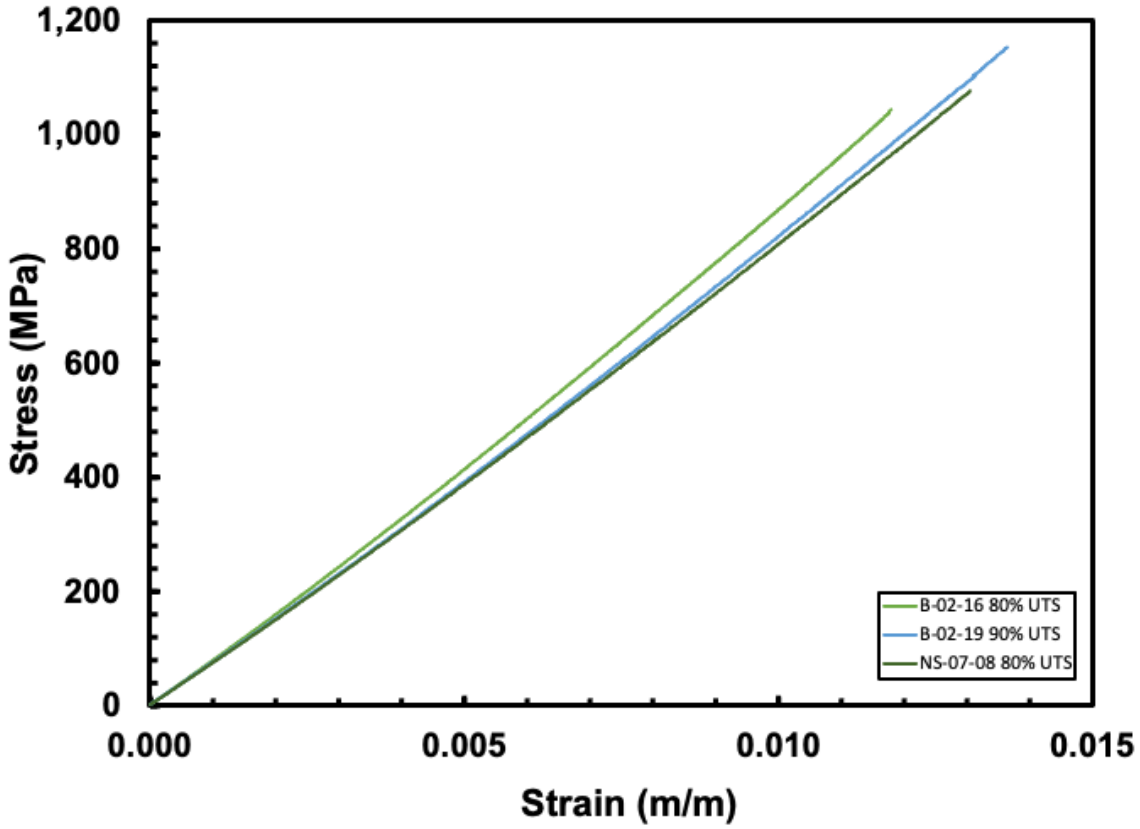

Figure 23: Effects of prior fatigue on tensile stress-strain behavior of the baseline composite and the NanoStitch composite with 0/90 fiber orientation

5.3.3 Tension-Tension Fatigue Testing of ±45 Composites.

A summary of the tension-tension fatigue tests performed on the ±45 specimens is presented in Table 16. The results of the tension-tension fatigue tests for the ±45 specimens of both baseline and NanoStitch composites are also presented in Figure 24 as stress vs. cycles to failure (S-N) curves.

Table 16: A summary of tension-tension fatigue results for the ±45 specimens of baseline and NanoStitch composites

Type	Specimen	Max Stress (MPa)	Max Stress (% UTS)	Target Max Stress (% UTS)	Cycles to Failure (N)
Baseline	B-05-24	105	38.00	40	Run Out
	B-05-05	131	47.41	50	Run Out
	B-05-25	144	52.09	55	1,237
	B-05-08	159	57.54	60	18,384
	B-05-17	155	56.14	60	11,354
	B-05-11	177	64.11	70	311
	B-05-12	180	64.96	70	138
	B-05-14	181	65.50	70	3,918
	B-05-07	164	59.36	80	1
	B-05-10	194	70.21	80	10
	B-05-23	206	74.55	80	2070
NanoStitch	NS-02-03	137	48.17	50	Run Out
	NS-02-06	137	47.97	50	Run Out
	NS-02-22	151	52.92	55	57,033
	NS-02-25	151	52.80	55	20,831
	NS-02-11	163	57.07	60	7,433
	NS-02-21	164	57.51	60	9,859
	NS-02-16	189	66.23	70	6,417
	NS-02-24	187	65.64	70	6,603
	NS-02-05	213	74.65	80	1,465
	NS-02-15	207	72.61	80	3,883
	NS-02-14	214	74.95	85	14
	NS-02-26	209	73.20	85	7
	NS-02-01	212	74.15	90	5

As expected, the 0/90 specimens are very resistant to tension-tension cycling. In contrast, the cyclic stresses used in fatigue tests of the ±45 specimens of the two composites are much lower than those used to test the 0/90 specimens. Fatigue runout of 200,000 cycles was achieved at 131 MPa (47.4% of the UTS) for the ±45 baseline composite and at 137 MPa (48.2% of the UTS) for the ±45 NanoStitch composite. As seen in Table 16 and Figure 24, the addition of the NanoStitch layers did not degrade fatigue performance of the composite with ±45 fiber orientation. The two composites with ±45 fiber orientation exhibit very similar fatigue performance. The two ±45 S-N

curves in Figure 24 have nearly the same slope, indicating that the ±45 S-N data for the baseline composite and those for the NanoStitch composite can be fitted with similar power law equations.

Likewise, the 0/90 fatigue limit obtained for the 0/90 NanoStitch composite is approximately 80% of the 0/90 UTS, while the ±45 fatigue limit is only about 48% of the ±45 UTS. Results in Figure 25 confirm the earlier conclusion, namely that the addition of the CNT forests does not degrade the fatigue performance of the composite with ±45 fiber orientation. In fact, the tension-tension fatigue performance of the ±45 NanoStitch composite is slightly better, especially at higher maximum stress levels, than that of the ±45 baseline composite.

Also included in Table 16 is the target max stress that was commanded by the controller. When the target max stress is compared to the stress experienced by the specimen, it can be seen that the actual stress is on average 5.07% less than the target stress, while the 0/90° specimens only had an average deviation of 0.52%. The MTS load frame was tuned for stiffer samples, however it was decided that the larger deviations experienced by the ±45° specimens were not significant enough to warrant retuning.

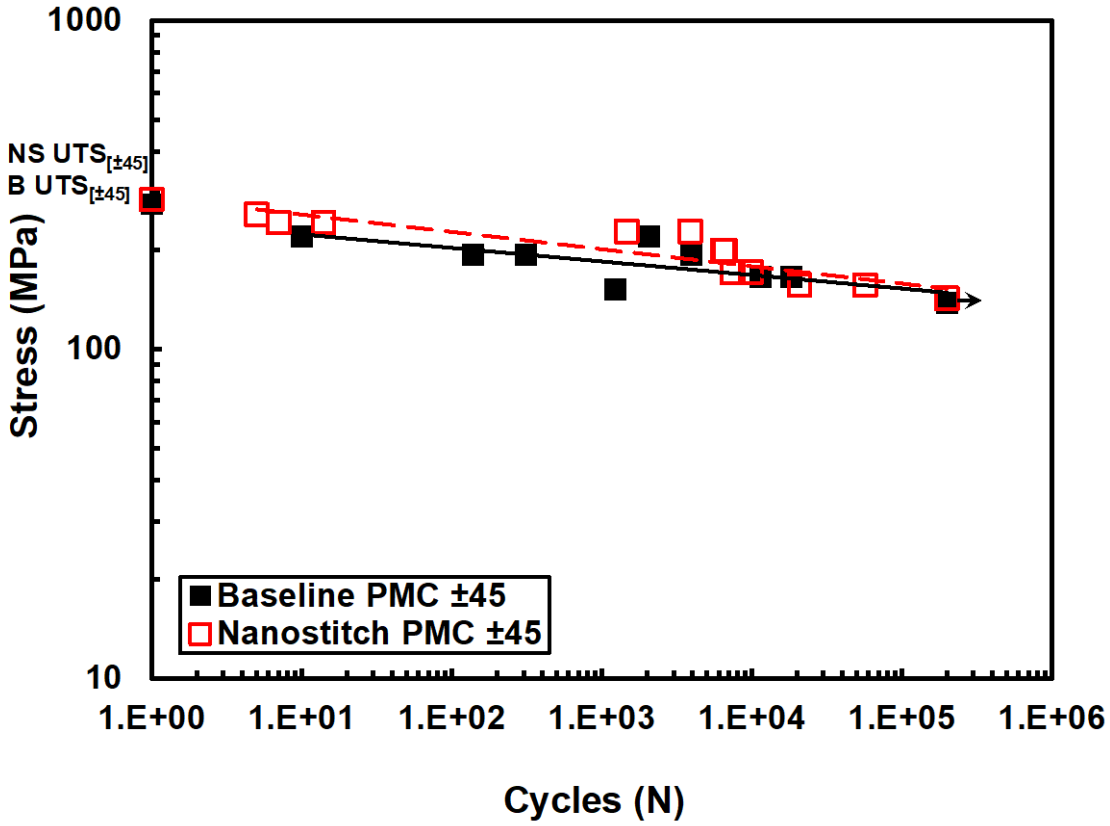

Figure 24: Fatigue S-N curves for baseline and NanoStitch specimens with ±45 fiber orientation. Arrow indicates that failure of specimen did not occur when the test was terminated.

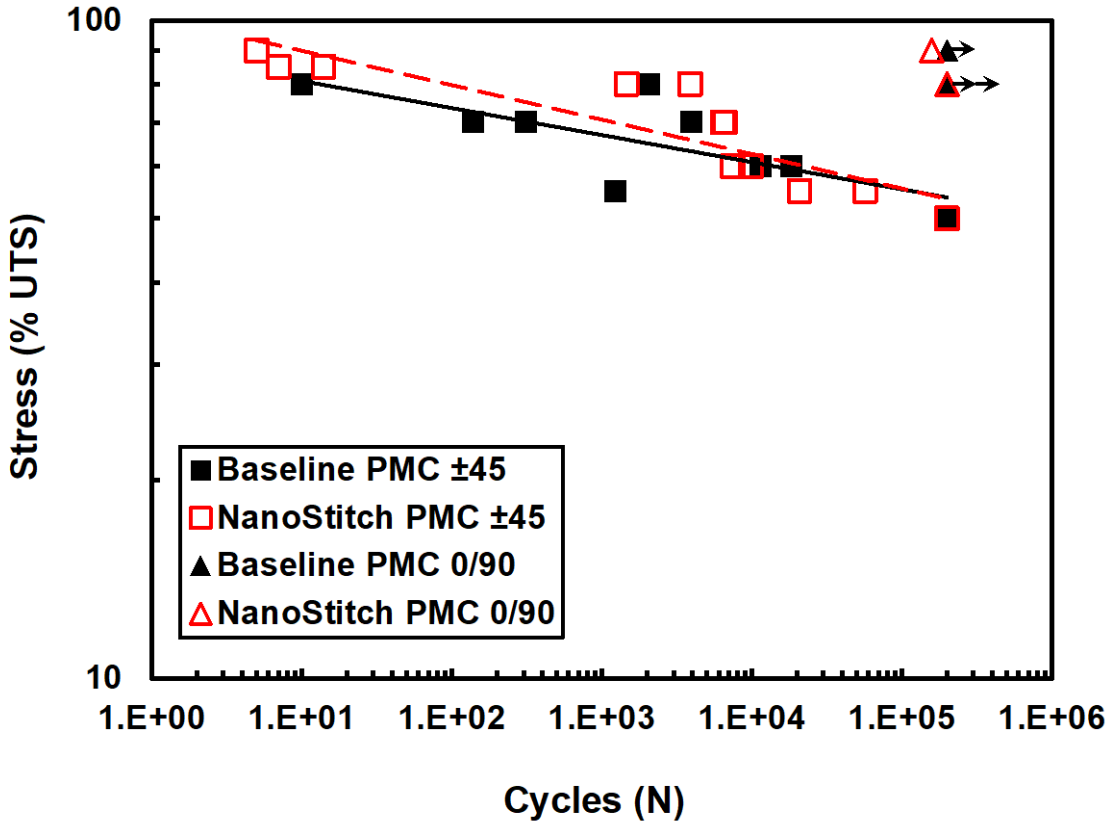

Figure 25: Fatigue S-N curves for baseline and NanoStitch specimens with 0/90 and ±45 fiber orientation. Arrow indicates that failure of specimen did not occur when the test was terminated. Maximum stress is shown as %UTS.

Figure 26 shows typical stress-strain hysteresis response for both baseline and NanoStitch composites with ±45 fiber orientation. Because the composite accumulates little strain with fatigue cycles, the hysteresis stress-strain loops in Figure 26 were each shifted by 0.001 m/m along the strain axis for the sake of presentation. The hysteresis stress-strain loops in Figure 26 are markedly nonlinear. While the shape of the loops and the hysteresis do not appear to change much with cycles, they clearly indicate non-linear deformation.

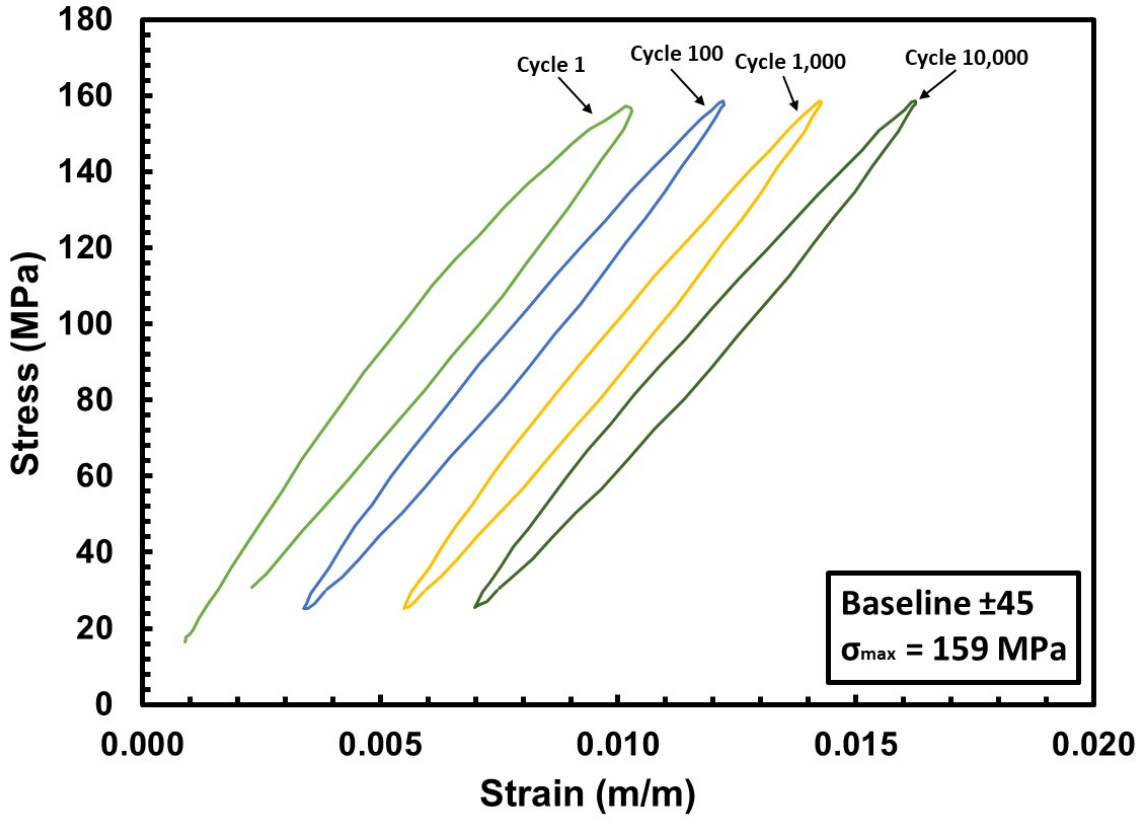

Figure 26: Hysteresis stress-strain response of the baseline specimen with ±45 fiber orientation (σ_{max} = 159 MPa, N_f= 18,384). Hysteresis stress-strain loops for cycles 100 to 10,000 are each shifted by 0.001 m/m along the strain axis for presentation purposes.

As mentioned earlier, change in hysteresis modulus (determined from the maximum and minimum stress-strain data points during a load cycle) during fatigue test is a reflection of damage development in the composite. Figures 27 and 28 presents the change in normalized modulus (i.e. modulus normalized by the modulus produced in the first cycle) with fatigue cycles for the ±45 specimens of the baseline composite and the NanoStitch composite, respectively. Notably, several ±45 specimens of both composites show increasing hysteresis modulus with cycling during fatigue test. Such modulus increase is attributed to a phenomenon known as fiber tow "scissoring." During tension-

tension fatigue, a ±45 composite specimen is under in-plane normal and shear stresses that cause fibers to realign in the direction of applied load (fiber tow "scissoring"), which results in increasing stiffness.

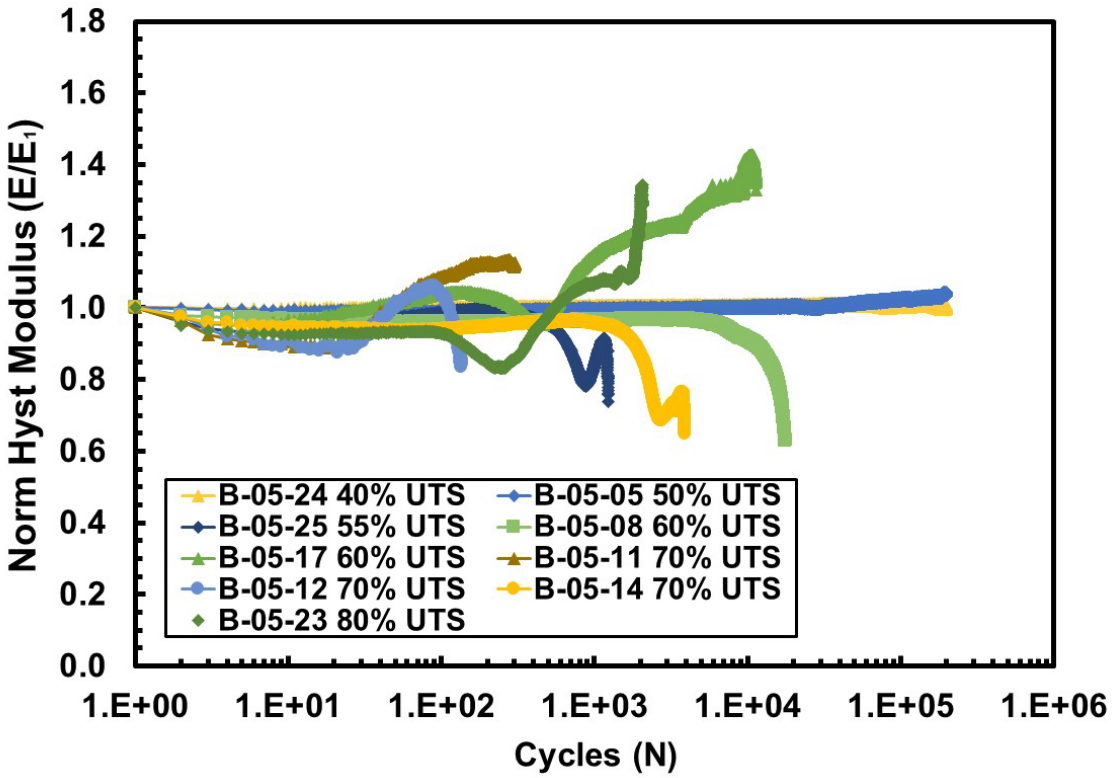

Figure 27: Normalized modulus vs. fatigue cycles for the baseline composite specimens with ±45 fiber orientation. Specimens B-05-24 and B-05-05 achieved fatigue runout of 200,000 cycles without failure.

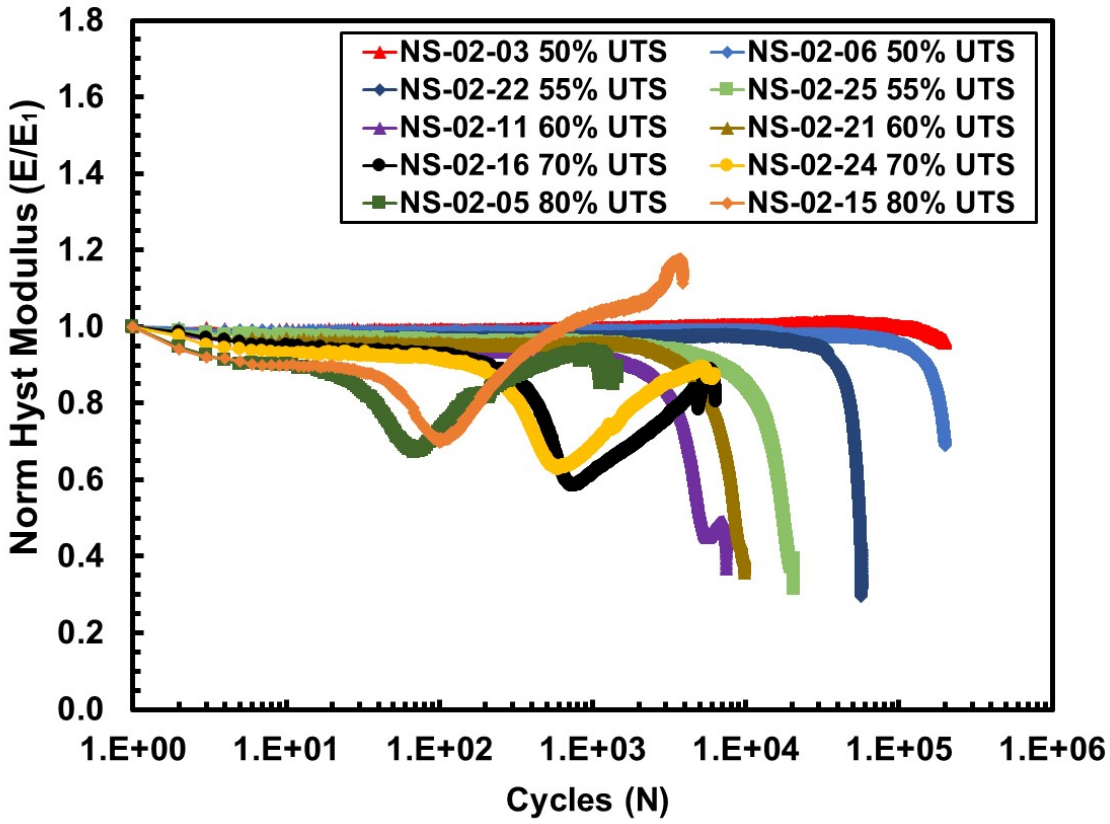

Figure 28: Normalized modulus vs. fatigue cycles for the NanoStitch composite specimens with ±45 fiber orientation. Specimens NS-02-03 and NS-02-06 achieved runout of 200,00 cycles without failure.

The dips observed in Figure 27 and 28, followed by increases in modulus can be explained by non-homogenous deformation as damage occurs, since the damage is not occurring homogenously throughout the specimen. This phenomena seems to only occur at higher stress levels. A possible explanation for this is that damage is accumulated much more quickly at higher peak stress levels and therefore, do not allow for damage to be more evenly distributed across the gauge section. Rather, the damage is more concentrated and causes more significant non-homogenous deformation and/or scissoring.

Strain accumulation with fatigue cycles for the ±45 specimens of the baseline and the NanoStitch composites is presented in Figures 29 and 30, respectively. Unlike in the case of 0/90 specimens, where strain accumulations were minimal, ±45 specimens of both composites accumulate appreciable strains during fatigue tests. The baseline composite and the NanoStitch composite specimens that achieved fatigue runout of 200,000 cycles represent an exception – these specimens accumulated negligible strains during fatigue cycling. Large strains accumulated in fatigue tests by other ±45 specimens are hardly surprising. In the case of ±45 composite specimens, the early increase in strain with cycles is most likely the result of the buildup of microstructural damage as well as some time-dependent creep strain (caused by the positive tensile mean stress). The later onset of interlaminar shear is the likely source of the further upward turning of the strain vs. cycles curves in Figures 29 and 30. We note that on average, ±45 NanoStitch composite specimens accumulate larger strains than the ±45 baseline composite specimens. Such larger strain accumulation with cycles may be due to the microstructural defects caused by the introduction of the NanoStitch layers during composite fabrication.

As the two NanoStitch composite specimens in Figure 30 that achieve runout approach 200,000 cycles, they begin to accumulate a little bit of strain, but not as rapidly as the modulus is changing in Figure 28. Due to the low stress that is being applied, 137 MPa (50% UTS), it is possible that the damage that is accumulating, is causing the stiffness to decrease, but not enough damage has accumulated yet to show a significant change in the strain.

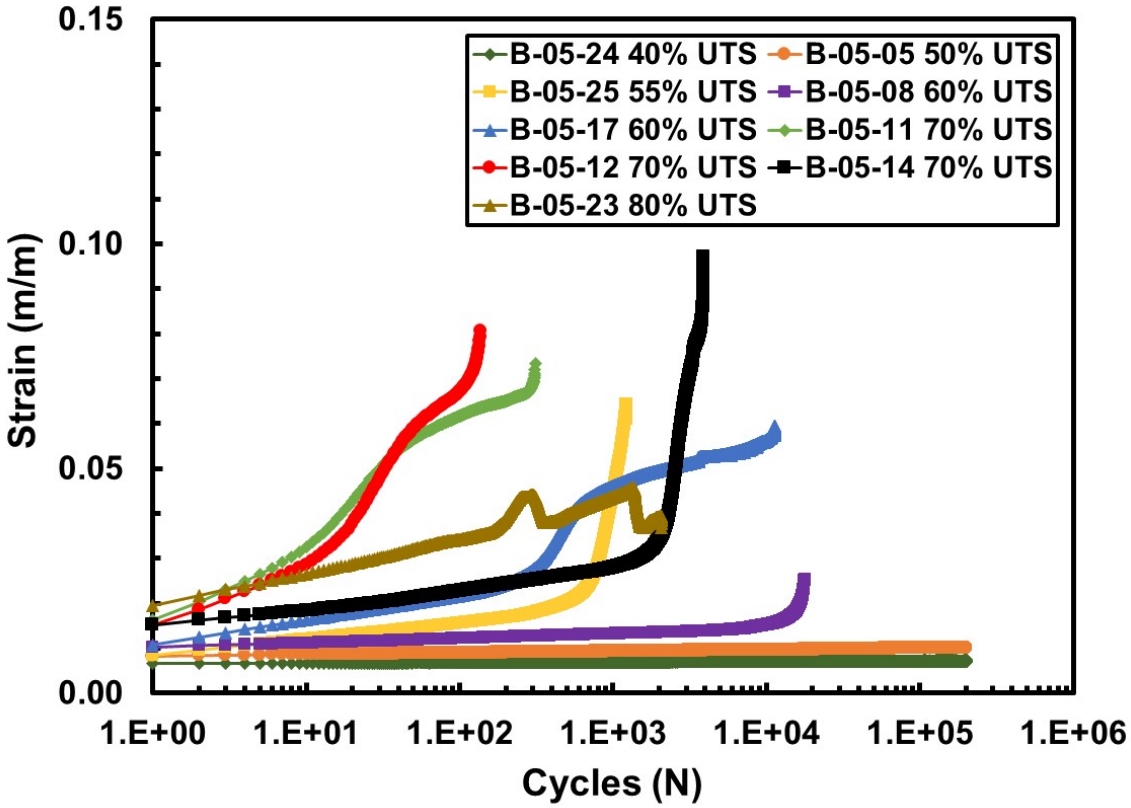

Figure 29: Strain accumulation with fatigue cycles for the baseline composite specimens with ±45 fiber orientation. Specimens B-05-24 and B-05-05 achieved fatigue runout of 200,000 cycles without failure.

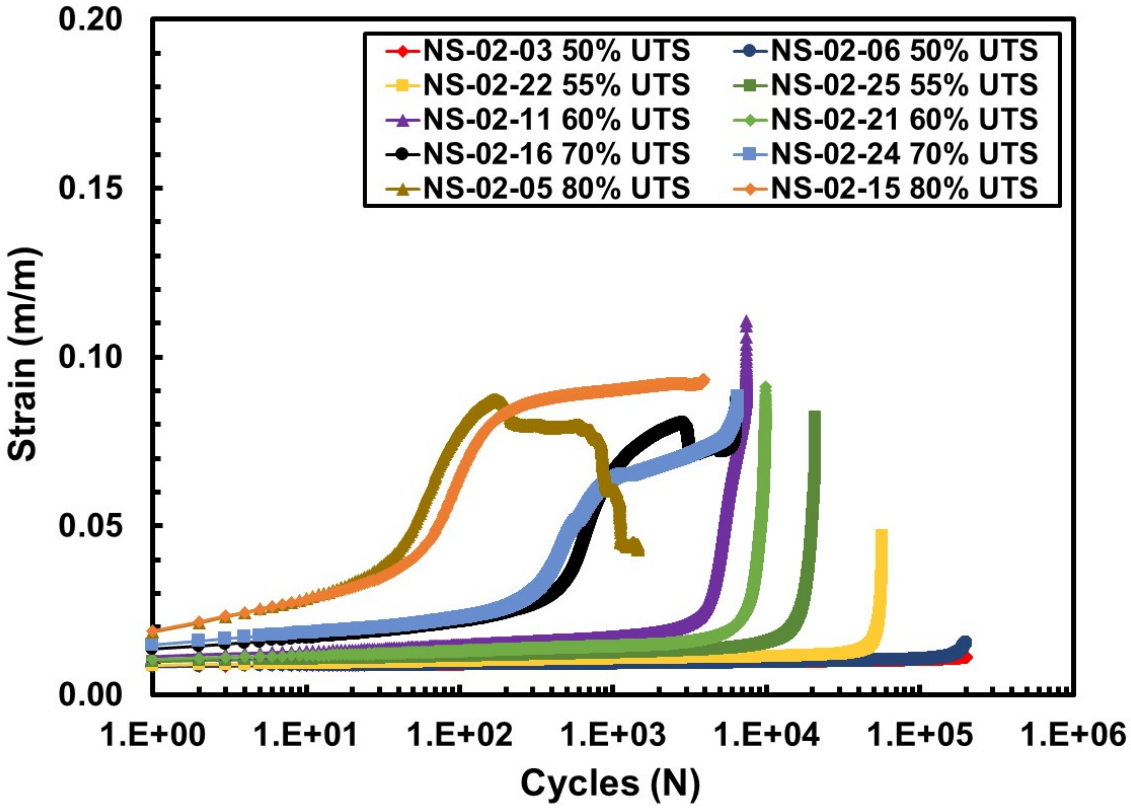

Figure 30: Strain accumulation with fatigue cycles for the NanoStitch composite specimens with ±45 fiber orientation. Specimens NS-02-03 and NS-02-06 achieved fatigue runout of 200,000 cycles without failure.

5.3.4 ±45 Retained Properties.

All specimens that achieved fatigue runout were tested in tension to failure tests to measure the retained properties. The tensile test was performed according to the procedure described in Section 5.2. The retained tensile properties are presented in Table 17, along with the initial modulus measurements.

Table 17: Retained tensile properties of the ±45 composite specimens subjected to 200,000 cycles of prior tension-tension fatigue.

Type	Specimen	Initial Modulus (GPa)	Retained Modulus (GPa)	Retained UTS (MPa)
Baseline	B-05-05	17.4	15.4	260
	B-05-24	18.3	15.9	269
NanoStitch	NS-02-03	19.3	14.7	264
	NS-02-06	18.9	12.7	228

The baseline composite specimen tested with the maximum stress of 50% UTS retained 88.51% of its elastic modulus, while the NanoStitch specimen tested with the maximum stress of 50% UTS retained an average of 71.68% of its modulus. We also note that both the ±45 baseline composite and the ±45 NanoStitch composite, on average, retain 95.72% and 86.36% of their tensile strength, respectively. A much lower modulus and tensile strength retention noted for the NanoStitch composite may be attributed to additional crack initiation points and matrix defects introduced during fabrication with the added CNTs.

Figure 31 shows the effects of prior fatigue on tensile stress-strain behavior of the baseline composite and the NanoStitch composite with ±45 fiber orientation. Results in Figure 31 demonstrate that 200,000 cycles of prior fatigue had little effect on the stress-strain behavior of the baseline composite and the NanoStitch composite with ±45 fiber orientation. Tensile stress-strain curves obtained for the pre-fatigued specimens are qualitatively similar to those obtained for the as-processes specimens. All stress-strain curves exhibit an initial linear range, then depart from linearity and continues non-linearly until failure.

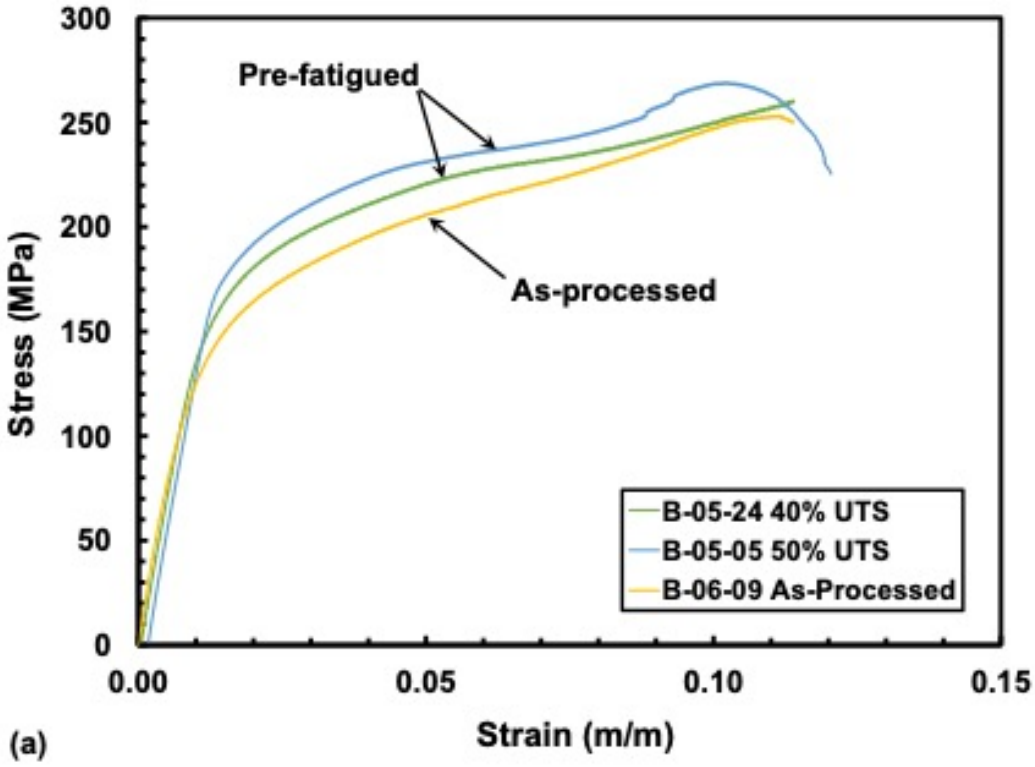

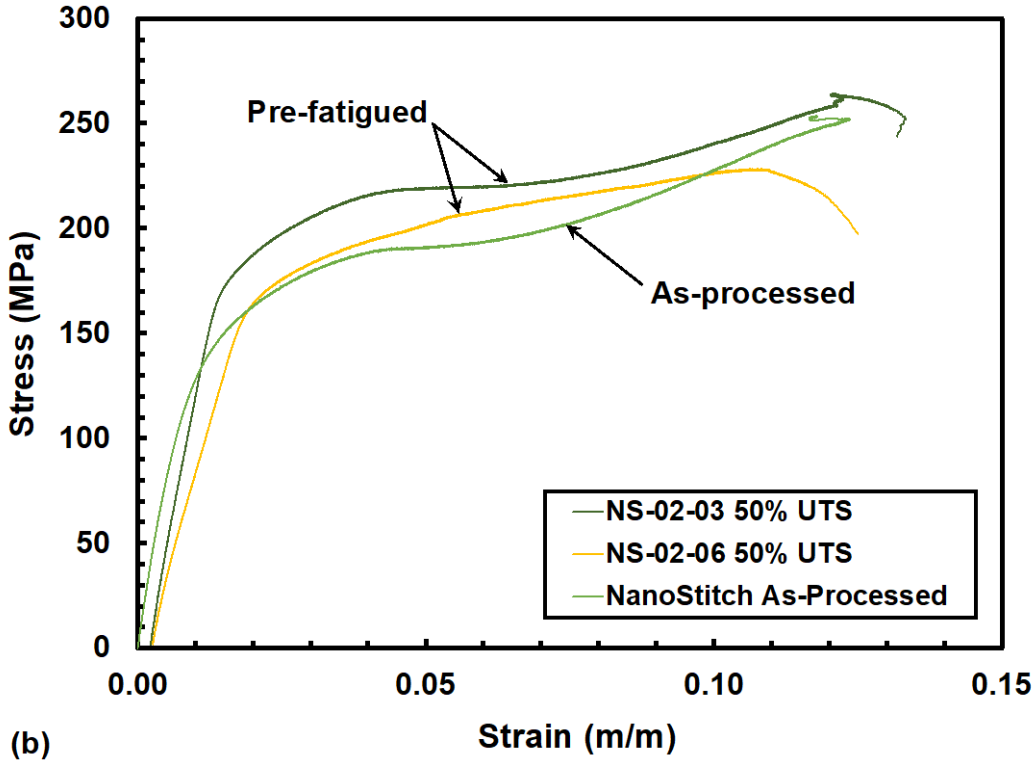

Figure 31: Effects of prior fatigue on tensile stress-strain behavior of (a) the baseline composite and (b) the NanoStitch composite with ±45 fiber orientation

5.4 Schapery's Nonlinear Viscoelastic Model – Formulation and Characterization

Increasing use of polymer matrix composites in critical load-bearing structures call for development of constitutive models capable of predicting the mechanical behavior of these materials. Experimental results obtained in this work revealed the nonlinear and time-dependent nature of the stress-strain behavior of the ±45 NanoStitch composite. This observation is not surprising. The off-axis stress-strain behavior of the 2D polymer composites is dominated by the polymer matrix. It is recognized that polymer materials generally exhibit nonlinear viscoelastic behavior. Constitutive models developed to represent the nonlinear viscoelastic behavior of polymers generally fall into two categories – differential and integral formulations. One such integral formulation is the thermodynamically based model of Schapery[16], [17]. Schapery's integral formulation is convenient for stress and strain analysis. This constitutive model accounts for the nonlinear material behavior through the use of the stress-dependent material function. The model parameters and material functions can be readily obtained by performing relatively simple creep and recovery tests.

The behavior of the NanoStitch composite with ±45 fiber orientation was characterized in terms of Schapery's nonlinear viscoelastic model[16], [17], using Peretz and Weitsman's procedure in "Nonlinear Viscoelastic Characterization of FM-73 Adhesive"[18]. For uniaxial loading the stress-strain relation reduces to:

$$\varepsilon(t) = g_0 A(0)\sigma + g_1 \int_0^t \Delta A(\psi - \psi') \frac{dg_2\sigma}{d\tau} d\tau \tag{1}$$

Where: A(0) is the initial component of the creep compliance, $\Delta A(\psi)$ is the transient component of the compliance.

ψ is the reduced time given by:

$$\psi = \psi(t) = \int_0^t \frac{d\tau'}{a_\sigma}$$
$$\psi' = \psi(\tau) = \int_0^\tau \frac{d\tau'}{a_\sigma} \tag{2}$$

And g_0, g_1, g_2, a_σ are the stress-dependent material functions. The material constants and functions in equation (1) – (3) are obtained from uniaxial creep and recovery tests detailed in Section 4.3. These tests involve the application of a single step stress of magnitude σ_0 and its removal after duration t_0, as shown in Figure 10 in Section 4.3.

The application of single step stress, σ_0, and its removal after duration t_0 can be mathematically described as:

$$\sigma = \begin{cases} \sigma_0, 0 < t < t_0 \\ 0, t_0 < t < t_1 \end{cases} \tag{3}$$

Alternatively, using the Heaviside function, H(t), to express the application of single step stress, σ_0, and its removal after duration t_0 as:

$$\sigma = \sigma_0[H(t) - H(t - t_0)] \tag{4}$$

We can then substitute equation (4) into equation (1), which then for $0 < t < t_0$ yields:

$$\varepsilon = \left[g_0^0 A(0) + g_1^0 g_2^0 \Delta A\left(\frac{t}{a_\sigma^0}\right)\right]\sigma_0 \tag{5}$$

And for $t_0 < t < t_1$:

$$\varepsilon = g_1^1\left[g_2^0\sigma_0\Delta A\left(\frac{t_0}{a_\sigma^0} + \frac{t-t_0}{a_\sigma^1}\right) + (g_2^0\sigma_0)\Delta A\left(\frac{t-t_0}{a_\sigma^1}\right)\right] \tag{6}$$

In equation (6), the superscripts represent different stress levels, in this case, stress level 0 and 1. For the case of a two-step creep and recovery test, $\sigma_b = 0$. If we denote the creep strain as ε_c, and the recovery strain as ε_r, equations (5) and (6) simplify to:

$$\varepsilon_c = \left[g_0A(0) + g_1g_2\Delta A\left(\frac{t}{a_\sigma}\right)\right]\sigma_0, \quad 0 < t < t_0 \tag{7}$$

$$\varepsilon_r = \sigma_0 g_2\left[\Delta A\left(\frac{t_0}{a_\sigma} + t - t_0\right) - \Delta A(t-t_0)\right], \quad t > t_0 \tag{8}$$

From there, we can make the assumption that the time-dependent portion of the creep compliance, ΔA, can be adequately represented by a power law:

$$\Delta A(\psi) = C\psi^n \tag{9}$$

We can then substitute equation (9) into equations (7) and (8) to obtain:

$$\varepsilon_c = \left[g_0A(0) + g_1g_2C\left(\frac{t}{a_\sigma}\right)^n\right]\sigma_0, \quad 0 < t < t_0 \tag{10}$$

$$\varepsilon_r = \frac{\Delta\varepsilon}{g_1}[(1+\lambda a_\sigma)^n - (\lambda a_\sigma)^n], \quad t > t_0 \tag{11}$$

Where:

$$\lambda = \frac{t-t_1}{t_1}$$

$$\Delta\varepsilon = \varepsilon(t_0) - \varepsilon(0) = g_1g_2C\psi_0^n\sigma$$

In other words, $\Delta\varepsilon$ represents the amount of strain that was accumulated during the creep period. To put things back into a general form, equation (5) and (6) can be reduced to:

$$\varepsilon = \left[g_0^a A(0) + g_1^a g_2^a C \left(\frac{t}{a_\sigma^a} \right)^n \right] \sigma_0, \quad 0 < t < t_0 \tag{12}$$

And for $t > t_0$:

$$\varepsilon = g_1^1 C \left[g_2^0 \sigma_0 \left(\frac{t_0}{a_\sigma^0} + \frac{t - t_0}{a_\sigma^1} \right)^n + (g_2^1 \sigma_1 - g_2^0 \sigma_0) \left(\frac{t - t_0}{a_\sigma^1} \right)^n \right] \tag{13}$$

The first step in determination of the model parameters is the determination of the stress range of the linear viscoelastic response. In this stress range, the creep strain is proportional to the applied stress, σ_0, and a full recovery of strain is achieved upon stress removal. Figure 32 presents the strain vs. time curves obtained for the NanoStitch composite specimens with ±45 orientation during the creep portion of the creep and recovery tests performed with creep stresses of 37 MPa (15% UTS), 49 MPa (20% UTS), 74 MPa (30% UTS), 98 MPa (40% UTS), 123 MPa (50% UTS), and 147 MPa (60% UTS). Creep curves obtained at stress levels within the linear viscoelastic range must be congruent. Results in Figure 32 show that for the ±45 NanoStitch composite, the range of linear viscoelastic behavior lies between zero stress and somewhere between σ_0 = 74 MPa (30% UTS) and σ_0 = 98 MPa (40% UTS). This range of linear viscoelastic behavior can also be estimated by constructing isochronous stress-strain curves (Figure 33) using the creep data obtained in creep and recovery tests. Note that the isochronous stress-strain curves in Figure 33 depart from linearity once the stress exceeds 73.5 MPa, which is also the threshold stress determined from the examination of the creep curves in Figure 32. Thus the analysis of the isochronous stress-strain curves corroborates the conclusions reached by examining the creep curves in Figure 32.

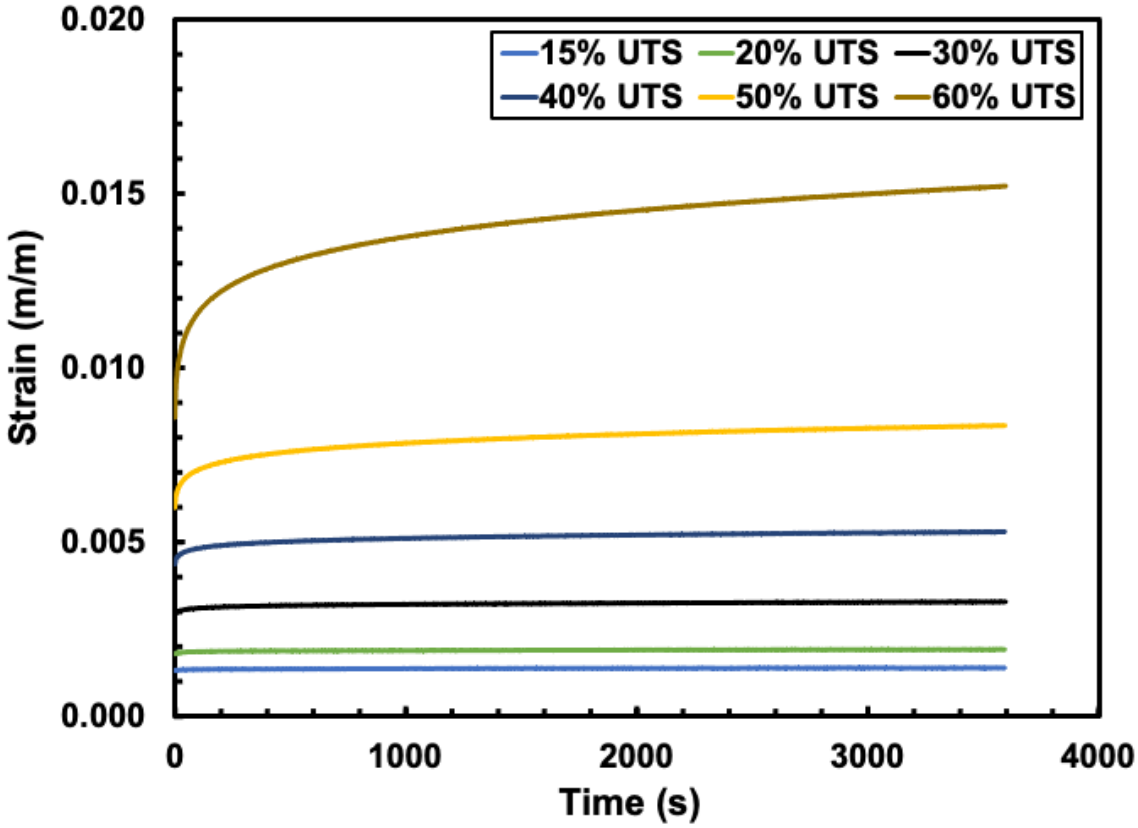

Figure 32: Strain vs. time curves obtained for the NanoStitch composite specimens with ±45 fiber orientation during the creep portion of the creep and recovery tests performed with creep stress of 37 MPa (15% UTS), 49 MPa (20% UTS), 74 MPa (30% UTS), 98 MPa (40% UTS), 123 MPa (50% UTS), and 147 MPa (60% UTS).

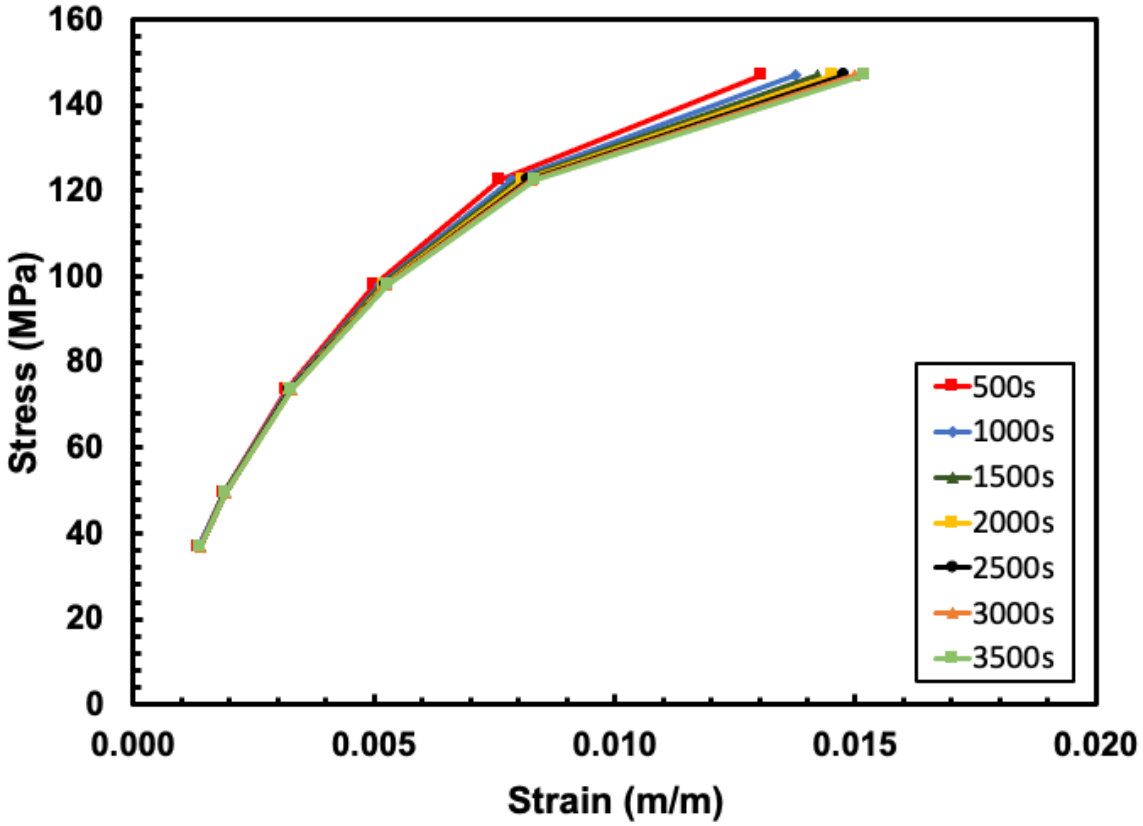

Figure 33: Isochronous stress-strain curves based on the strain vs. time data obtained for the NanoStitch composite specimen with ±45 fiber orientation during the creep portion of the creep and recovery tests performed with creep stresses of 37 MPa (15% UTS), 49 MPa (20% UTS), 74 MPa (30% UTS), 98 MPa (40% UTS), 123 MPa (50% UTS), and 147 MPa (60% UTS).

Using the published procedures[18], [19], we can express the creep and recovery experimental data produced for stresses within the linear viscoelastic range as:

$$\varepsilon(t) = \begin{cases} (D_0 + D_1 t^n)\sigma_0\,, 0 < t < t_0 \\ D_1[t^n - (t - t_0)^n]\sigma_0\,, \quad t > t_0 \end{cases} \; ; \; \sigma_0 \leq 74\ MPa \tag{14}$$

Now the values of the three model constants, A(0) = D_0, C = D_1, and n can be determined from the data obtained in the linear viscoelastic range. Schapery postulates that in the linear viscoelastic case $g_0 = g_1 = g_2 = a_\sigma = 1$.

Therefore, equation (10) combined with the power law in equation (14) becomes:

$$\varepsilon_c = A(0) + Ct^n \tag{15}$$

Equation (15) was then used to fit a calculated strain curve to the experimental data, employing a least squared error method:

$$E = \sum_{i=1}^{3500} (\varepsilon_i - \varepsilon_{i-calc})^2 \tag{16}$$

where E is the sum of the squared error between the experimental strain and the strain calculated from equation (15) for each of the 3500 data points of the creep data. Then the built-in solver function within Microsoft Excel was used to determine A(0), C, and n by minimizing the error. As a result, the following material properties were obtained from the experimental data in the linear range ($\sigma_0 = 74\ MPa$): A(0) = 2.659 x 10^{-3} MPa^{-1}, C = 2.765 x 10^{-4} $MPa^{-1}s^{-n}$, n = 9.998 x 10^{-2}, where t is in seconds.

We now proceed to determine the stress-dependent model functions from creep and recovery tests performed with the creep stress levels of 40%, 50%, and 60% UTS. For each of these stress levels, we first determine the creep strain, $\Delta\varepsilon$, from the creep test data. Next we use recovery data to calculate λ for each data point. Then we manipulate equation (11), to obtain the following:

$$\log\left(\frac{\Delta\varepsilon}{g_1}\right) = \log(\varepsilon_r) - \log[(1 + \lambda a_\sigma)^n - (\lambda a_\sigma)^n] \tag{17}$$

Theoretically, the left hand side (LHS) of equation (17) should be a constant, however, due to noise inherent in the experimental data, it is not the case. Still, using the right hand side (RHS) of equation (17) and an initial guess for a_σ, we can calculate the RHS for each time interval. The LHS is then found by averaging the RHS values. Next, a

sum of squared error method was used between the LHS and RHS calculated for each time interval to determine the a_σ value by minimizing the error. The built-in solver function in Microsoft Excel was used for this purpose. A g_1 value was then determined for each time interval using the following manipulation of equation (17):

$$g_1 = \frac{\Delta\varepsilon}{10^{\log(\varepsilon_r)-\log[(1+\lambda a_\sigma)^n-(\lambda a_\sigma)^n]}} \tag{18}$$

A final g_1 value was then determined by averaging the g_1 values obtained for each time interval. The values of the stress-dependent material functions a_σ and g_1 are presented in Table 18 for various levels of stress.

Next, we turn to the creep data to determine the remaining stress-dependent material functions g_0 and g_2 by fitting equation (14) to the recovery data. Considering the creep data produced at stress levels in the nonlinear viscoelastic range and the value of n obtained earlier, we determine parameters D_0 and D_1 using the least squared error method and the built-in solver function in Microsoft Office Excel. Once those values are determined, we can compare equations (10) and (14) to find g_0 and g_2 as follows:

$$D_0 = g_0 A(0) \rightarrow \ g_0 = \frac{D_0}{A(0)} \tag{19}$$

$$D_1 = C\,\frac{g_1 g_2}{(a_\sigma)^n} \rightarrow g_2 = \frac{D_1 (a_\sigma)^n}{C g_1} \tag{20}$$

The values of the stress-dependent material functions g_0 and g_2 are presented in Table 18 for various levels of stress.

Table 18: Stress-dependent material functions $\boldsymbol{g_0}$, $\boldsymbol{g_1}$, $\boldsymbol{g_2}$, and $\boldsymbol{a_\sigma}$.

Stress Level (% UTS)	**Stress Level (MPa)**	$\boldsymbol{\Delta\varepsilon}$ **(m/m)**	$\boldsymbol{a_\sigma}$	$\boldsymbol{g_1}$ **(m/m)**	$\boldsymbol{g_0}$ **(m/m)**	$\boldsymbol{g_2}$ **(m/m)**
15	**36.68**	7.462×10^{-5}	1	1	1	1
20	**49.27**	1.259×10^{-4}	1	1	1	1
30	**73.39**	3.720×10^{-4}	1	1	1	1
40	**98.15**	9.254×10^{-4}	9.043	0.5650	1.367	5.848
50	**122.40**	2.355×10^{-3}	15.51	0.5430	1.454	17.34
60	**146.96**	6.642×10^{-3}	20.71	0.5407	0.8714	51.62

Figure 34 compares the experimental creep curve (solid black line) obtained at the stress of 147 MPa (60% UTS), with the calculated creep curve (solid red line). As can be seen in Figure 34, the calculated creep curve matches the experimental data well, the two curves overlaps the experimental data at almost every point.

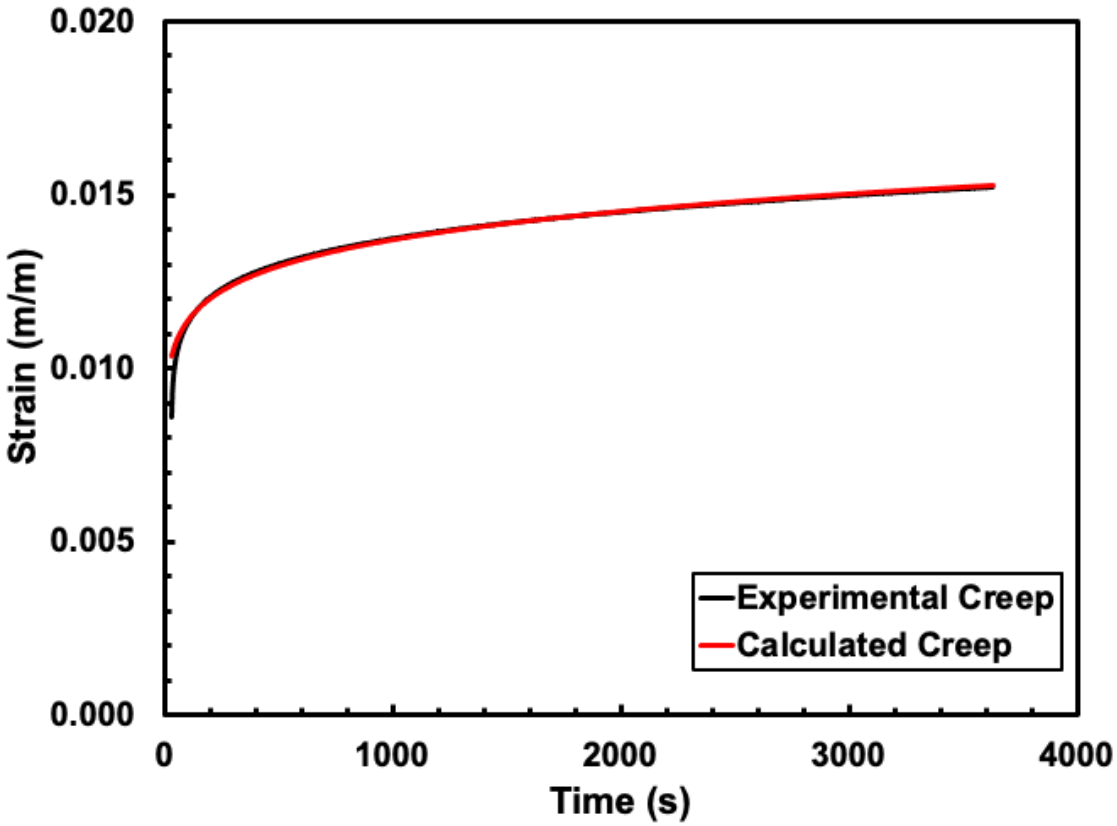

Figure 34: Creep at 147 MPa (60% UTS). A comparison between experimental data (solid black line) and predicted strain response (solid red line).

An additional objective of this work was to assess whether the Schapery's non-linear viscoelastic model characterized, via short-term creep and recovery tests, could adequately predict long-term creep performance of the NanoStitch composite with ±45 fiber orientation. This assessment was accomplished by comparing model predictions with the experimental data obtained in 100-h creep tests performed by Dr. Volodymyr P. Sabelkin at the Air Force Institute of Technology. The 100-h creep tests were conducted at 74 MPa (30% UTS), 98 MPa (40% UTS), and 147 MPa (60% UTS). A comparison of the model predictions with experimental results is presented in Figure 35, where the

experimental results are represented by solid lines and the prediction results are represented by dashed lines.

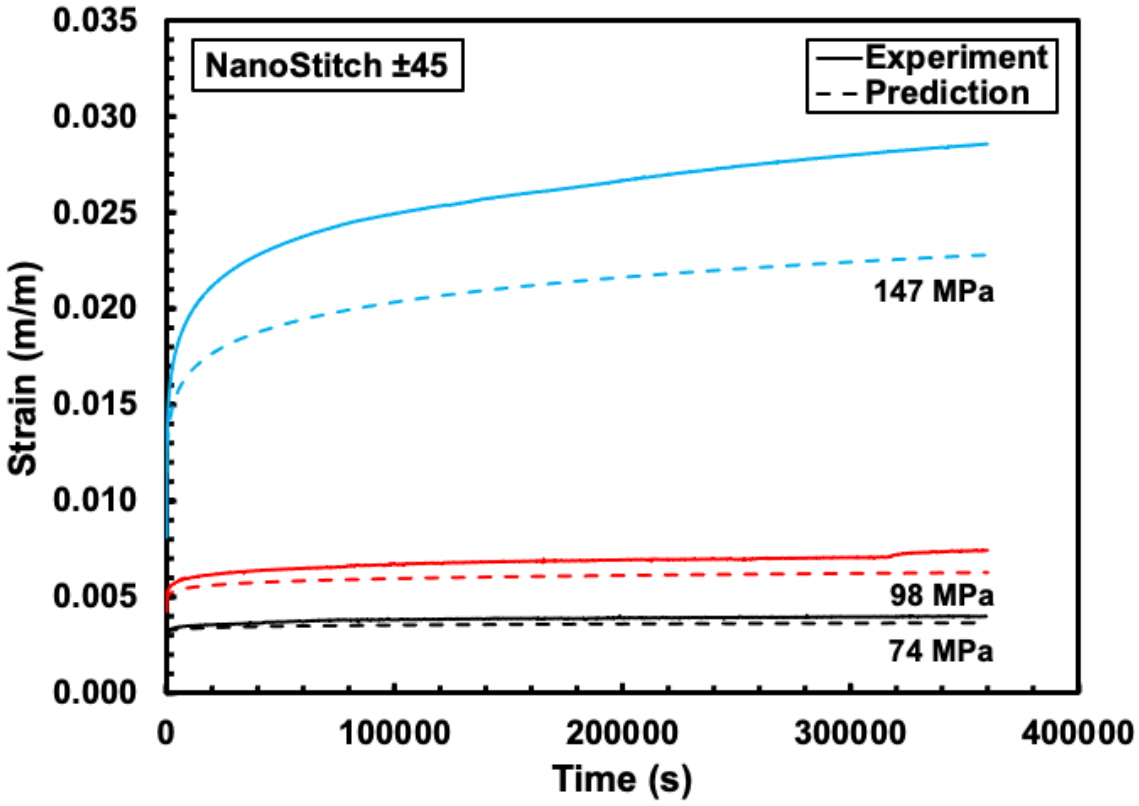

Figure 35: A comparison between experimental and predicted creep curves obtained for the NanoStitch composite with ±45 fiber orientation at 74 MPa (30% UTS), 98 MPa (40% UTS), and 147 MPa (60% UTS).

Generally, the model seems to underpredict the strain, but not by much at lower stress levels. However, at higher stress level, the model predictions deviate further from the experimental results. For the creep stress levels of 74 and 98 MPa, the predicted strain response is in a reasonably good agreement with the experimental data, although the model slightly underpredicts creep strain. However, the difference between the model

prediction and the experimental data becomes considerable at the creep stress of 147 MPa. In this case, the model significantly underpredicts creep strain. Additional fine-tuning of the model characterization procedure may alleviate this discrepancy. Using creep and recovery tests with somewhat longer creep and recovery periods for model characterization may produce more accurate model predictions.

5.5 Optical Microscopy Analysis

Typical failure of the 0/90 baseline composite specimens tested in tension to failure is shown in Figures 36 and 37. Failure seen in Figures 36 and 37 is localized. There is a single, dominant fracture plane, which is largely normal to the direction of applied load. We note that the typical failure mode of the 0/90 NanoStitch composite tested in tension to failure differs little if at all from that of the 0/90 baseline composite.

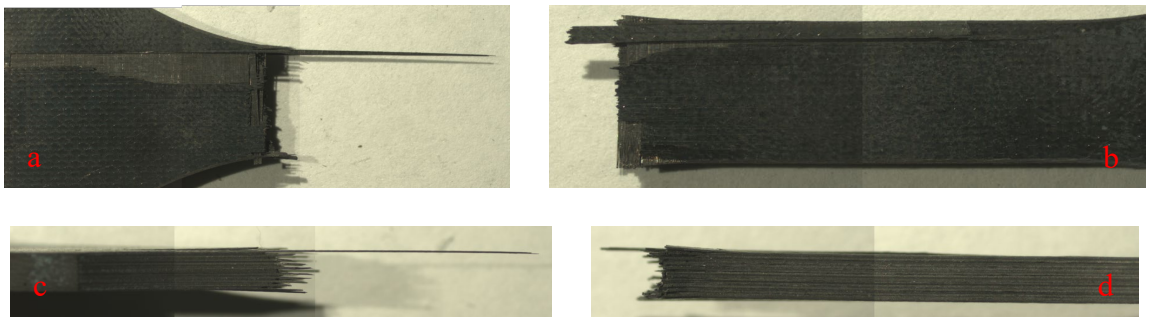

Figure 36: Stitched images of the 0/90 baseline composite specimen B-02-15 tested in tension to failure. (a-b) face view and (c-d) side view.

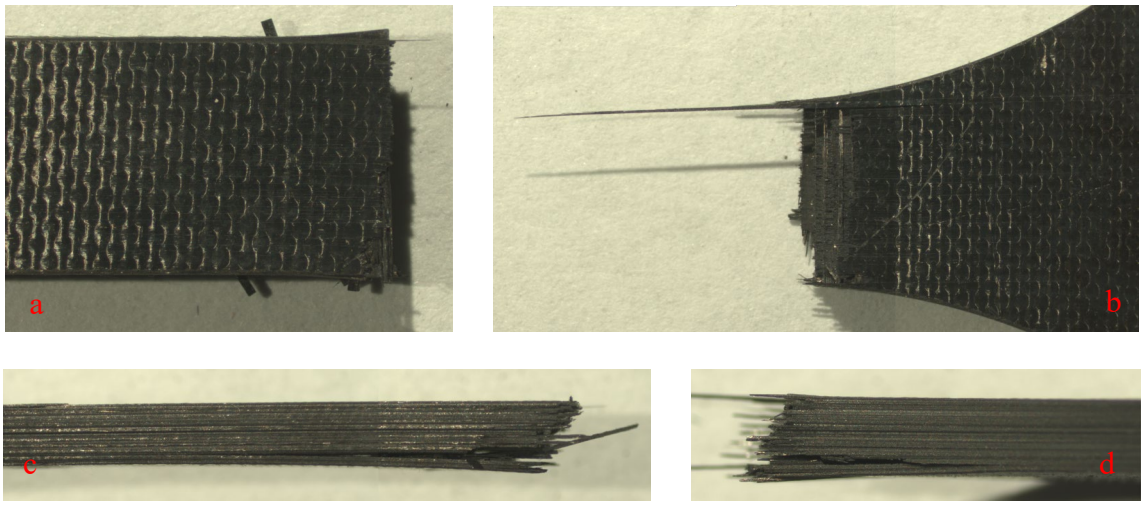

Figure 37: Stitched images of the 0/90 NanoStitch composite specimen NS-07-26 tested in tension to failure. (a-b) face view and (c-d) side view.

In contrast, failure of the 0/90 baseline composite (Figure 38) and of the 0/90 NanoStitch composite (Figure 39) subjected to tension-tension fatigue involves two dominant fracture planes, as well as, significant ply delamination spanning the entire test specimen. The delamination can be clearly seen in the side views (Figures 38 (b) and 39 (b)). Note that the specimens depicted in Figures 38 and 39 achieved fatigue runout of 200,000 cycles then failed in tension test. The failure mode seen in Figures 38 and 39 is attributed to progressive damage accumulation with fatigue cycling. It is likely that multiple damage events occurred on the microlevel (i.e. fiber and/or matrix level) during the 200,000 fatigue cycles. Such damage events can occur, in multiple locations throughout the test specimen, causing non-homogenous deformation, which, in turn, could lead to multiple failures on the macrolevel occurring in multiple locations during post-fatigue tension testing.

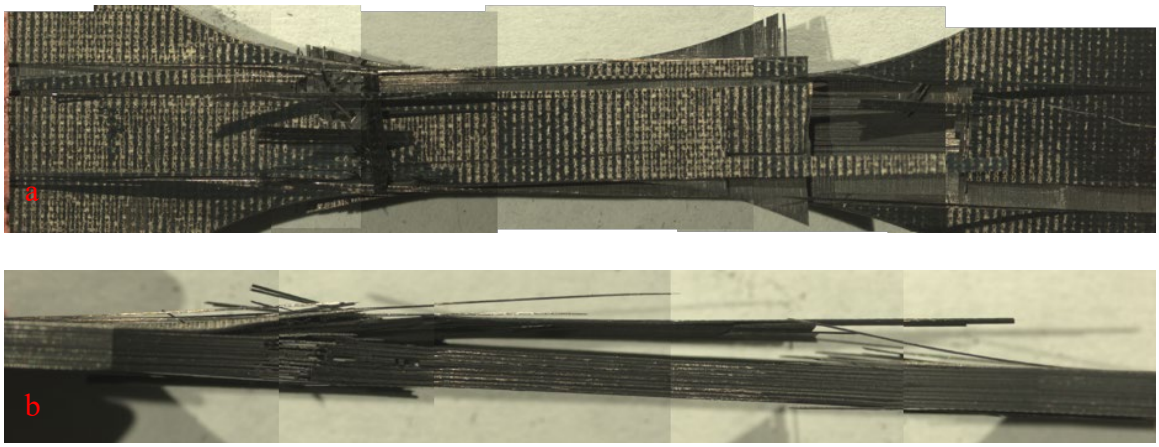

Figure 38: Stitched images of the 0/90 baseline composite specimen B-02-16 tested in tension-tension fatigue (σ_{max} = 827 MPa, N_f > 200,000 – fatigue runout), then failed in a tension test. (a) face view and (b) side view.

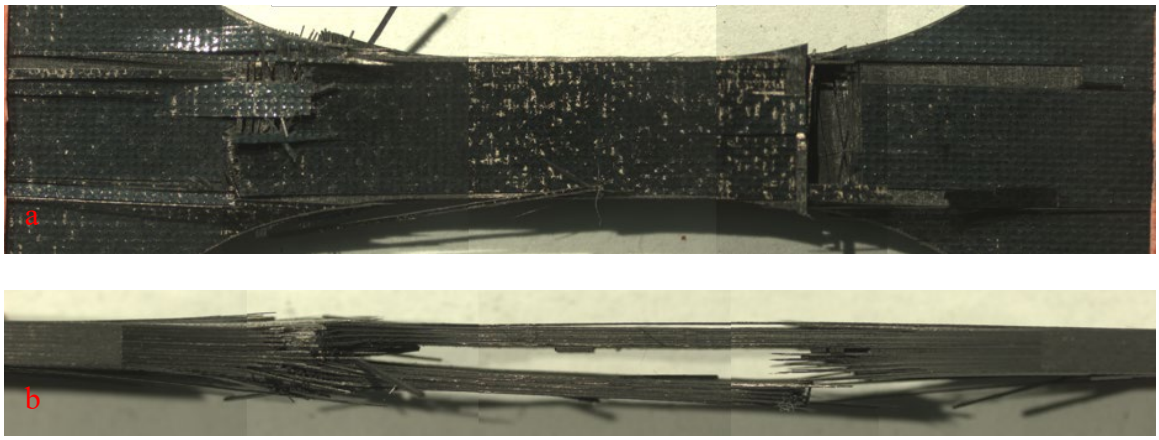

Figure 39: Stitched images of the 0/90 NanoStitch composite specimen NS-07-08 tested in tension-tension fatigue (σ_{max} = 887 MPa, N_f > 200,000 – fatigue runout), then failed in a tension test. (a) face view and (b) side view.

Figures 40 and 41 show typical failure in tension-tension fatigue of the ±45 baseline composite and NanoStitch composite specimens. Note that the two composites exhibit typical failure modes. Damage consumes most of, if not all of, the gauge section. Fiber tow "scissoring" is also clearly seen in Figures 40 and 41. Additional failure

surfaces of ±45 baseline composite and NanoStitch composite specimens are shown in Figures 42 and 43, respectively. These specimens did not separate into two parts upon failure. However, considerable ply delamination and fiber tow scissoring are evident. Once again, the failure mode of the ±45 NanoStitch composite is similar to that of the ±45 baseline composite. Both ±45 composites exhibit similar amounts of ply delamination and matrix failure. The images reveal show removal of the first and in some cases, the second ply, in various locations along the specimens, thus uncovering the plies below.

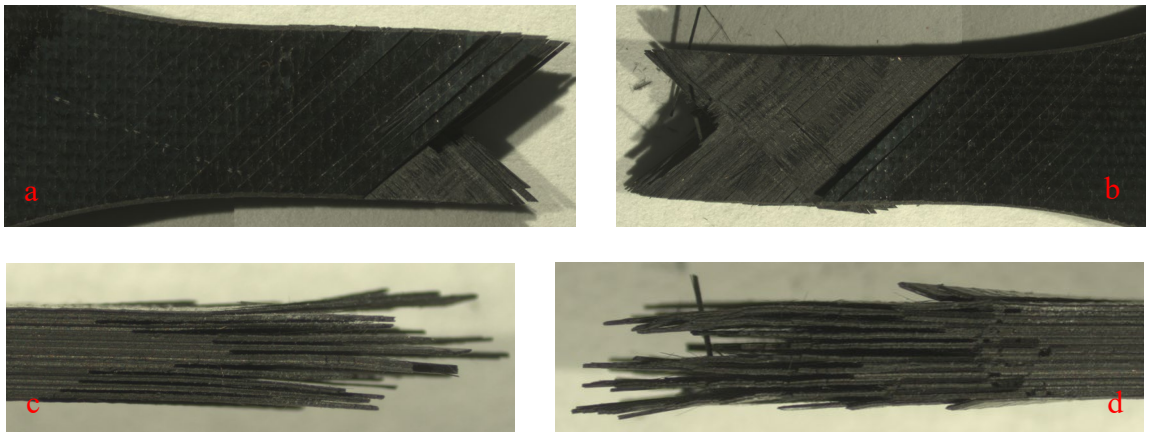

Figure 40: Stitched images of the ±45 baseline composite specimen B-05-10 tested in tension-tension fatigue (σ_{max} = 194 MPa, N_f = 10). (a) face view and (b) side view.

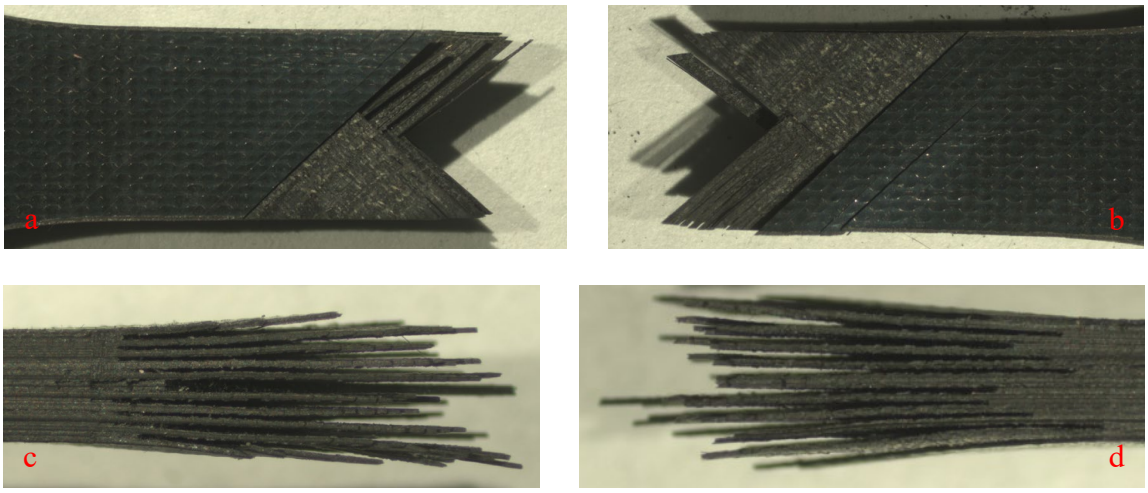

Figure 41: Stitched images of the ±45 NanoStitch composite specimen NS-02-25 tested in tension-tension fatigue (σ_{max} = 151 MPa, N_f = 20,831). (a) face view and (b) side view.

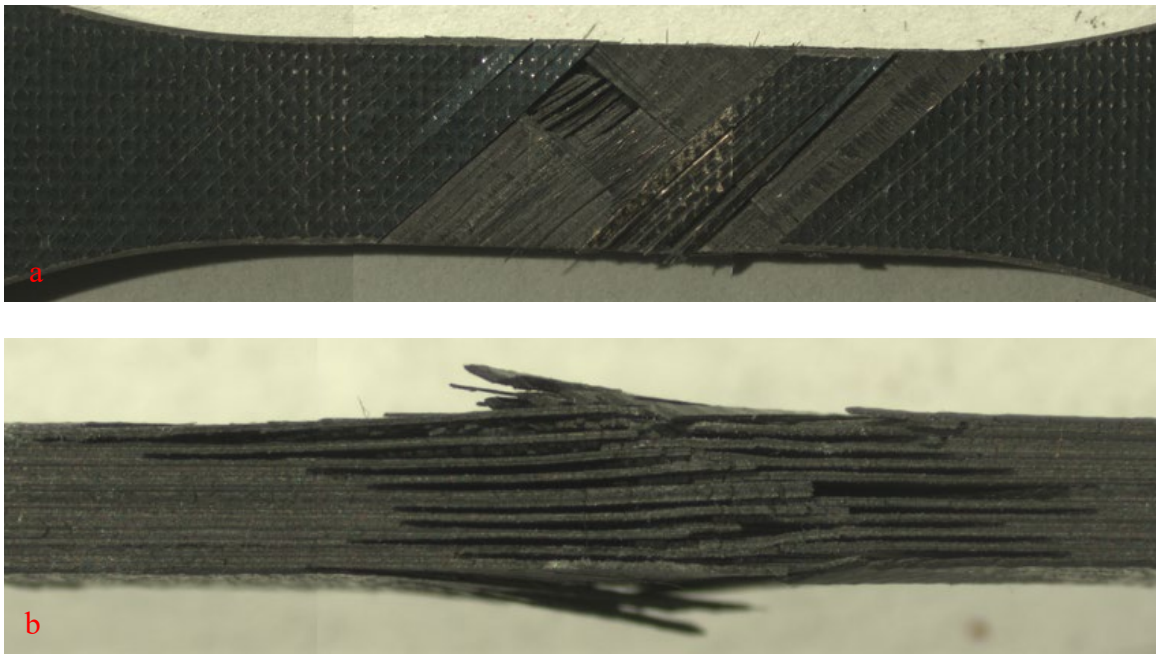

Figure 42: Stitched images of the ±45 baseline composite specimen B-05-05 tested in tension-tension fatigue (σ_{max} = 131 MPa, N_f > 200,000 – fatigue runout), then failed in a tension test. (a) face view and (b) side view.

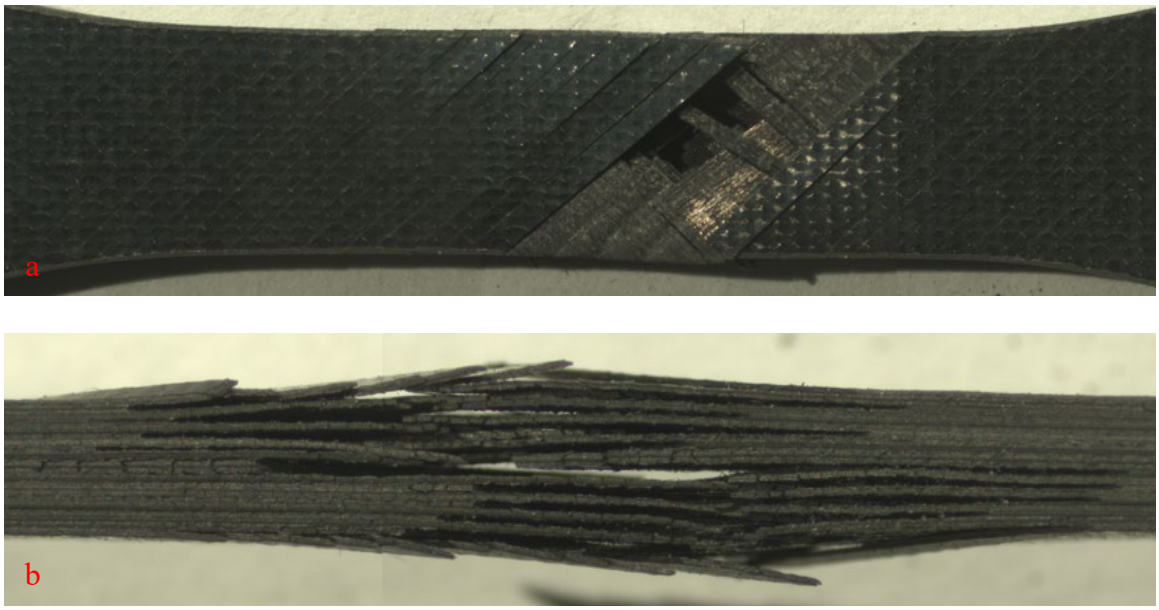

Figure 43: Stitched images of the ±45 NanoStitch composite specimen NS-02-11 tested in tension-tension fatigue (σ_{max} = 163 MPa, N_f = 7,433). (a) face view and (b) side view.

VI. Conclusions and Recommendations

6.1 Conclusions of Research

The tensile properties of two different material systems, baseline composite and NanoStitch composite were examined at room temperature. For each composite, both on-axis (0/90) and off-axis (±45) properties were measured in tension-to-failure tests. As expected, the 0/90 specimens of both composites performed significantly better than the ±45 specimens, in terms of stiffness, UTS, fatigue life, and fatigue run-out stress. A comparison of the results obtained for the NanoStitch composite to those obtained for the baseline composite reveals little difference in the mechanical behavior. In-plane properties and performance of the NanoStitch composite were no worse (and in some cases slightly better) than those of the baseline composite. The NanoStitch composite was reported to have improved interlaminar shear properties due to the incorporation of the CNT layers. It is frequently the case that improvement in one material property is achieved at the cost of diminishing the others. Hence it is important that the in-plane properties and performance of the NanoStitch composite are comparable and in some cases better than those of the baseline composite. We note that the UTS of the NanoStitch composite was 7.2% higher than that of the baseline composite for the 0/90 fiber orientation and 3.3% higher for the ±45 fiber orientation. The elastic modulus of the NanoStitch composite was 3.1% higher than that of the baseline composite for the 0/90 fiber orientation and 13.0% higher for the ±45 fiber orientation. Tension-tension fatigue response of both composites with 0/90 and ±45 fiber orientation was also examined. Tension-tension fatigue tests were conducted at 1.0 Hz and a ratio of minimum stress to

maximum stress of 0.1. Fatigue run-out was defined as 2 x 10^5 cycles. The tension-tension fatigue performance of the NanoStitch composite was slightly improved compared to that of the baseline composite for both 0/90 and ±45 fiber orientations.

Finally, the time-dependent viscoelastic deformation behavior of the NanoStitch composite with ±45 fiber orientation was investigated in creep and recovery tests. The experimental results were evaluated in context of Schapery's nonlinear viscoelastic model. The results of this study revealed that the creep response of the ±45 NanoStitch composite could be modeled using Schapery's nonlinear viscoelastic formulation. Furthermore, the results revealed that Schapery's nonlinear viscoelastic model characterized through short-term creep and recovery tests could reasonably well predict the results of the long-term (100-h) creep experiments for creep stresses below 147 MPa. At creep stress of 147 MPa the model noticeable underpredicts creep strain accumulation.

6.3 Recommendations for Future Research

Additional duplicate tests are recommended for future work in order to corroborate and gain statistical confidence in the data collected in this study. It is especially recommended that properties and performance of the NanoStitch composite with a different layup (for example a quasi-isotropic layup) be also studied.

The as-processed, as well as, tested specimens should be examined under an SEM in order to more fully characterize the damage and failure mechanisms.

The NanoStitch composite was found to perform relatively similar to the baseline composite under uniaxial, in-plane loading. Additional efforts could be directed toward assessing whether the addition of the CNTs improves other properties of the composite

(for example, its thermal or electrical properties). Should the NanoStitch composite be found to exhibit improved thermal or electrical properties, the range of its application can be broadened.

Schapery's nonlinear viscoelastic model was characterized for the ±45 NanoStitch composite, using fairly short-term creep and recovery tests. Furthermore, only one set of creep and recovery data was used. It is recommended that the creep and recovery tests be duplicated to gain statistical confidence. Additionally, it should be explored whether the accuracy of the model predictions of the long-term creep behavior could be improved by using somewhat longer-term creep and recovery tests for model characterization. It is also recommended that Schapery's nonlinear viscoelastic model be characterized for the baseline composite and the characterization results obtained for the two composites be compared. Finally, the model should be characterized for the NanoStitch composite with quasi-isotropic layup.

Appendix: Additional Optical Micrographs

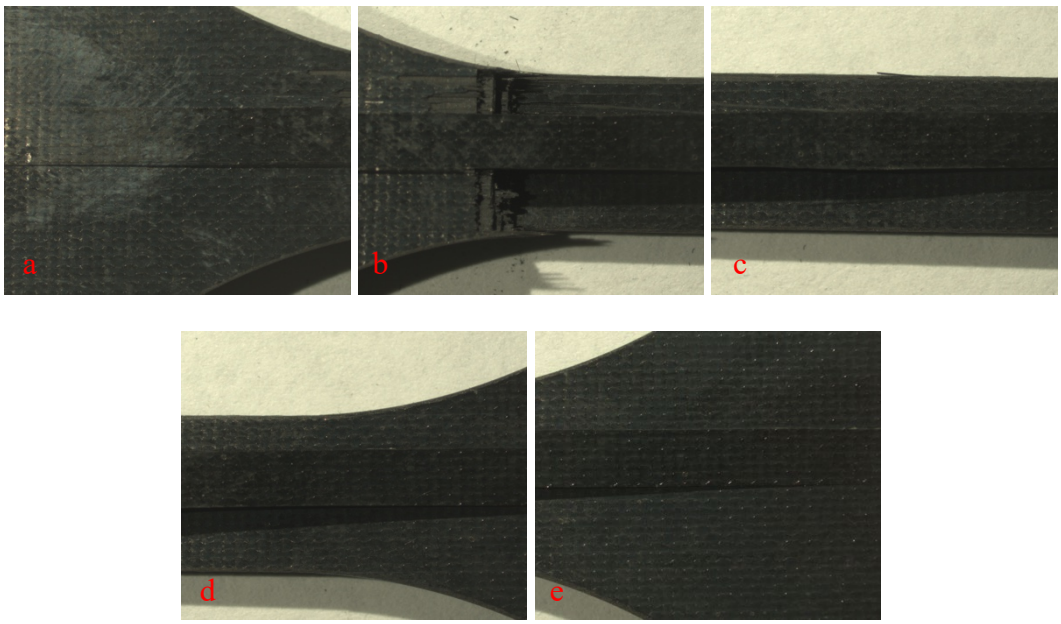

Figure 44: Images of the 0/90 baseline composite specimen B-02-22 tested in tension to failure. (a-e) face view.

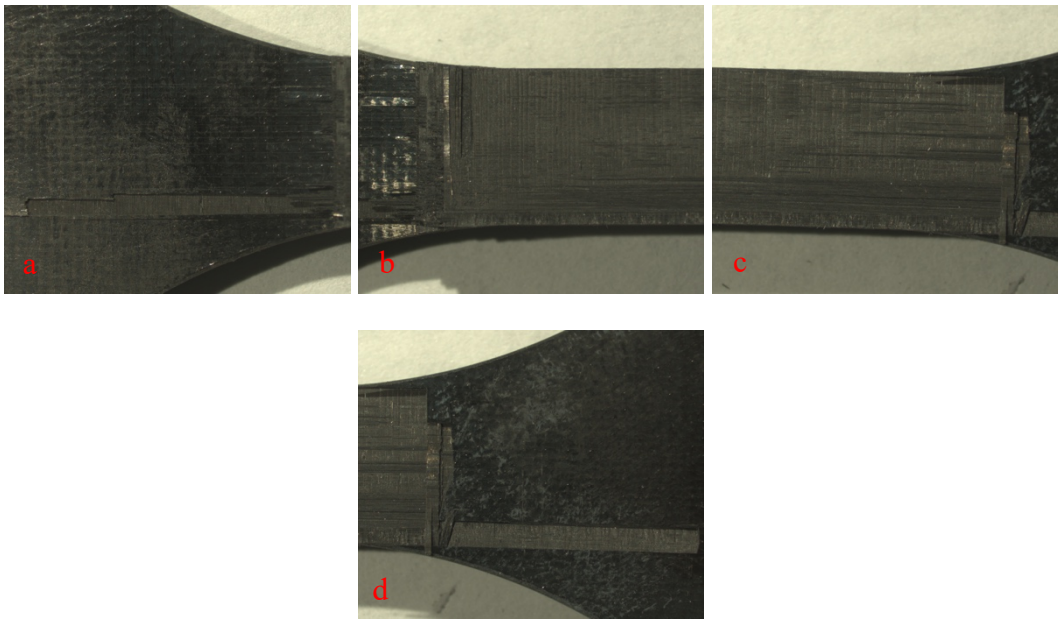

Figure 45: Images of the 0/90 baseline composite specimen B-02-22 tested in tension to failure. (a-d) face view.

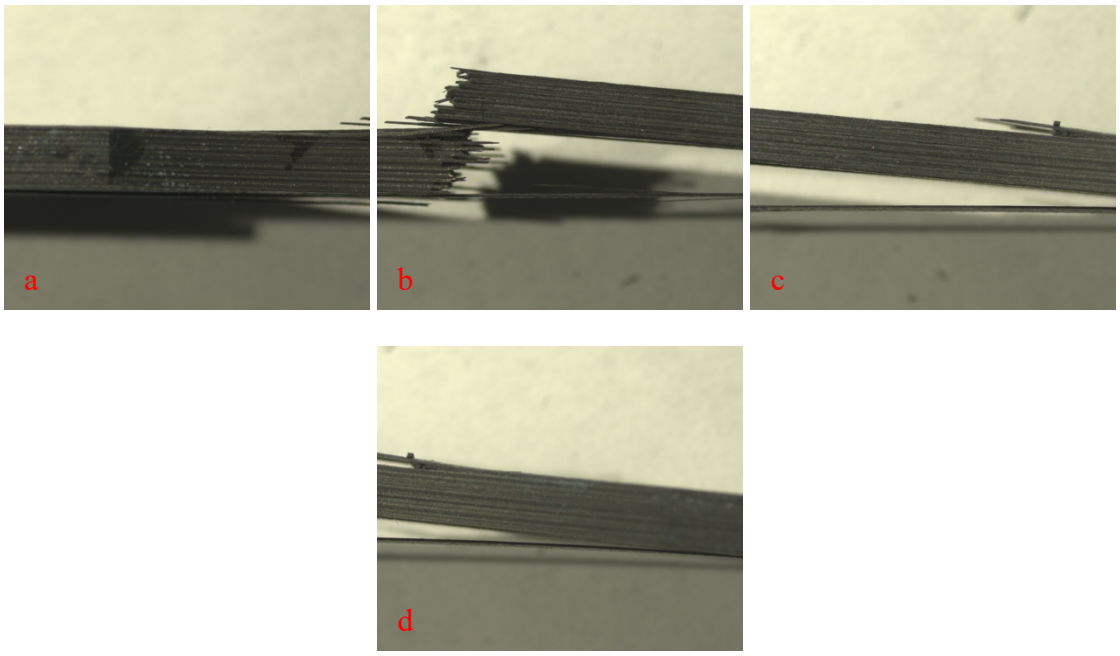

Figure 46: Images of the 0/90 baseline composite specimen B-02-22 tested in tension to failure. (a-d) side view.

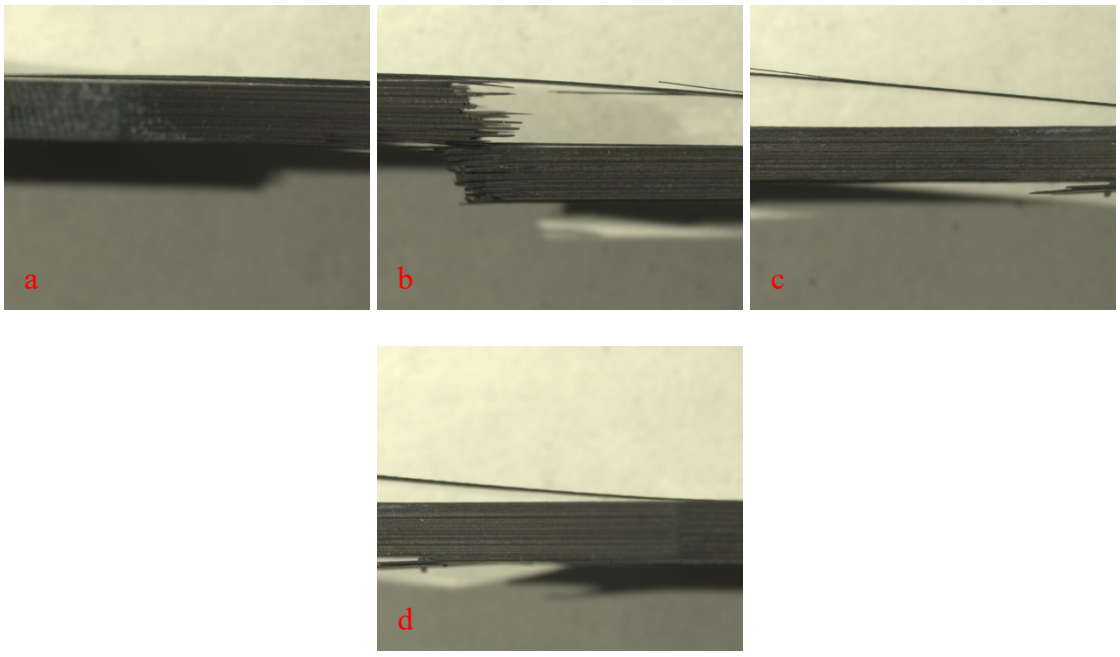

Figure 47: Images of the 0/90 baseline composite specimen B-02-22 tested in tension to failure. (a-d) side view.

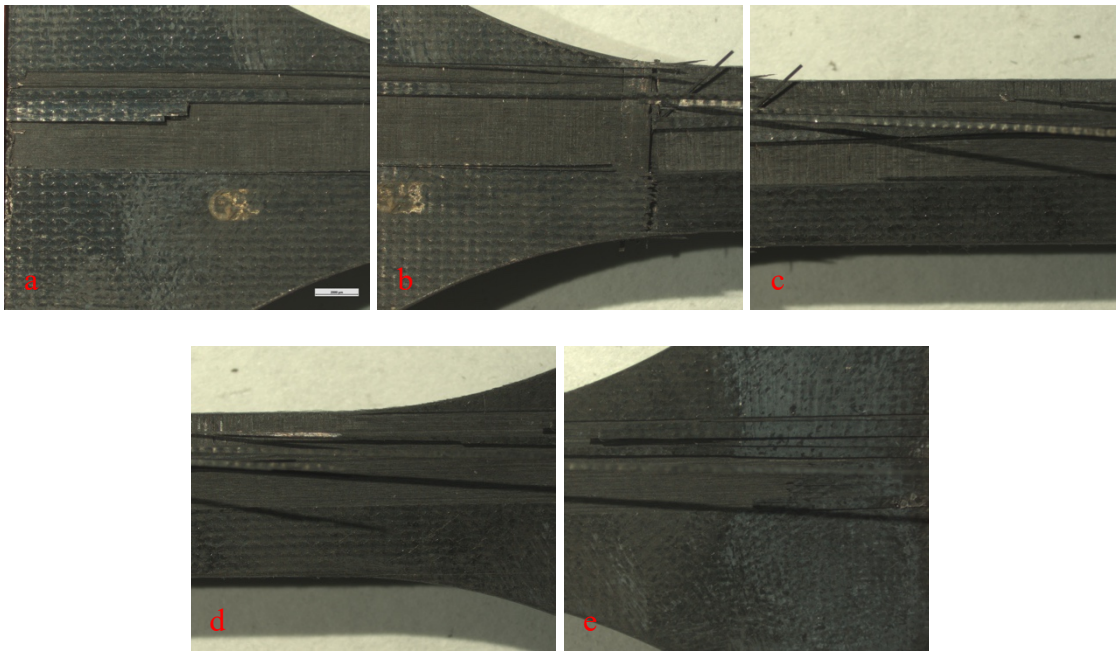

Figure 48: Images of the 0/90 baseline composite specimen B-02-12 tested in tension to failure. (a-e) face view.

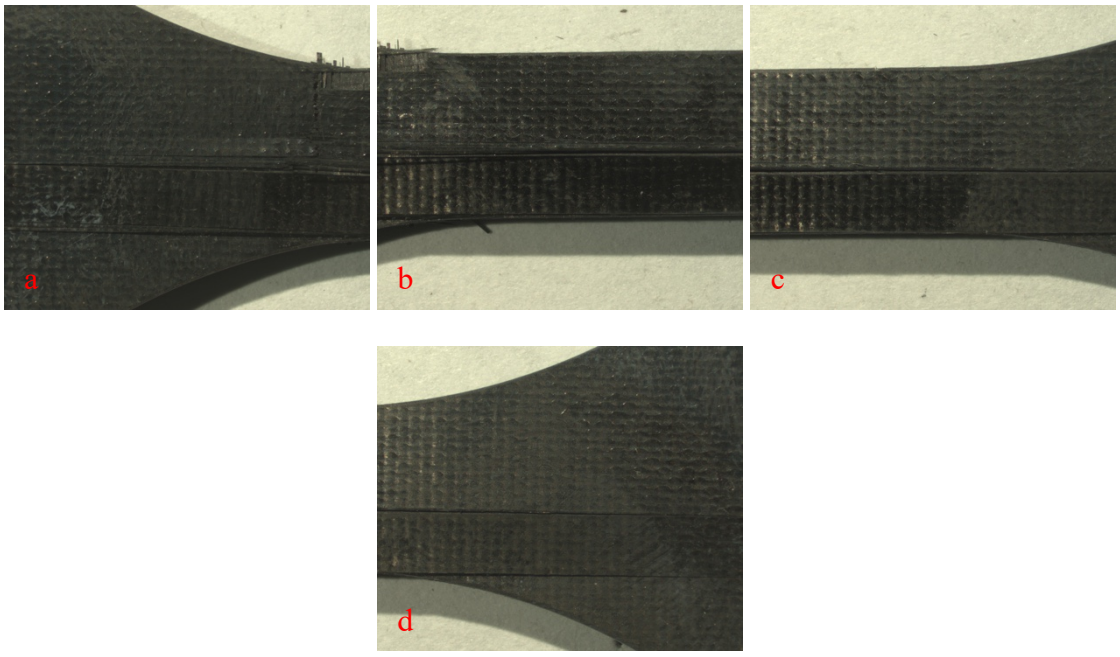

Figure 49: Images of the 0/90 baseline composite specimen B-02-12 tested in tension to failure. (a-d) face view.

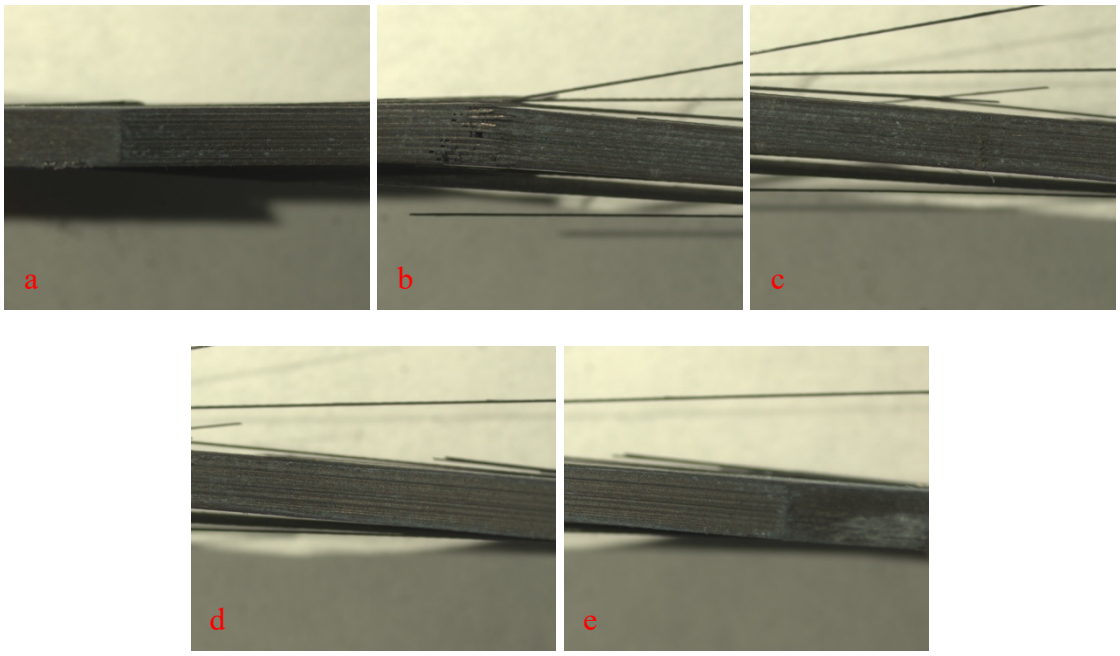

Figure 50: Images of the 0/90 baseline composite specimen B-02-12 tested in tension to failure. (a-e) side view.

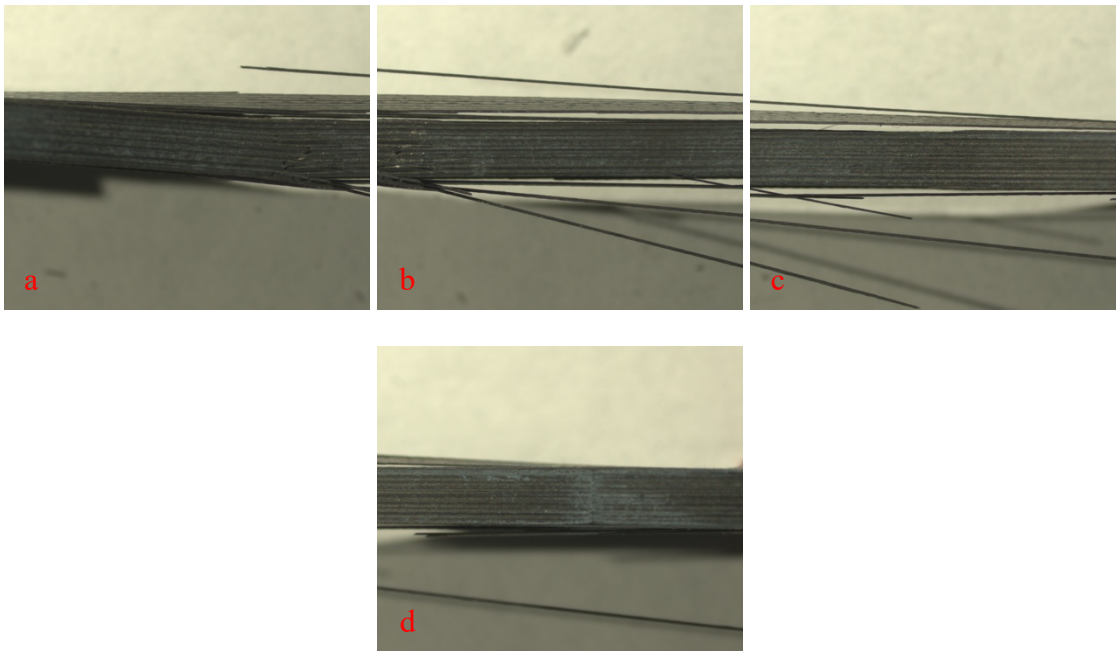

Figure 51: Images of the 0/90 baseline composite specimen B-02-12 tested in tension to failure. (a-d) side view.

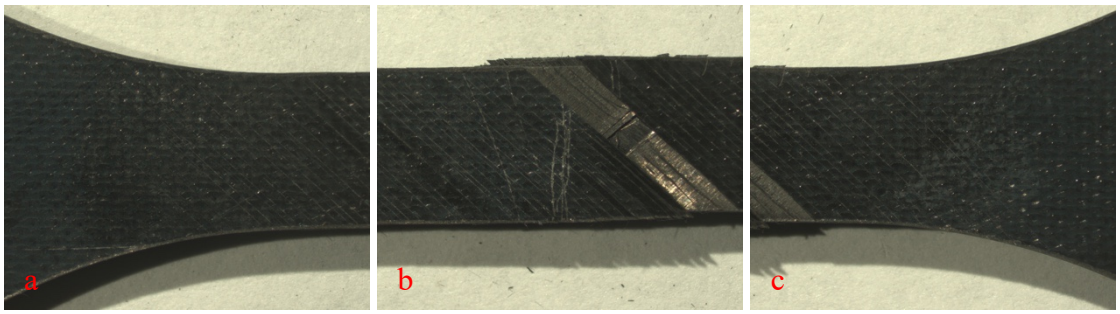

Figure 52: Images of the ±45 baseline composite specimen B-05-06 tested in tension to failure. (a-c) face view.

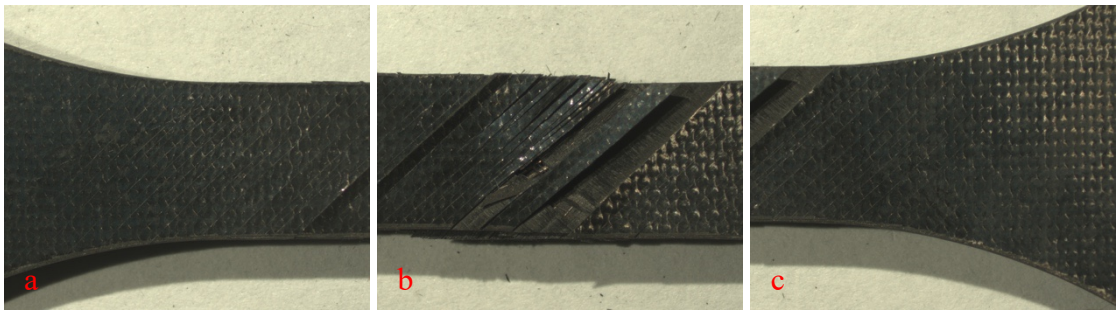

Figure 53: Images of the ±45 baseline composite specimen B-05-06 tested in tension to failure. (a-c) face view.

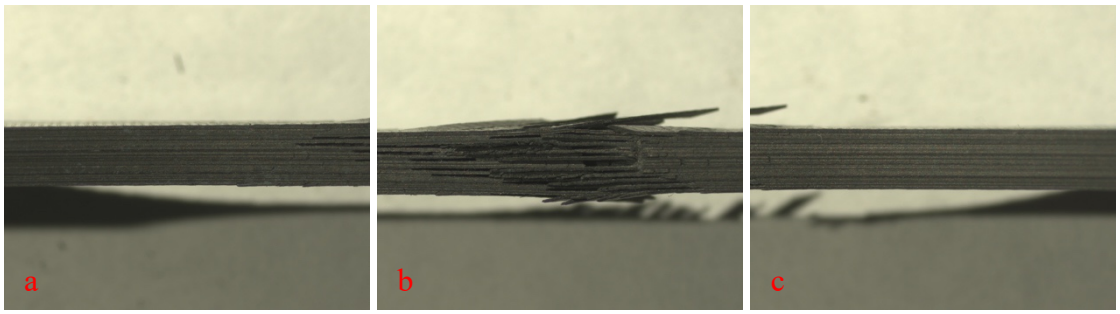

Figure 54: Images of the ±45 baseline composite specimen B-05-06 tested in tension to failure. (a-c) side view.

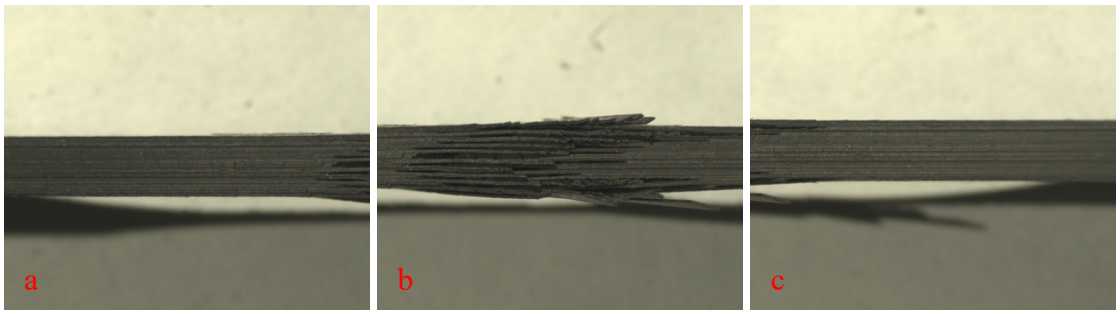

Figure 55: Images of the ±45 baseline composite specimen B-05-06 tested in tension to failure. (a-c) side view.

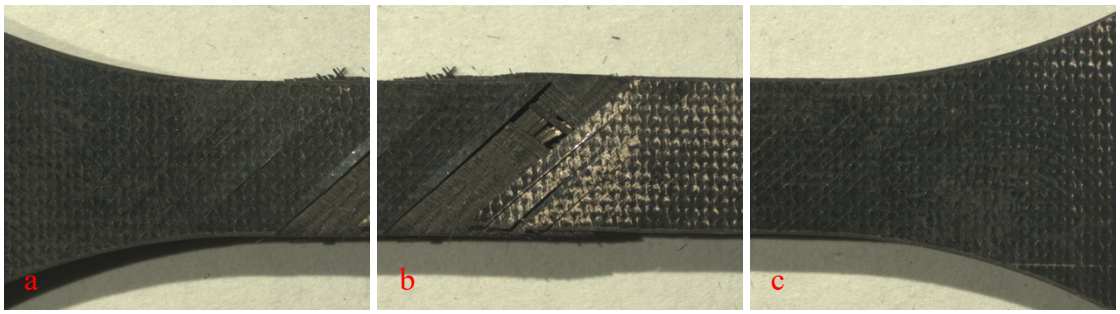

Figure 56: Images of the ±45 baseline composite specimen B-05-15 tested in tension to failure. (a-c) face view.

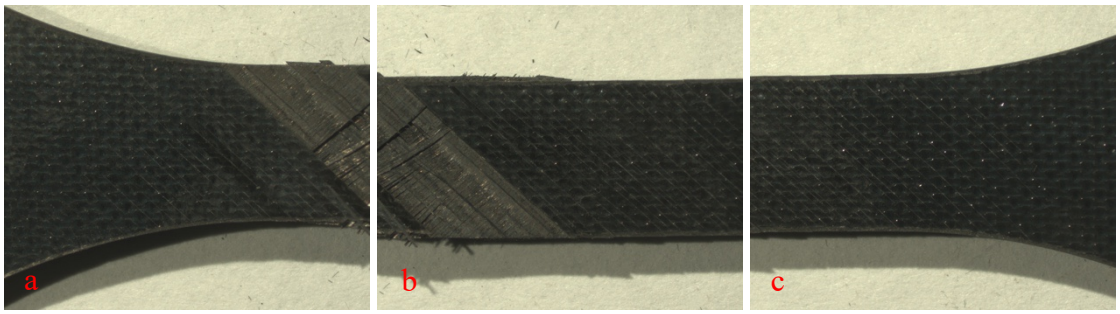

Figure 57: Images of the ±45 baseline composite specimen B-05-15 tested in tension to failure. (a-c) face view.

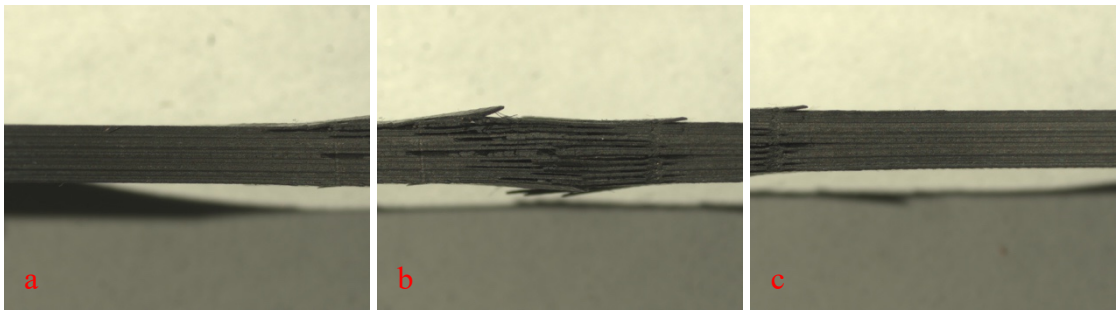

Figure 58: Images of the ±45 baseline composite specimen B-05-15 tested in tension to failure. (a-c) side view.

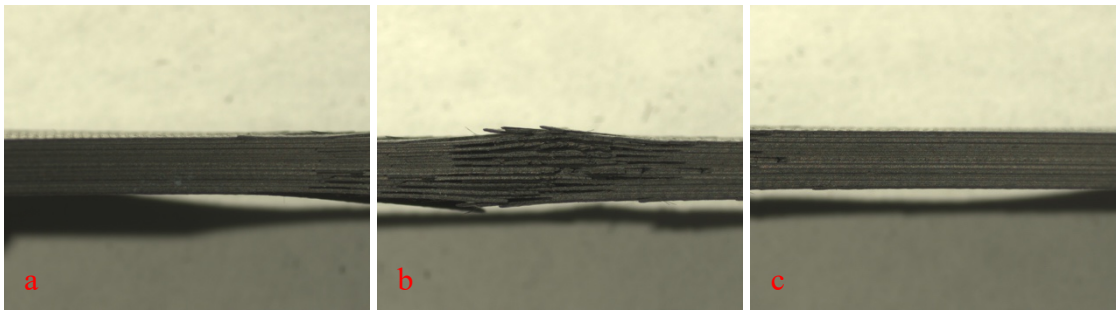

Figure 59: Images of the ±45 baseline composite specimen B-05-15 tested in tension to failure. (a-c) side view.

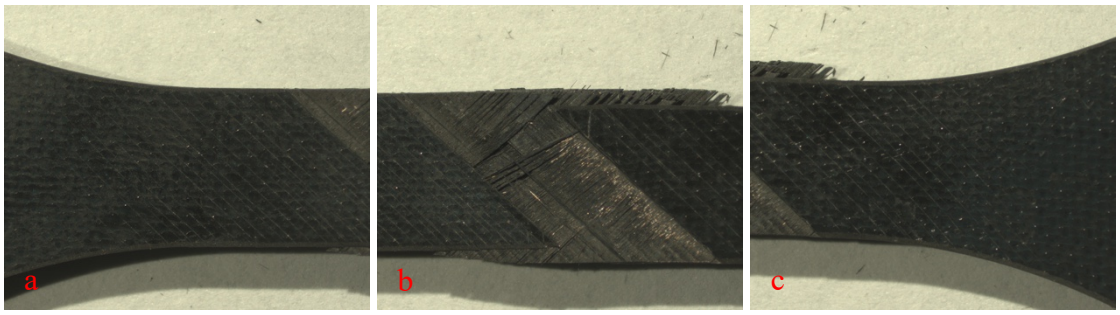

Figure 60: Images of the ±45 baseline composite specimen B-05-19 tested in tension to failure. (a-c) face view.

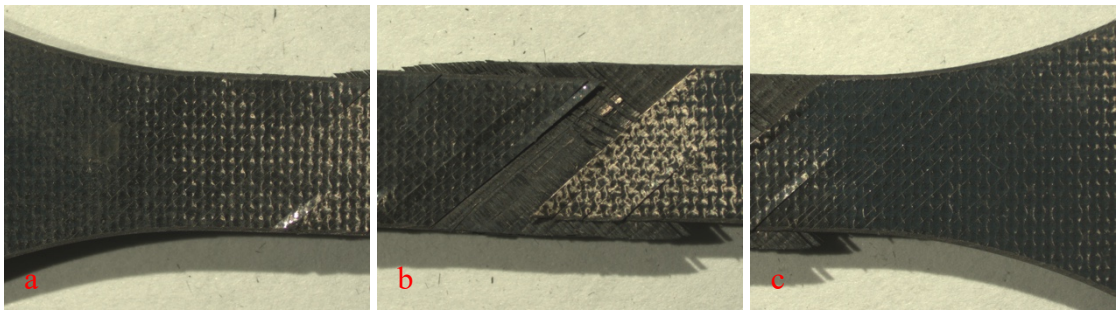

Figure 61: Images of the ±45 baseline composite specimen B-05-19 tested in tension to failure. (a-c) face view.

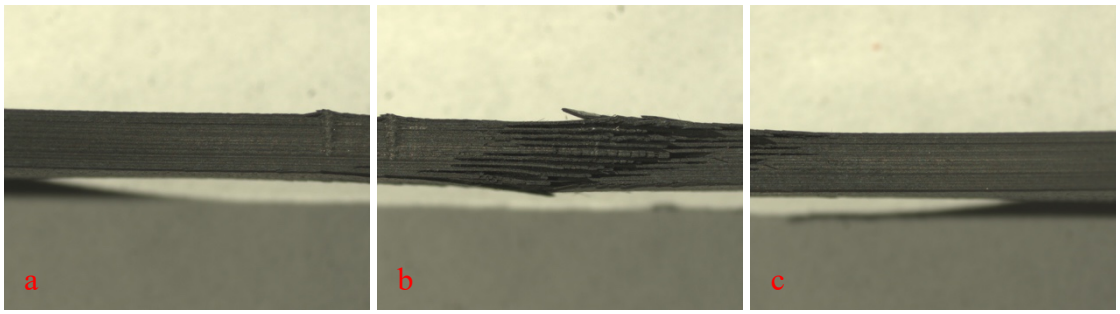

Figure 62: Images of the ±45 baseline composite specimen B-05-19 tested in tension to failure. (a-c) side view.

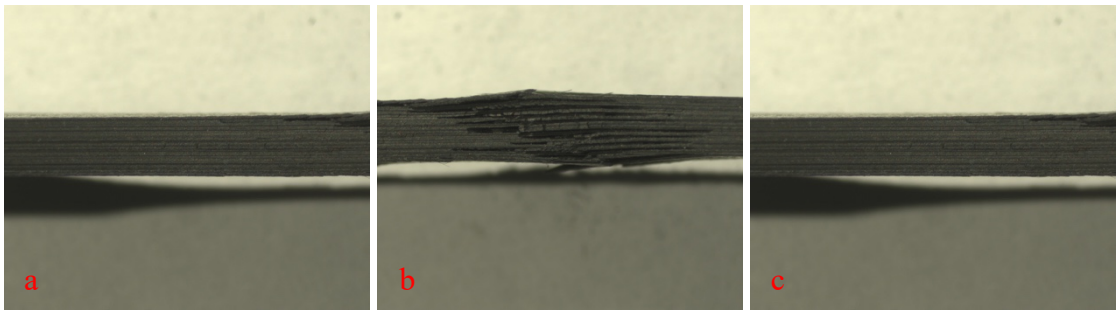

Figure 63: Images of the ±45 baseline composite specimen B-05-19 tested in tension to failure. (a-c) side view.

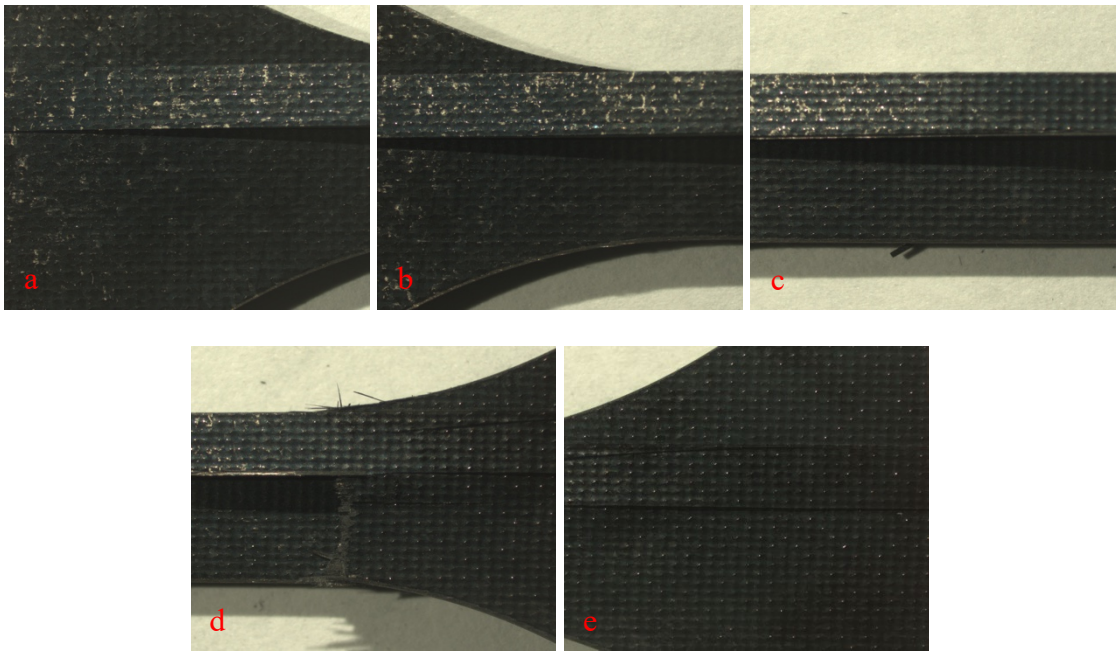

Figure 64: Images of the 0/90 NanoStitch composite specimen NS-07-07 tested in tension to failure. (a-e) face view.

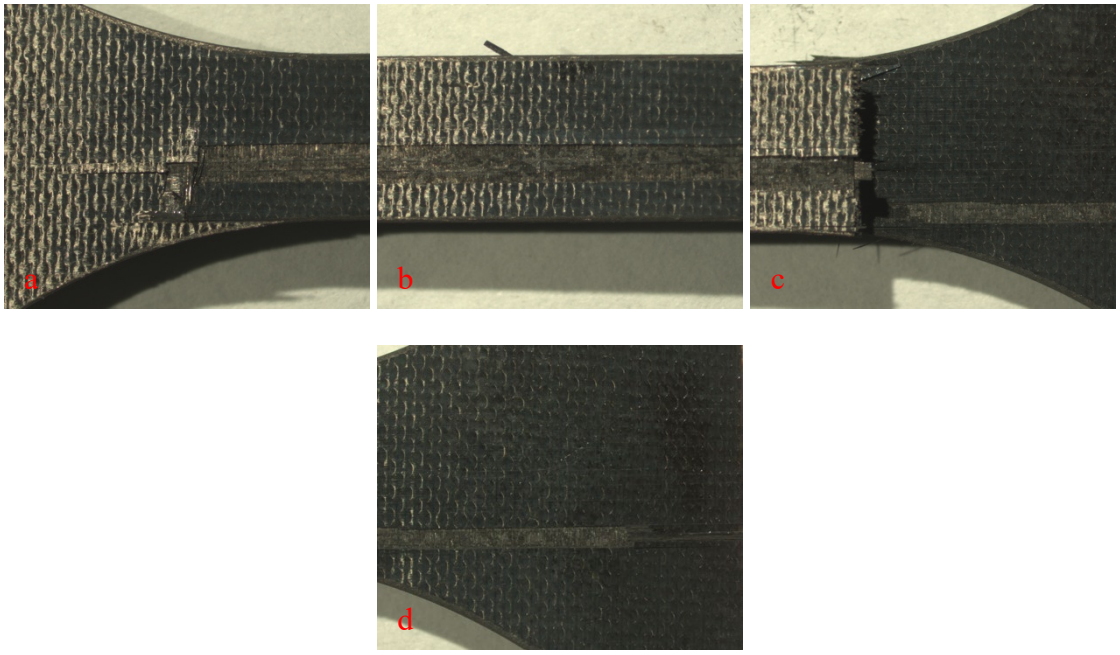

Figure 65: Images of the 0/90 NanoStitch composite specimen NS-07-07 tested in tension to failure. (a-d) face view.

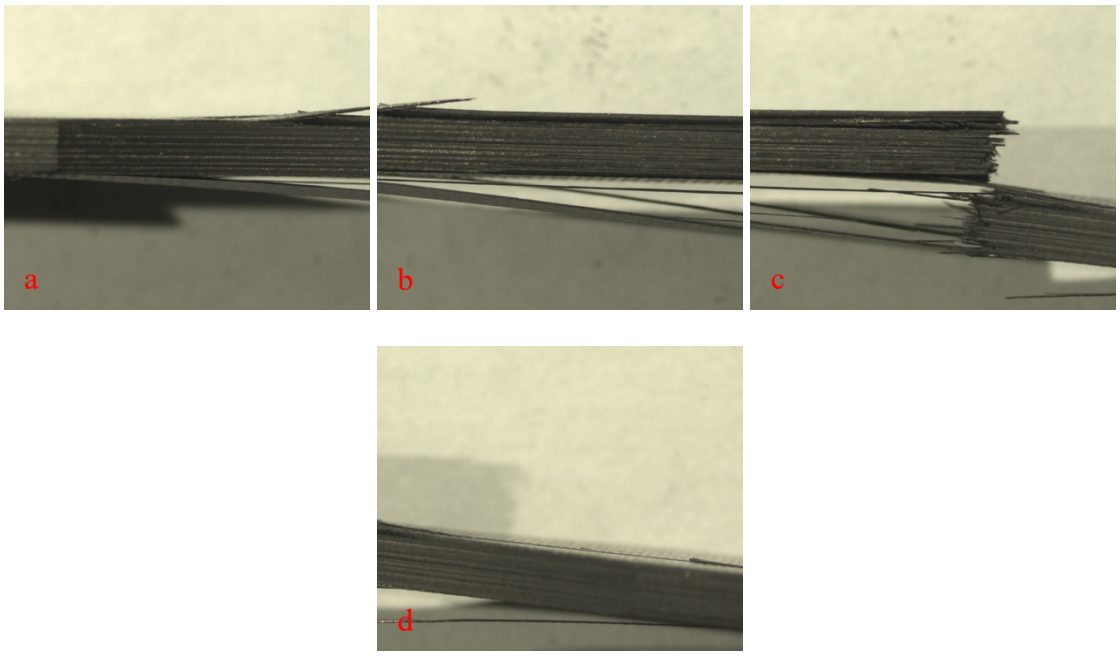

Figure 66: Images of the 0/90 NanoStitch composite specimen NS-07-07 tested in tension to failure. (a-d) side view.

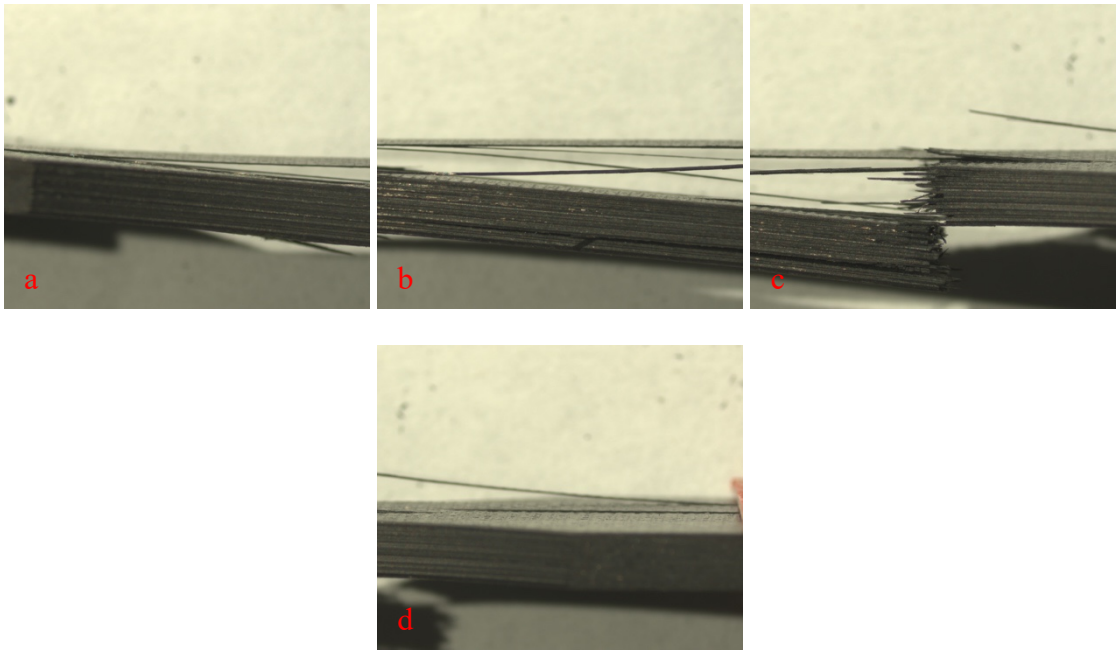

Figure 67: Images of the 0/90 NanoStitch composite specimen NS-07-07 tested in tension to failure. (a-d) side view.

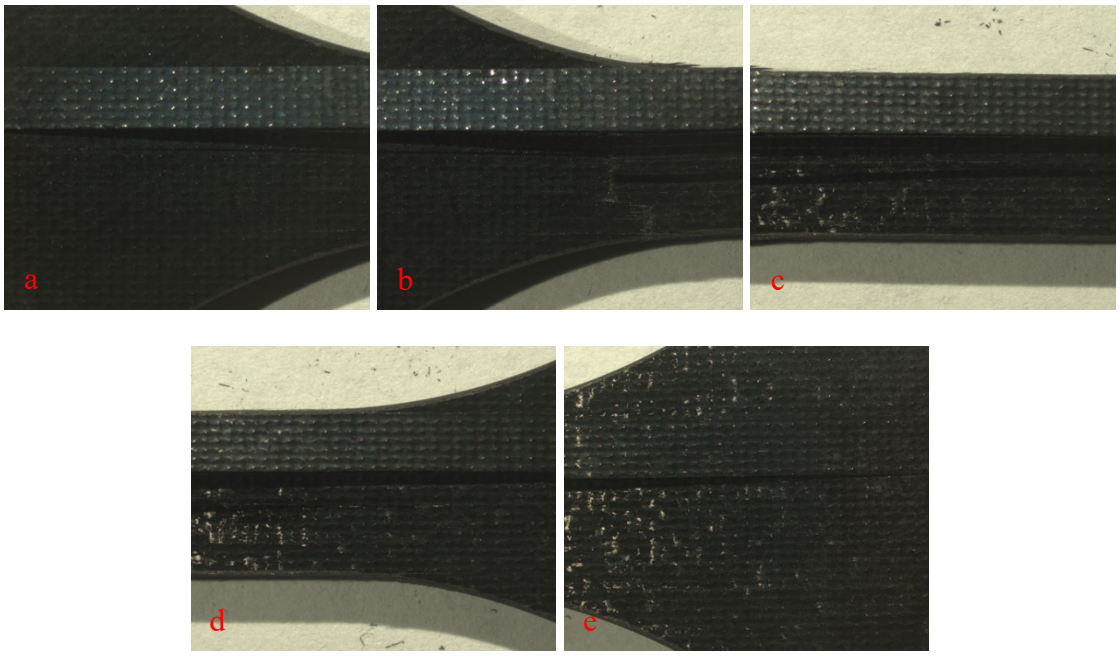

Figure 68: Images of the 0/90 NanoStitch composite specimen NS-07-17 tested in tension to failure. (a-e) face view.

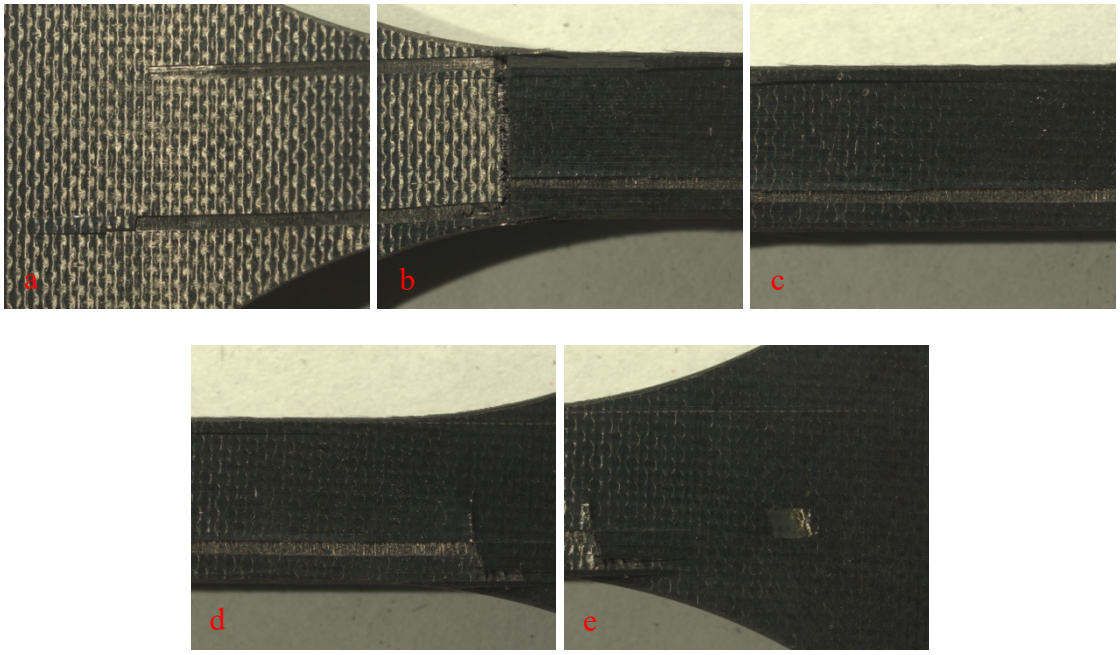

Figure 69: Images of the 0/90 NanoStitch composite specimen NS-07-17 tested in tension to failure. (a-e) face view.

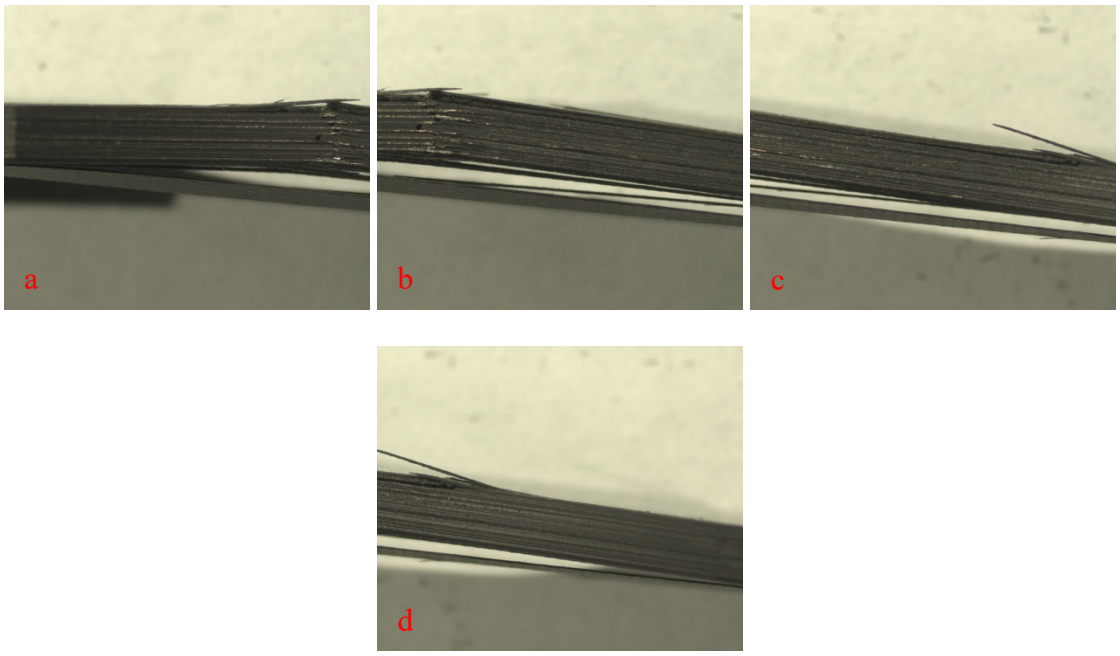

Figure 70: Images of the 0/90 NanoStitch composite specimen NS-07-17 tested in tension to failure. (a-d) side view.

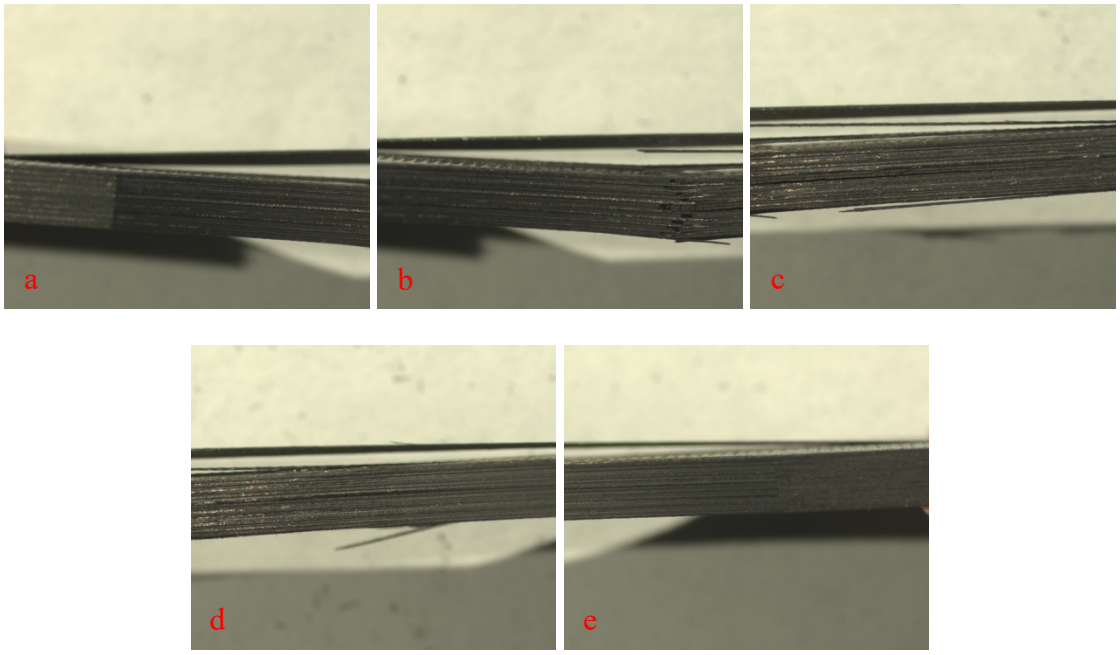

Figure 71: Images of the 0/90 NanoStitch composite specimen NS-07-17 tested in tension to failure. (a-e) side view.

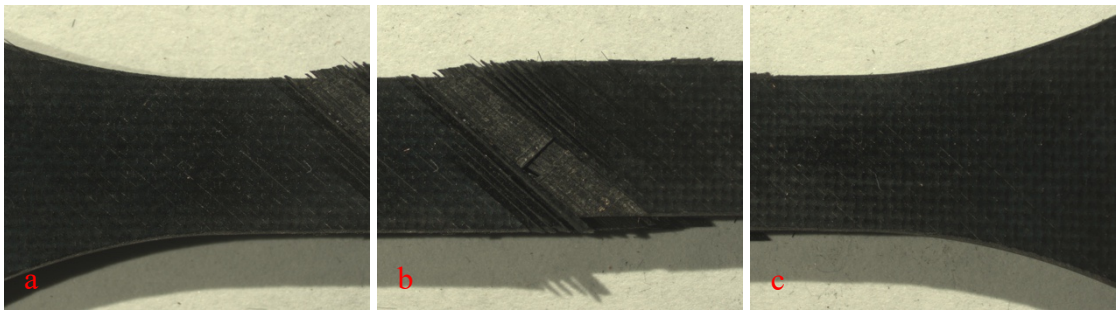

Figure 72: Images of the ±45 NanoStitch composite specimen NS-02-02 tested in tension to failure. (a-c) face view.

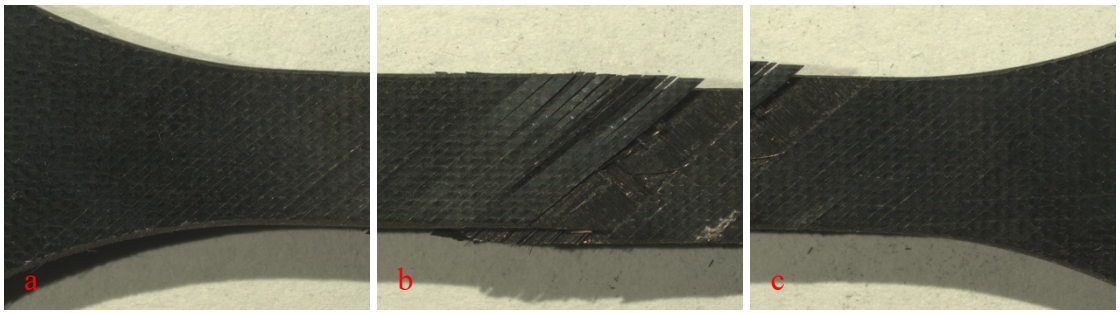

Figure 73: Images of the ±45 NanoStitch composite specimen NS-02-02 tested in tension to failure. (a-c) face view.

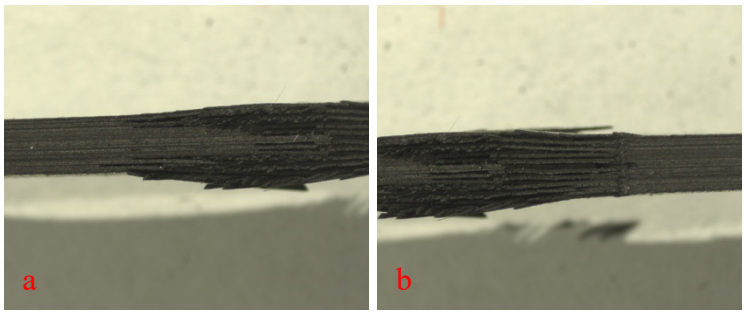

Figure 74: Images of the ±45 NanoStitch composite specimen NS-02-02 tested in tension to failure. (a-b) side view.

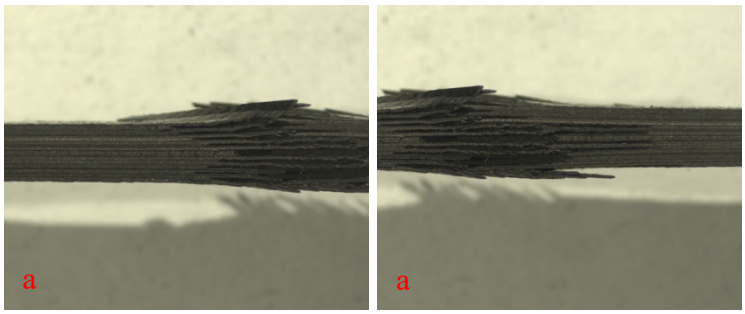

Figure 75: Images of the ±45 NanoStitch composite specimen NS-02-02 tested in tension to failure. (a-b) side view.

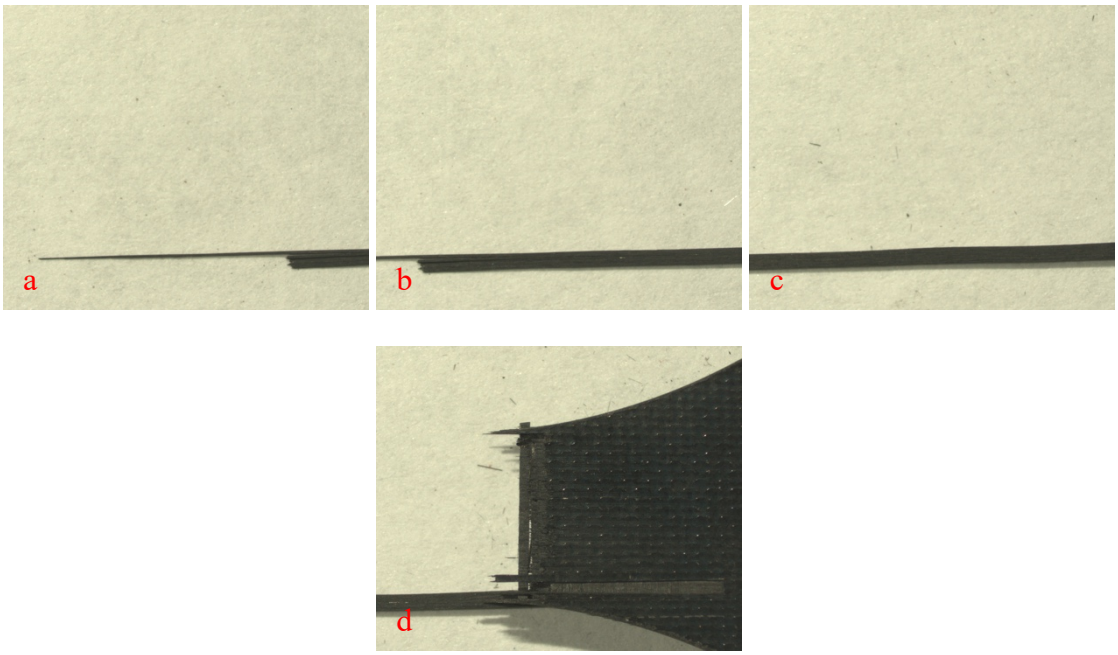

Figure 76: Images of the ±45 NanoStitch composite specimen NS-02-12 tested in tension to failure. (a-d) face view.

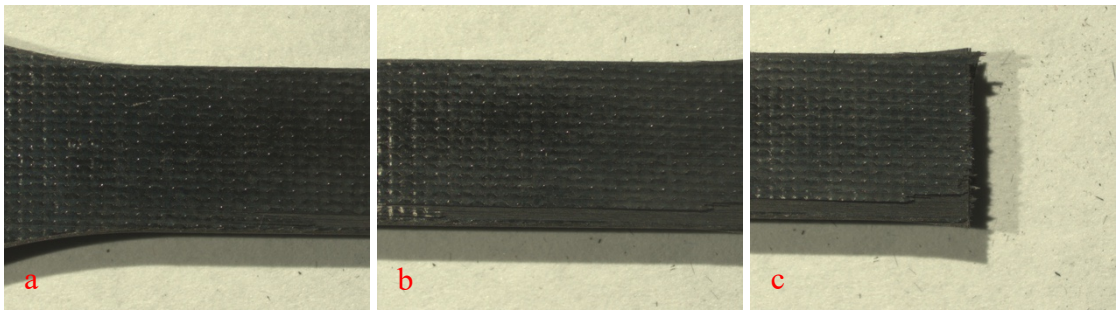

Figure 77: Images of the ±45 NanoStitch composite specimen NS-02-12 tested in tension to failure. (a-c) face view.

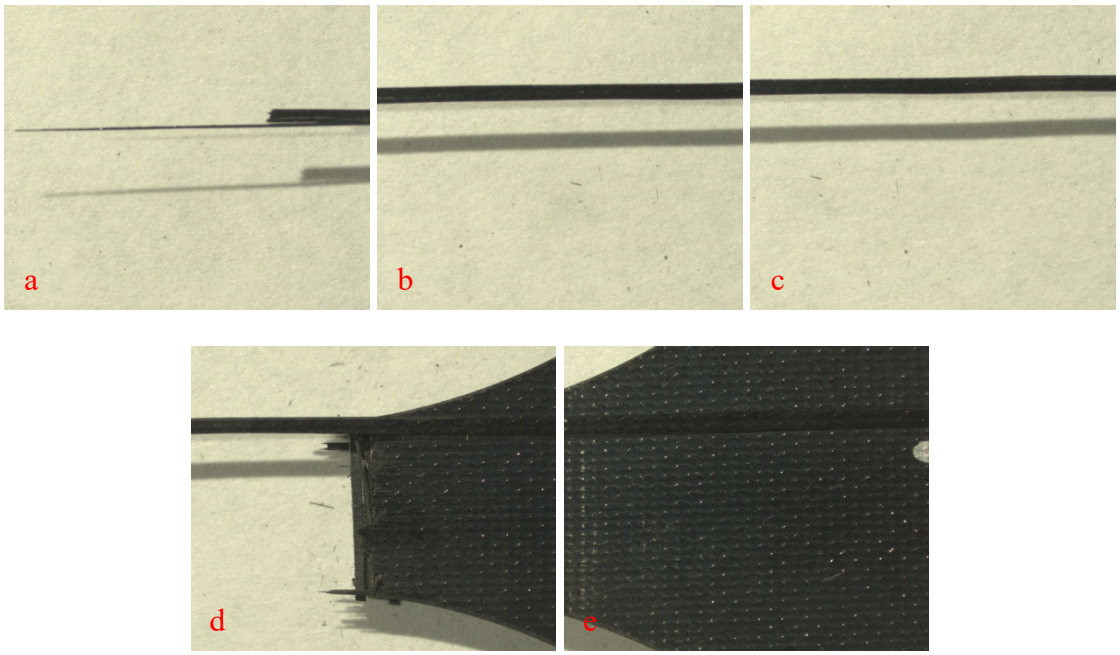

Figure 78: Images of the ±45 NanoStitch composite specimen NS-02-12 tested in tension to failure. (a-e) face view.

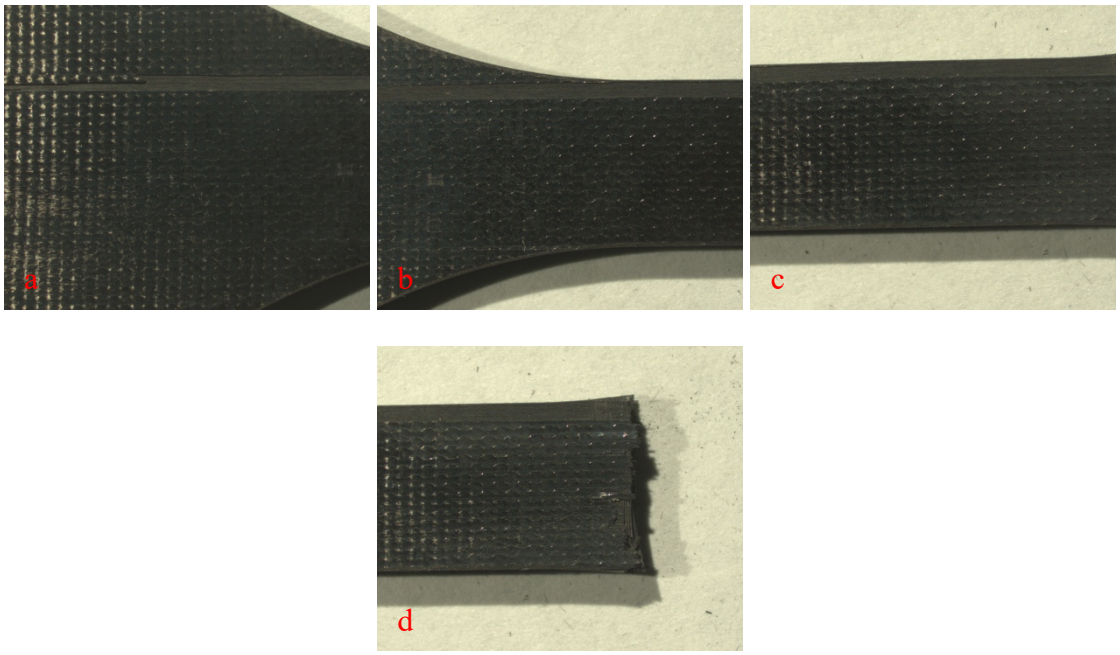

Figure 79: Images of the ±45 NanoStitch composite specimen NS-02-12 tested in tension to failure. (a-d) face view.

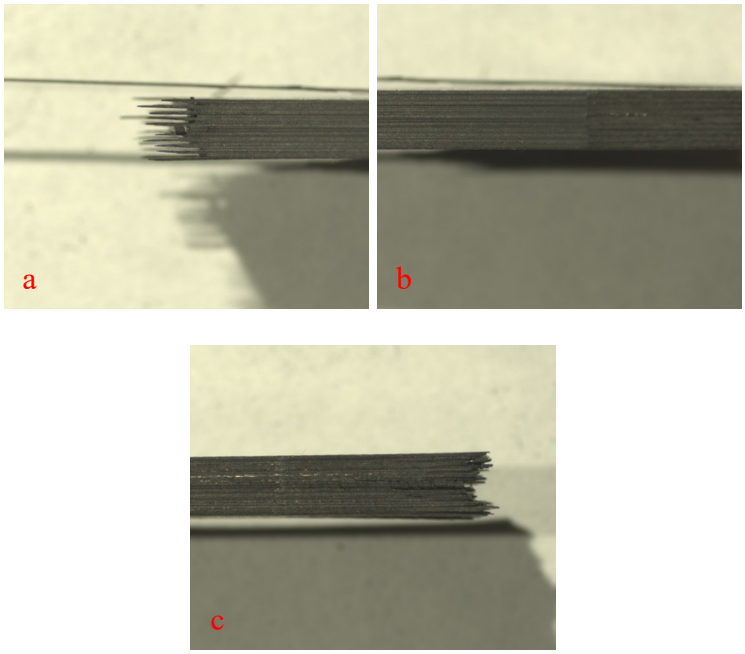

Figure 80: Images of the ±45 NanoStitch composite specimen NS-02-12 tested in tension to failure. (a-c) side view.

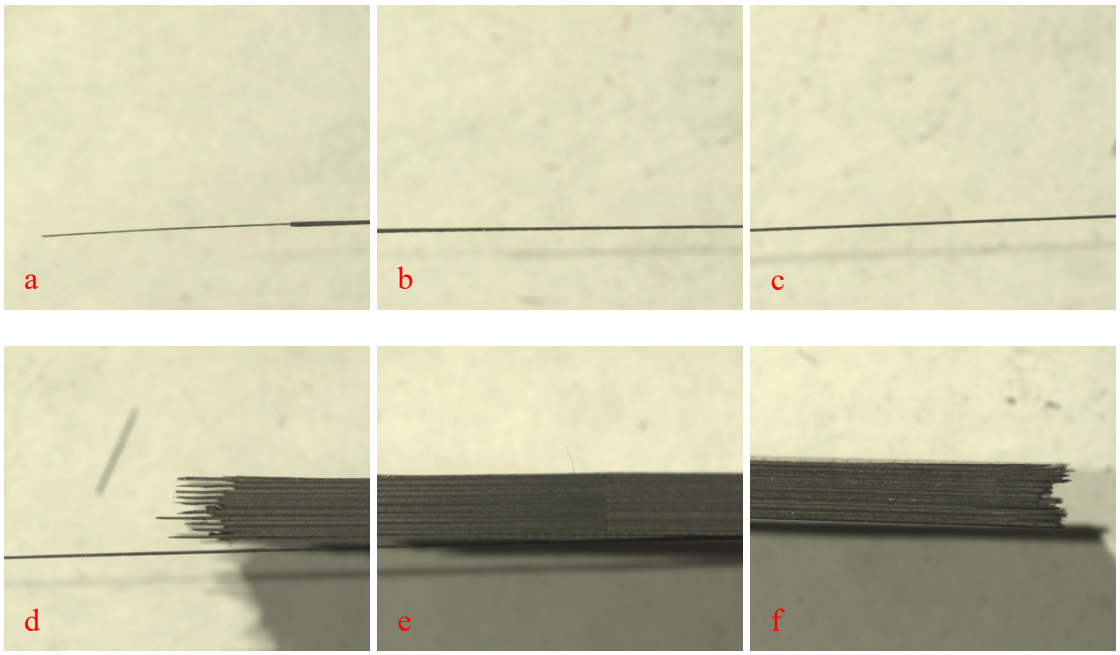

Figure 81: Images of the ±45 NanoStitch composite specimen NS-02-12 tested in tension to failure. (a-f) side view.

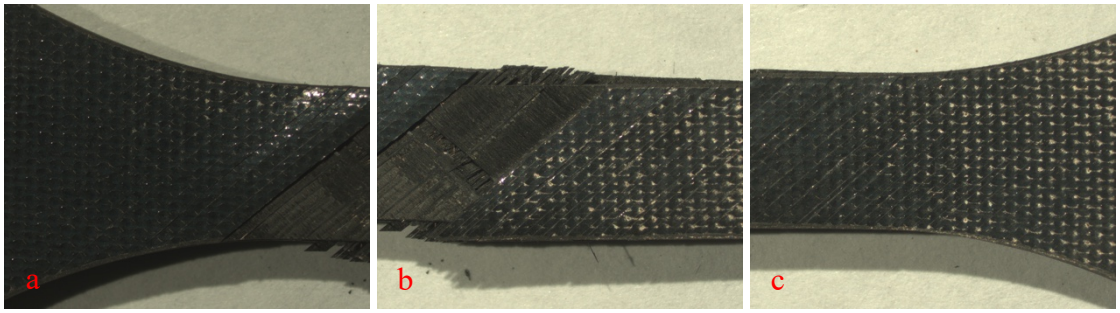

Figure 82: Images of the ±45 NanoStitch composite specimen NS-02-20 tested in tension to failure. (a-c) face view.

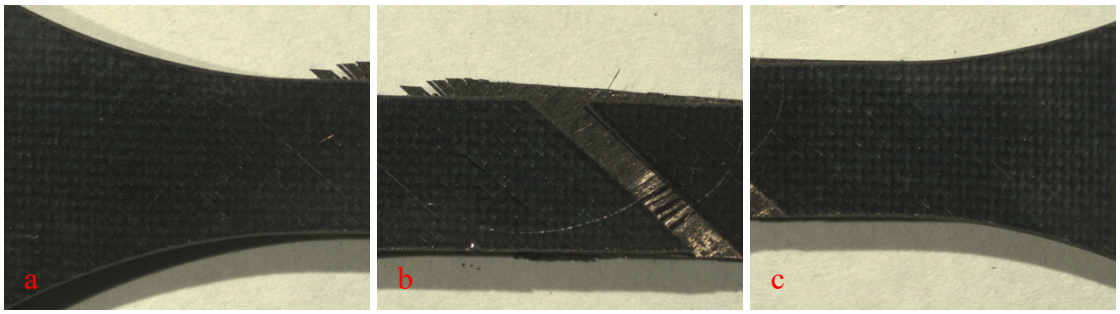

Figure 83: Images of the ±45 NanoStitch composite specimen NS-02-20 tested in tension to failure. (a-c) face view.

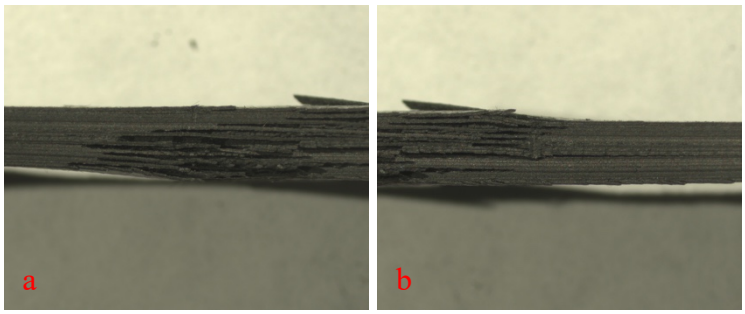

Figure 84: Images of the ±45 NanoStitch composite specimen NS-02-20 tested in tension to failure. (a-b) side view.

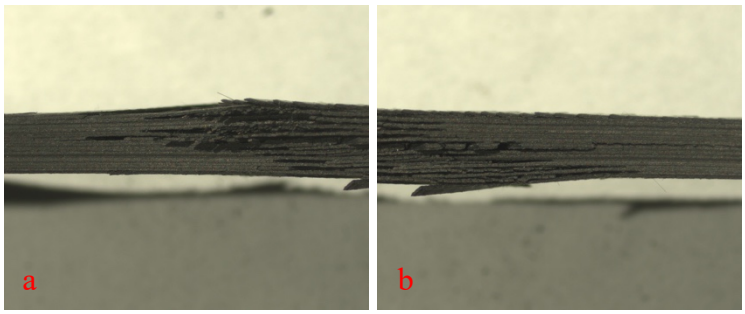

Figure 85: Images of the ±45 NanoStitch composite specimen NS-02-20 tested in tension to failure. (a-b) side view.

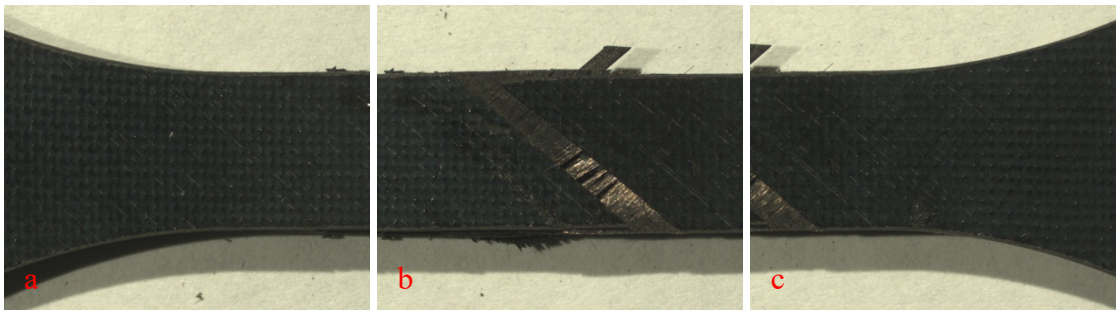

Figure 86: Images of the ±45 NanoStitch composite specimen NS-02-07 tested in tension to failure. (a-c) face view.

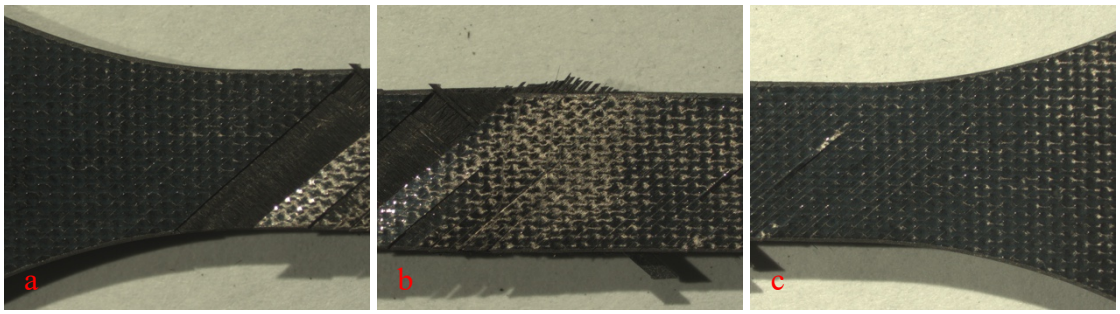

Figure 87: Images of the ±45 NanoStitch composite specimen NS-02-07 tested in tension to failure. (a-c) face view.

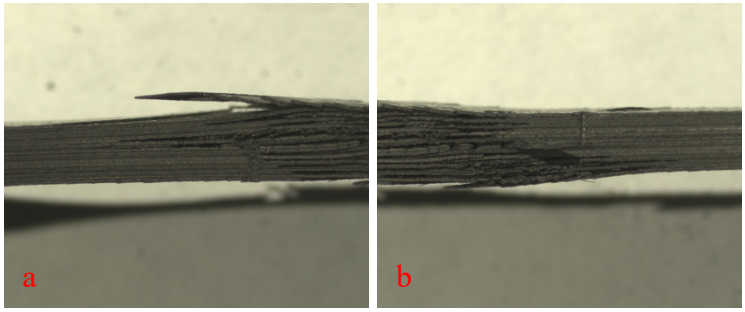

Figure 88: Images of the ±45 NanoStitch composite specimen NS-02-07 tested in tension to failure. (a-b) side view.

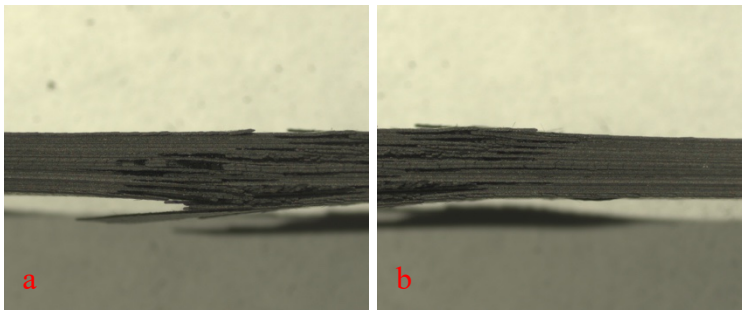

Figure 89: Images of the ±45 NanoStitch composite specimen NS-02-07 tested in tension to failure. (a-b) side view.

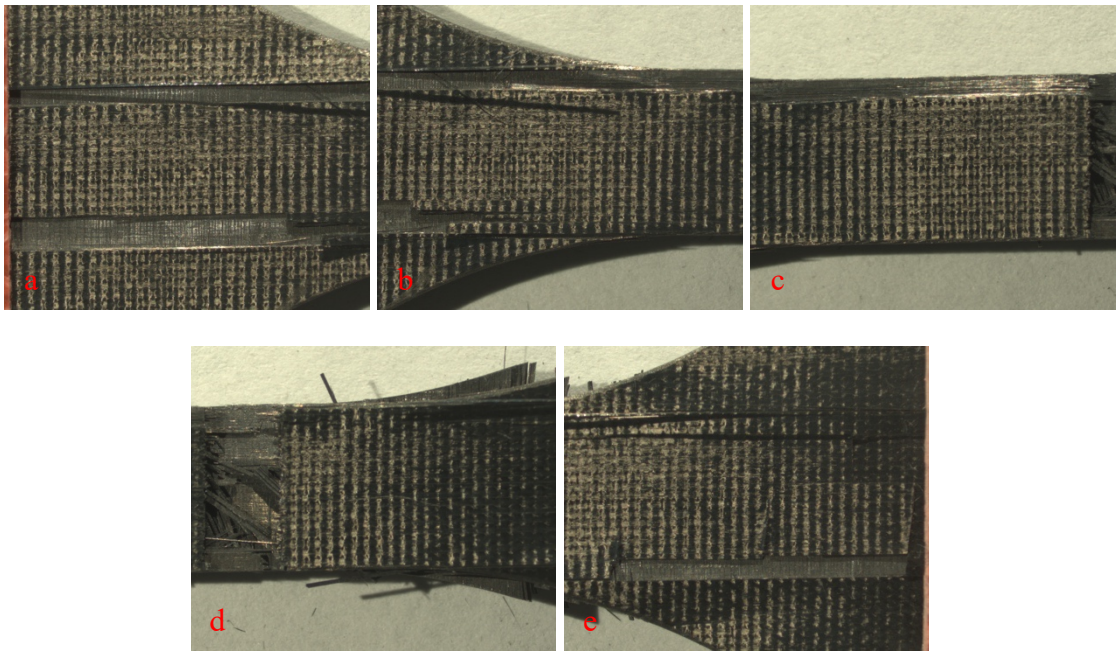

Figure 90: Images of the 0/90 baseline composite specimen B-02-19 tested in tension-tension fatigue (σ_{max} = 932 MPa, N_f > 200,000 – fatigue runout), then failed in a tension test. (a-e) face view.

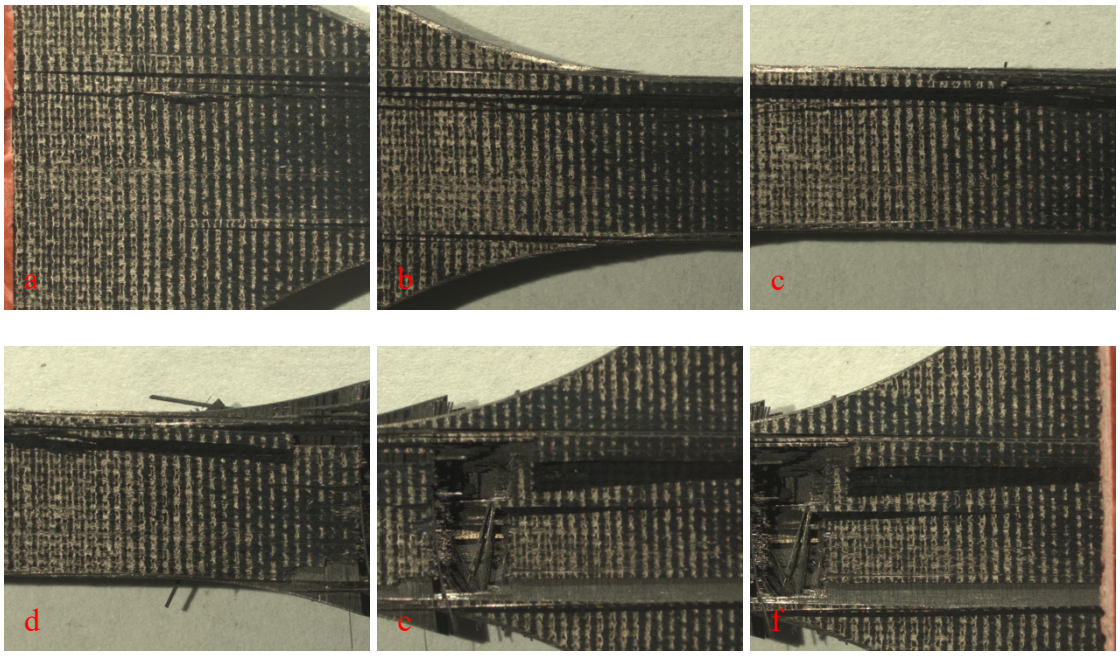

Figure 91: Images of the 0/90 baseline composite specimen B-02-19 tested in tension-tension fatigue (σ_{max} = 932 MPa, N_f > 200,000 – fatigue runout), then failed in a tension test. (a-f) face view.

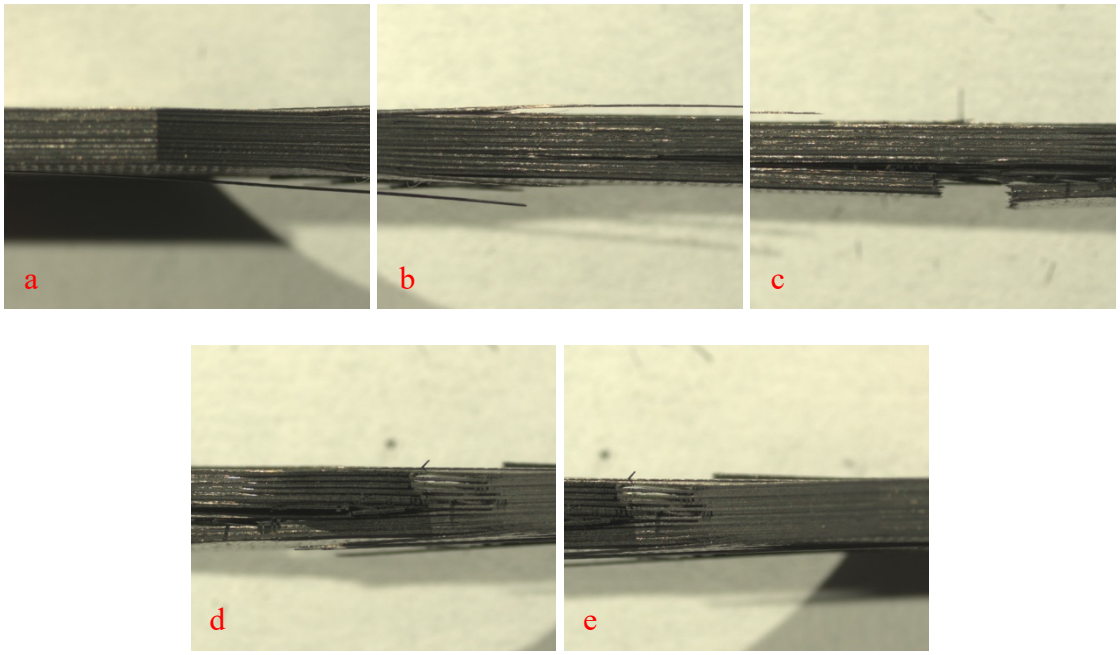

Figure 92: Images of the 0/90 baseline composite specimen B-02-19 tested in tension-tension fatigue (σ_{max} = 932 MPa, N_f > 200,000 – fatigue runout), then failed in a tension test. (a-e) side view.

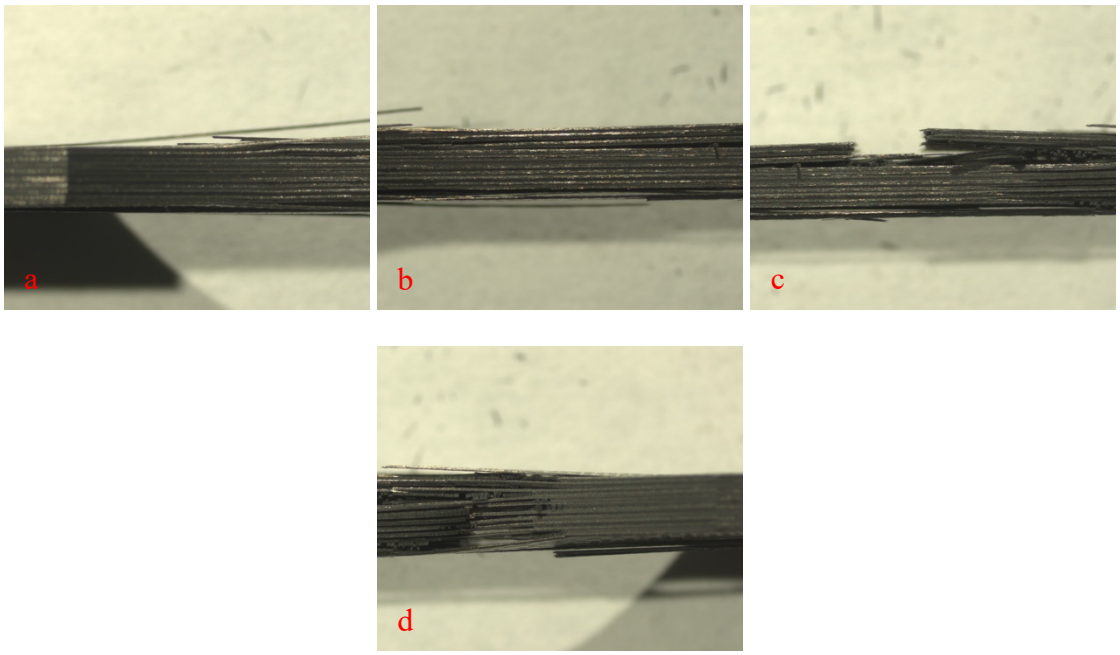

Figure 93: Images of the 0/90 baseline composite specimen B-02-19 tested in tension-tension fatigue (σ_{max} = 932 MPa, N_f > 200,000 – fatigue runout), then failed in a tension test. (a-d) side view.

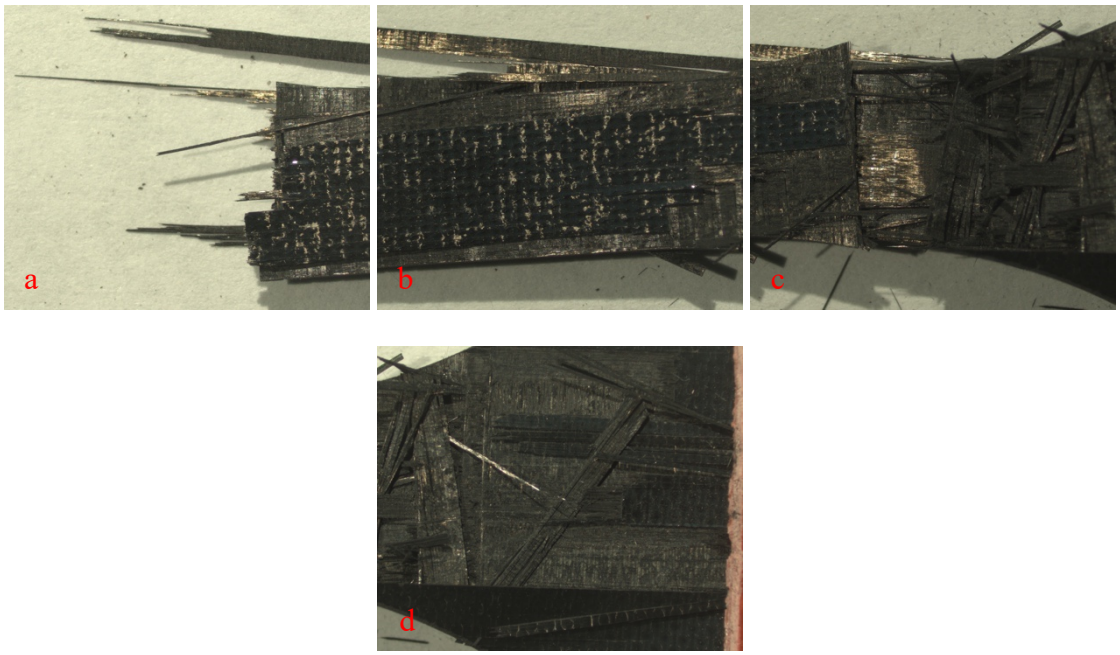

Figure 94: Images of the 0/90 NanoStitch composite specimen NS-07-16 tested in tension-tension fatigue (σ_{max} = 997 MPa, N_f = 158,023). (a-d) face view.

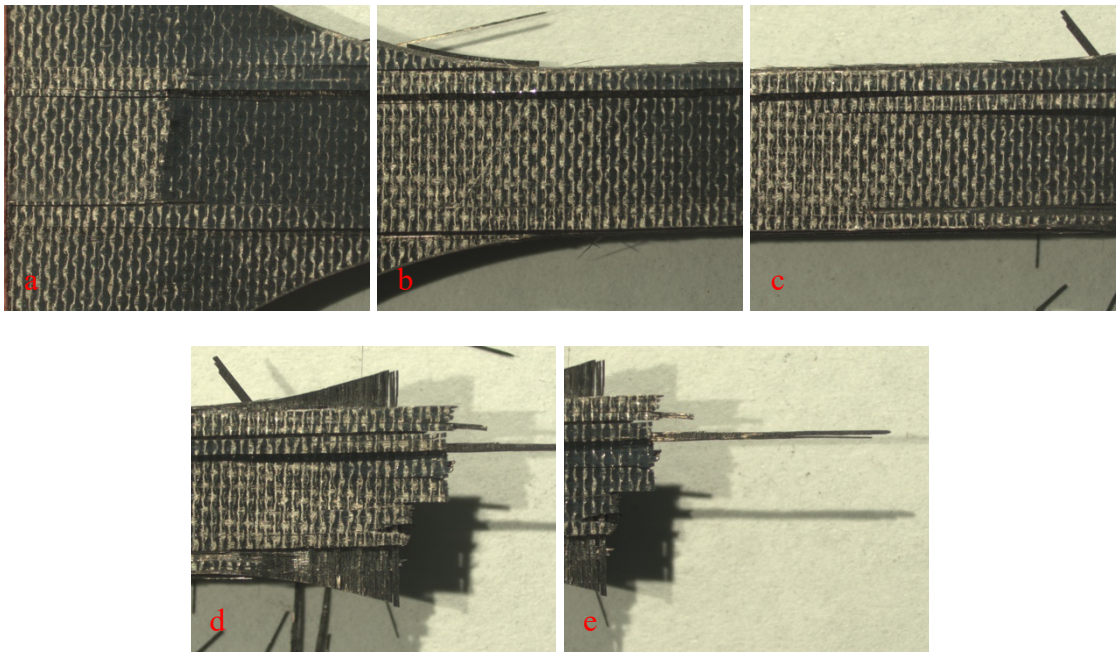

Figure 95: Images of the 0/90 NanoStitch composite specimen NS-07-16 tested in tension-tension fatigue (σ_{max} = 997 MPa, N_f= 158,023). (a-e) face view.

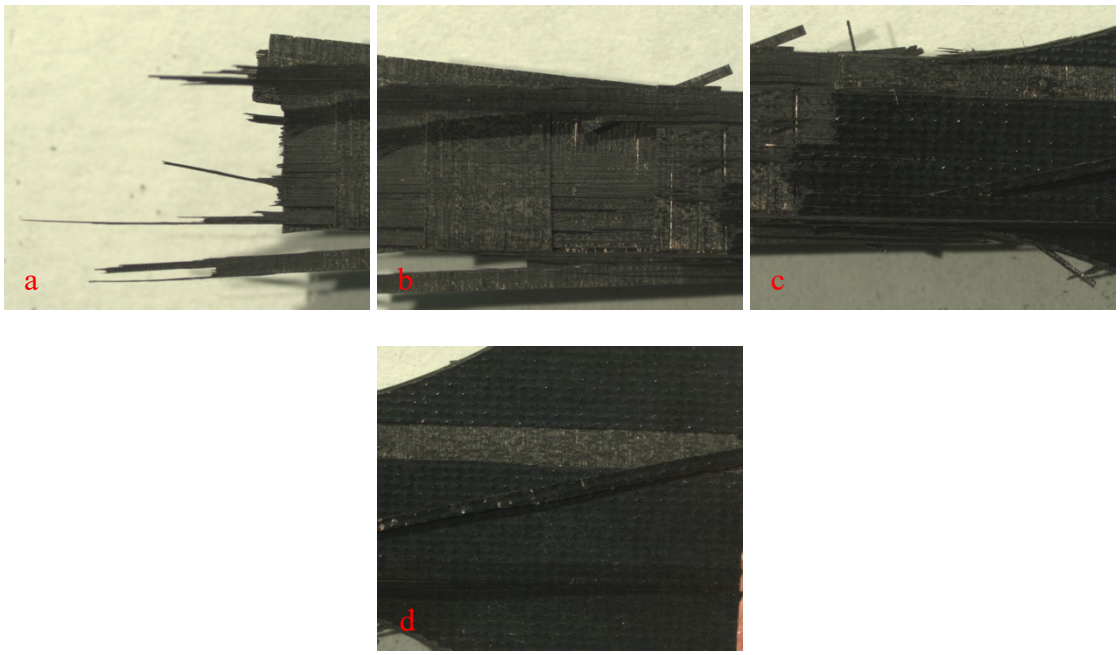

Figure 96: Images of the 0/90 NanoStitch composite specimen NS-07-16 tested in tension-tension fatigue (σ_{max} = 997 MPa, N_f= 158,023). (a-d) face view.

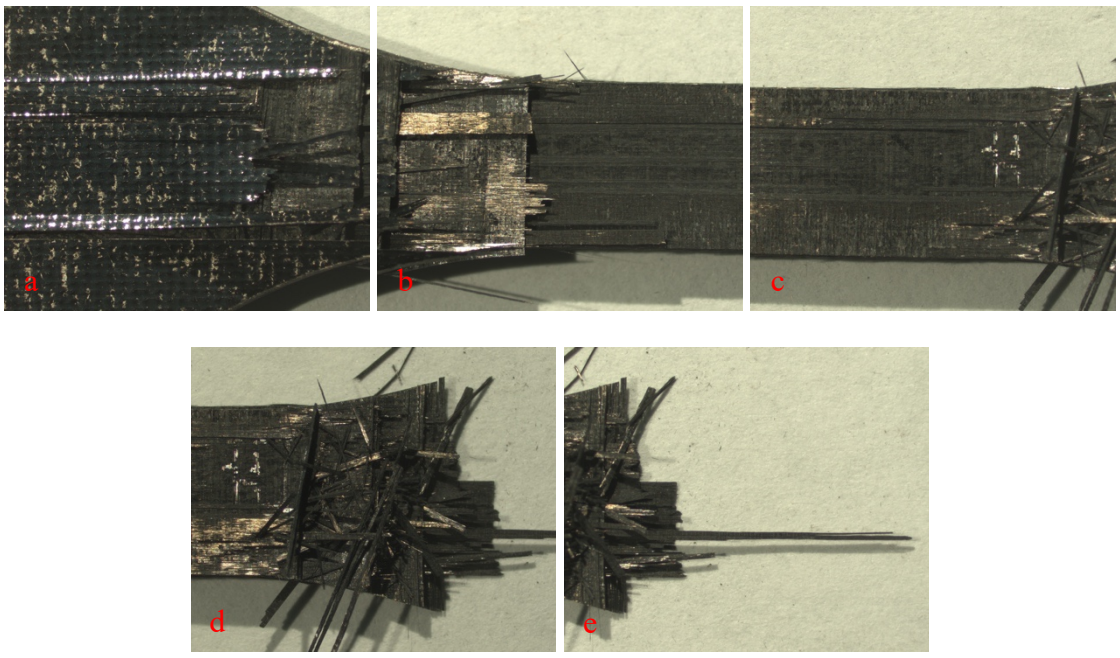

Figure 97: Images of the 0/90 NanoStitch composite specimen NS-07-16 tested in tension-tension fatigue (σ_{max} = 997 MPa, N_f= 158,023). (a-e) face view.

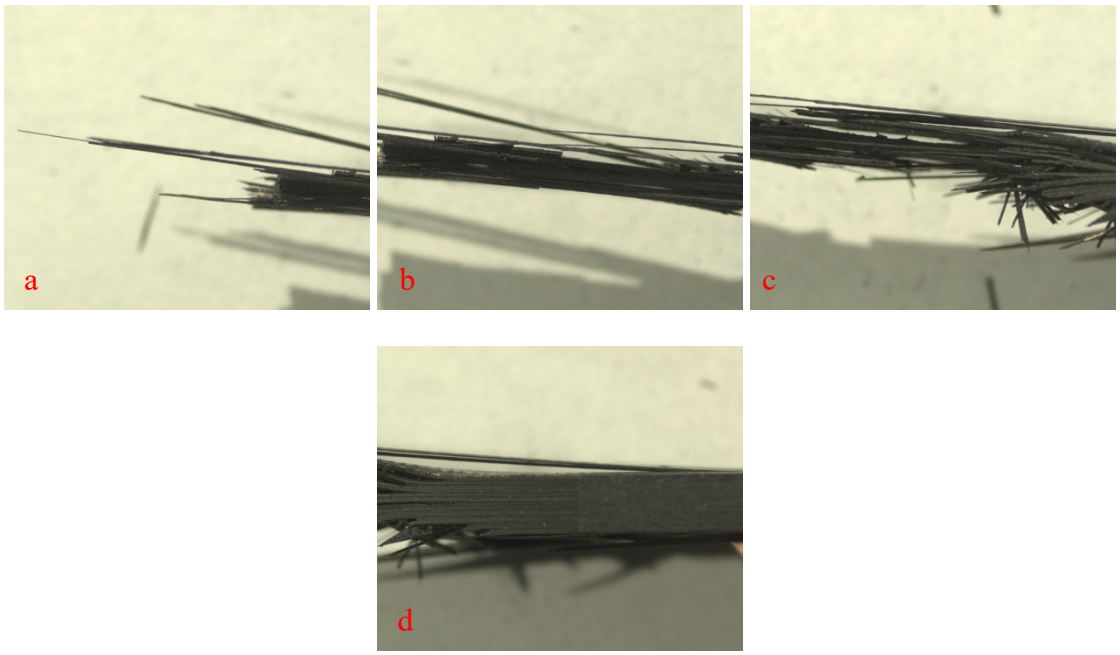

Figure 98: Images of the 0/90 NanoStitch composite specimen NS-07-16 tested in tension-tension fatigue (σ_{max} = 997 MPa, N_f= 158,023). (a-d) side view.

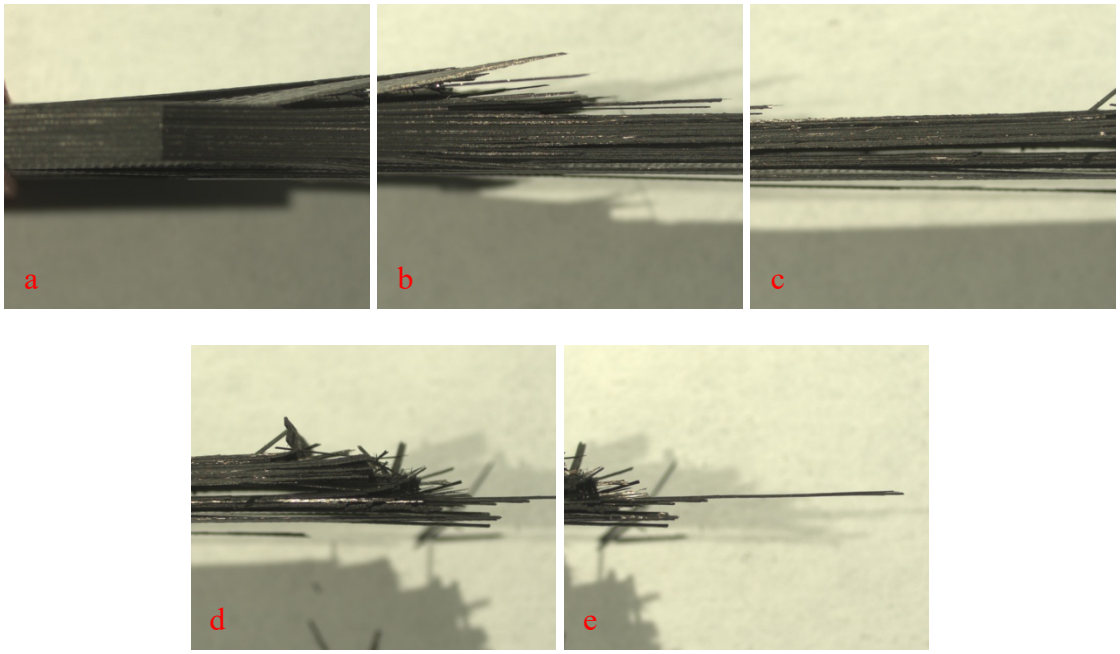

Figure 99: Images of the 0/90 NanoStitch composite specimen NS-07-16 tested in tension-tension fatigue (σ_{max} = 997 MPa, N_f= 158,023). (a-e) side view.

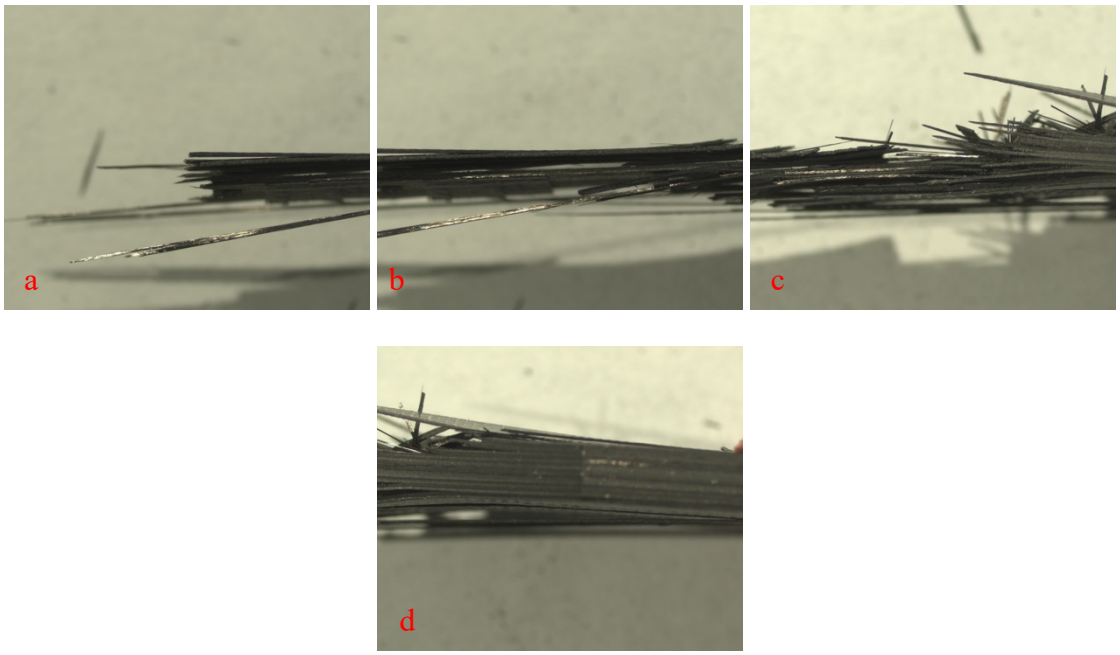

Figure 100: Images of the 0/90 NanoStitch composite specimen NS-07-16 tested in tension-tension fatigue (σ_{max} = 997 MPa, N_f= 158,023). (a-d) side view.

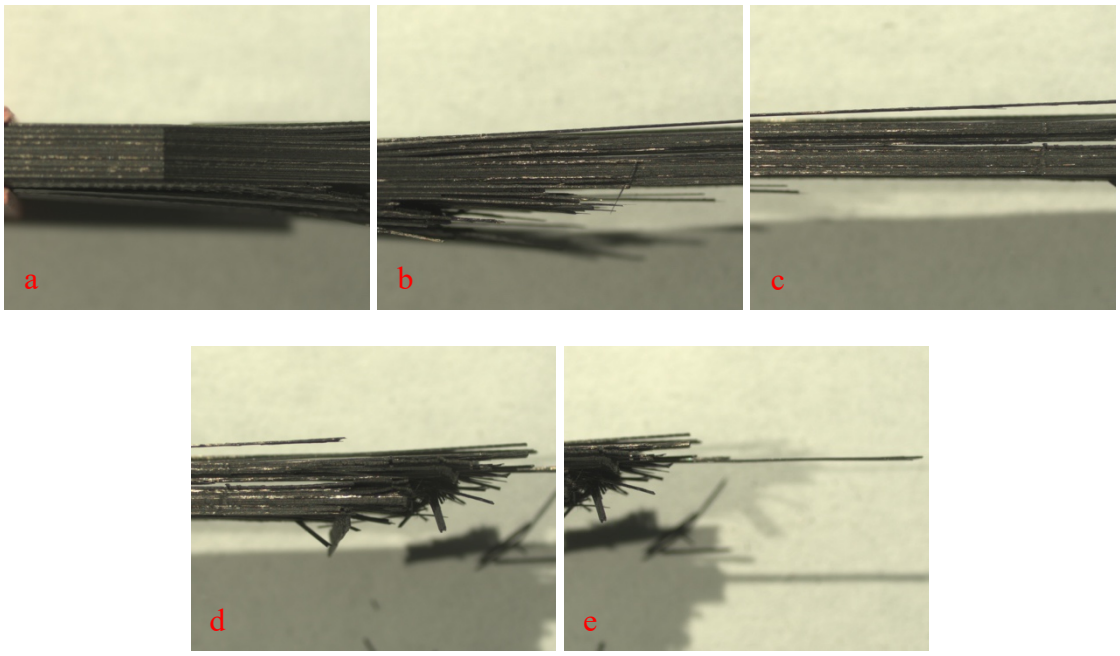

Figure 101: Images of the 0/90 NanoStitch composite specimen NS-07-16 tested in tension-tension fatigue (σ_{max} = 997 MPa, N_f= 158,023). (a-e) side view.

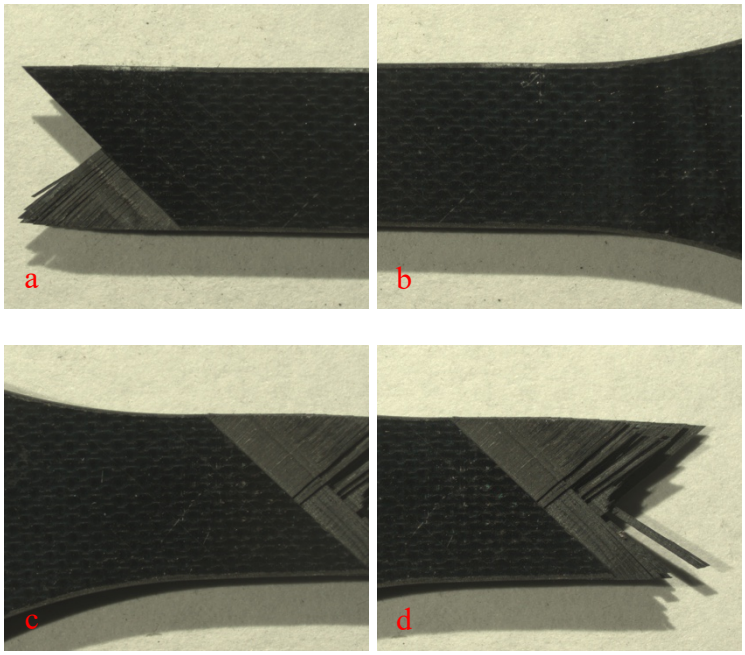

Figure 102: Images of the ±45 baseline composite specimen B-05-08 tested in tension-tension fatigue (σ_{max} = 159 MPa, N_f= 18,384). (a-d) face view.

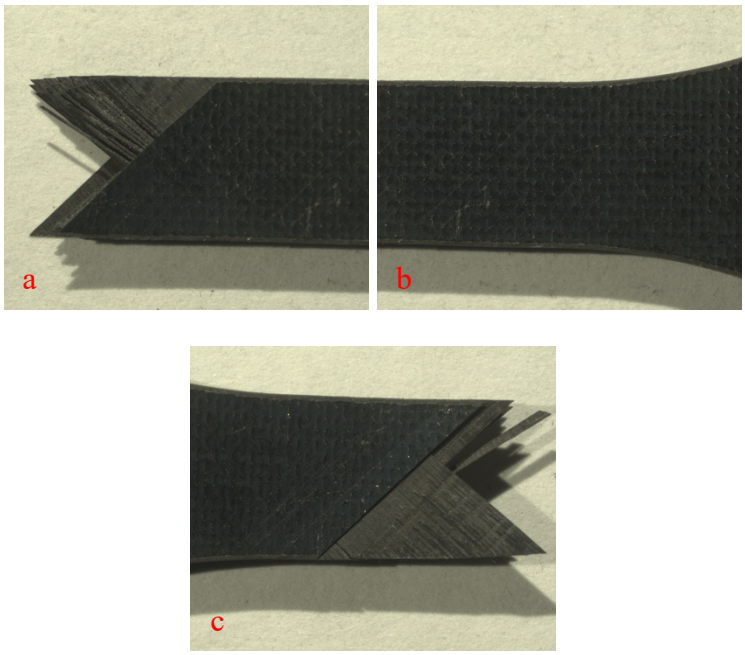

Figure 103: Images of the ±45 baseline composite specimen B-05-08 tested in tension-tension fatigue (σ_{max} = 159 MPa, N_f = 18,384). (a-c) face view.

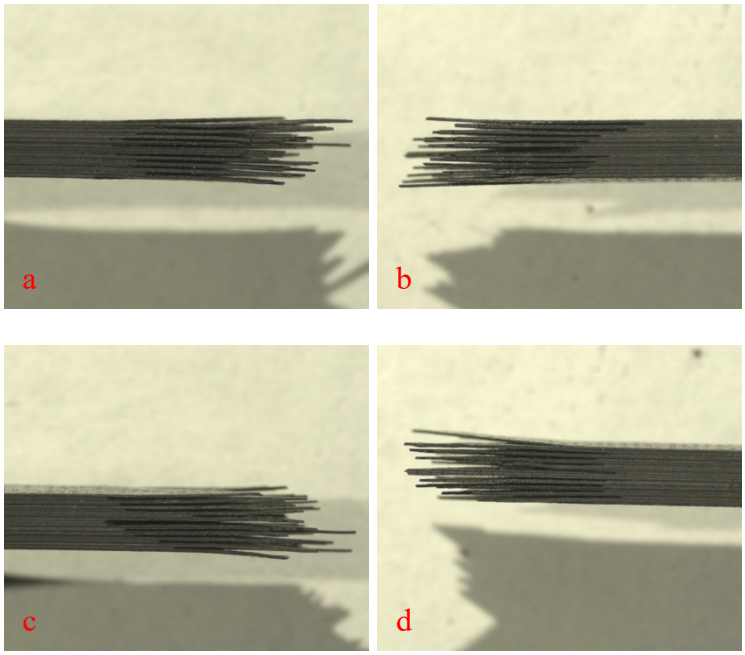

Figure 104: Images of the ±45 baseline composite specimen B-05-08 tested in tension-tension fatigue (σ_{max} = 159 MPa, N_f = 18,384). (a-d) side view.

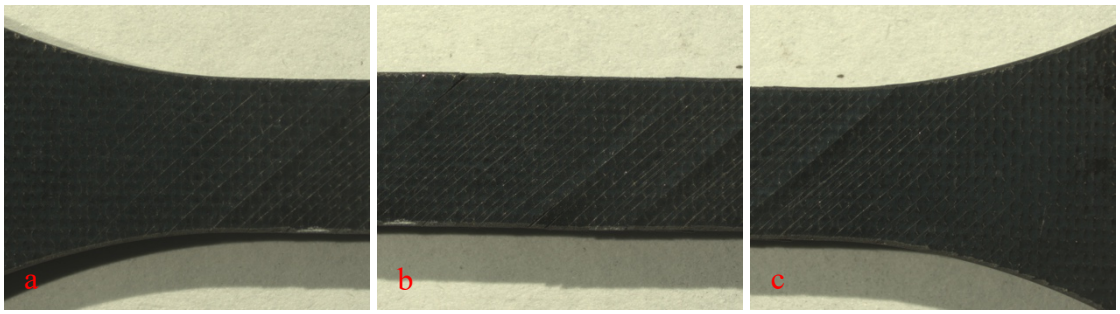

Figure 105: Images of the ±45 baseline composite specimen B-05-24 tested in tension-tension fatigue (σ_{max} = 105 MPa, N_f > 200,000 – fatigue runout), then failed in a tension test. (a-c) face view.

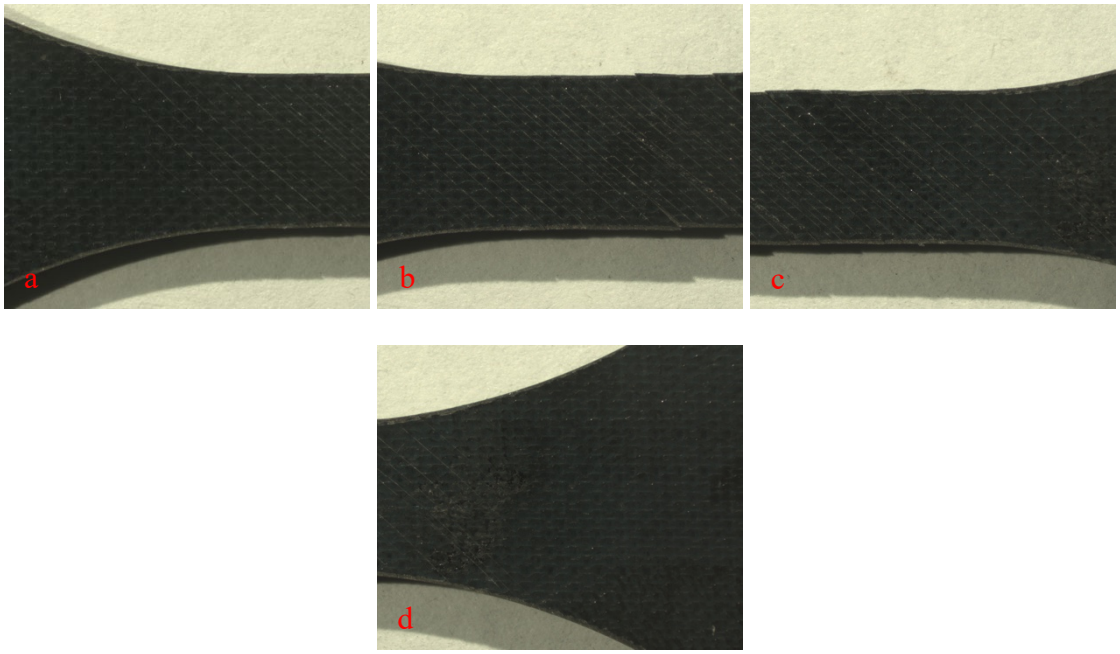

Figure 106: Images of the ±45 baseline composite specimen B-05-24 tested in tension-tension fatigue (σ_{max} = 105 MPa, N_f > 200,000 – fatigue runout), then failed in a tension test. (a-d) face view.

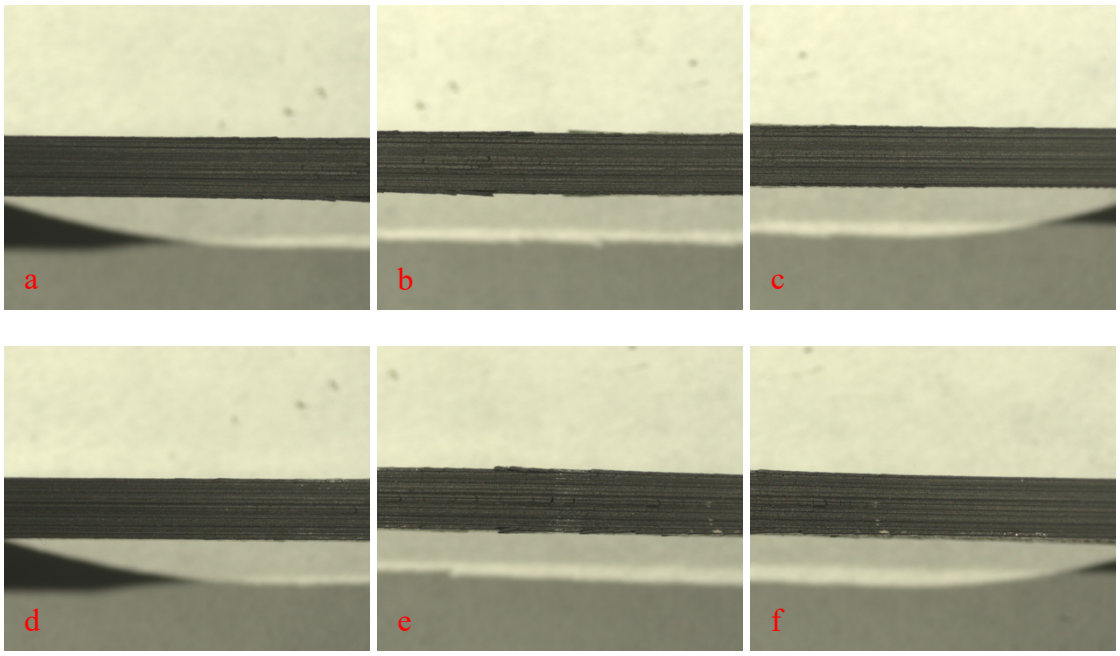

Figure 107: Images of the ±45 baseline composite specimen B-05-24 tested in tension-tension fatigue (σ_{max} = 105 MPa, N_f > 200,000 – fatigue runout), then failed in a tension test. (a-f) side view.

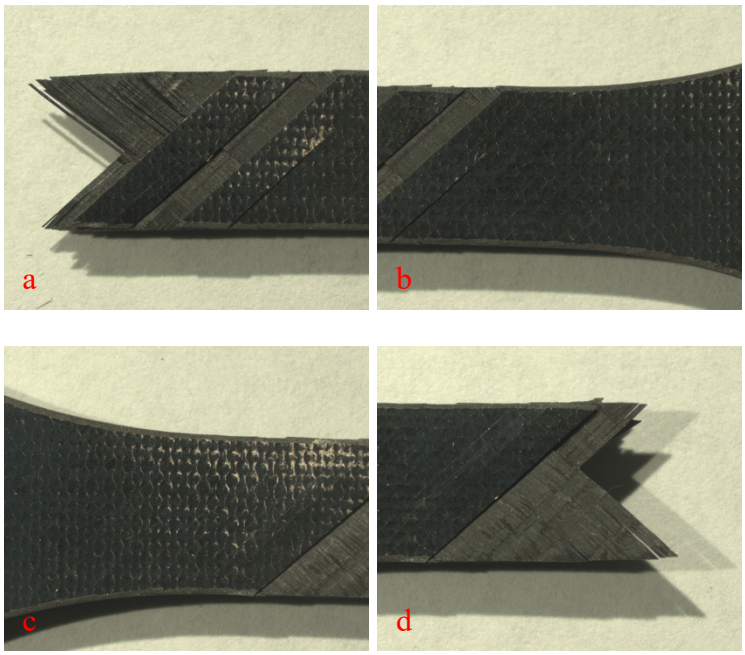

Figure 108: Images of the ±45 baseline composite specimen B-05-14 tested in tension-tension fatigue (σ_{max} = 181 MPa, N_f = 3,918). (a-d) face view.

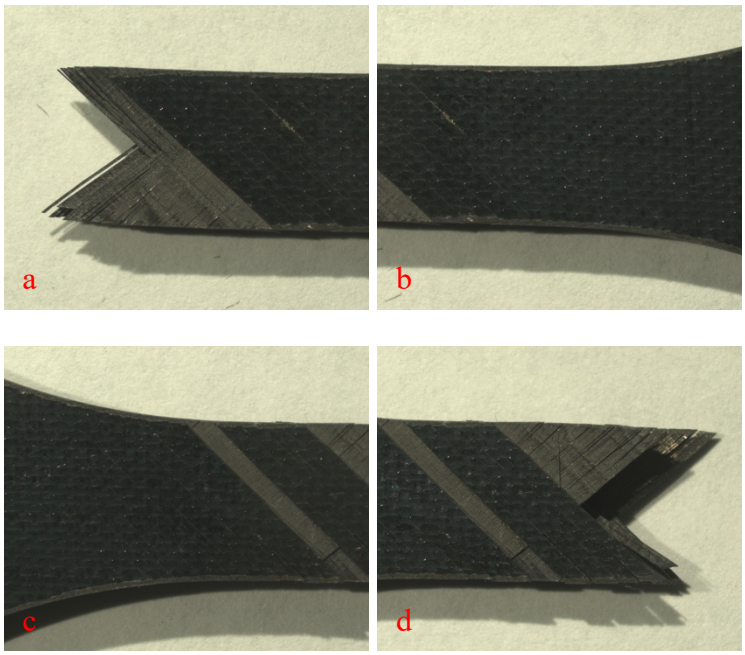

Figure 109: Images of the ±45 baseline composite specimen B-05-14 tested in tension-tension fatigue (σ_{max} = 181 MPa, N_f = 3,918). (a-d) face view.

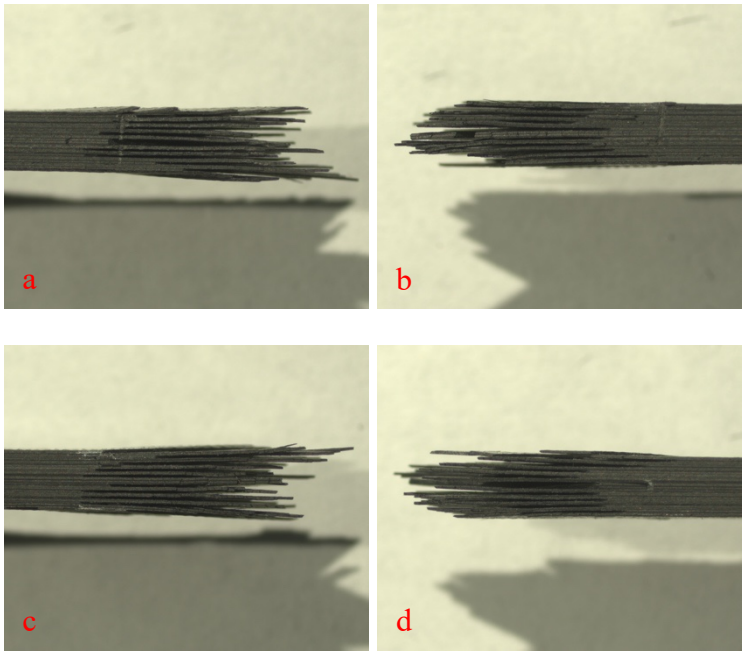

Figure 110: Images of the ±45 baseline composite specimen B-05-14 tested in tension-tension fatigue (σ_{max} = 181 MPa, N_f = 3,918). (a-d) side view.

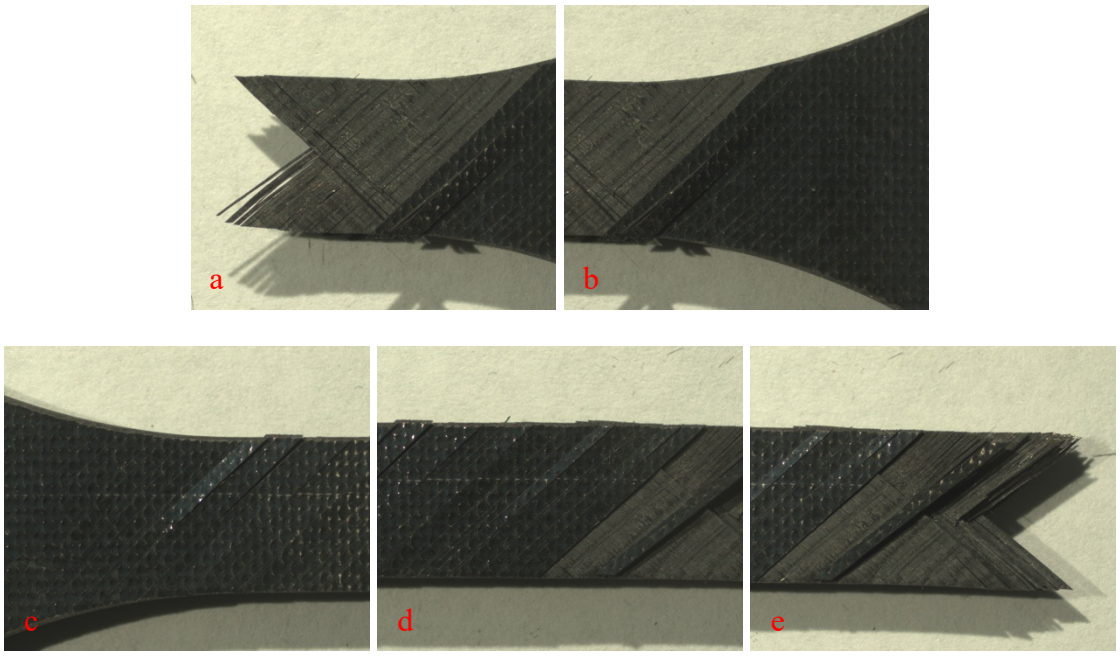

Figure 111: Images of the ±45 baseline composite specimen B-05-23 tested in tension-tension fatigue (σ_{max} = 206 MPa, N_f = 2,070). (a-e) face view.

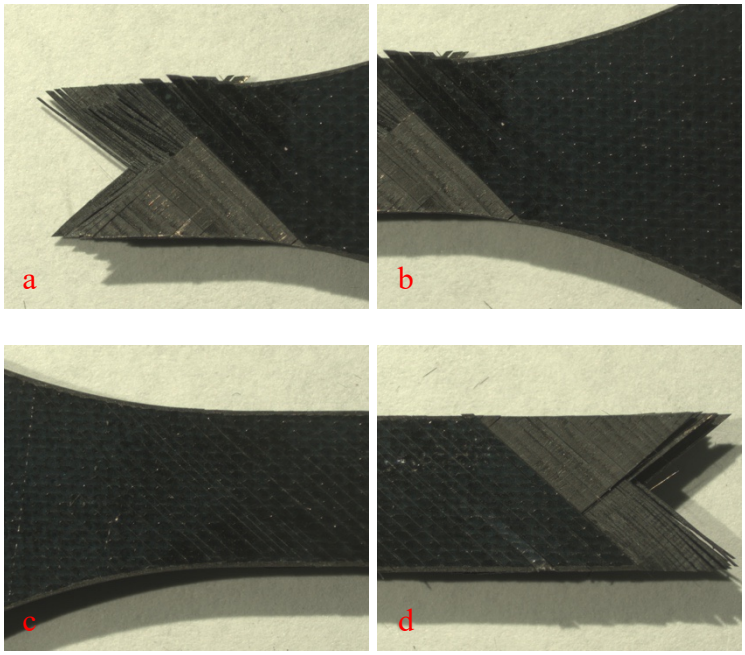

Figure 112: Images of the ±45 baseline composite specimen B-05-23 tested in tension-tension fatigue (σ_{max} = 206 MPa, N_f = 2,070). (a-d) face view.

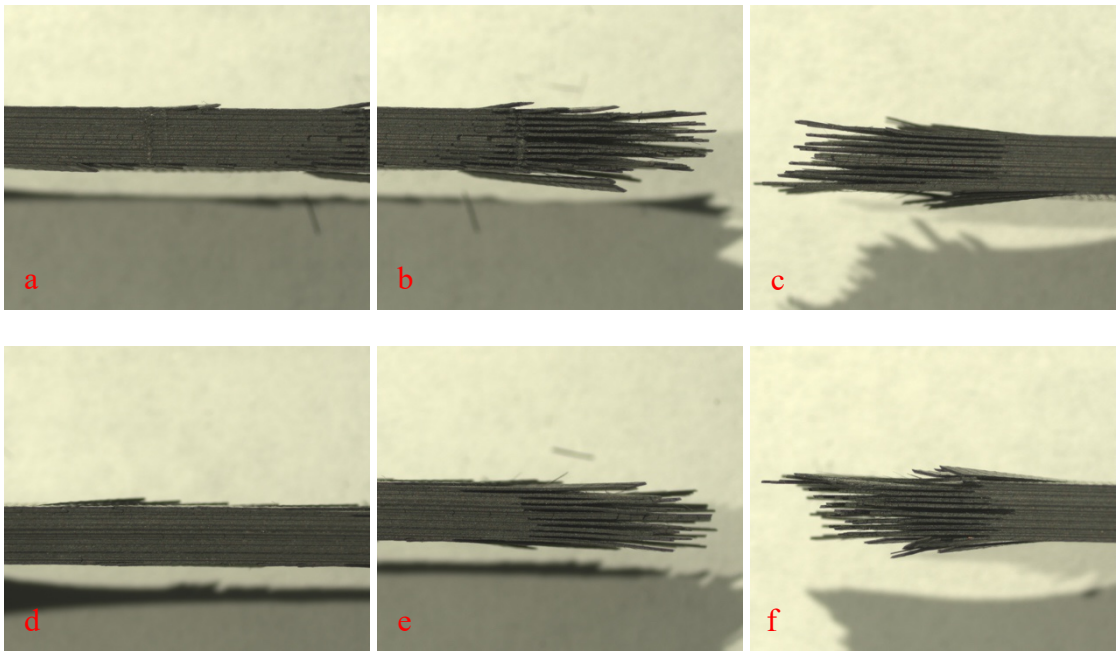

Figure 113: Images of the ±45 baseline composite specimen B-05-23 tested in tension-tension fatigue (σ_{max} = 206 MPa, N_f = 2,070). (a-f) side view.

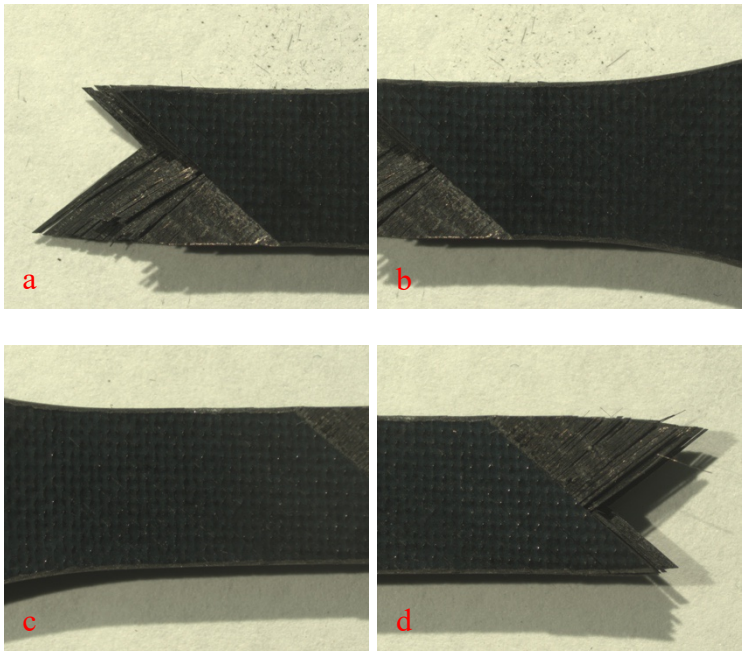

Figure 114: Images of the ±45 NanoStitch composite specimen NS-02-06 tested in tension-tension fatigue (σ_{max} = 137 MPa, N_f > 200,000 – fatigue runout), then failed in a tension test. (a-d) face view.

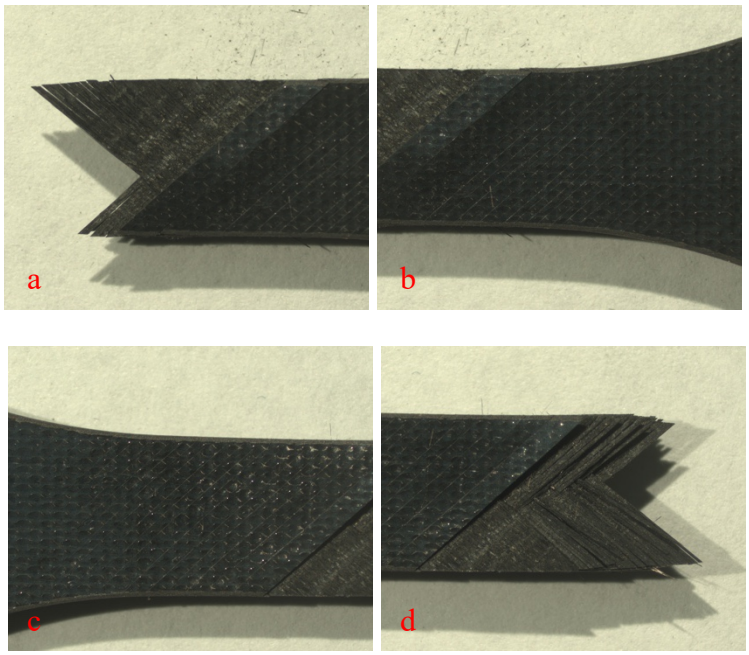

Figure 115: Images of the ±45 NanoStitch composite specimen NS-02-06 tested in tension-tension fatigue (σ_{max} = 137 MPa, N_f > 200,000 – fatigue runout), then failed in a tension test. (a-d) face view.

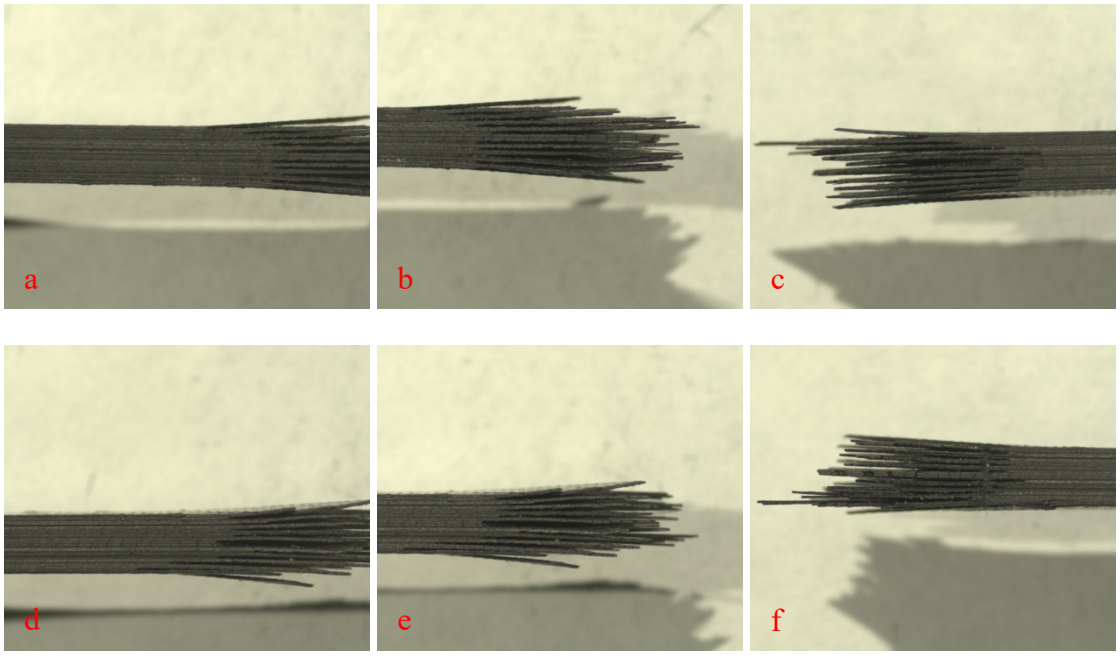

Figure 116: Images of the ±45 NanoStitch composite specimen NS-02-06 tested in tension-tension fatigue (σ_{max} = 137 MPa, N_f > 200,000 – fatigue runout), then failed in a tension test. (a-f) side view.

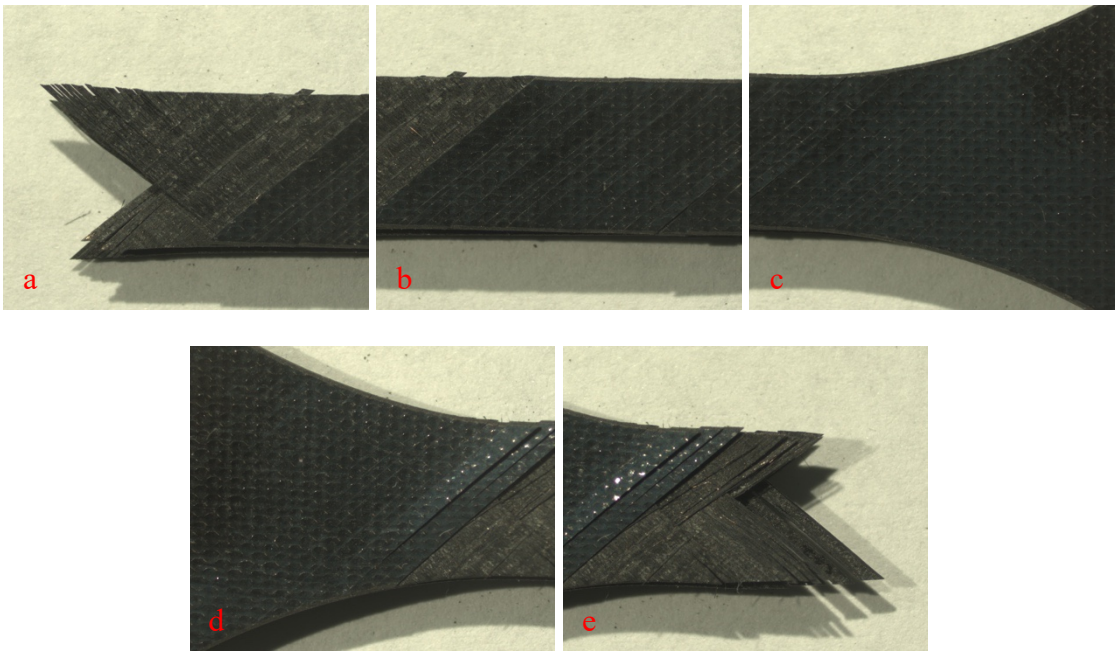

Figure 117: Images of the ±45 NanoStitch composite specimen NS-02-24 tested in tension-tension fatigue (σ_{max} = 187 MPa, N_f = 6,603). (a-e) face view.

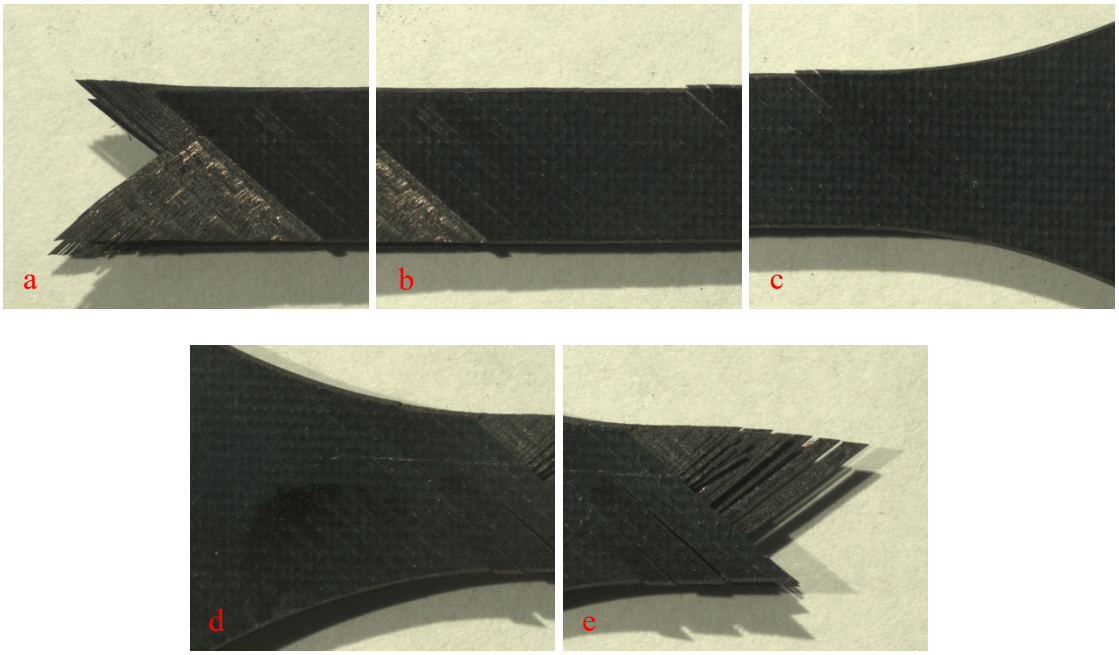

Figure 118: Images of the ±45 NanoStitch composite specimen NS-02-24 tested in tension-tension fatigue (σ_{max} = 187 MPa, N_f = 6,603). (a-e) face view.

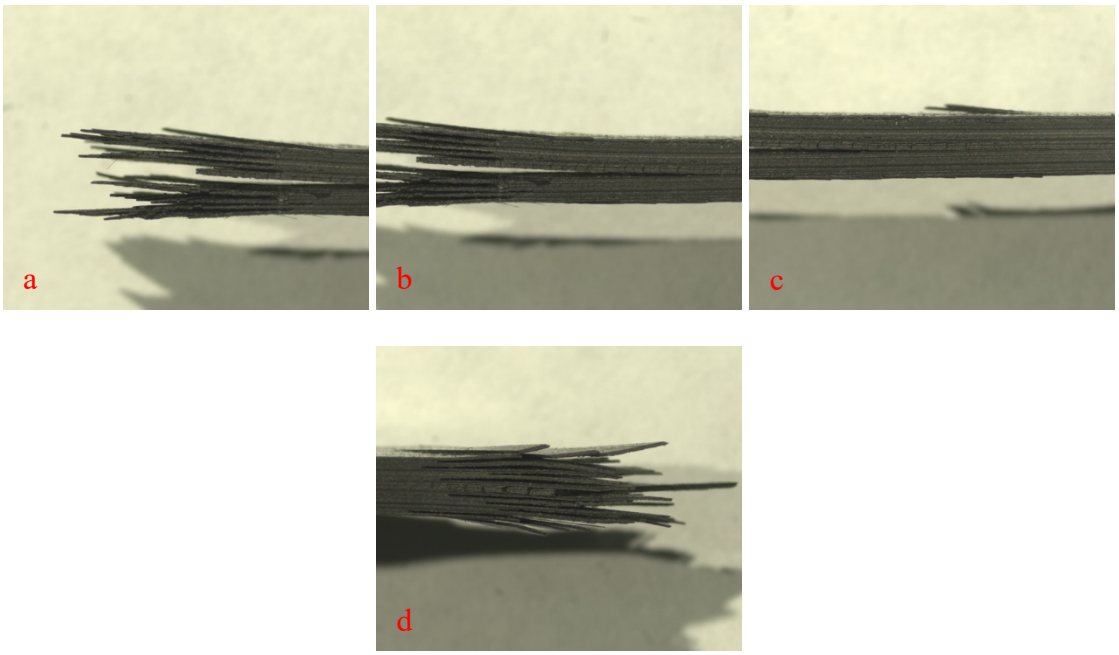

Figure 119: Images of the ±45 NanoStitch composite specimen NS-02-24 tested in tension-tension fatigue (σ_{max} = 187 MPa, N_f = 6,603). (a-d) side view.

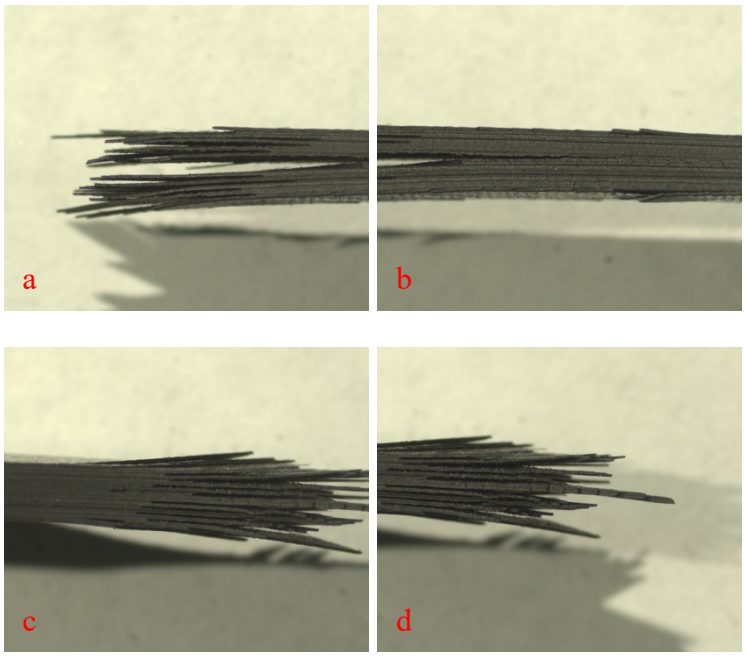

Figure 120: Images of the ±45 NanoStitch composite specimen NS-02-24 tested in tension-tension fatigue (σ_{max} = 187 MPa, N_f = 6,603). (a-d) side view.

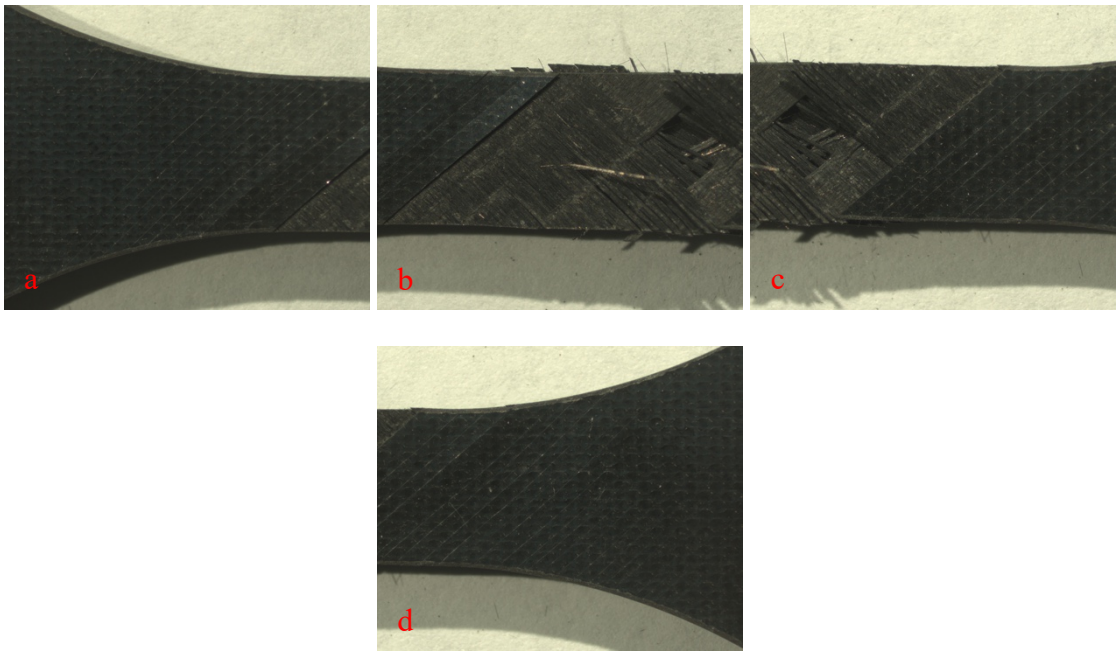

Figure 121: Images of the ±45 NanoStitch composite specimen NS-02-03 tested in tension-tension fatigue (σ_{max} = 137 MPa, N_f > 200,000 – fatigue runout), then failed in a tension test. (a-d) face view.

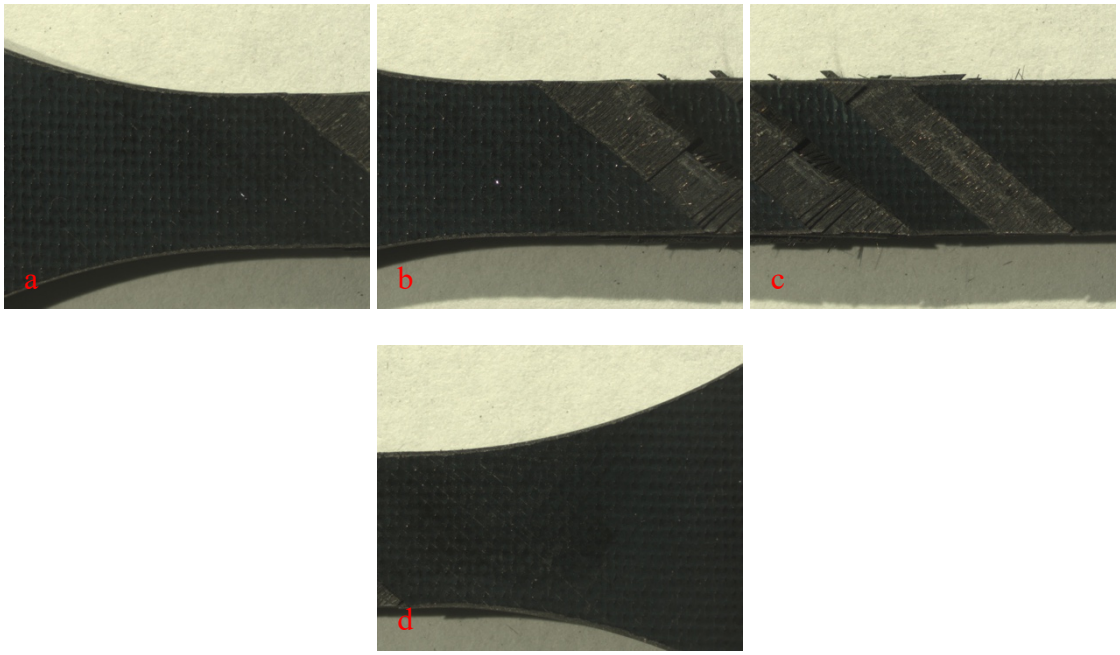

Figure 122: Images of the ±45 NanoStitch composite specimen NS-02-03 tested in tension-tension fatigue (σ_{max} = 137 MPa, N_f > 200,000 – fatigue runout), then failed in a tension test. (a-d) face view.

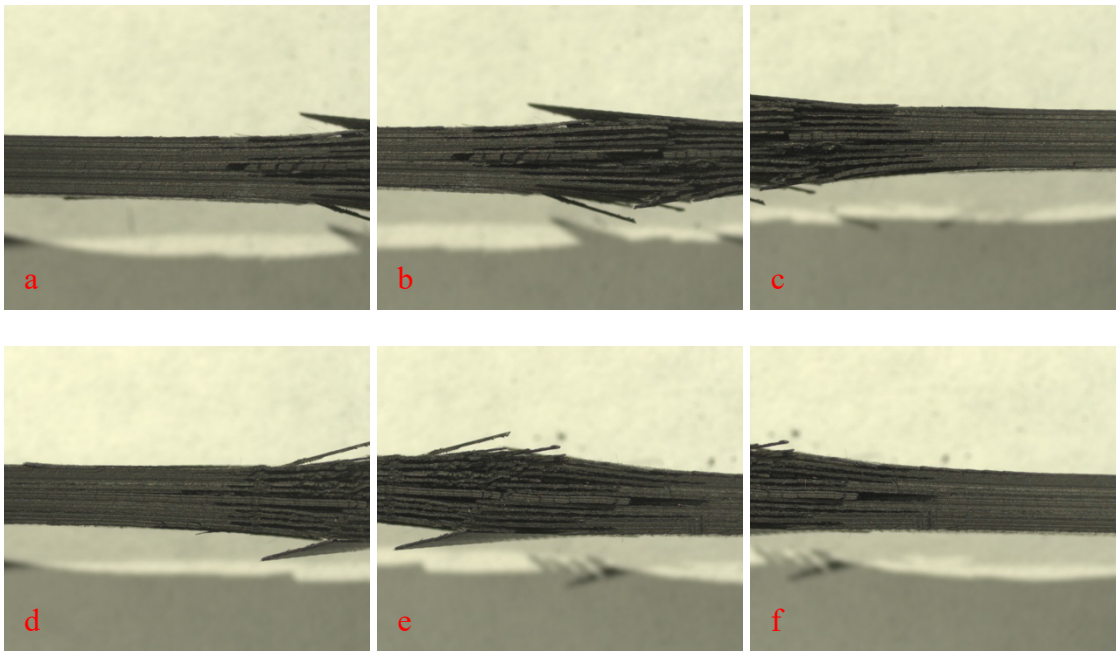

Figure 123: Images of the ±45 NanoStitch composite specimen NS-02-03 tested in tension-tension fatigue (σ_{max} = 137 MPa, N_f > 200,000 – fatigue runout), then failed in a tension test. (a-f) side view.

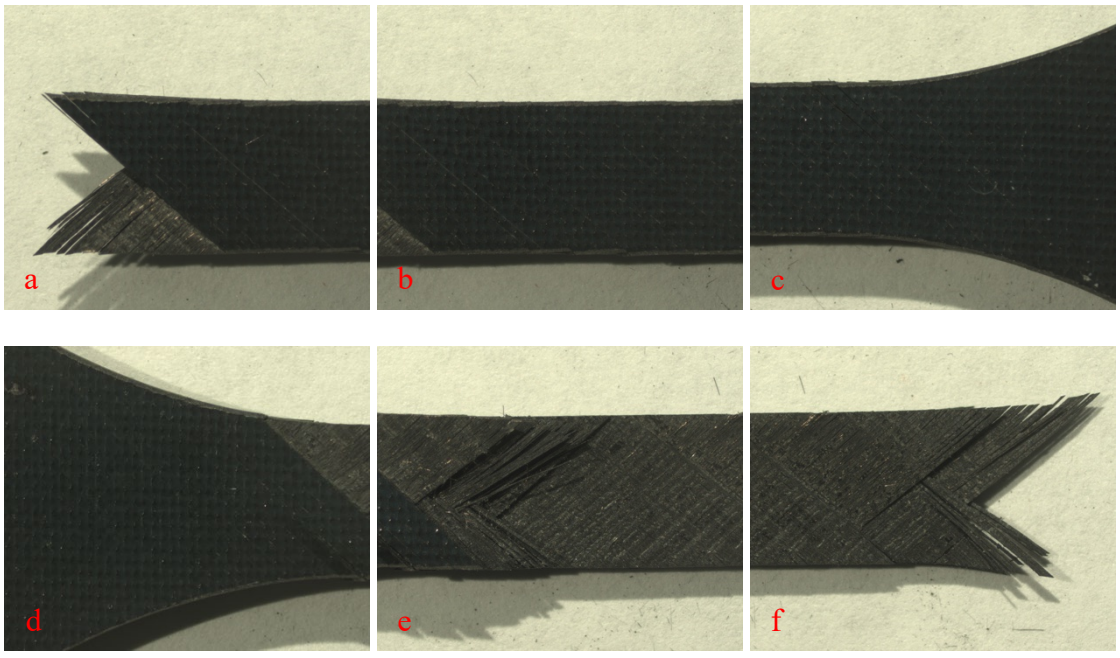

Figure 124: Images of the ±45 NanoStitch composite specimen NS-02-15 tested in tension-tension fatigue (σ_{max} = 207 MPa, N_f = 3,883). (a-f) face view.

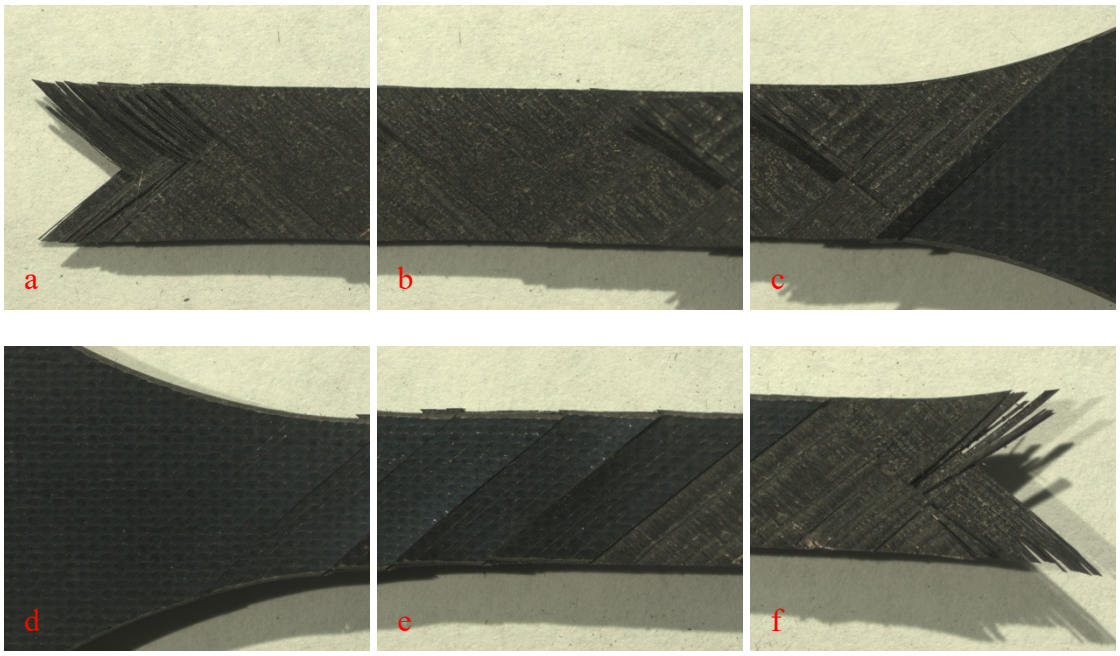

Figure 125: Images of the ±45 NanoStitch composite specimen NS-02-15 tested in tension-tension fatigue (σ_{max} = 207 MPa, N_f = 3,883). (a-f) face view.

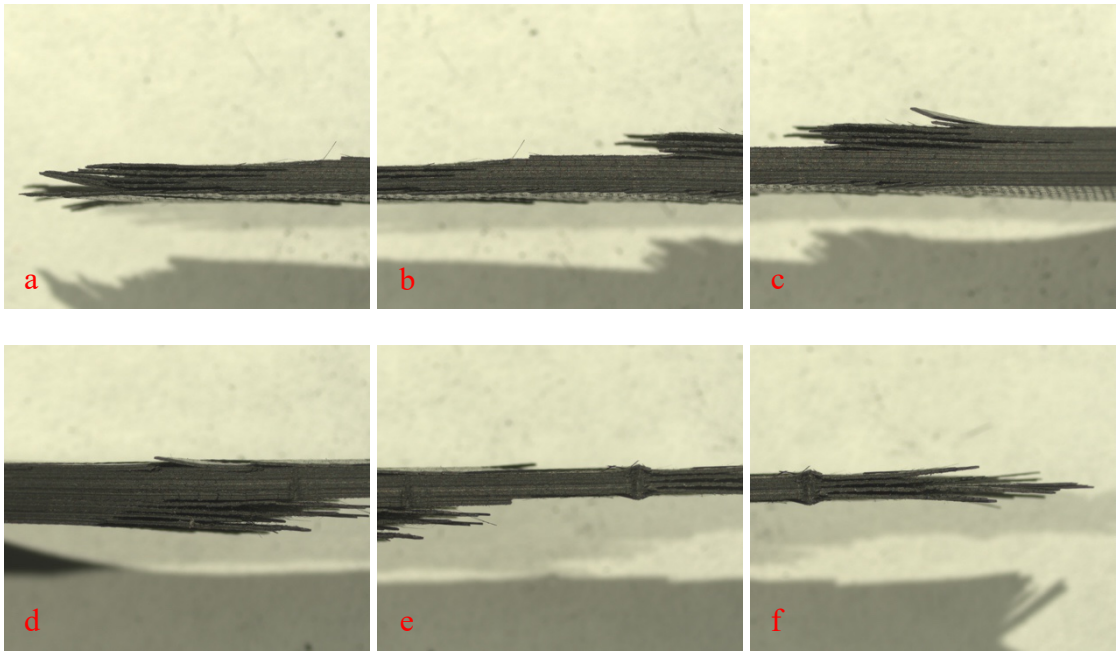

Figure 126: Images of the ±45 NanoStitch composite specimen NS-02-15 tested in tension-tension fatigue (σ_{max} = 207 MPa, N_f = 3,883). (a-f) side view.

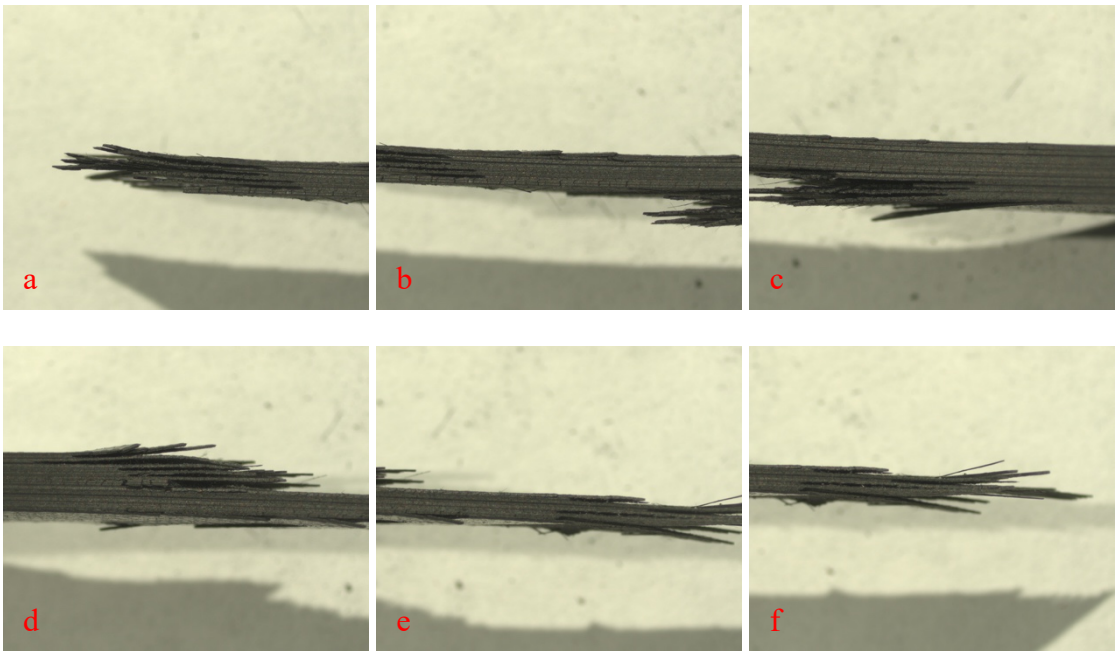

Figure 127: Images of the ±45 NanoStitch composite specimen NS-02-15 tested in tension-tension fatigue (σ_{max} = 207 MPa, N_f = 3,883). (a-f) side view.

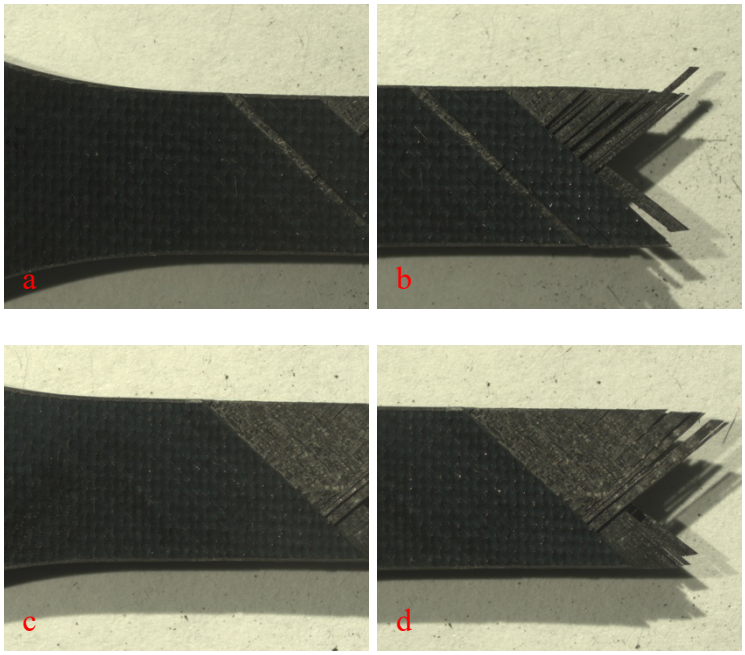

Figure 128: Images of the ±45 NanoStitch composite specimen NS-02-21 tested in tension-tension fatigue (σ_{max} = 164 MPa, N_f = 9,859). (a-d) face view.

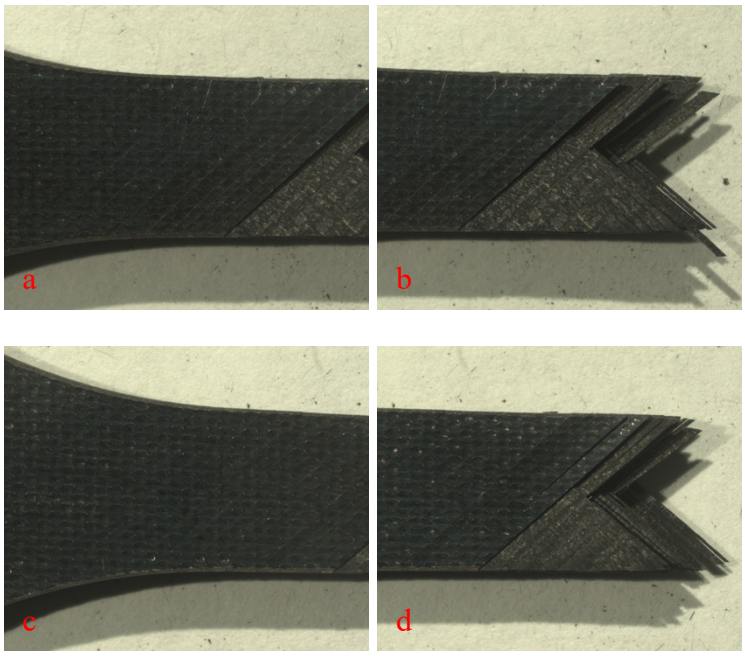

Figure 129: Images of the ±45 NanoStitch composite specimen NS-02-21 tested in tension-tension fatigue (σ_{max} = 164 MPa, N_f= 9,859). (a-d) face view.

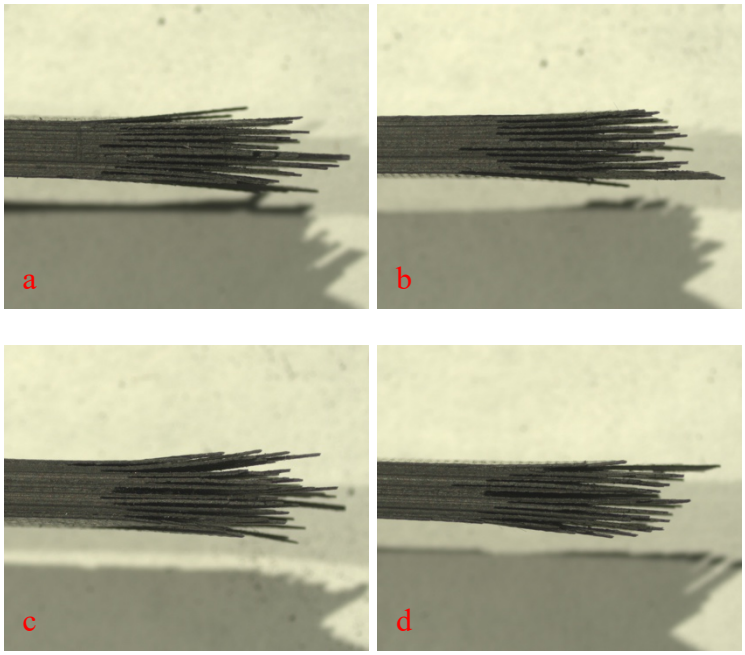

Figure 130: Images of the ±45 NanoStitch composite specimen NS-02-21 tested in tension-tension fatigue (σ_{max} = 164 MPa, N_f= 9,859). (a-d) side view.

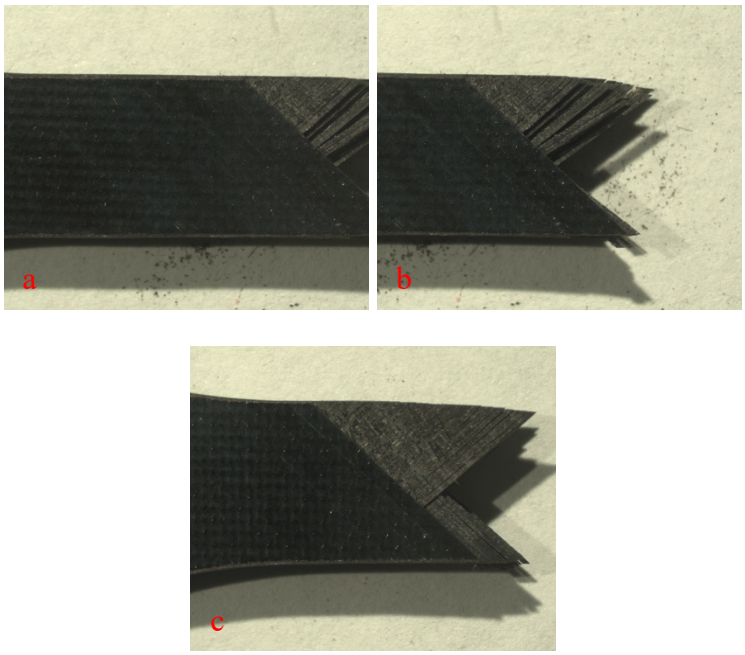

Figure 131: Images of the ±45 NanoStitch composite specimen NS-02-22 tested in tension-tension fatigue (σ_{max} = 151 MPa, N_f = 57,033). (a-c) face view.

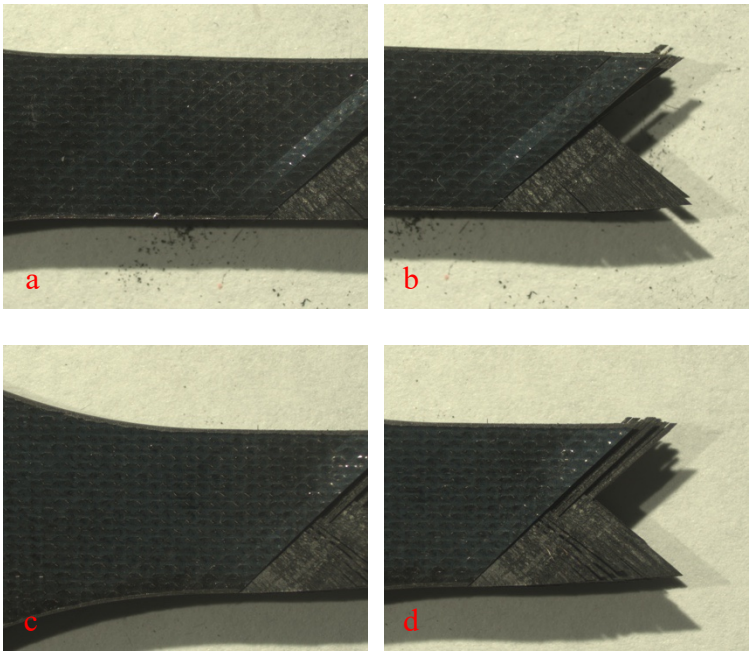

Figure 132: Images of the ±45 NanoStitch composite specimen NS-02-22 tested in tension-tension fatigue (σ_{max} = 151 MPa, N_f = 57,033). (a-d) face view.

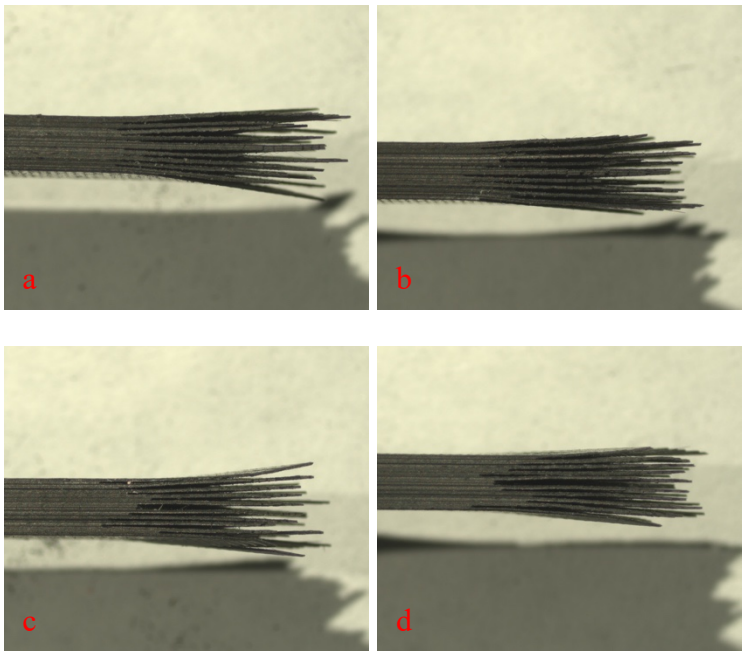

Figure 133: Images of the ±45 NanoStitch composite specimen NS-02-22 tested in tension-tension fatigue (σ_{max} = 151 MPa, N_f = 57,033). (a-d) side view.

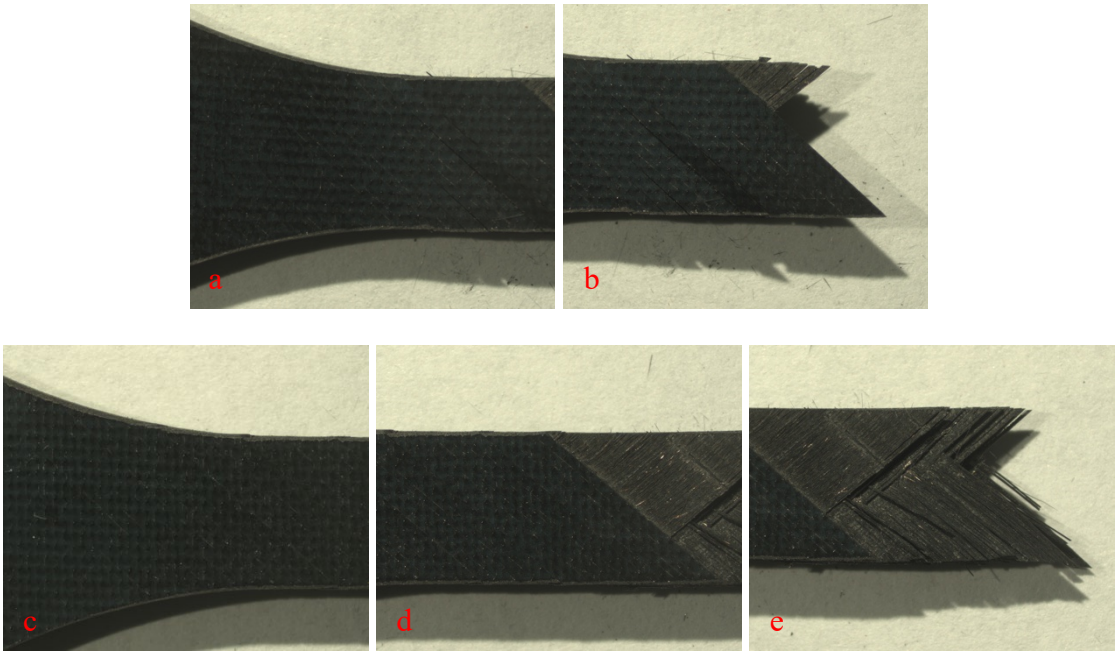

Figure 134: Images of the ±45 NanoStitch composite specimen NS-02-05 tested in tension-tension fatigue (σ_{max} = 213 MPa, N_f = 1,465). (a-e) face view.

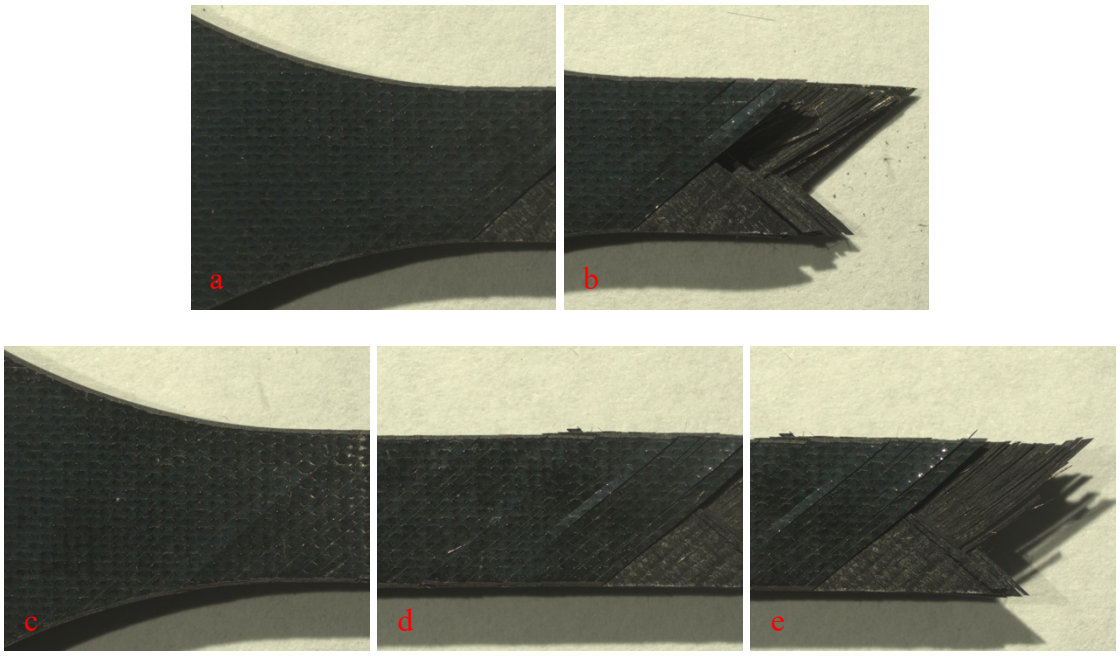

Figure 135: Images of the ±45 NanoStitch composite specimen NS-02-05 tested in tension-tension fatigue (σ_{max} = 213 MPa, N_f= 1,465). (a-e) face view.

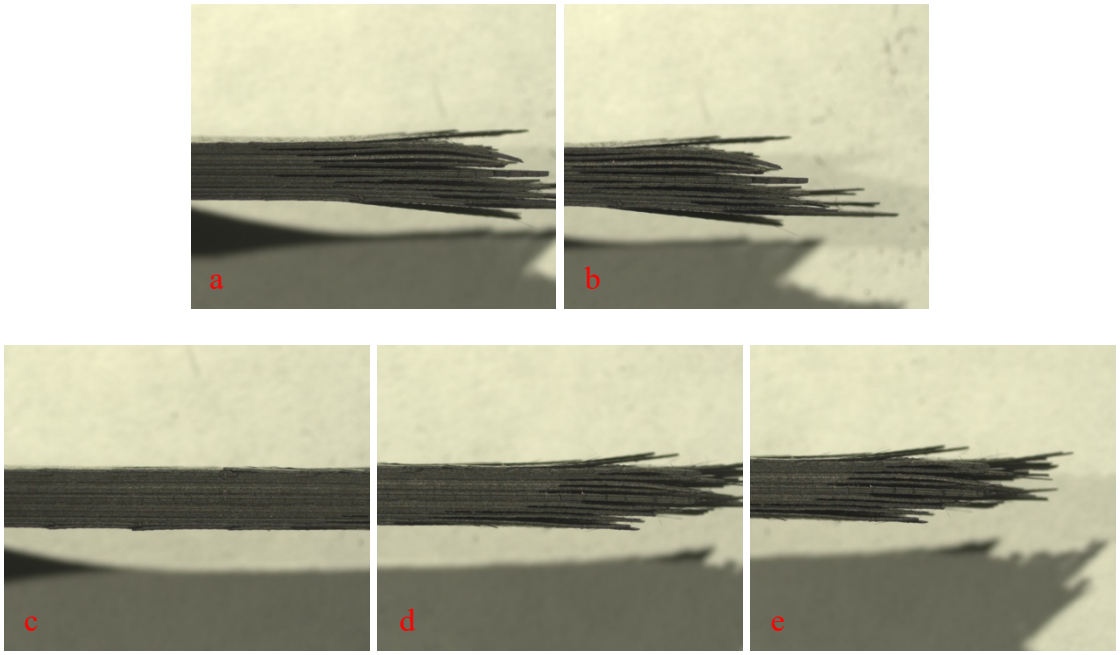

Figure 136: Images of the ±45 NanoStitch composite specimen NS-02-05 tested in tension-tension fatigue (σ_{max} = 213 MPa, N_f= 1,465). (a-e) side view.

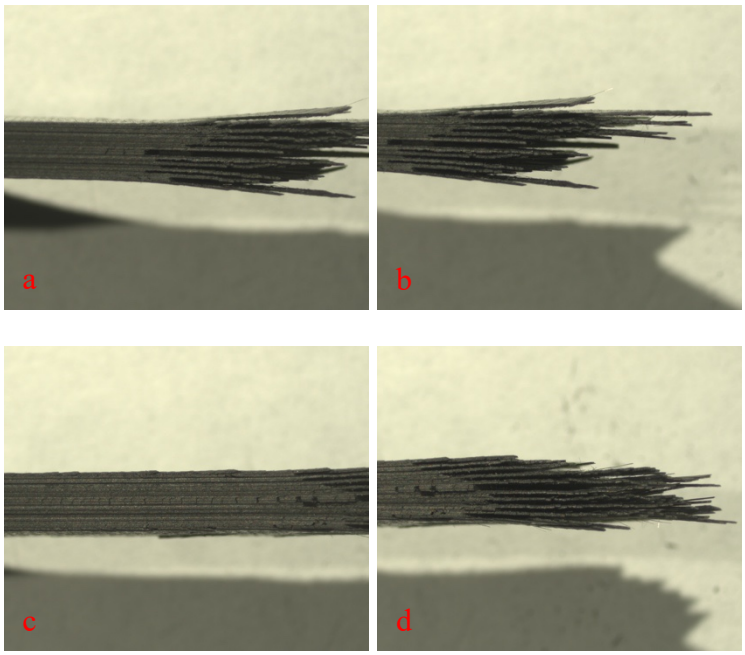

Figure 137: Images of the ±45 NanoStitch composite specimen NS-02-05 tested in tension-tension fatigue (σ_{max} = 213 MPa, N_f= 1,465). (a-d) side view.

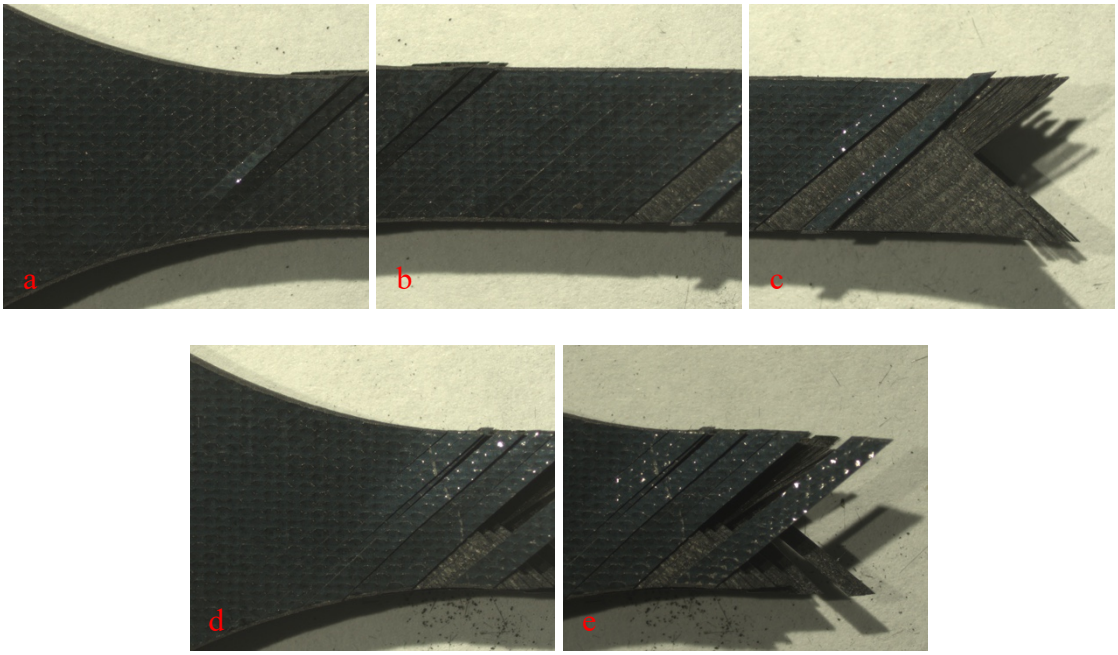

Figure 138: Images of the ±45 NanoStitch composite specimen NS-02-16 tested in tension-tension fatigue (σ_{max} = 189 MPa, N_f= 6,417). (a-e) face view.

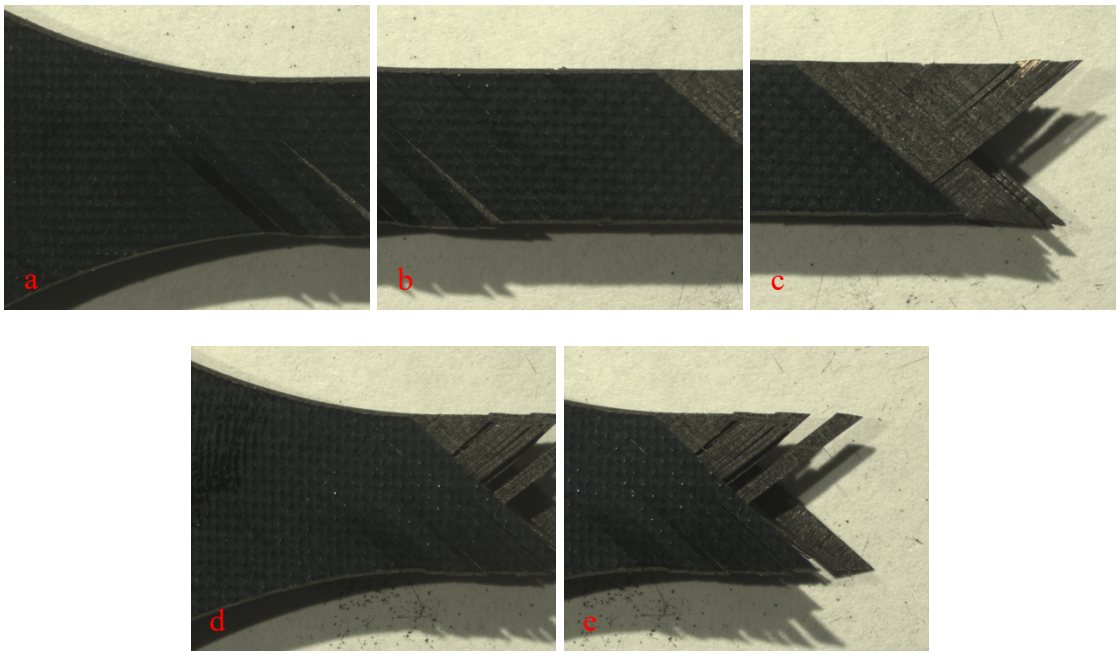

Figure 139: Images of the ±45 NanoStitch composite specimen NS-02-16 tested in tension-tension fatigue (σ_{max} = 189 MPa, N_f= 6,417). (a-e) face view.

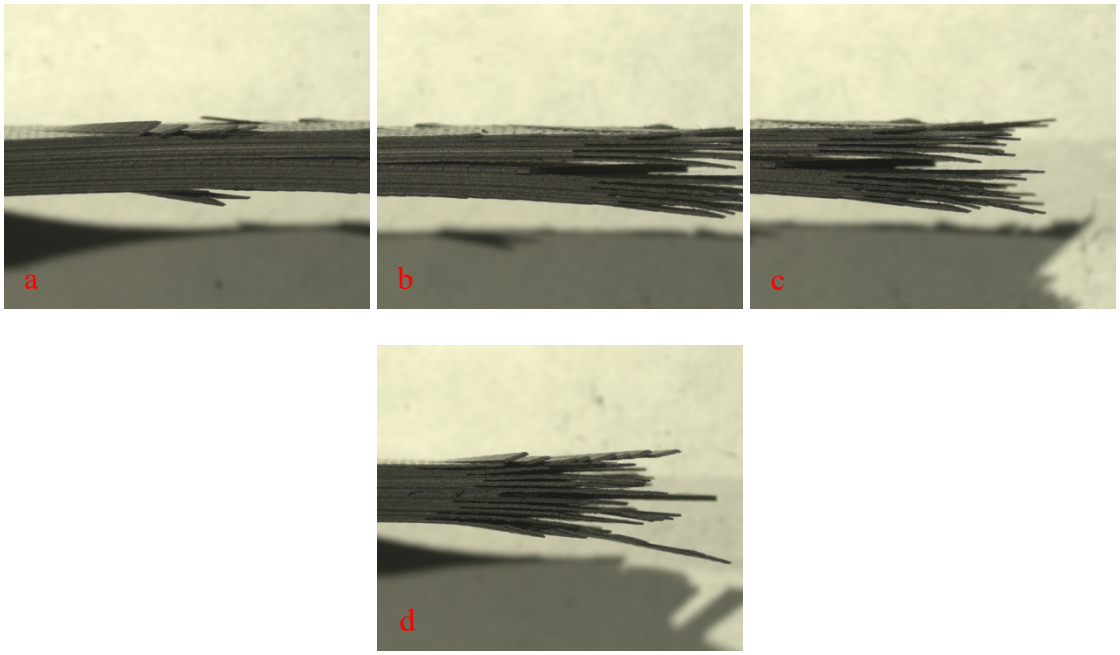

Figure 140: Images of the ±45 NanoStitch composite specimen NS-02-16 tested in tension-tension fatigue (σ_{max} = 189 MPa, N_f= 6,417). (a-d) side view.

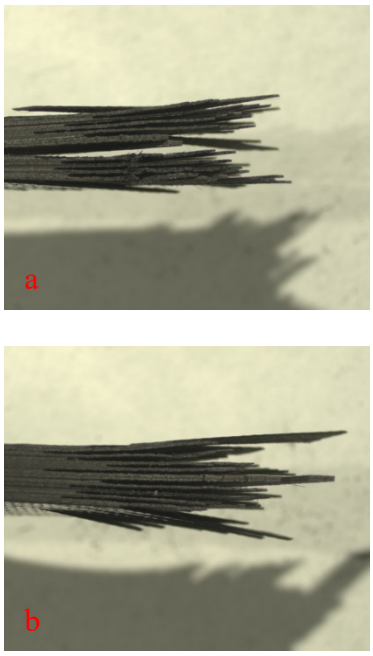

Figure 141: Images of the ±45 NanoStitch composite specimen NS-02-16 tested in tension-tension fatigue (σ_{max} = 189 MPa, N_f = 6,417). (a-b) side view.

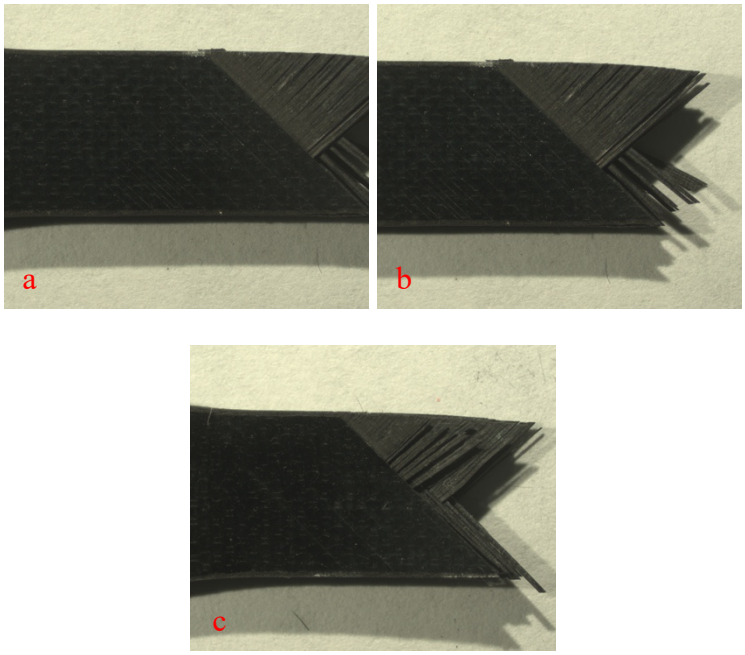

Figure 142: Images of the ±45 baseline composite specimen B-05-07 tested in tension-tension fatigue (σ_{max} = 164 MPa, N_f = 1). (a-c) face view.

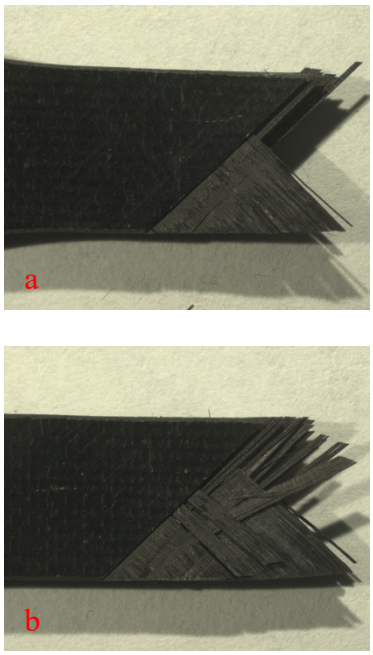

Figure 143: Images of the ±45 baseline composite specimen B-05-07 tested in tension-tension fatigue (σ_{max} = 164 MPa, N_f = 1). (a-b) face view.

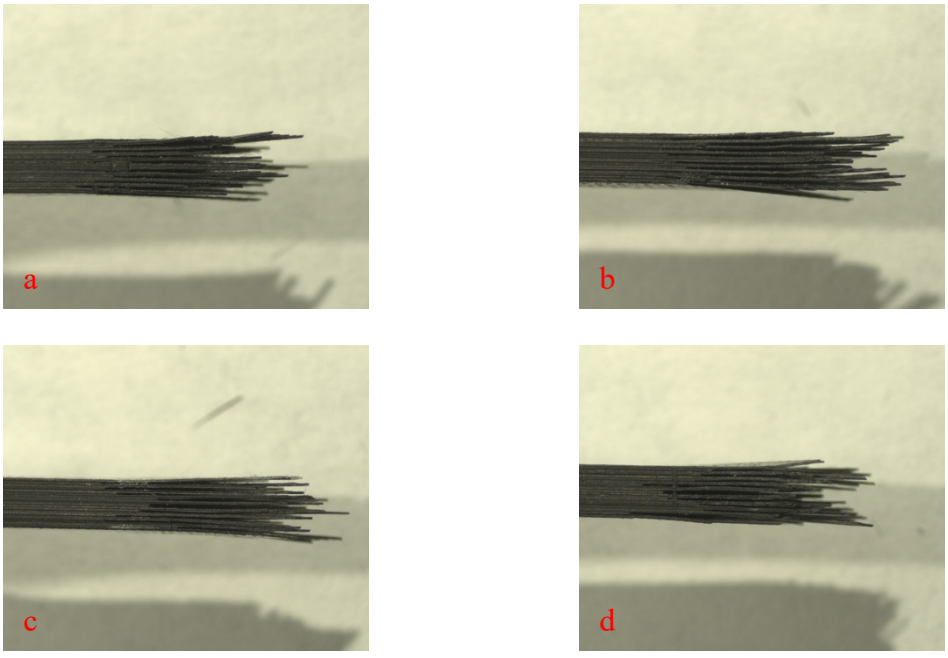

Figure 144: Images of the ±45 baseline composite specimen B-05-07 tested in tension-tension fatigue (σ_{max} = 164 MPa, N_f = 1). (a-d) side view.

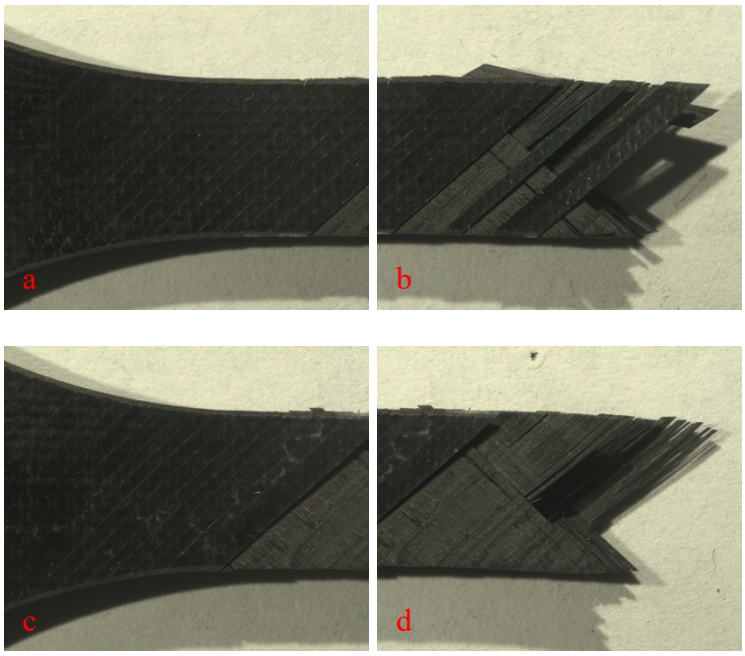

Figure 145: Images of the ±45 baseline composite specimen B-05-12 tested in tension-tension fatigue (σ_{max} = 180 MPa, N_f= 138). (a-d) face view.

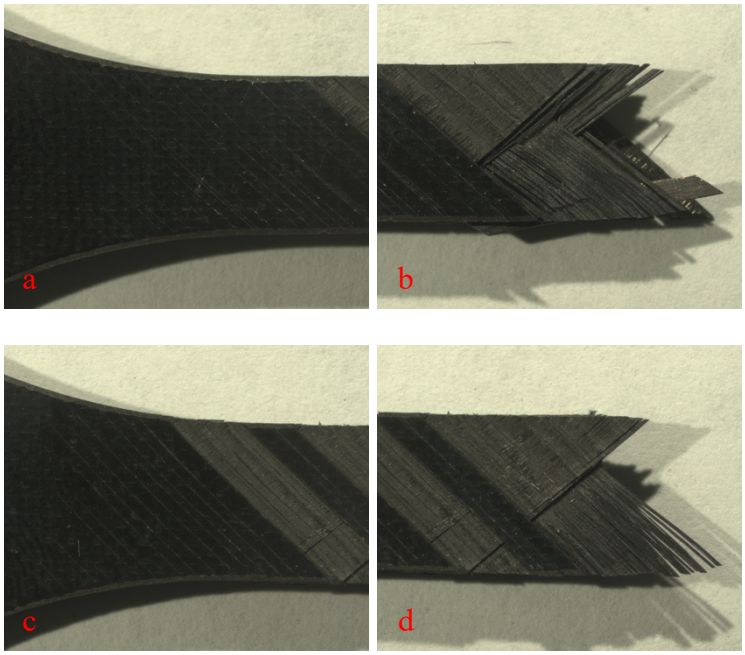

Figure 146: Images of the ±45 baseline composite specimen B-05-12 tested in tension-tension fatigue (σ_{max} = 180 MPa, N_f= 138). (a-d) face view.

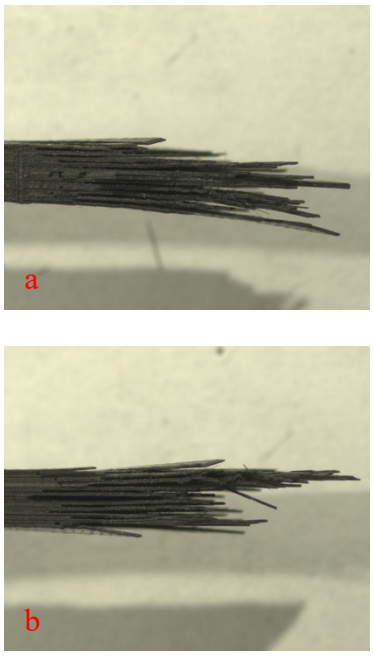

Figure 147: Images of the ±45 baseline composite specimen B-05-12 tested in tension-tension fatigue (σ_{max} = 180 MPa, N_f= 138). (a-b) side view.

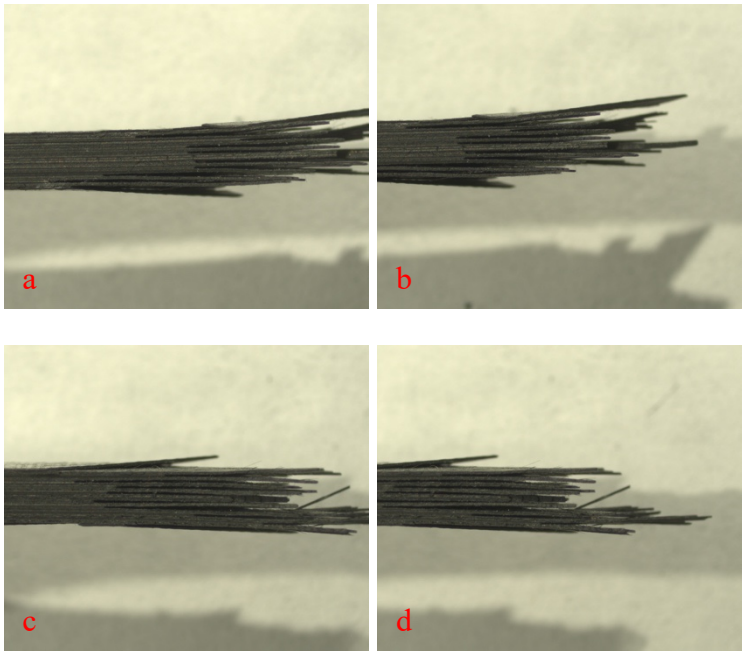

Figure 148: Images of the ±45 baseline composite specimen B-05-12 tested in tension-tension fatigue (σ_{max} = 180 MPa, N_f= 138). (a-d) side view.

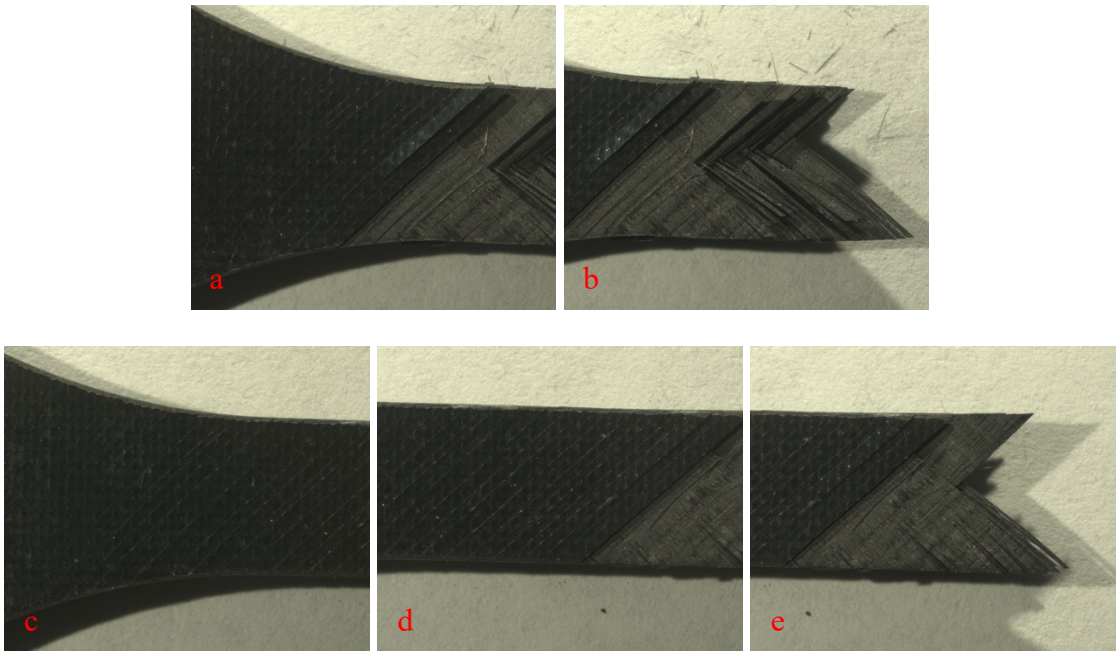

Figure 149: Images of the ±45 baseline composite specimen B-05-17 tested in tension-tension fatigue (σ_{max} = 155 MPa, N_f = 11,354). (a-e) face view.

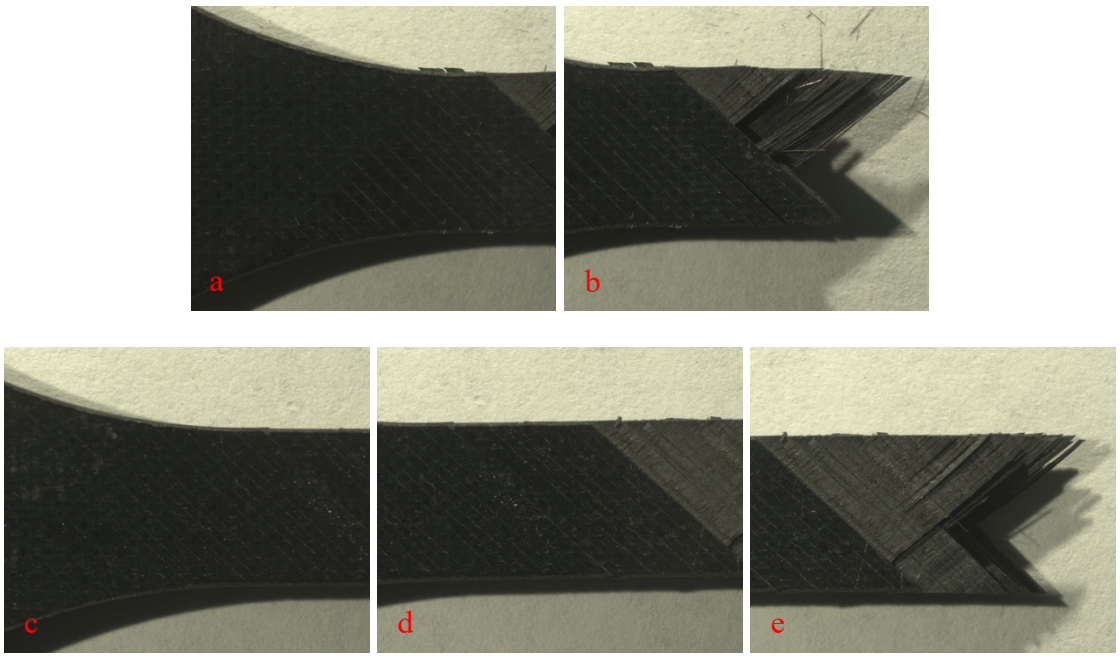

Figure 150: Images of the ±45 baseline composite specimen B-05-17 tested in tension-tension fatigue (σ_{max} = 155 MPa, N_f = 11,354). (a-e) face view.

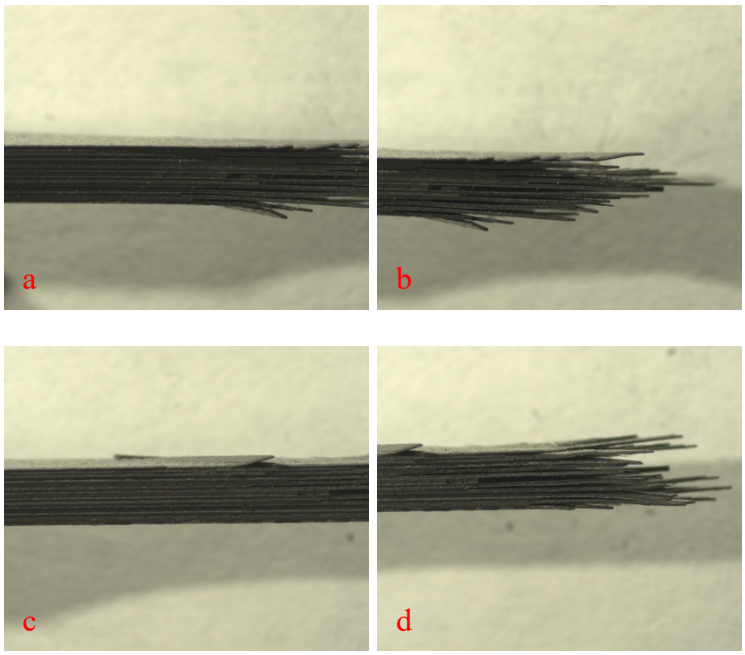

Figure 151: Images of the ±45 baseline composite specimen B-05-17 tested in tension-tension fatigue (σ_{max} = 155 MPa, N_f = 11,354). (a-d) side view.

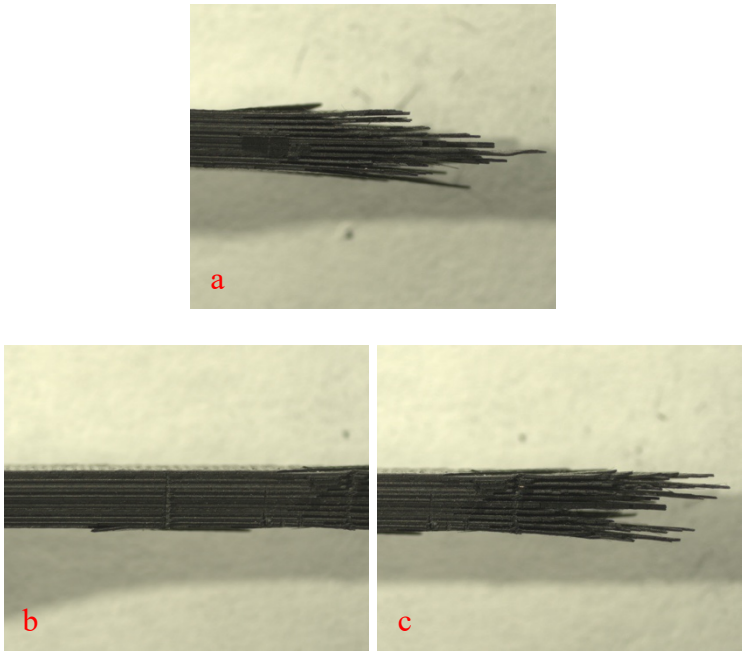

Figure 152: Images of the ±45 baseline composite specimen B-05-17 tested in tension-tension fatigue (σ_{max} = 155 MPa, N_f = 11,354). (a-c) side view.

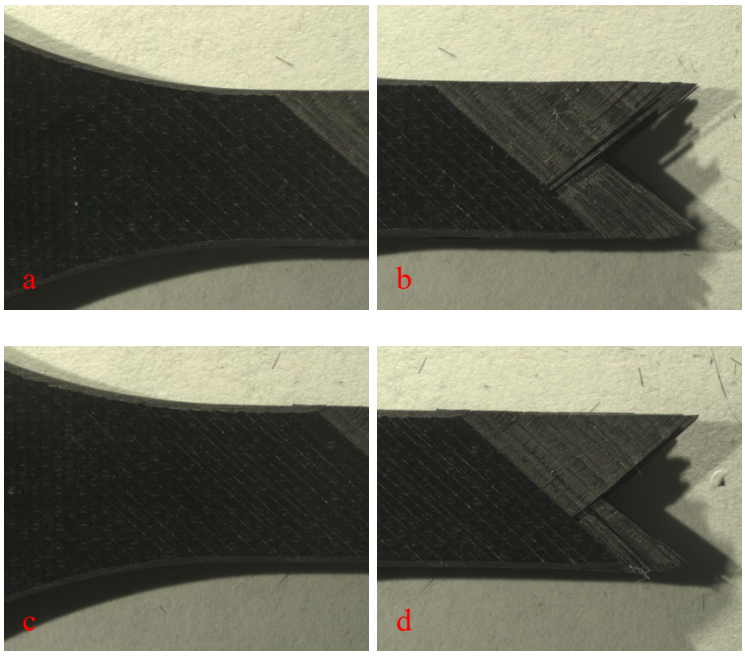

Figure 153: Images of the ±45 baseline composite specimen B-05-11 tested in tension-tension fatigue (σ_{max} = 177 MPa, N_f = 311). (a-d) face view.

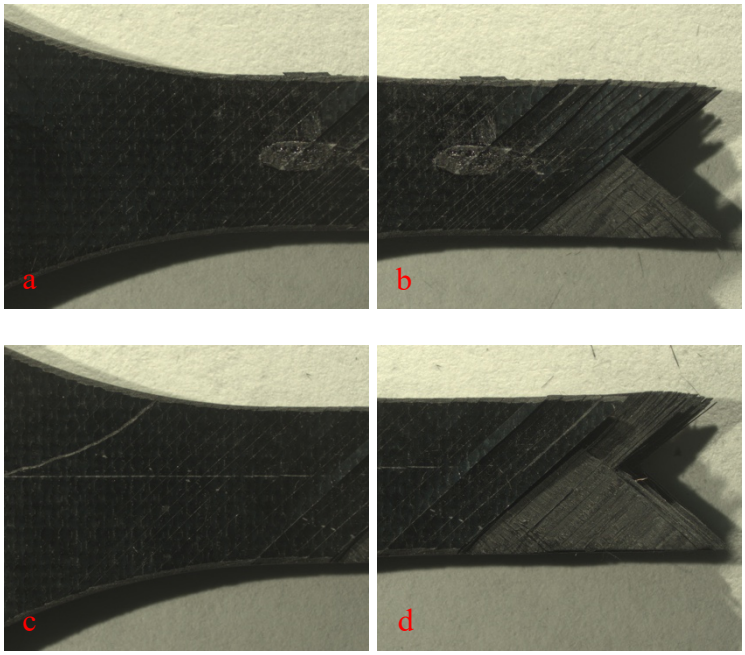

Figure 154: Images of the ±45 baseline composite specimen B-05-11 tested in tension-tension fatigue (σ_{max} = 177 MPa, N_f = 311). (a-d) face view.

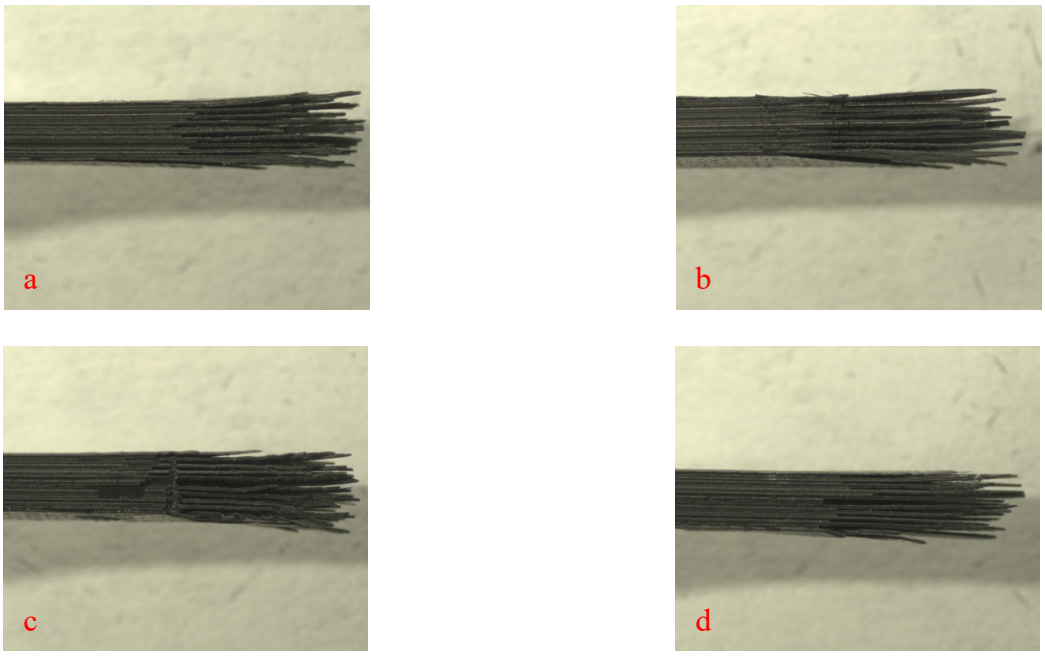

Figure 155: Images of the ±45 baseline composite specimen B-05-11 tested in tension-tension fatigue (σ_{max} = 177 MPa, N_f = 311). (a-d) side view.

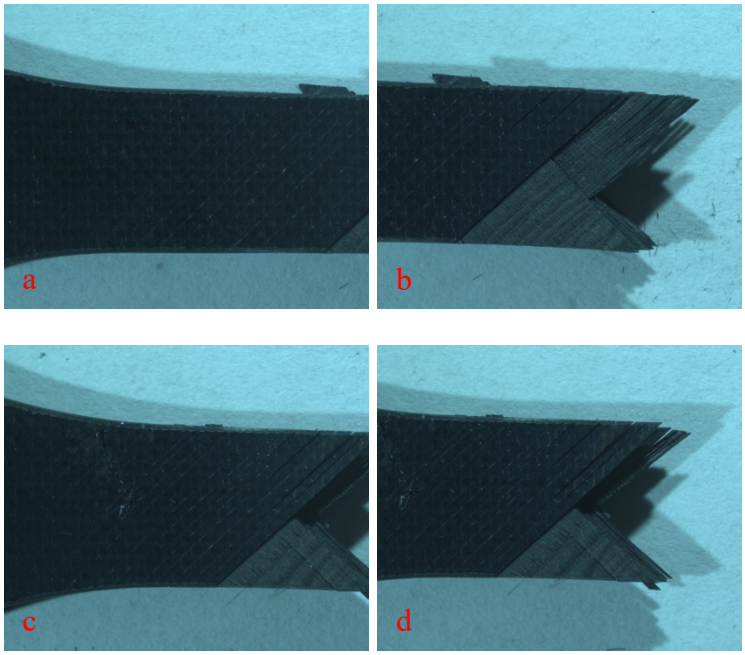

Figure 156: Images of the ±45 baseline composite specimen B-05-25 tested in tension-tension fatigue (σ_{max} = 144 MPa, N_f = 1,237). (a-d) face view.

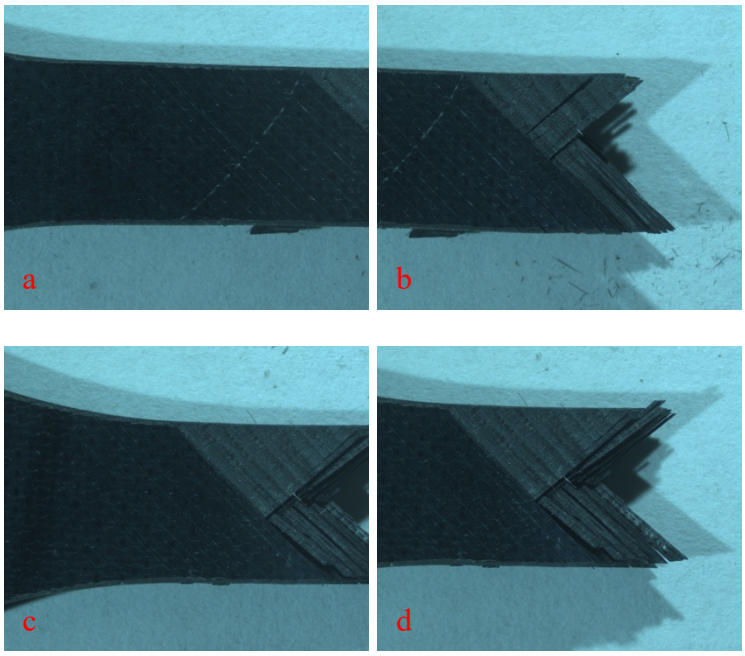

Figure 157: Images of the ±45 baseline composite specimen B-05-25 tested in tension-tension fatigue (σ_{max} = 144 MPa, N_f = 1,237). (a-d) face view.

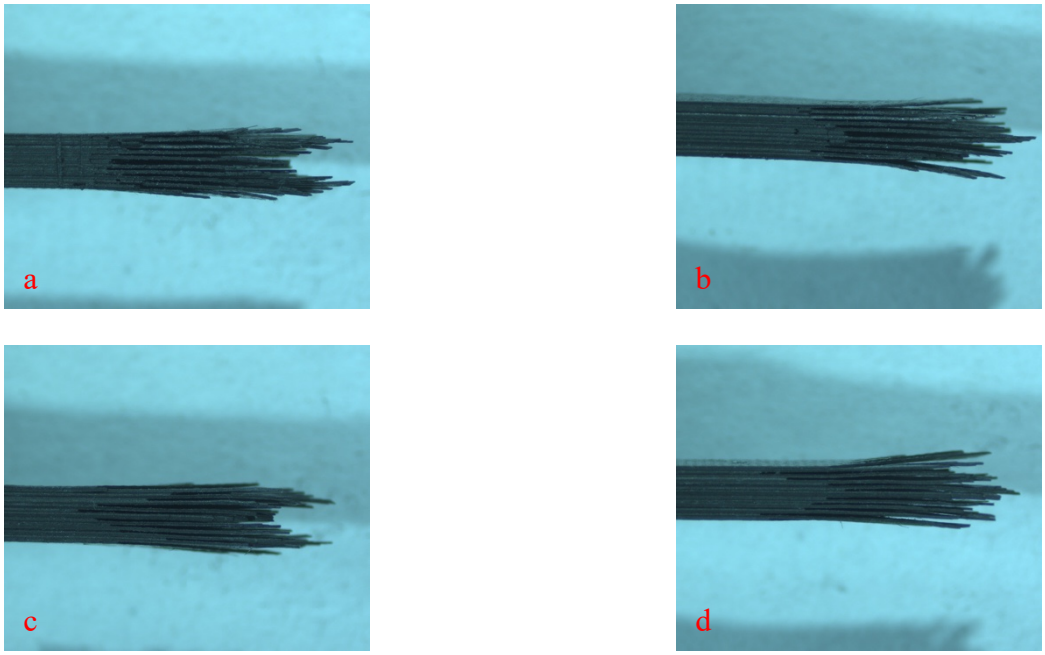

Figure 158: Images of the ±45 baseline composite specimen B-05-25 tested in tension-tension fatigue (σ_{max} = 144 MPa, N_f = 1,237). (a-d) side view.

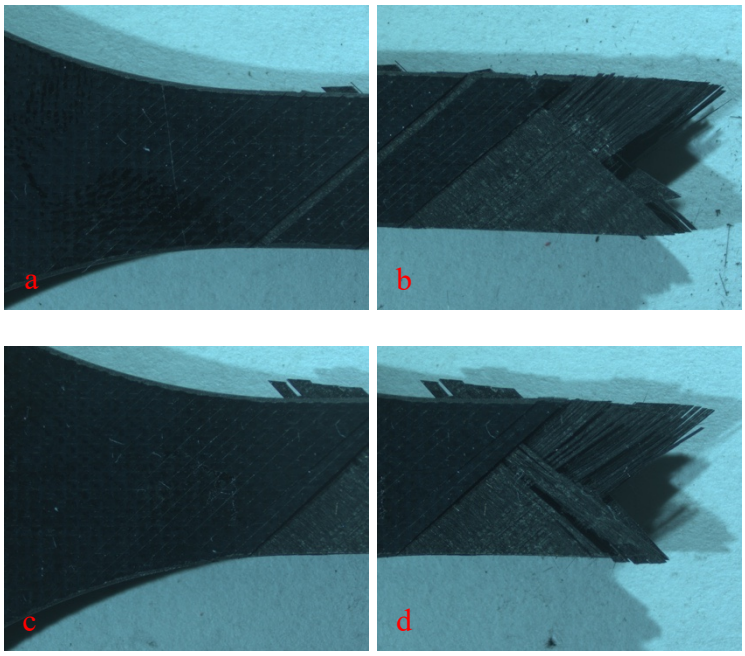

Figure 159: Images of the ±45 NanoStitch composite specimen NS-02-01 tested in tension-tension fatigue (σ_{max} = 212 MPa, N_f = 5). (a-d) face view.

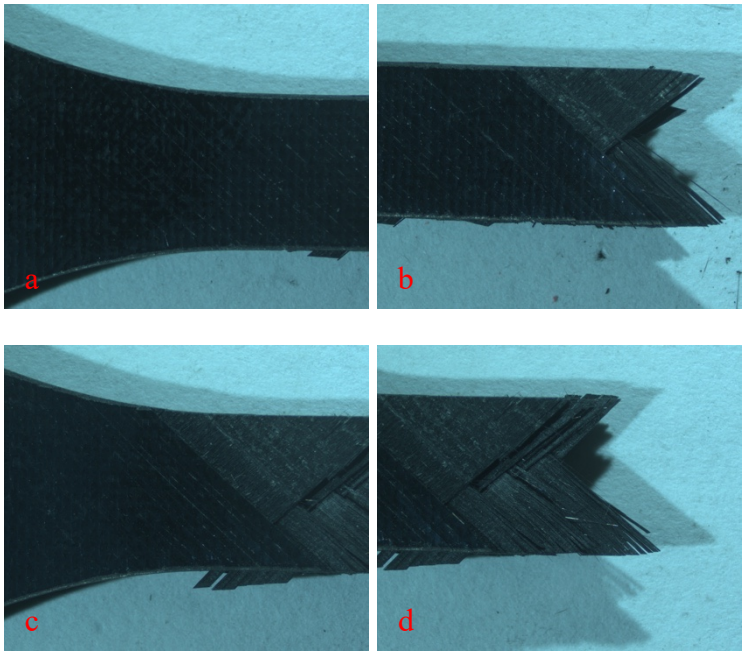

Figure 160: Images of the ±45 NanoStitch composite specimen NS-02-01 tested in tension-tension fatigue (σ_{max} = 212 MPa, N_f = 5). (a-d) face view.

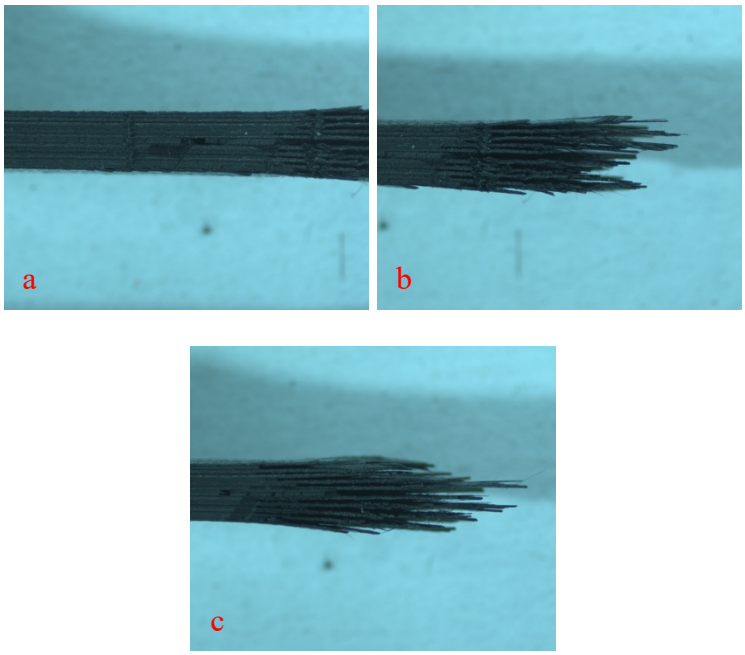

Figure 161: Images of the ±45 NanoStitch composite specimen NS-02-01 tested in tension-tension fatigue (σ_{max} = 212 MPa, N_f = 5). (a-c) side view.

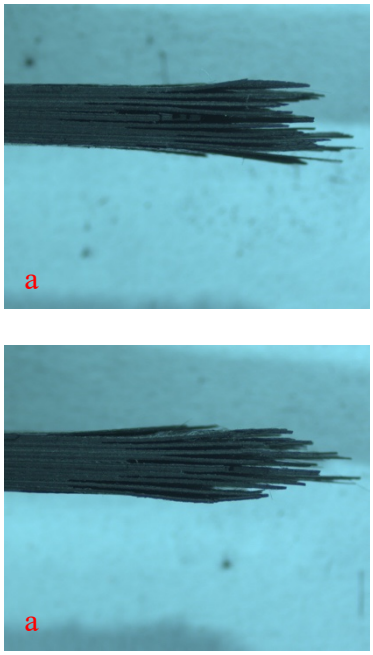

Figure 162: Images of the ±45 NanoStitch composite specimen NS-02-01 tested in tension-tension fatigue (σ_{max} = 212 MPa, N_f = 5). (a-b) side view.

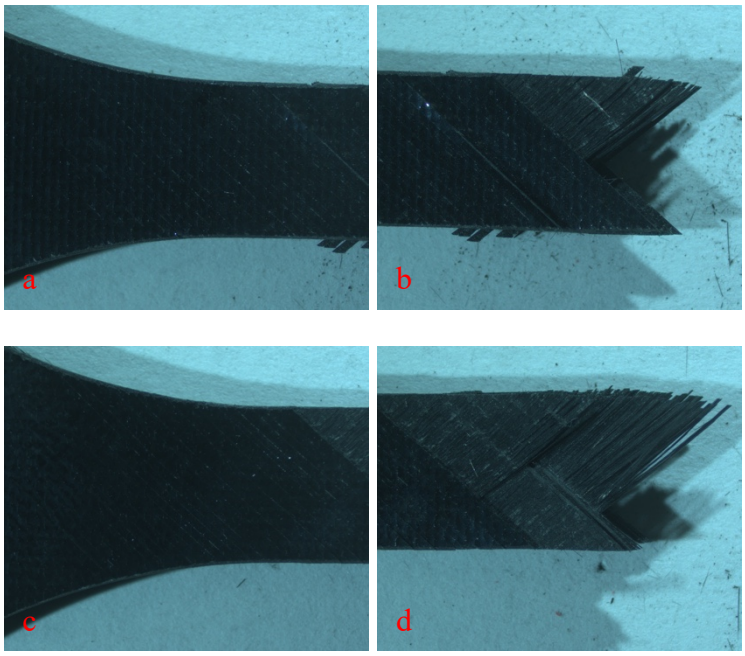

Figure 163: Images of the ±45 NanoStitch composite specimen NS-02-26 tested in tension-tension fatigue (σ_{max} = 209 MPa, N_f = 7). (a-d) face view.

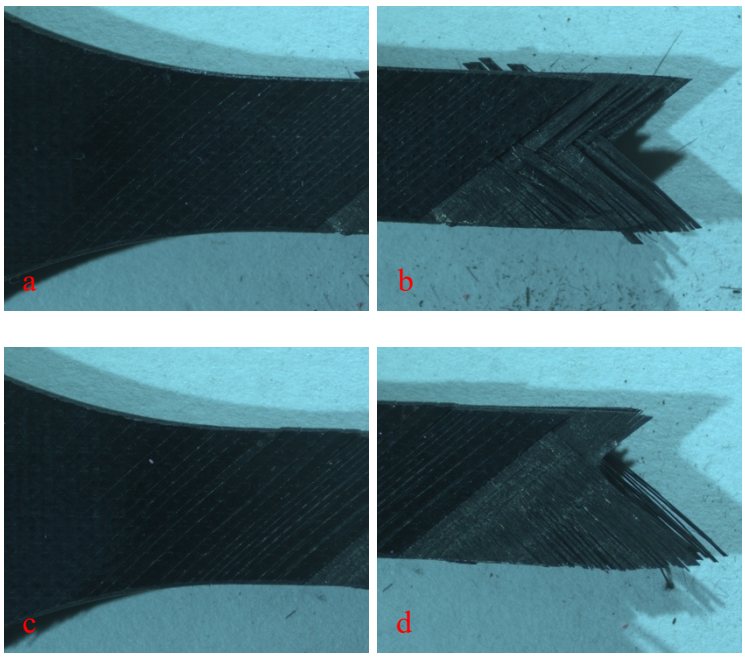

Figure 164: Images of the ±45 NanoStitch composite specimen NS-02-26 tested in tension-tension fatigue (σ_{max} = 209 MPa, N_f = 7). (a-d) face view.

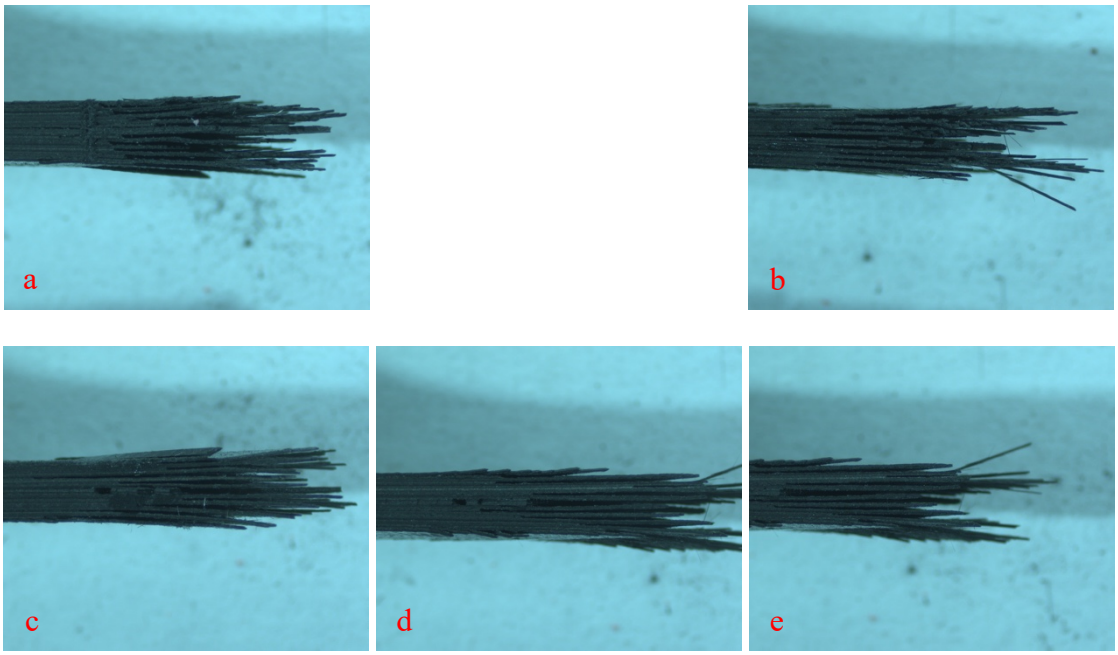

Figure 165: Images of the ±45 NanoStitch composite specimen NS-02-26 tested in tension-tension fatigue (σ_{max} = 209 MPa, N_f = 7). (a-e) side view.

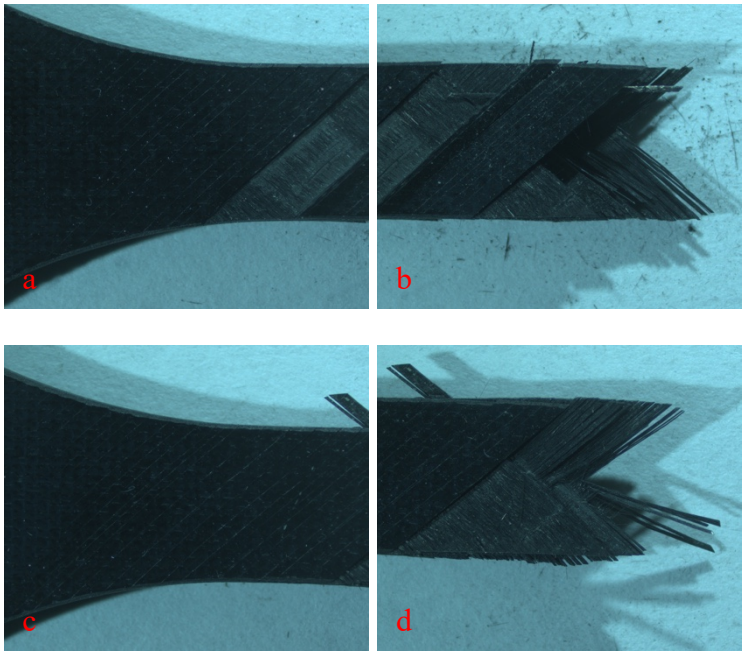

Figure 166: Images of the ±45 NanoStitch composite specimen NS-02-14 tested in tension-tension fatigue (σ_{max} = 214 MPa, N_f = 14). (a-d) face view.

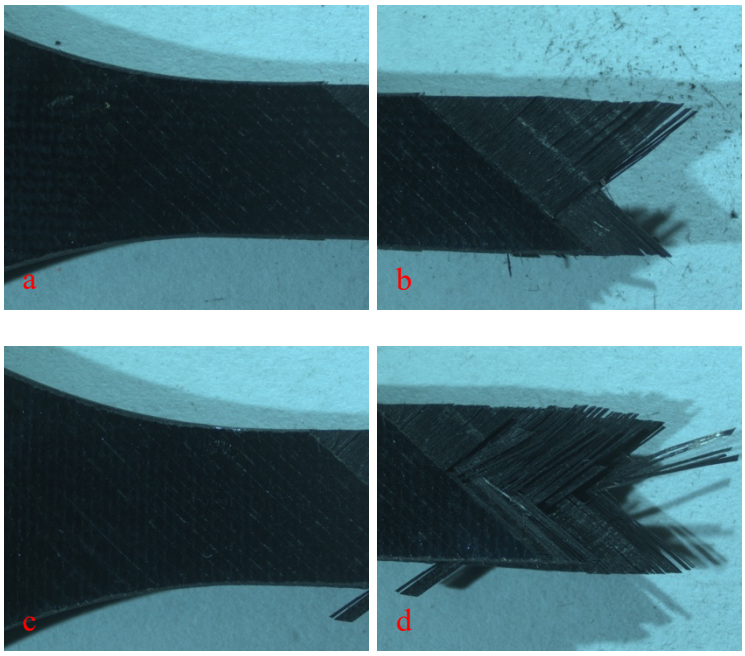

Figure 167: Images of the ±45 NanoStitch composite specimen NS-02-14 tested in tension-tension fatigue (σ_{max} = 214 MPa, N_f = 14). (a-d) face view.

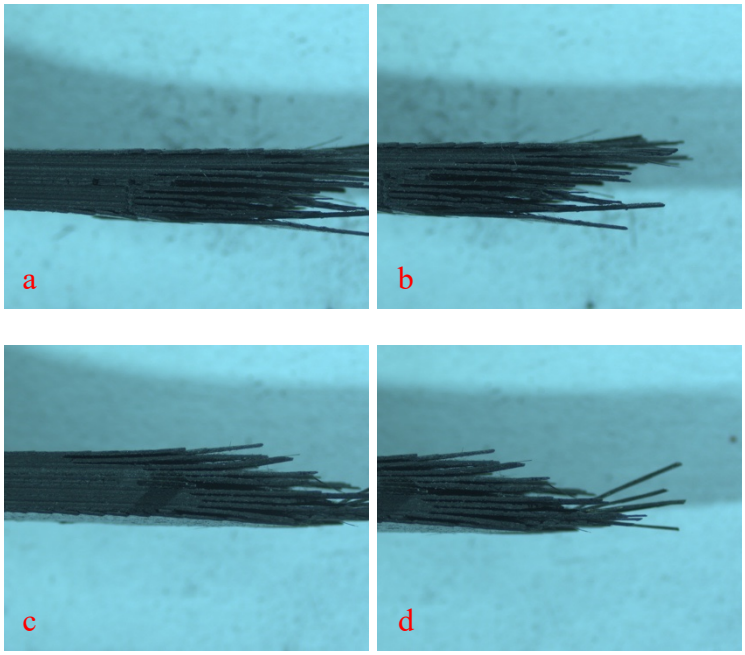

Figure 168: Images of the ±45 NanoStitch composite specimen NS-02-14 tested in tension-tension fatigue (σ_{max} = 214 MPa, N_f = 14). (a-d) side view.

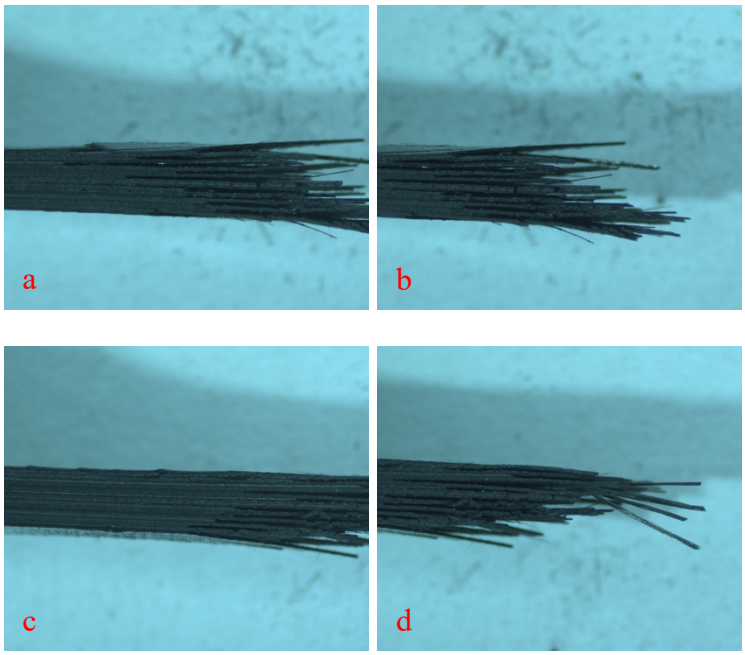

Figure 169: Images of the ±45 NanoStitch composite specimen NS-02-14 tested in tension-tension fatigue (σ_{max} = 214 MPa, N_f = 14). (a-d) side view.

Bibliography

[1] S. Wicks *et al.*, "Nano-Engineered Composites Reinforced with Aligned Carbon Nanotubes (CNT)," in *Nanotechnology 2008: Materials, Fabrication, Particles, and Characterization*, 1st ed., vol. 1, NSTI-Nanotech, 2008, pp. 194–197.

[2] E. J. Garcia, B. L. Wardle, J. A. Hart, and N. Yamamoto, "Fabrication and Multifunctional Properties of a Hybrid Laminate and Aligned Carbon Nanotubes Grown In Situ," *Composite Science and Technology*, no. 68, pp. 2034–2041, Mar. 2008.

[3] E. J. Garcia, B. L. Wardle, and A. J. Hart, "Joining Prepreg Composite Interfaces with Aligned Caron Nanotubes," *Composites: Part A*, no. 39, pp. 1065–1070, Mar. 2008.

[4] C. Gouldstone, D. Degtiarov, and R. D. Williams, "Reinforcing Ply Drop Interfaces Using Vertically-Aligned Carbon Nanotubes Forests," presented at the International SAMPE Technical Conference, Jan. 2014.

[5] H. Conway, D. Chebot, C. Gouldstone, and R. Williams, "Fatigue Response of Carbon Fiber Epoxy Laminate with Vertically-Aligned Carbon Nanotubes Interfacial Reinforcement," May 2015.

[6] W. Callister and D. Rethwisch, *Materials Science and Engineering: An Introduction*, 8th ed. Wiley, 2010.

[7] W. Smith, *Principles of Material Science and Engineering*, 1st ed. McGraw-Hill, 1986.

[8] "Toray T300 Standard Modulus Carbon Fiber Datasheet." Toray Composite Materials America, Apr. 13, 2018.

[9] "Hexcel HexTow AS4 Carbon Fiber Datasheet." Hexcel, Accessed: Jan. 14, 2021. [Online].

[10] X. Ni, C. Furtado, N. K. Fritz, R. Kopp, P. P. Camanho, and B. L. Wardle, "Interlaminar to Intralaminar Mode I and II Crack Bifurcation Due to Aligned Carbon Nanotube Reinforcement of Aerospace-Grade Advanced Composites," *Composite Science and Technology*, no. 190, pp. 1–11, 2020.

[11] R. Guzman de Villoria, P. Hallander, L. Ydrefors, P. Nordin, and B. L. Wardle, "In-Plane Strength Enhancement of Laminated Composites via Aligned Carbon Nanotube Interlaminar Reinforcement," *Composite Science and Technology*, no. 133, pp. 33–39, 2016.

[12] S. G. Miller *et al.*, "Out-Life Characteristics of IM7/977-3 Composites." NASA, Jul. 15, 2020, Accessed: Jan. 04, 2021. [Online].

[13] "Cytec CYCOM 977-3 Epoxy Resin System Datasheet." Cytec.

[14] "Hexcel HexTow IM7 Carbon Fiber Datasheet." Hexcel.

[15] M. Wilkinson, "Mechanical Properties and Fatigue Behavior of Unitized Composite Airframe Structures at Elevated Temperature," Air Force Institute of Technology, Wright Patterson AFB, 2014.

[16] Y. C. Lou and R. A. Schapery, "Viscoelastic Characterization of a Nonlinear Fiber-Reinforced Plastic," *Journal of Composite Materials*, vol. 5, no. 2, pp. 208–234, Feb. 1971.

[17] R. A. Schapery, “On the Characterization of Nonlinear Viscoelastic Materials,” *Polymer Engineering and Science*, vol. 9, no. 4, pp. 295–310, Jul. 1969.
[18] D. Peretz and Y. Weitsman, “Nonlinear Viscoelastic Characterization of FM-73 Adhesive,” *Journal of Rheology*, vol. 26, no. 3, pp. 245–261, 1982.
[19] K. L. Jerina, B. A. Sanders, R. A. Schapery, and R. W. Tung, “Short Fiber Reinforced Composite Materials,” *American Society for Testing and Materials*, vol. 1982, no. 772, Jan. 1982.

REPORT DOCUMENTATION PAGE

Form Approved
OMB No. 074-0188

1. REPORT DATE *(DD-MM-YYYY)*	2. REPORT TYPE	3. DATES COVERED *(From – To)*
25-03-2021	Master's Thesis	August 2019 – March 2021

TITLE AND SUBTITLE

Mechanical Properties and Performance of a Novel Nano-Engineered Unitized Composite for Aerospace Systems

5a. CONTRACT NUMBER

5b. GRANT NUMBER

5c. PROGRAM ELEMENT NUMBER

6. AUTHOR(S)

Lam, Benjamin C., Second Lieutenant, USAF

5d. PROJECT NUMBER

5e. TASK NUMBER

5f. WORK UNIT NUMBER

7. PERFORMING ORGANIZATION NAMES(S) AND ADDRESS(S)
Air Force Institute of Technology
Graduate School of Engineering and Management (AFIT/ENY)
2950 Hobson Way, Building 640
WPAFB OH 45433-8865

8. PERFORMING ORGANIZATION REPORT NUMBER

AFIT-ENY-MS-21-M-306

9. SPONSORING/MONITORING AGENCY NAME(S) AND ADDRESS(ES)

Intentionally Left Blank

10. SPONSOR/MONITOR'S ACRONYM(S)

11. SPONSOR/MONITOR'S REPORT NUMBER(S)

12. DISTRIBUTION/AVAILABILITY STATEMENT
DISTRUBTION STATEMENT A. APPROVED FOR PUBLIC RELEASE; DISTRIBUTION UNLIMITED.

13. SUPPLEMENTARY NOTES
This material is declared a work of the U.S. Government and is not subject to copyright protection in the United States.

14. ABSTRACT
Carbon nanotubes (CNTs) exhibit outstanding mechanical properties, such as exceptionally high tensile stiffness and strength, combined with excellent electrical and thermal characteristics. This research investigates the mechanical properties and performance of a newly developed hybrid nano-engineered composite. The carbon fiber/polymer matrix composite incorporates a forest of vertically aligned CNTs, called NanoStitch, between the prepreg plies. Basic tensile properties of both material systems were investigated for both on-axis [0/90] and off-axis [±45] fiber orientations at room temperature. Tension-tension fatigue tests were performed with a frequency of 1.0 Hz and a ratio of minimum stress to maximum stress of R= 0.05. Fatigue run-out was set to $2x10^5$ cycles. The presence of the NanoStitch reinforcement did not result in a decrease in tensile or fatigue properties when compared to the control PMC. Additionally, creep and recovery tests were performed to study the time-dependent deformation behavior of the nano-engineered composite with ±45 fiber orientation. The test results were analyzed in context of Schapery's nonlinear viscoelastic model. The model was successfully characterized and validated using experimental data. Thus it was determined that Schapery's viscoelastic deformation theory can be used to predict the off-axis deformation behavior of the hybrid nano-engineered composite.

15. SUBJECT TERMS
Composite, Nano-Engineered, Carbon Nanotubes

16. SECURITY CLASSIFICATION OF:			17. LIMITATION OF ABSTRACT	18. NUMBER OF PAGES	19a. NAME OF RESPONSIBLE PERSON
a. REPORT	b. ABSTRACT	c. THIS PAGE			Dr. Marina Ruggles-Wrenn, AFIT/ENY
U	U	U	UU	172	19b. TELEPHONE NUMBER *(Include area code)* (937) 255-3636, ext. 4641 (marina.ruggles-wrenn@afit.edu)

Standard Form 298 (Rev. 8-98)
Prescribed by ANSI Std. Z39-18